UNIVERSITY OF CALIFORNIA

Los Angeles

Geologic Mapping and Geophysical Modeling of the Surface of Ceres: Insights into the Structural, Mechanical, and Compositional Properties of the Solar System's Innermost Dwarf Planet

A dissertation submitted in partial satisfaction of the

requirements for the degree of Doctor of Philosophy

in Geophysics & Space Physics

by

Kynan Horace George Hughson

2019

ABSTRACT OF THE DISSERTATION

Geologic Mapping and Geophysical Modeling of the Surface of Ceres:
Insights into the Structural, Mechanical, and Compositional Properties of the Solar System's Innermost Dwarf Planet

by

Kynan Horace George Hughson
Doctor of Philosophy in Geophysics & Space Physics
University of California, Los Angeles, 2019
Professor Christopher T. Russell, Chair

When NASA's Dawn mission arrived at Ceres on March 6, 2015 it made history by becoming the first spacecraft to enter orbit around a second extraterrestrial object after leaving the asteroid Vesta in September 2012. Dawn thoroughly investigated the surface and deep interior of the dwarf planet Ceres, the largest object in the main asteroid belt, through a series of successively lower mapping orbits until its end of mission on November 1, 2018. Prior to Dawn's arrival Ceres was known to be the largest C-type asteroid, and was suspected of being rich in water ice and other hydrated materials. As a putative remnant of the earliest phases of rocky planet formation, Ceres was thought to contain clues as to how planetesimals accreted and how volatiles arranged themselves throughout the inner solar system during the tumultuous era of planet formation. The Dawn mission's goals were to further elucidate the structure and

composition of the early solar system, which would lead to an increased understanding of the conditions present during terrestrial planet formation, and to determine the chemical, geological, and structural nature of the largest surviving planetary embryos: Vesta and Ceres. At Ceres, this was accomplished by meticulously characterizing the surface geology, surface and near-surface geochemistry, and interior structure via a combination of photo geology; visible, infrared, and nuclear spectroscopy; and gravimetry. This dissertation contributes to the objectives of the Dawn mission by aiding in the global geologic mapping effort of Ceres, identifying and classifying geological features indicative of its compositional and physical properties, and then applying geophysical techniques to these features in order to estimate these properties, particularly the water ice content of the near-surface. Understanding the quantity and distribution of water ice in the upper layer of Ceres is paramount for understanding both its geochemical evolution and the nature of the early solar system. The investigations presented in this dissertation reveal that Ceres is ubiquitously covered in geologic features suggestive of significant quantities of near-surface ground ice, namely large constructional mountains and hills, and a broad spectrum of lobate flow and mass wasting deposits. The observed mass wasting features exhibits physical characteristics and runout efficiencies similar to many ground ice mediated flows on Earth, Mars, and Iapetus such as long run-out landslides and frozen debris flows. Additionally, many craters on Ceres were observed to emanate fluidized appearing ejecta similar to examples found on Mars, Ganymede, and other icy worlds. Analyzing the mobilities of these ejecta using a kinematic-dynamic sliding ejecta emplacement model indicated that the cerean crust is significantly weaker than competent silicate rock at impacting conditions, and that the frictional properties of its surface are consistent with a rock-ice mixture. Finally, a unique fractured terrain named Nar Sulcus was identified on Ceres' southern hemisphere that displayed topography

suggestive of elastic flexure. By applying a flexural-cantilever model to the observed topography, the flexural rigidity of the cerean crust was estimated to be similar to those of outer solar system moons such as Europa, Ganymede, and Enceladus, which are several orders of magnitude less rigid than the terrestrial planets. From the aforementioned observations and investigations, the ground ice content of the cerean crust is estimated to be ~30-70 vol %, although there is likely significant regional heterogeneity in its distribution. This result is significant as it independently supports the interpretation that Ceres is a water rich dwarf planet, and that large quantities of ice can be sequestered within massive C-type asteroids over geologically long time periods. This is particularly exciting as carbonaceous chondrites are the most spectrally similar meteorites to C-type asteroids, and their water is the most isotopically similar to the Earth's oceans. In light of the results presented in this dissertation, and by a myriad of other authors, it increasingly appears that a significant portion of the Earth's water was likely delivered by Ceres-like asteroids.

The dissertation of Kynan Horace George Hughson is approved.

Abby Kavner

Seul Gi Moon

Gilles F. Peltzer

Christopher T. Russell, Committee Chair

University of California, Los Angeles

2019

For Michelle, Katheryn, Sharon, and Michael

TABLE OF CONTENTS

LIST OF FIGURES

LIST OF TABLES

ACKNOWLEDGMENTS

This dissertation would not have been possible without generous financial support from NASA's Discovery program, UCLA Graduate Division through the Dissertation Year Fellowship, and the UCLA Department of Earth, Planetary, and Space Sciences.

Thank you to my advisor, Professor Christopher T. Russell, for the opportunity to work on NASA's Dawn mission. His support, both financial and professional, and belief that an undergraduate geophysicist from rural New Brunswick could substantially contribute to the exploration of new worlds is the foundation on which this dissertation is built. I am especially grateful for the encouragement he gave me to pursue my own scientific ideas, and his patience when testing those ideas turned out to be much more difficult than I originally anticipated.

Thank you to my committee members, Professor Abby Kavner, Assistant Professor Seul Gi Moon, and Professor Gilles F. Peltzer for many informative and scientifically stimulating discussions. Their comments and constructive criticisms thoroughly strengthened this dissertation.

Thank you to the Dawn Science Team for warmly welcoming an inexperienced graduate student. Not only did they treat me and my ideas with respect, but they also provided me with multiple opportunities to contribute to the mission's science goals. Specifically, I thank Debra Buzckowski, Jean-Philippe Combe, Britney Schmidt, Jennifer Scully, Hanna Sizemore, and David Williams for allowing me to participate in the geological mapping campaign of Ceres,

trusting me to characterize the geology of the first surface H_2O detection on Ceres, and inviting me to be part of the team's 'ground ice working group'.

I collectively thank the many other faculty at UCLA and the University of New Brunswick who have, either directly or indirectly supported my educational and research goals, including: Ray Ingersoll, Craig Manning, Kevin McKeegan, Jonathan Mitchell, Ben Newling, William Newman, John Spray, John Wasson, An Yin, and Ed Young.

Thank you to my many friends who supported me throughout this undertaking, and continue to entertain my fringe hypotheses about how the universe works. Thank you Amanda, Ashley, Bryce, David, Emily, Erik, Erin, Heather, Jennifer, Jon, Kaitlyn, Michelle J., Mickey, Mojhgan, Raquel, Ricky, Sandy; I'm proud to call each and every one of you my friend.

I thank my parents Sharon and Michael, as well as my sister Katheryn, for the sacrifices they made for me. Words will never be able express how grateful I am for their enduring love and support.

Finally, I thank my wife, Michelle. Not a single word would have been possible without you.

Chapter 2 is adapted from works that the author of this dissertation undertook as both a lead and co-author, which are published as:

- J.-P. Combe, T. B. McCord, F. Tosi, E. Ammannito, F. G. Carrozzo, M. C. De Sanctis, A. Raponi, S. Byrne, M. E. Landis, K. H. G. Hughson, C. A. Raymond, C. T. Russell,

(2016). Detection of local H_2O exposed at the surface of Ceres. *Science* 353, Issue 6303. DOI: 10.1126/science.aaf3010

- K. H. G. Hughson, C. T. Russell, D. A. Williams, D. L. Buczkowski, S. C. Mest, J. H. Pasckert, J. E. C. Scully, J.-P. Combe, T. Platz, O. Ruesch, F. Preusker, R. Jaumann, A. Nass, T. Roatsch, A. Nathues, M. Schaefer, B. E. Schmidt, H. T. Chilton, A. Ermakov, S. Singh, L. A. McFadden, C. A. Raymond, (2018). The Ac-5 (Fejokoo) quadrangle of Ceres: Geologic map and geomorphological evidence for ground ice mediated surface processes. *Icarus* 316, 63-83. https://doi.org/10.1016/j.icarus.2017.09.035

Chapter 3 is based upon works that the author of this dissertation undertook as a co-author, which are published as:

- J.-P. Combe, A. Raponi, F. Tosi, M. C. De Sanctis, F. G. Carrozzo, F. Zambon, E. Ammannito, K. H. G. Hughson, A. Nathues, M. Hoffmann, T. Platz, G. Thangjam, N. Schorghofer, S. Schröder, S. Byrne, M. E. Landis, O. Ruesch, T. B. McCord, K. E. Johnson, S. M. Singh, C. A. Raymond, C. T. Russell, (2019). Exposed H_2O-rich areas detected on Ceres with the dawn visible and infrared mapping spectrometer. *Icarus* 318, 22-41. https://doi.org/10.1016/j.icarus.2017.12.008
- D. L. Buczkowski, B. E. Schmidt, D. A. Williams, S. C. Mest, J. E. C. Scully, A. I. Ermakov, F. Preusker, P. Schenk, K. A. Otto, H. Hiesinger, D. O'Brien, S. Marchi, H. Sizemore, K. Hughson, H. Chilton, M. Bland, S. Byrne, N. Schorghofer, T. Platz, R. Jaumann, T. Roatsch, M. V. Sykes, A. Nathues, M. C. De Sanctis, C. A. Raymond, C. T. Russell, (2016). The geomorphology of Ceres. *Science* 353, Issue 6303. DOI: 10.1126/science.aaf4332

- B. E. Schmidt, K. H. G. Hughson, H. T. Chilton, J. E. C. Scully, T. Platz, A. Nathues, H. Sizemore, M. T. Bland, S. Byrne, S. Marchi, D. P. O'Brien, N. Schorghofer, H. Hiesinger, R. Jaumann, J. H. Pasckert, J. D. Lawrence, D. Buczkowski, J. C. Castillo-Rogez, M. V. Sykes, P. M. Schenk, M. C. De Sanctis, G. Mitri, M. Formisano, J.-Y. Li, V. Reddy, L. LeCorre, C. T. Russell, C. A. Raymond, (2017). Geomorphological evidence for ground ice on dwarf planet Ceres. *Nature Geoscience* 10, 338-343. https://doi.org/10.1038/ngeo2936

Chapter 4 is an adapted version of the following publication, of which the author of this dissertation was the lead author:

- K. H. G. Hughson, C. T. Russell, B. E. Schmidt, H. T. Chilton, H. Sizemore, P. M. Schenk, C. A. Raymond, (2019a). Fluidized appearing ejecta on Ceres: Implications for the mechanical properties, frictional properties, and composition of its shallow subsurface. *Journal of Geophysical Research:Planets* 124. https://doi.org/10.1029/2018JE005666

Chapter 5 is an adapted version of the following publication, of which the author of this dissertation was the lead author:

- K. H. G. Hughson, C. T. Russell, B. E. Schmidt, B. Travis, F. Preusker, A. Neesemann, H. G. Sizemore, P. M. Schenk, D. L. Buczkowski, J. C. Castillo-Rogez, C. A. Raymond, (2019b). Normal faults on Ceres: Insights into the mechanical properties and thermal history of Nar Sulcus. *Geophysical Research Letters* 46, 80-88. https://doi.org/10.1029/2018GL080258

VITA

Education

May 2017: Master of Science, Geophysics & Space Physics, University of California, Los Angeles

May 2014: Bachelor of Science with Honors, Physics & Geology, University of New Brunswick, Fredericton

Honors and Awards

Sept. 2018: UCLA Dissertation Year Fellowship

Sept. 2018: UCLA Department of Earth, Planetary, and Space Sciences, Eugene B. Waggoner Prize

Sept. 2018: UCLA Department of Earth, Planetary, and Space Sciences, Excellence in Teaching Award

May 2017: Joint Japan Geophysical Union-American Geophysical Union Meeting, Outstanding Student Paper Award

Dec. 2015: American Geophysical Union Fall Meeting, Outstanding Student Paper Award

May 2014: University of New Brunswick, Lieutenant Governor's Silver Medal in Science

Lead Author Publications

2019: Hughson, K. H. G. et al. *Journal of Geophysical Research* (2019a)

2019: Hughson, K. H. G. et al. (2019b), *Geophysical Research Letters* 40, 80-88

2018: Hughson, K. H. G. et al. (2018), *Icarus* 316, 63-83

Co-author Publications

2019: Chilton, H. T. et al. (2019), *Journal of Geophysical Research* 124

2019: Combe, J.-P. et al. (2019), *Icarus* 318, 22-41

2019: Ermakov, A. I. et al. (2019), *Journal of Geophysical Research* 124

2019: Singh, S. et al. (2019), *Icarus* 318, 147-169

2019: Sizemore, H. G. et al. (2019), *Journal of Geophysical Research* 123

2018: Buczkowski, D. L. et al. (2018), *Journal of Geophysical Research* 123, 3188–3204

2018: Platz, T. et al. (2018), *Icarus* 316, 140-153

2018: Ruesch, O. et al. (2018), *Icarus* 316, 14-27

2018: Scully, J. E. C. et al. (2018), *Icarus* 316, 46-62

2017: Sizemore, H. G. et al. (2017), *Geophysical Research Letters* 44, 6570–6578

2017: Schmidt, B. E. et al. (2017), *Nature Geoscience* 10, 338-343

2016: Buczkowski, D. L. et al. (2016), *Science* 353, Issue 6303

2016: Combe, J.-P. et al. (2016), *Science* 353, Issue 6303

Lead Author Conference Presentations

American Geophysical Union, Fall Meeting: 2015, 2016, 2017, 2018

Asia Oceania Geosciences Society, Annual Meeting: 2018

Geological Society of America, Annual Meeting: 2015a, 2015b, 2016, 2017, 2018

Joint Meeting of the Japanese and American Geophysical Unions: 2017

Lunar and Planetary Science Conference: 2015, 2016a, 2016b, 2017, 2018

1 Introduction and Background

1.1 Ceres and the Early Solar System

The history of the solar system can be broadly divided into three evolutionary periods: the solar nebula phase, the primordial phase, and the modern phase (Coradini et al., 2011). The solar nebula phase is conventionally considered to coincide with the condensation of the first solids from the nebular gas cloud/circumsolar disc, and end with the dispersal of said nebular gas as the Sun entered the T Tauri phase of its evolution. Despite this period in the history of our solar system lasting only ~10 Ma from its creation 4.568 Ga ago, the gas/ice giants likely formed in their entirety during this phase (Coradini et al., 2010). As the protoplanetary disk rotated, its gas and dust components settled to the mid-plane, and gradually clumped together to form larger and larger bodies (e.g. Goldreich and Ward, 1973). Numerous models have been proposed to explain the details of the processes by which clumping and sticking of dust particles results in the formation of planetesimals, which likely took place during the first 5 million years of the solar system (e.g. O'Brien and Sykes, 2011). At the end of the solar nebula phase the protoplanetary disk is thought to have been populated with ten-km scale planetesimals, hundred-km scale planetary embryos, and the four giant planets: Jupiter, Saturn, Uranus, and Neptune (Coradini et al., 2011).

Astronomical observations of young solar systems that are still coalescing conceptually support the aforementioned model of planetary formation. For example, the Atacama Large Millimeter/submilimeter Array (ALMA) has observed a dust rich protoplanetary disk around the star HD 163296 (e.g. Pinte et al., 2018). A giant planet, has been observed within the plane of this disk, at ~260 AU from HD 163296 (Pinte et al., 2018), which provides direct evidence for the formation of planets in accretion disks (e.g. Lagrange et al., 2010) (Figure 1-1). Thus,

applying the spirit of uniformitarianism, it is reasonable to assume that the planets in our solar system also formed from accretion within a protoplanetary disk.

The primordial phase of solar system evolution consisted primarily of the accretion of the terrestrial planets as well as the dynamical excitation and clearing of the main asteroid belt via resonances with Jupiter and Saturn (Morbidelli et al., 2009) (Figure 1-2). Under current best estimates for the initial conditions of the solar system, the Nice model predicts that at approximately 3.8-4.0 Gyr ago Jupiter and Saturn fell into a 2:1 resonance that destabilized the orbits of the other planets and caused the ancient Kuiper belt to be scattered into the inner solar system as well as its current location (Gomes et al., 2005). This event likely triggered the Late Heavy Bombardment (LHB) of the inner planets as well as the incorporation of outer solar system material into the main belt; however, the interpretation of much of the physical evidence for the LHB, namely the provenance of $^{40}Ar/^{39}Ar$ dated Apollo lunar samples, remains hotly debated (Boehnke & Harrison, 2016). Additionally, it has been theorized that prior to the stabilization of Jupiter's orbit its inward migration depleted much of the main asteroid belt and made it an inhospitable region for planet formation, thus further obfuscating the origin of main belt material and preserving existing planetary embryos such as 4 Vesta (hereafter referred to as simply Vesta) and 1 Ceres (hereafter referred to simply as Ceres) in more or less their current form (Walsh et al., 2011). The LHB conventionally marks the end of the primordial phase of the solar system.

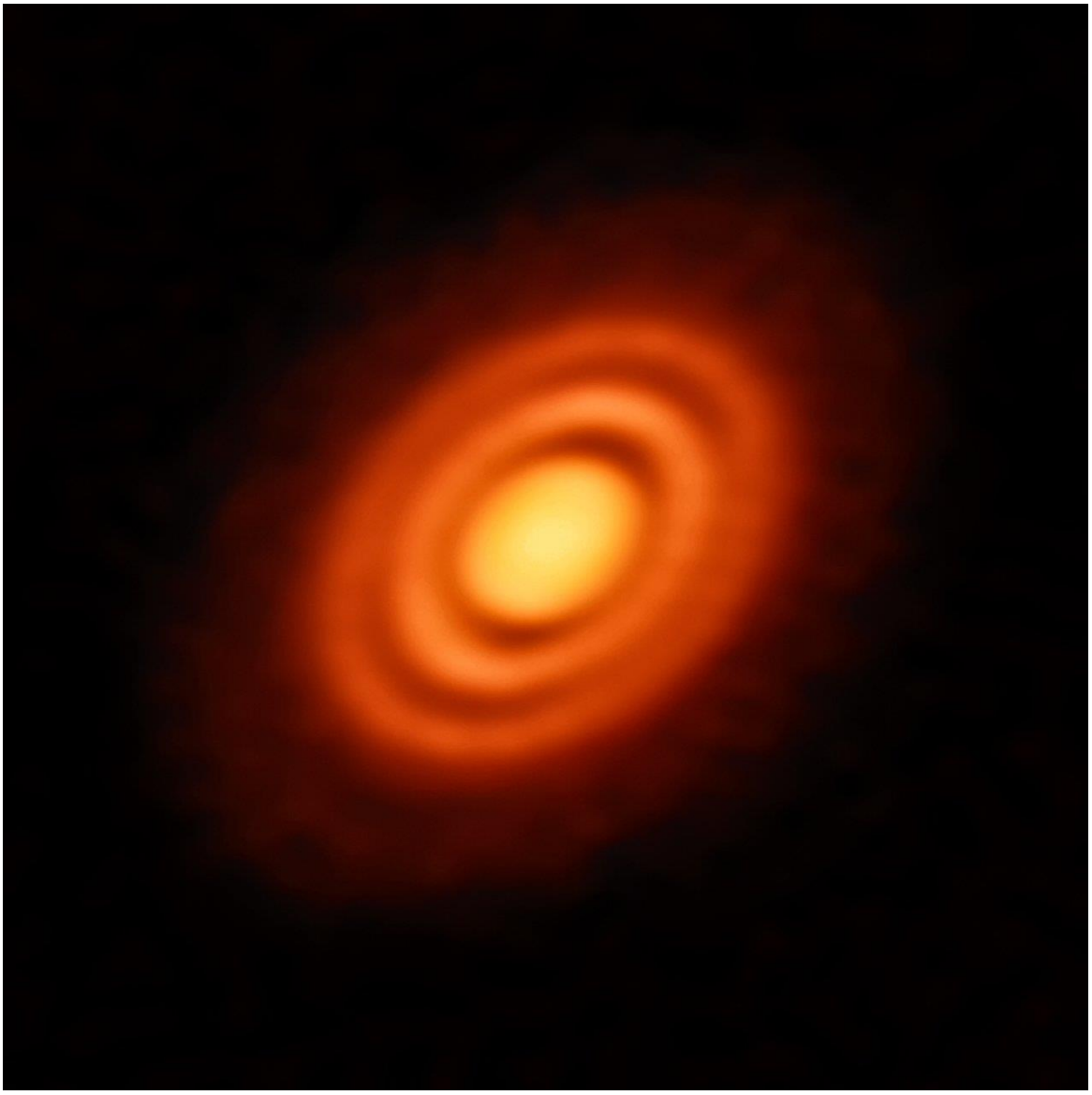

Figure 1-1. Image of a protoplanetary disk around the star HD 163296 as seen by ALMA. The three concentric annular gaps between the bright rings are indicative of dust grain and gas depletion, which are likely due to the presence of newly formed giant planets each roughly the mass of Saturn. Image credit: ESO, ALMA (ESO/NAOJ/NRAO); A. Isella; B. Saxton (NRAO/AUI/NSF)

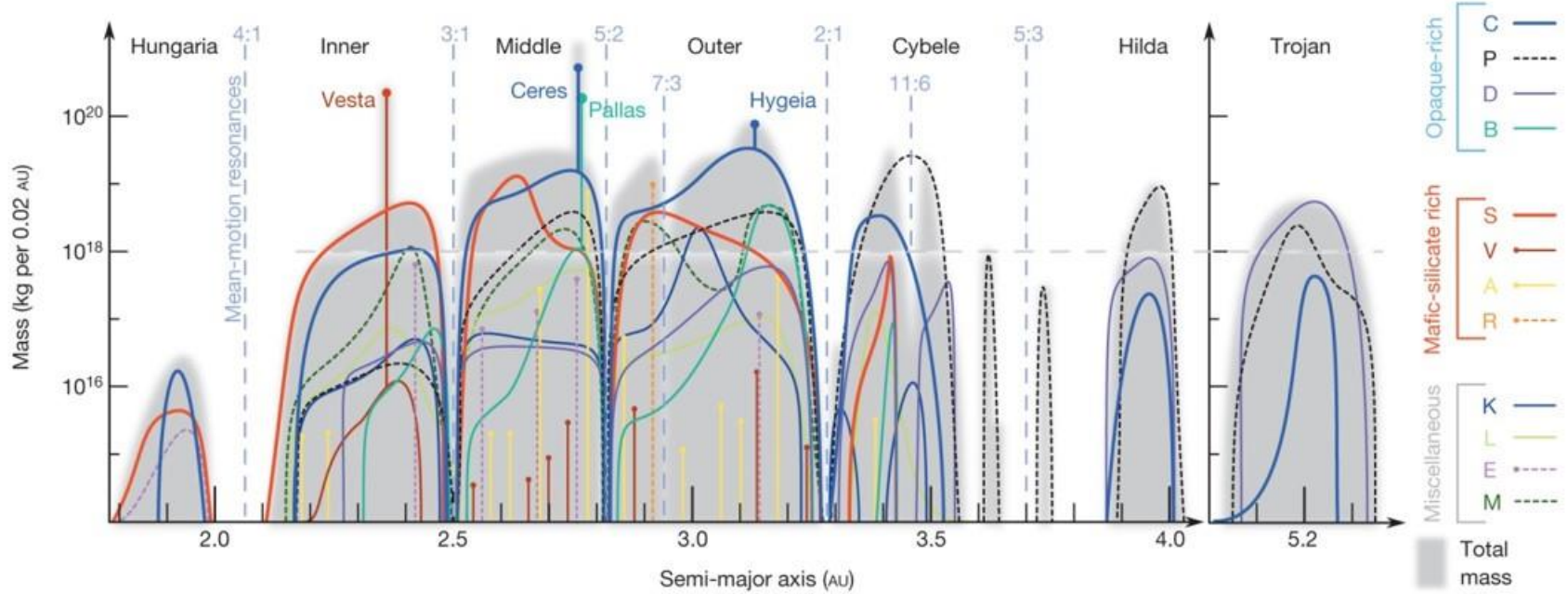

Figure 1-2. Mass density plot of the main asteroid belt adapted from Figure 3 in DeMeo & Carry (2014). Each colored line represents a different spectral class of asteroid. The grey background is the total mass within each 0.02 AU bin. Note the large number of strong mean-motion resonances with Jupiter (dashed vertical lines) that exist between the inner and outer portions of the main belt, and the paucity of material around these resonances. These strong interactions with the giant planets (particularly Jupiter) render the modern main belt an inhospitable environment for accretion.

The modern period extends from the end of the LHB until the present time, and is characterized by secular collisional and dynamical evolution of the planets and planetesimals.

The dwarf planet Ceres is the largest object in the main asteroid belt (Figure 1-3) both in terms of volume (mean geometric radius 469.7 km ±0.2 km; Preusker et al., 2016) and mass ($9.38416 \pm 0.00013 \times 10^{20}$ kg; Park et al., 2016); it single handedly accounts for approximately one third of the mass between Mars and Jupiter (e.g. Pitjeva, 2003). Ceres is the only recognized dwarf planet in the inner solar system and has a mean density of 2162 ± 8 kg/m^3, which suggests a composition that is rich in water ice and/or hydrated materials (Russell et al., 2016; Thomas et al., 2005; McCord & Sotin, 2005; Castillo-Rogez & McCord, 2010; Zolotov, 2009). Like a handful of other large asteroids (e.g. 2 Pallas and 4 Vesta) Ceres is thought to have remained largely intact since its formation, which is poorly constrained to either the solar nebula phase or early primordial phase (first few Ma of this period) of the solar system (Coradini et al., 2011). Hubble Space Telescope observations have determined that Ceres has an average geometric albedo of ~0.09 that in general displays very little global variability (Li et al., 2016). This low albedo makes Ceres an exceptionally dark object. The visible and near-IR spectral features of Ceres are typical of C-type asteroids, and are somewhat compatible with carbonaceous chondrite meteorites (Rivkin et al., 2006). Unlike Vesta, no meteorites have been convincingly linked directly to Ceres; this is mainly due to spectral discrepancies between Ceres and CM chondrites (the class of meteorites most spectrally similar to Ceres) in both the UV and 3-μm region (Burbine, 1998).

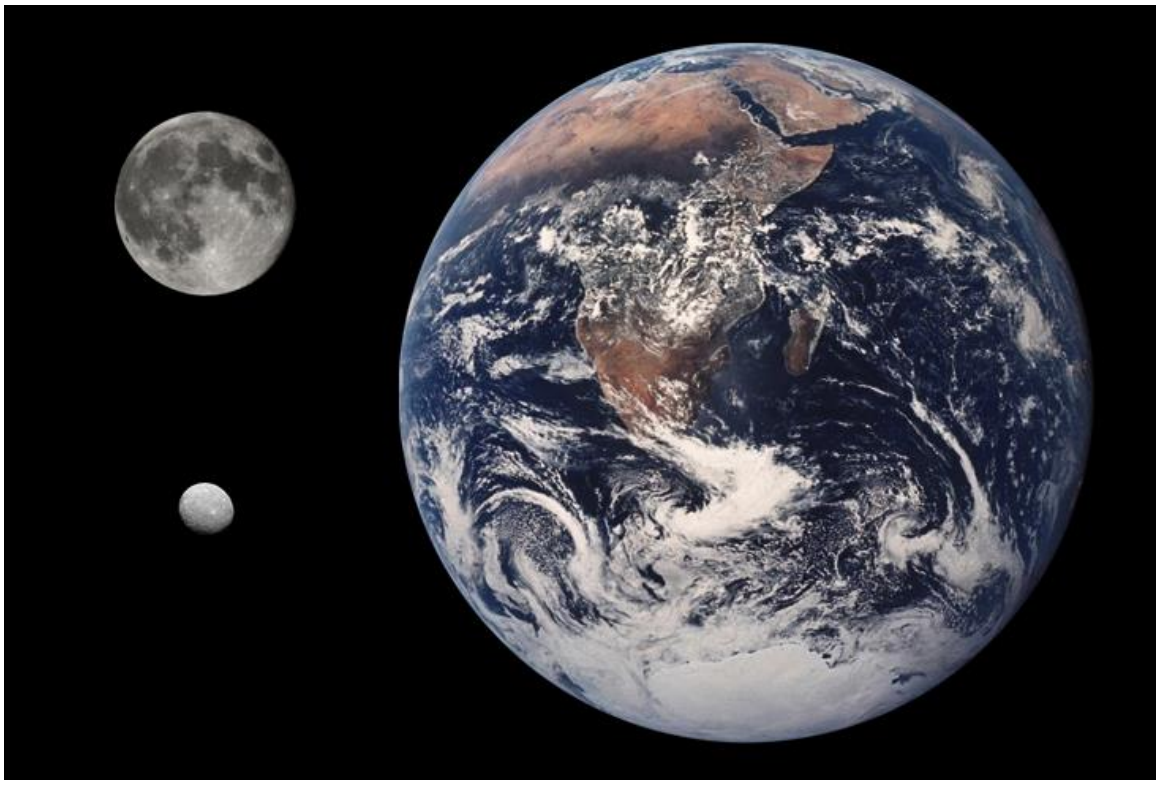

Figure 1-3. A comparison of the relative sizes of the Earth (right), Moon (top left), and Ceres (bottom left). With a mean diameter of 948 km, Ceres has only ~2% the volume of Earth's moon, and a disk area roughly equal to that of the American state of Texas. Image Credit: NASA/JPL.

1.2 NASA's Dawn Mission to Vesta and Ceres

As the terrestrial planets accreted from collisions of planetary embryos and planetesimals during the primordial phase of our solar system, the vast majority of the geological and geochemical information regarding rocky planet formation contained within these building blocks was lost. This was primarily due to disassembly and thermal processing of these planetesimals and planetary embryos as they were assimilated into the growing and differentiating terrestrial planets (Chambers, 2014). Thus, in order to study the processes that created the main belt, planetesimals, planetary embryos, and by extension the terrestrial planets, as well as the thermal, chemical, and dynamical properties of the early solar system it is necessary to observe the surviving protoplanets from the earliest phases of our solar system. Recognizing this, in 2001 NASA selected the Discovery class Dawn mission to explore the two most massive main belt protoplanets: Vesta and Ceres.

The Dawn mission had three primary science drivers (Russell & Raymond, 2011):

1. Investigate the conditions that existed during the earliest stages of solar system formation by observing the two largest inner solar system relics of that era;
2. Characterize the geology, composition, and structure of Vesta and Ceres; thus improving our understanding of the building blocks of terrestrial planets; and
3. Compare and contrast the formation and evolution of two seemingly very different protoplanets, the apparently anhydrous Vesta versus the apparently water-rich Ceres, in order to better understand what factors control planetary growth and evolution.

In order to carry out its mission of basic exploration, the Dawn spacecraft was equipped with three scientific instrument packages in addition to its communication array which also served as a radio science package capable of returning detailed gravimetric and radar data (Konopliv et al., 2011). These instrument suites were Dawn's Framing Camera (FC) imagers, Visual and InfraRed spectrometer (VIR), and Gamma Ray and Neutron Detector (GRaND) (Figure 1-4).

Dawn's doubly redundant FC is a multispectral charge-coupled device imager with a 1024 x 1024 pixel active area. In addition to its panchromatic imaging capabilities the FC can employ seven narrow band color filters centered at the following wavelengths: 438 nm, 555 nm, 653 nm, 749 nm, 829 nm, 917 nm, and 965 nm (Sierks et al., 2011). The primary science objectives of the FC were to globally characterize the geology and geomorphology of Vesta and Ceres via panchromatic and stereographic imaging, provide color imagery of both these protoplanets, and search for any possible moons around either object.

The hyperspectral VIR instrument combines a 432 band visible spectrometer (0.25-1.05 μm; 1.8 nm/band) with a 432 band infrared spectrometer (1.0-5.0 μm; 9.8 nm/band) on a common optical hub. VIR has full imaging capabilities and is able to function as either a scanning or pushbroom spectrometer. Each VIR data pixel contains the full spectral range of the instrument (De Sanctis et al., 2011). While the exact spatial resolution of VIR images varies significantly with imaging mode and photometric parameters, as a rule of thumb its resolving power is reduced by a factor of three relative to coincidently taken FC images. The primary science objectives of the VIR instrument were to characterize the mineralogy on the surface of both Vesta and Ceres, determine the distribution and relative abundances of major surface mineral species on both objects, and measure the thermal environment on both protoplanets.

The GRaND instrument is a nuclear spectrometer consisting of 21 individual sensors, which separately measure planetary gamma rays and neutrons as well as background signal from the spacecraft and space environment. While GRaND's spatial resolution is nominally around three orders of magnitude more coarse (approximately hundreds of kilometers as opposed to hundreds of meters) than the highest resolution FC and VIR images, it provides direct measurements of the abundances of many elements of geological interest, including but not limited to: Fe, Ni, Si, Cl, Th, K, C, and importantly, H. The data acquired by GRaND reflects the composition of approximately the upper 1 m of the target surface (Prettyman et al., 2011). The primary science objectives of GRaND were to globally measure the abundance of major rock forming elements, including hydrogen, on Vesta and Ceres, and to characterize planetary scale variations in those elements in the upper ~1 m of each objects' surface.

Additionally, the primary objective of the radio science experiment was to determine the gravity field at both Vesta and Ceres to a wavelength resolution of at least 90 km, and characterize each object's internal structure.

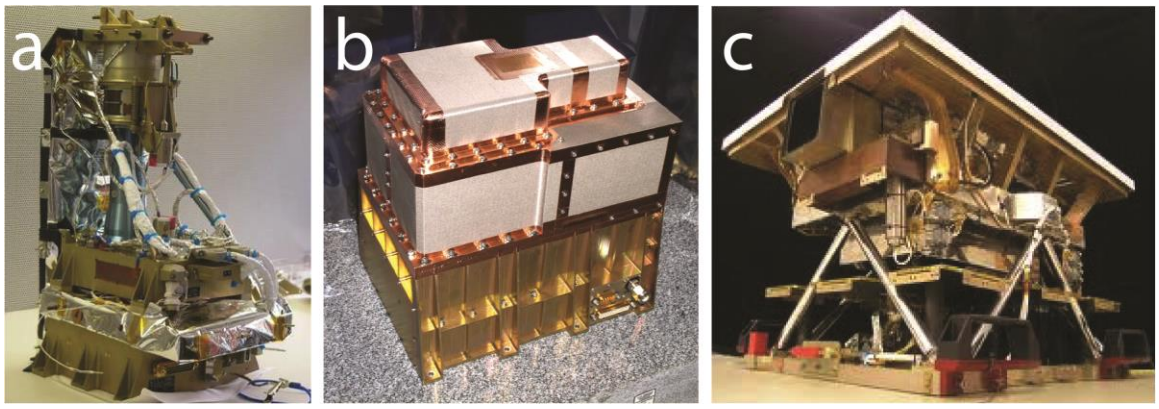

Figure 1-4. The Dawn spacecraft's three primary scientific instruments. (a) one of the two framing cameras (FC) provided by the Max Planck Institute for Solar System Research (Image credit: MPS). (b) the Gamma Ray and Neutron Detector (GRaND) contributed by the Los Alamos National Laboratory (Image credit: LANL). (c) the visible and infrared (VIR) mapping spectrometer provided by the Italian Space Agency and the Italian National Institute for Astrophysics (Image credit: INAF/ASI).

Launched in 2007, Dawn executed a Mars gravity assist in 2009 before entering orbit around Vesta in July of 2011. Dawn remained at Vesta until September 2012 when it broke orbit for Ceres. Located at a heliocentric distance of ~2.15-2.57, Vesta is the second most massive inner solar system asteroid comprising ~9% of the total mass of the main belt (Russell et al., 2012). In addition to its mass, Vesta is the second largest main belt object with a mean geometric diameter of ~525 km (Russell et al., 2012). During its investigation, Dawn observed Vesta to be a highly oblate spheroid whose surface geology was completely dominated by impact craters and impact cratering processes (Jaumann et al., 2012). Mineralogical observations of Vesta's surface by Dawn confirmed the connection between the Howardite-Eucrite-Diogenite (HED) meteorites and Vesta (e.g. McSween et al., 2013), while its two largest impact basins, Rheasilvia and Veneneia, were interpreted as the causative agents for these meteorites and the vestoid family of asteroids, as well as creating Vesta's distinctive oblate shape (Buratti et al., 2013) (Figure 1-5). In line with pre-Dawn expectations, the spacecraft observed this anhydrous silicate world to be fully differentiated into a HED-like crust, olivine-rich mantle, and iron core via controlled inversions from the radio science calculated gravity field (e.g. Neumann et al., 2014).

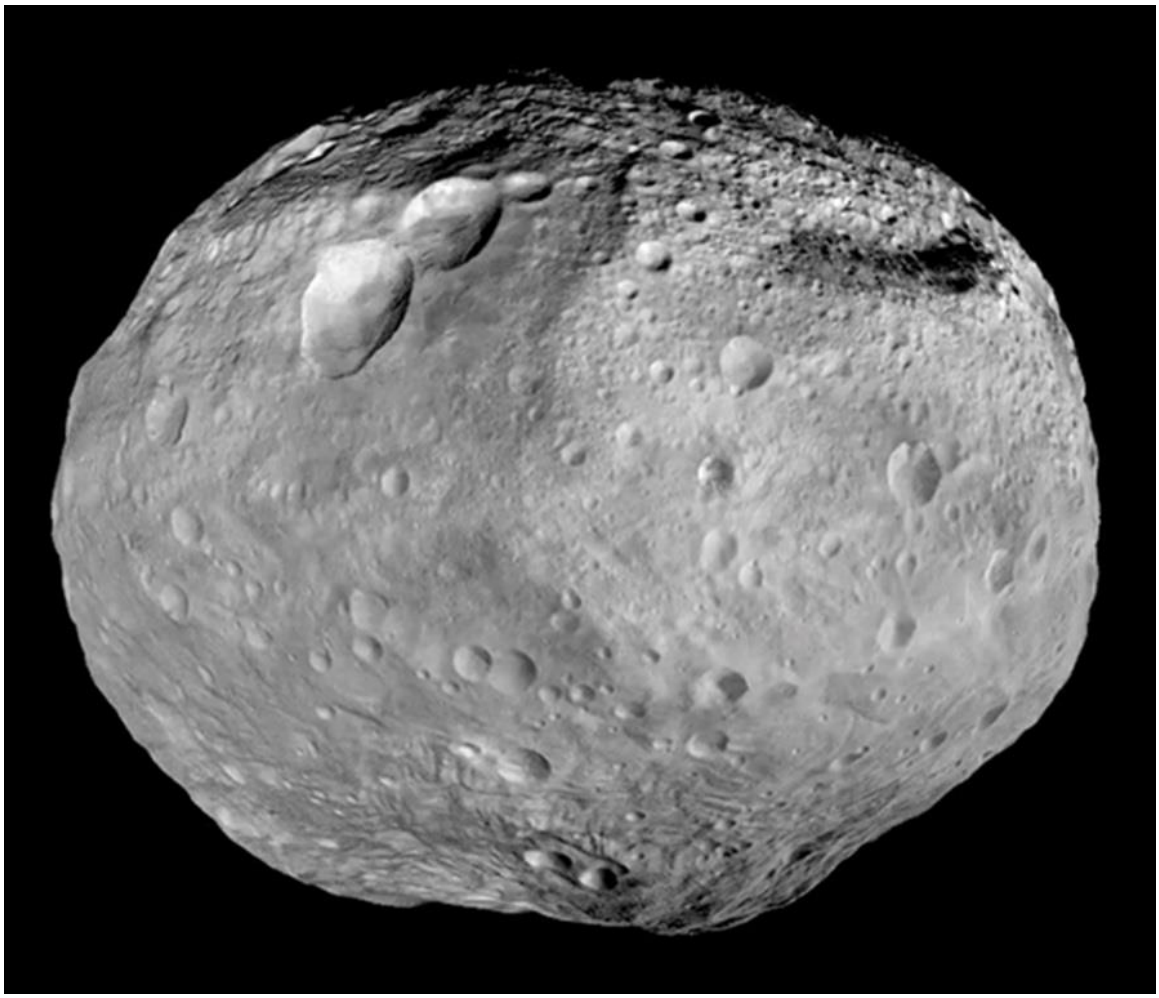

Figure 1-5. Full view of Vesta's ~570 km wide disk as seen by Dawn. The towering mountain at the bottom of the image, which is coincident with Vesta's south pole, is the central peak of the massive Rheasilvia impact basin. This impact event is the likely source of the vestoid family asteroids and HED meteorites. Image credit: NASA/JPL-Caltech/UCAL/MPS/DLR/IDA.

Dawn made history after a three year cruise ending in March 2015 when it entered into orbit around the dwarf planet Ceres becoming the first and, as of this writing, only spacecraft to ever orbit two unique extraterrestrial bodies. It also became the first manmade vehicle to directly encounter a dwarf planet, narrowly beating NASA's New Horizons spacecraft's July 2015 flyby of the Pluto-Charon system. This impressive feat was enabled by Dawn's use of highly efficient solar-electric xenon ion propulsion modules (Figure 1-6).

Despite Ceres' significant size (Ceres mean geometric radius is nearly twice as large as that of the next largest asteroid: Vesta, Figure 1-7) as well as it being the first asteroid known to science (Ceres was discovered on New Year's Day 1801 by Italian astronomer Giuseppe Piazzi), its genesis, orbital evolution, structure, composition, and surface geology remained poorly constrained prior to Dawn's arrival. Upon arrival, Dawn's first impressions of Ceres were very much similar to those at Vesta: a dusty world dominated by simple impact craters. This impression quickly gave way under scrutiny when Dawn started observing a plethora of intriguing geomorphic landforms distributed ubiquitously across its surface, such as: complex craters, central pit craters, floor fractured craters, collections of localized highly bright material (hereafter referred to as faculae), hills and mountains (hereafter referred to as tholi and montes respectively), long run-out and lobate mass wasting deposits, fluidized appearing ejecta, and rift zones (Figure 1-8). None of the aforementioned features have analogues on Vesta.

In addition to these intriguing landforms, Dawn's VIR and GRaND instruments observed spectral and elemental evidence for abundant water ice exposed sporadically at the surface and ubiquitously present at depths greater than a few decimeters for absolute latitudes greater than ~45° (Combe et al., 2016; Combe et al., 2019; Prettyman et al., 2017). VIR also detected strong spectral absorption features globally at 2.7 μm, 3.1 μm, and between 3.9-4.0 μm; however, the

band depth of each absorption feature displayed significant variability with geographic location (Figure 1-9 and Figure 1-10). The combination 2.7 μm and 3.1 μm absorption features are most likely caused by several weight percent of ammoniated OH-bearing phyllosilicate phases such as NH_4-montmorillonite and NH_4-annite (De Sanctis et al., 2015), while the 3.9-4.0 μm absorption is due to Mg- and occasionally Na-carbonates (De Sanctis et al., 2016; Carrozzo et al., 2018). These mineral phases are commonly associated with CI/CM chondrites, and indicate that the entire surface of Ceres underwent a significant degree of aqueous alteration (Rubin et al., 2007). This poses an interesting conundrum as water ice is not stable on the surface of Ceres at its current environmental conditions (Hayne & Ahronson, 2005).

Elemental hydrogen observations taken by Dawn's GRaND instrument further indicated an intimate relationship between the surface material and a subsurface water ice reservoir. From neutron observations, GRaND determined that the upper meter of Ceres contained ~16 wt. % water equivalent hydrogen at the equator, which increased steadily up towards ~29 wt. % at each pole (Figure 1-11). This represents a global surface abundance of hydrogen more than four orders of magnitude larger than what was observed at Vesta (Prettyman et al., 2017). While Prettyman et al. (2017) predicted that pore filling ground ice would become stable at the surface at absolute latitude greater than ~45°, the exact phases in which the GRaND detected hydrogen manifests, their quantities, and their distribution in the upper few km of Ceres remain largely unknown.

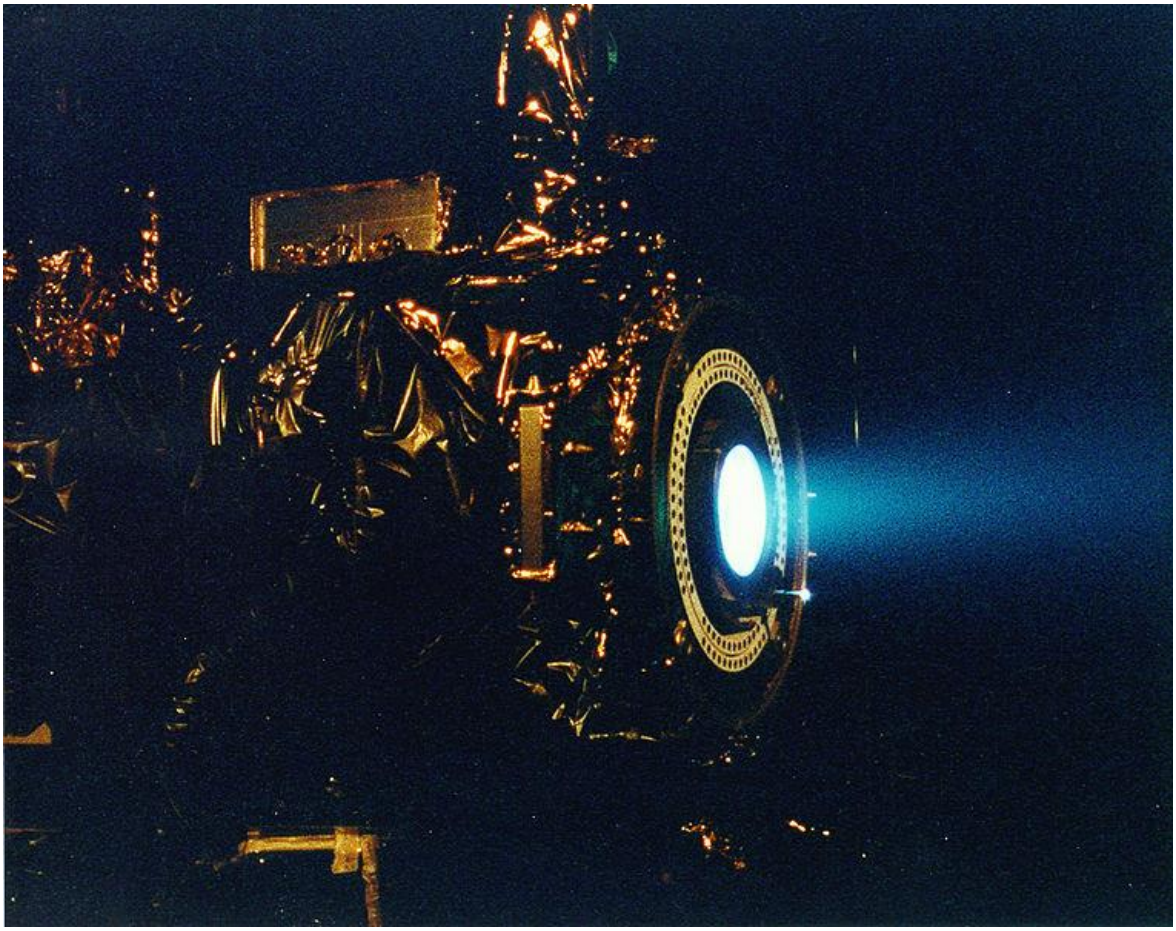

Figure 1-6. A view of an electrostatic xenon ion thruster being test fired at NASA's Jet Propulsion Laboratory. Three similarly designed ion engines were installed on the Dawn spacecraft, each with a miniscule thrust of 90 mN but an enormous specific impulse of 3,100 s. Over the lifetime of the mission Dawn achieved nearly ~11 km/s of delta-v using its ion thrusters, and accumulated more than 48,000 hours of ion thruster use. At the time of this writing these record setting accomplishments in the use of solar-electric propulsion still stand strong.

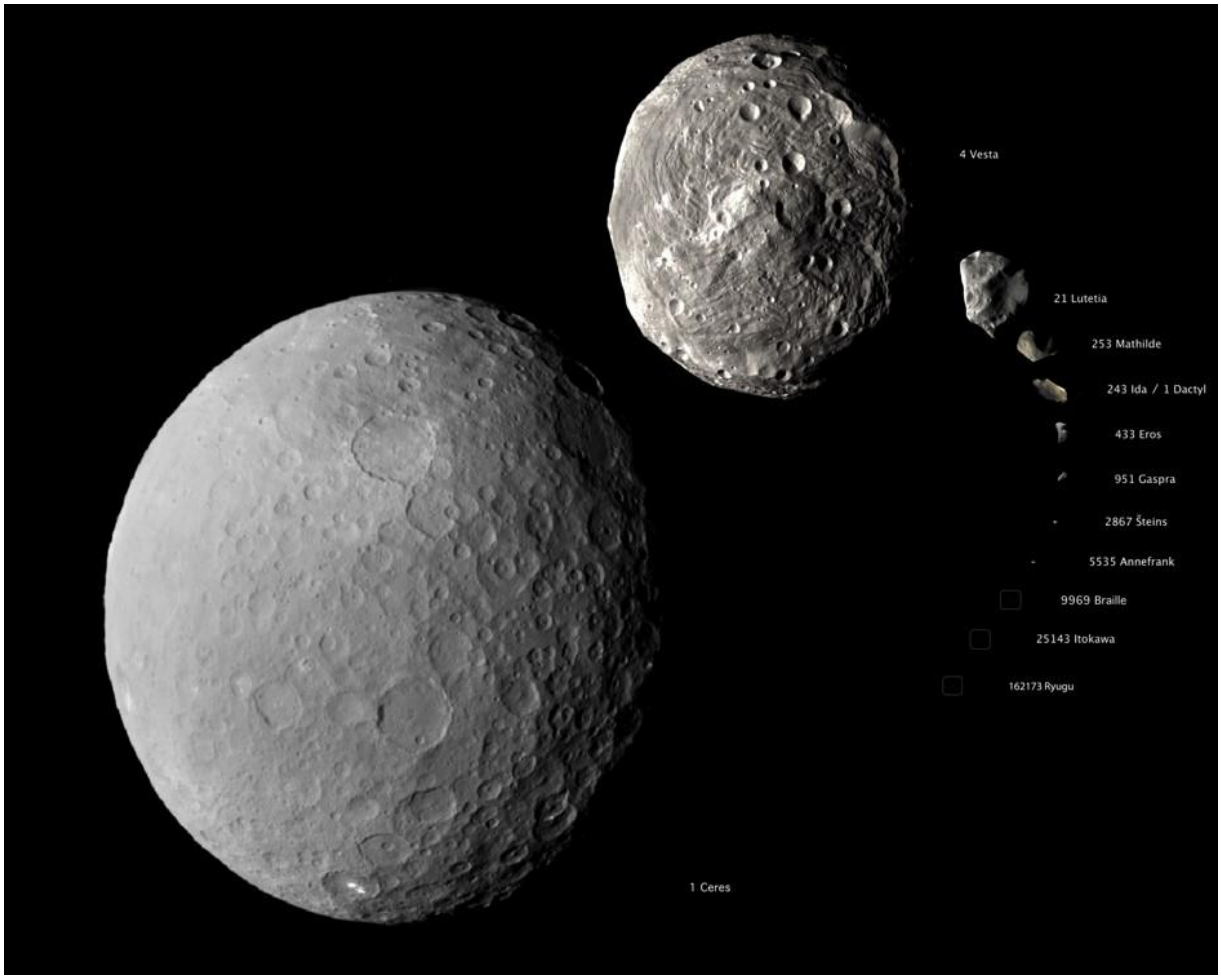

Figure 1-7. Ceres shown to scale relative to other asteroids explored by human spacecraft. Specifically note that Ceres' diameter is roughly two times that of the next largest asteroid (Vesta).

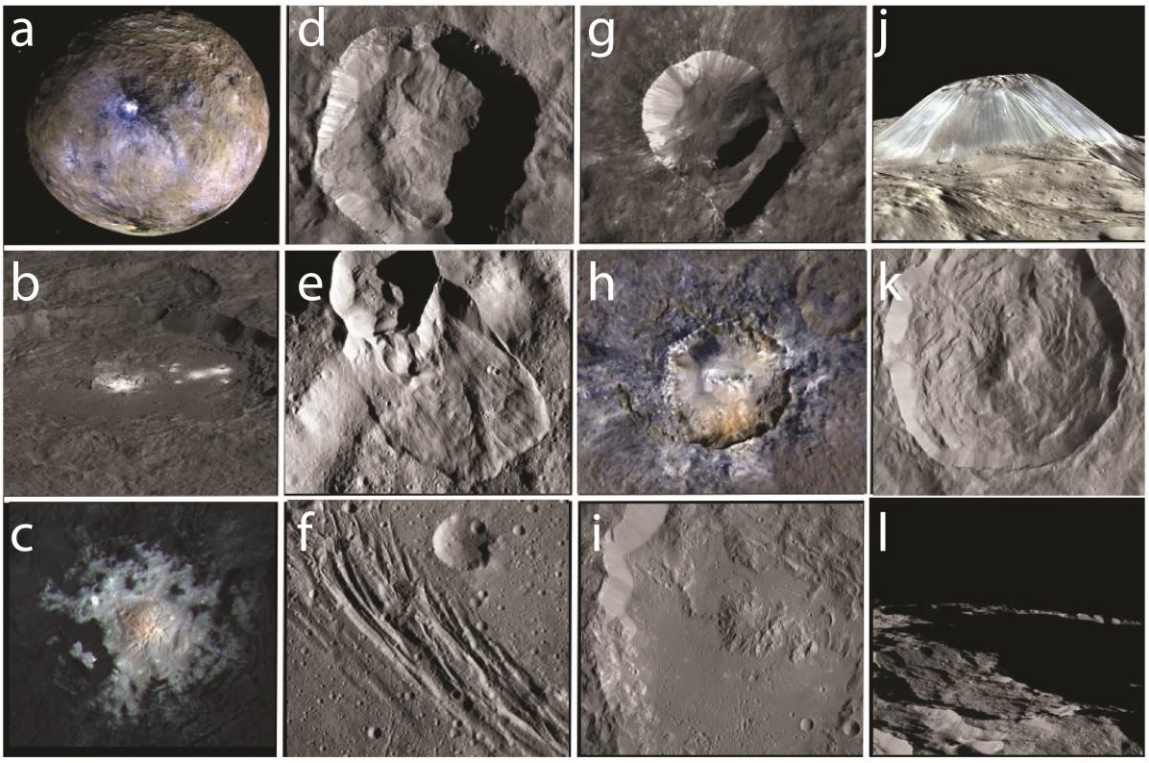

Figure 1-8. A collage of unique and intriguing landforms on Ceres. (a) depicts a full disk false color mosaic of Ceres highlighting the most recognizable feature on Ceres: Occator crater and its enigmatic facula. (b) shows a close up of Occator; the central bright region is Cerealia facula while the numerous bright spots to the right are Vinalia faculae. (c) a close up false color mosaic of Cerealia facula; the bright material which comprises the facula is interpreted to be composed largely of the sodium carbonate natrite (De Sanctis et al., 2016). Further analyses of Occator are available in a special issue of the journal *Icarus* (see Scully et al. (2019)). (d) and (e) depict unusual lobate mass wasting deposits that have no analogue on asteroid Vesta; features like these are largely the subject of Chapter 3. (f) shows the extensional fractures in Ceres' southern hemisphere known as Nar Sulcus; they are the focus of Chapter 5. (g) shows the unusually terraced Oxo crater: the first location of surface H_2O detection on Ceres (Combe et al., 2016). (h) shows of false color image of Haulani crater highlighting FAE, which is largely the subject of Chapter 4. (i) shows the smooth floor of Ikapati crater, which is likely due to extensive impact

melting of the ice-rich crust; while common on Ceres, impact melt was infrequently observed on Vesta (Le Corre et al., 2013). (j) perspective view of the solitary ~4 km tall mountain Ahuna Mons; this feature is one of many possible constructional features on Ceres suggesting that the dwarf planet may recently have been, or continues to be geologically active (Ruesch et al., 2016). (k) depicts Kokopelli crater and its mottled internal arrangement of troughs and ridges; the morphology of this crater and many others like it is reminiscent of craters observed on the icy satellites of Jupiter and Saturn. (l) illustrates a persistently shadowed region near Ceres' south pole; due to its current low obliquity of ~4° Ceres is one of only three solar system objects known to have these continually shaded regions, the other two being Mercury and the Moon (Schorghofer et al., 2016). Image credit: NASA/JPL-Caltech/UCLA/MPS/DLR/IDA.

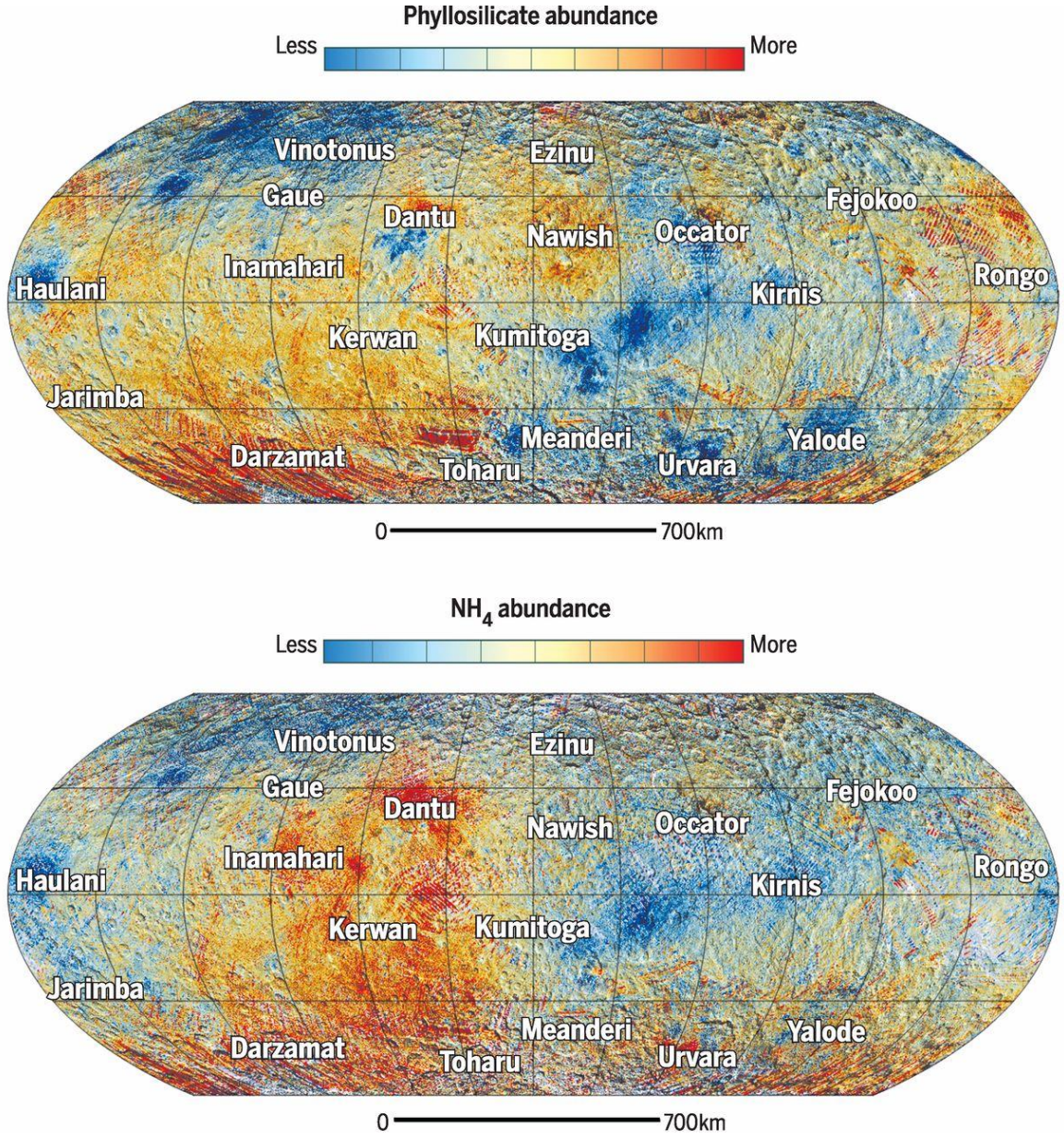

Figure 1-9. Qualitative abundance maps for the presence of phyllosilicates and ammonium on the surface of Ceres based upon the depths of the 2.7 μm and 3.1 μm absorption bands, respectively. Note while there is general regional agreement between the two maps they do exhibit local discrepancies, which may be the result of ammonium salt or other exotic chemistry. This image was adapted from Ammannito et al. (2016).

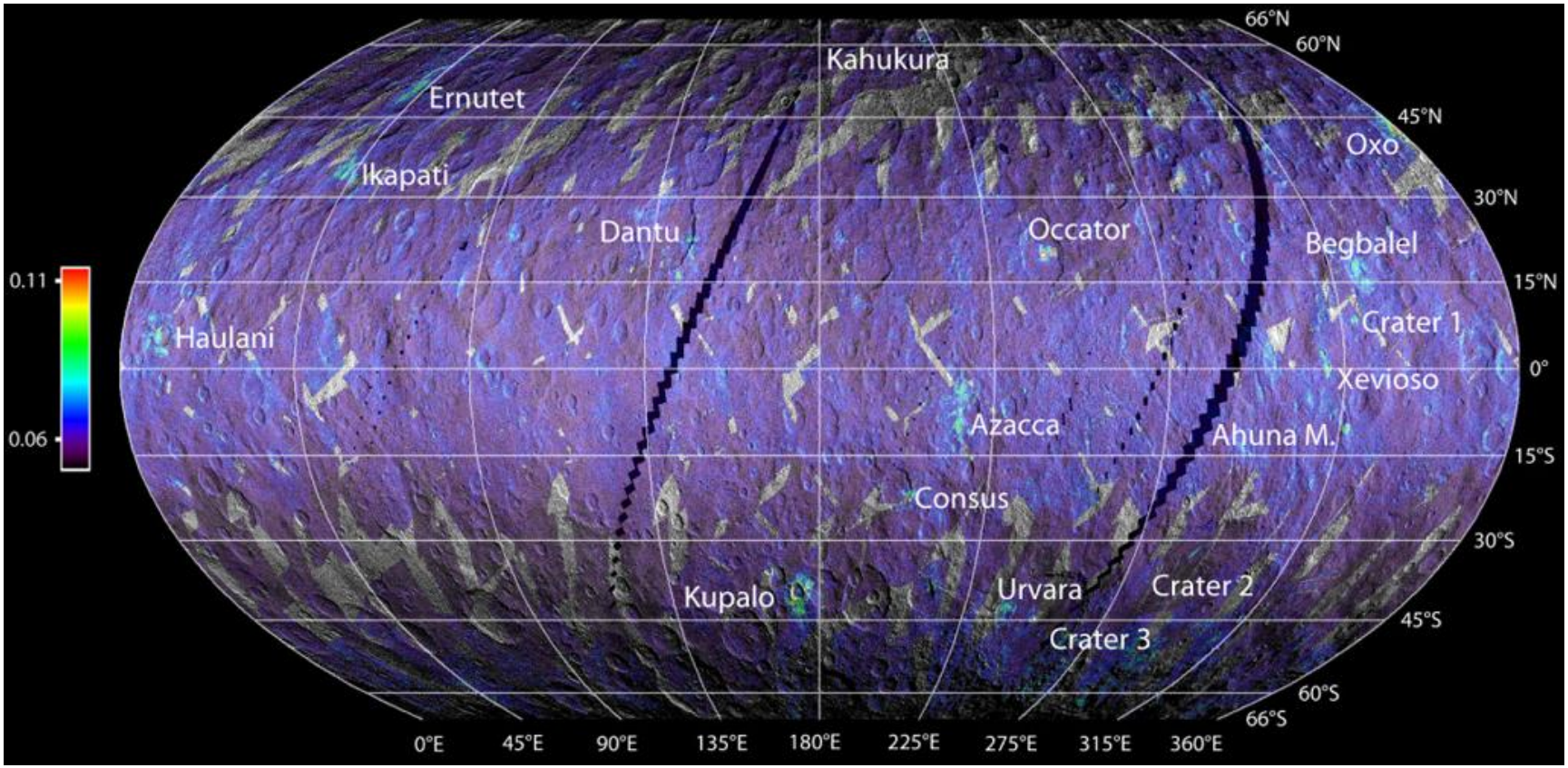

Figure 1-10. Band depth intensity map of the 3.9 μm absorption feature on Ceres. This absorption band is largely associated with carbonate mineral. In this map warmer colors indicate increased abundances of carbonates. Note that zone of high intensity 3.9 μm absorption tend to correlate with fresh appearing impact craters and large tholi/montes. This image is adapted from Carrozzo et al. (2018).

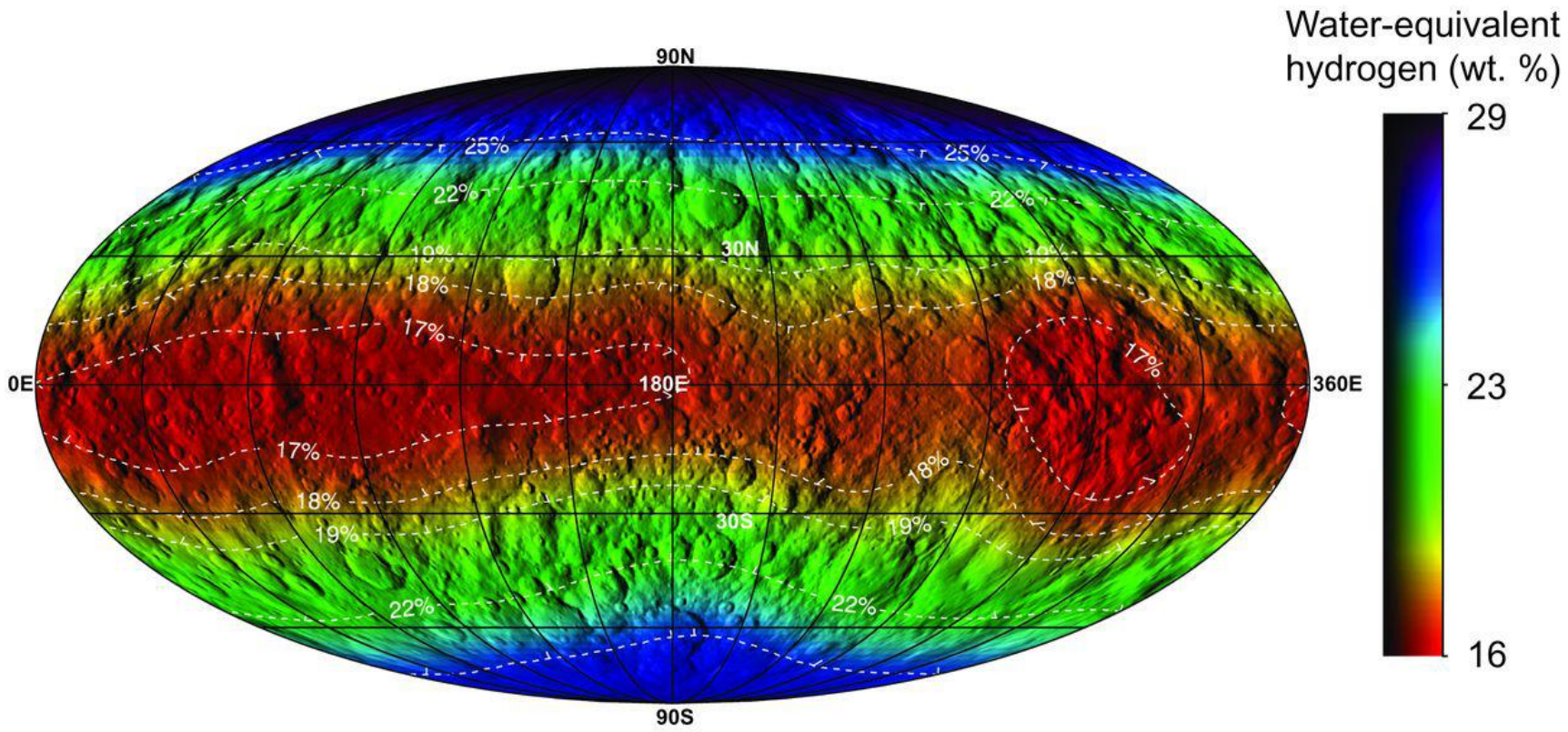

Figure 1-11. The lower bound distribution of water equivalent hydrogen within the top ~1 m of Ceres' regolith. This determination was made using thermal and epithermal neutron counting data taken by Dawn's GRaND instrument. To first order, the abundance of hydrogen in the upper regolith of Ceres correlates largely with latitude; the poles appear enriched in hydrogen relative to the seemingly depleted equatorial region. Note that while this latitudinal trend in poleward hydrogen enrichment is broadly symmetrical

there do exist regions of minor longitudinal enrichment and depletion. Additionally, the north pole appears superficially enriched in hydrogen relative to the south pole. This image was adapted from Prettyman et al. (2017).

Finally, structural inversions of Ceres derived from its gravity field as measured by Dawn suggest that unlike the fully differentiated Vesta, Ceres is only partially differentiated into a low density ice-rich rocky crust ~40 km thick overlain on top of a significantly denser silicate mantle (Ermakov et al, 2017) (Figure 1-12). The density of this upper layer was estimated by Ermakov et al. (2017) to be only ~1300 kg/m^3, which implies either a significant fraction of its volume (at least several tens of percent) comes from either water ice or void space, or that material at depth departs radically form the observed surface composition and is almost entirely composed of low density or porous material. The later of these aforementioned options seems extremely unlikely. Fu et al. (2017) used numerical modeling of Ceres observed topographic power spectrum and structural models to estimate the rheological and compositional properties of the upper ~100 km of its surface. They determined that the surface must have a relatively high viscosity of ~10^{25} Pa·s which decays by about one order of magnitude per 10 km depth to a minimum of ~10^{21} Pa·s in order to account for the viscous relaxation observed in cerean topographic features with wavelengths greater than or equal to ~200 km. They conclude that this mechanical limitation combined with the inferred crustal density from Ermakov et al. (2017) limits the crust to no more than 25 vol. % water ice, ~36 vol. % phyllosilicates and/or carbonates, ~29 vol. % high strength low density material (such as hydrated salts or methane clathrate), and ~10 vol. % porosity. However, this estimate is only valid at the scale of several tens of kilometers, and does not consider local variations in water ice abundance or thermal history. Thus, the questions of how much water ice exists in the near-surface of Ceres, how it is distributed, and how it manifests in the surface geology remain largely enigmatic.

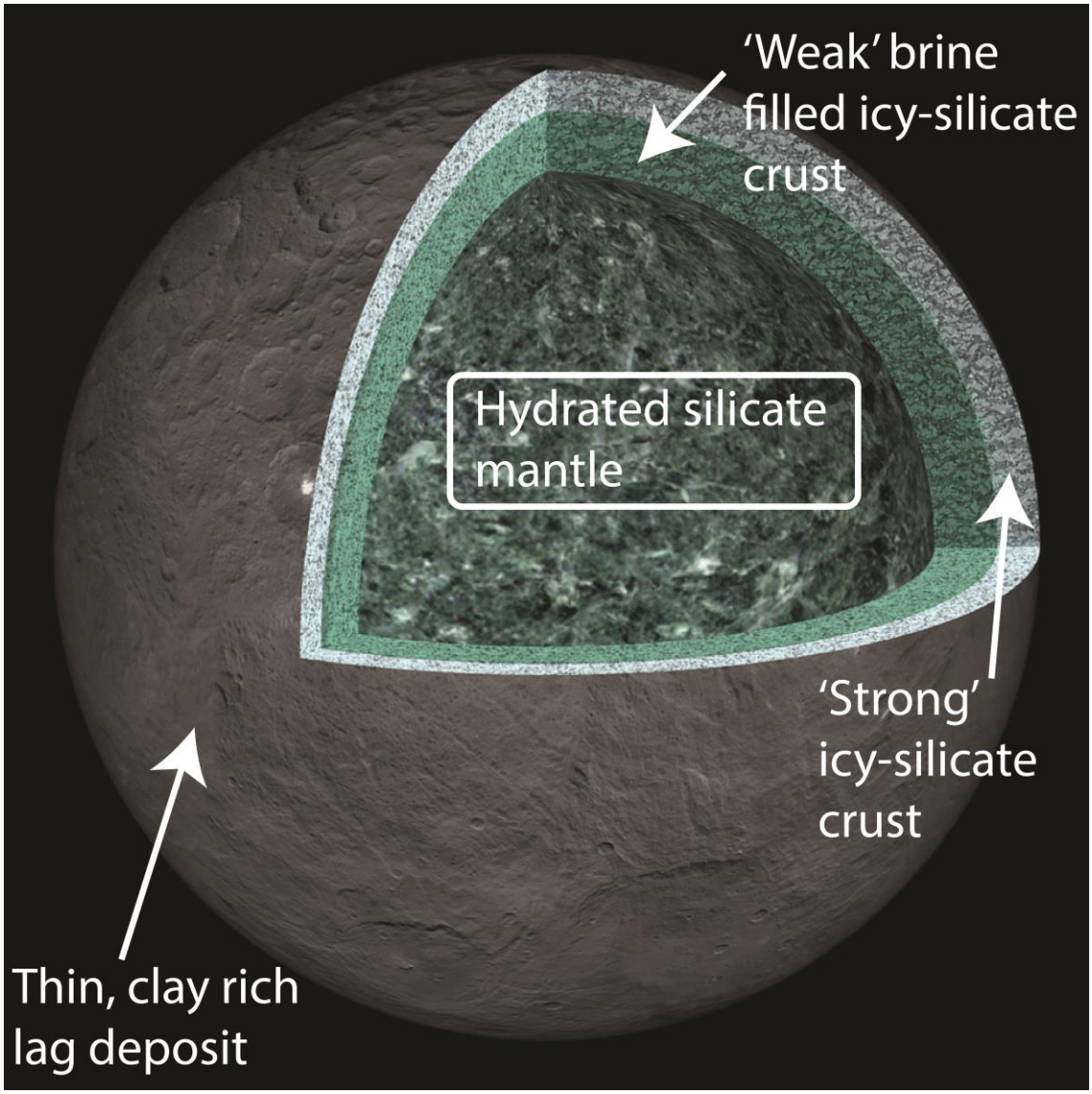

Figure 1-12. Schematic representation of the current understanding of Ceres' structure. The upper most lag deposit is likely the product of global aqueous alteration of silicate material followed by desiccation via sublimation, and is thought to be of sub-kilometer scale thickness. The 'strong' and 'weak water ice-rich crustal layer inferred from gravity and topography (Ermakov et al., 2017; Fu et al., 2017) are estimated to extend to depths of ~40 km and ~100 km, respectively. The internal mantle of Ceres is thought to be primarily composed of hydrated silicates such as clay and serpentine group minerals (e.g. McCord & Sotin, 2005). Image credit: NASA/JPL-Caltech/UCLA/MPS/DLR/IDA.

1.3 The Importance of Water Ice on Ceres and the Contributions of this Dissertation

Determining the physical, compositional, and mechanical properties of the outer layer of Ceres is paramount to better constraining its structure and understanding its evolution. The early results from the Dawn mission described in section 1.2 presented convincing evidence for significant global aqueous alteration of cerean surface materials, exposed water ice at numerous geologically diverse locations, high latitude surface saturating ice tables, and a low density variable viscosity crust. However, the observation made by the VIR instrument only reflect the composition of the upper ~100 μm of Ceres' surface; this sensitive depth range extends to ~1 m for nuclear spectra obtained by GRaND, and the gravimetric results have a depth resolution of several tens to hundreds of kilometers. Thus there exists a gap in our current understanding of the structure, water ice content, and distribution of water ice in the upper ~100 m to ~10 km of Ceres. However, there exist many landforms on the surface whose geomorphology suggests a genetic connection to ground ice at this scale, these include: lobate mass wasting deposits, fluidized-appearing ejecta, numerous tholi/montes, pitted terrain, and fractured terrain (Crown et al., 2018; Hughson et al., 2018; Hughson et al., 2019a; Hughson et al., 2019b; Ruesch et al., 2016; Schmidt et al., 2017; Sizemore et al., 2017; Sori et al., 2017). Investigating the geology and structure of these landforms will provide insight into some of the most pressing scientific questions about Ceres: how much H_2O exists in its upper ~10 km, what phases does it form, and how is it distributed?

This information is of scientific interest since knowing the distribution and quantity of near-surface H_2O, and in which phases it exists, is imperative to understanding the current thermal state of Ceres, understanding its current assemblage of surface features and processes, and constraining geochemical and geophysical models of its evolution and structure that are very

sensitive to the final H_2O content and mechanical properties of its outer layer. Determining the proportion of ground ice relative to other proposed molecular H_2O bearing phases such as hydrated salts and methane/carbon dioxide clathrates would further constrain the redox/pH conditions under which surface materials formed, which would give useful insight into the degree of serpentinization of the putative silicate core, Ceres' thermal history, and even where Ceres formed during the solar nebula/primordial periods of the solar system (Castillo-Rogez et al., 2018; McCord & Sotin, 2005). This in turn would shed additional light on the evolution of other solar system objects such as carbonaceous chondrite meteorites, which are geochemically similar to the surface of Ceres and thus may have formed in a similar environment; and the Earth itself, which likely originated from the accretion of Ceres-sized objects (Rivkin et al., 2006). Secondarily, constraining the ice content of the near surface is also of astrobiological interest, as these regions could be potentially habitable zones for microbial life, or could have been in the geologic past. Regions of well-constrained composition/high water content also make attractive targets for future in situ or sample return robotic missions because of their astrobiological potential and plausible link to CM/CI meteorites. Finally, and somewhat whimsically, developing a global inventory of the water resources in the shallow subsurface of Ceres will help guide and enable economic and efficient resource extraction by future human and/or robotic explorers. Efficient conversion of the abundant water resources on Ceres into consumables such as molecular hydrogen, oxygen, and liquid water would inevitably be a boon for exploration of the outer solar system.

The purpose of this dissertation is to contribute to the geological, mechanical, and compositional characterization of Ceres, with a focus on the ground ice content of the upper few kilometers, via: global and regional geologic mapping (see Chapter 2), geomorphological and

geophysical characterization of cerean lobate mass wasting deposits (see Chapter 3), geomorphometric analysis and physical emplacement modeling of cerean fluidized appearing ejecta (FAE) (see Chapter 4), and thermo-flexural modeling of elastically supported terrain in Ceres' Nar Sulcus region (see Chapter 5). The major results of these investigations are: (1) Ceres is ubiquitously covered with landforms (particularly landslides, FAE, tholi, and fractured terrain) suggestive of extensive near-surface ground ice in the ~10 km of its crust (see Chapter 2), (2) cerean mass wasting deposits have no analogue on Vesta and have physical characteristics that make them most similar to frozen debris flows, terrestrial supraglacial landslides, and long run-out landslides seen on Mars and icy satellites (e.g. Iapetus) (see Chapter 3); (3) Ceres' crust is rheologically dominated by ice-like phase, and pore filling ground ice is likely present globally on Ceres at depths of only a few meters to ~1-5 km (see Chapter 4); and (4) at least locally to the Nar Sulcus fractures Ceres has a very thin elastic layer and its crust is composed of ~70 vol. % ice-like phases to a depth of at least ~2 km (see Chapter 5). Chapter 6, 'Synthesis and Conclusions', provides a synthetic analysis of the findings presented in chapters two through five and discusses their implications towards Ceres, its relationship with Vesta, and to planetary science in general.

Chapter 2 is primarily sourced from work published by the author of this dissertation in the journal *Icarus* (Hughson et al., 2018), and work co-authored by the author of this dissertation published in the journals *Icarus* and *Science* (Combe et al., 2016; Combe et al., 2019). Chapter 3 is based upon published work co-authored by the author of this dissertation in the journals *Science*, *Nature Geoscience*, and the *Journal of Geophysical Research - Planets* (Buczkowski et al., 2016, Chilton et al., 2019, Schmidt et al., 2017). Chapter 4 is sourced primarily from work published by the author of this dissertation in the *Journal of Geophysical Research - Planets*

(Hughson et al., 2019a). Chapter 5 is primarily based upon work published by the author of this dissertation in the journal *Geophysical Research Letters* (Hughson et al., 2019b).

2 Initial Exploration and Geologic Map of the Fejokoo Quadrangle of Ceres

2.1 Geologic Mapping of Ceres: A Planetary Perspective

In traditional terrestrial geology, geologic mapping is an interpretative scientific process where the mapper(s) aspires to understand the composition, structure, and history of geologic materials exposed at the Earth's surface and at depth, and to reduce these complex observations and interpretations into consistent map units and symbols (e.g. Bernknopf et al., 1993). The goal of this process is to synoptically present the geological evolution, history, and current state of any area of geologic interest regardless of scale; thus geologic mapping is a crucial tool for unraveling the mysteries of solid planet surfaces, such as their relative stratigraphic chronologies, which geologic processes were active in the past, and the current and historical stress state of the surface (e.g. Carr et al., 1994; Marchi et al., 2012; Hiesinger et al., 2016; Williams et al., 2018b). Geologists traditionally formulate their maps based upon field observations such as measurements, sketches, and rock type interpretations recorded directly into their notebooks. These observations are then used to define a set of self-consistent map units based on objective physical properties. However, the advent of technological field systems and airborne/space based remote sensing assets over the past ~50 years has radically redefined what geologic mappers can accomplish both in and out of the field. The Dawn mission, with its high precision cameras and spectrometers, embodies many of these recent advances in remote sensing technology as all the geologic mapping was completed remotely.

The Dawn Science Team conducted a geologic mapping campaign for Ceres similar to the one that was implemented on the asteroid Vesta (Williams et al., 2014; Yingst et al., 2014), including the production of a Survey-, High Altitude Mapping Orbit (HAMO), and Low Altitude Mapping Orbit-based global maps (Roatsch et al., 2016a; Roatsch et al., 2016b, Williams et al.,

2018b) (Figure 2-1 and Figure 2-2), and a series of 15 individual Low Altitude Mapping Orbit (LAMO)-based 1:500,000 scale quadrangle maps. The scientific goals of the Ceres geologic mapping campaign were threefold: (1) analyze the surface for important features, structures, and trends that provide insight into the geology and history of the dwarf planet, (2) provide geologic and chronostratigraphic context for future analyses of any data returned by the Dawn spacecraft, and (3) inform the scientific community at large about the current understanding of Ceres as spatial resolution increased throughout Dawn's mission at Ceres.

To enable efficient systematic mapping of the entire surface of Ceres at a scale of 1:500,000, the surface was partitioned into 15 roughly equal area quadrangles (Figure 2-3). Each quadrangle was named after a prominent impact crater found within its borders; all features on Ceres are named after deities and festivals of the harvest. Each quadrangle was assigned a principal mapper who completed the bulk of the geological mapping. Neighboring quadrangle mappers and VIR team spectroscopists also contributed significantly to the development these maps. The results of this mapping are presented in a special issue of the journal *Icarus* (316). The author of this dissertation is the lead author of the publication on the geologic map of the Ac-5 Fejokoo quadrangle of Ceres (Hughson et al., 2018), and is a co-author on three additional publications regarding the geologic mapping of the Ac-1 Asari (Ruesch et al., 2018), Ac-4 Ezinu (Scully et al., 2018), and Ac-10 Rongo (Platz, et al., 2018) quadrangles of Ceres. Additionally, the author of this dissertation is also a co-author on a publication regarding the compositional analysis of the Fejokoo quadrangle (Singh, et al., 2019).

GEOLOGIC MAP of CERES
- Global dataset based on quadrangle mapping published in
Special Issue, Icarus Volume 316 (December 2018)

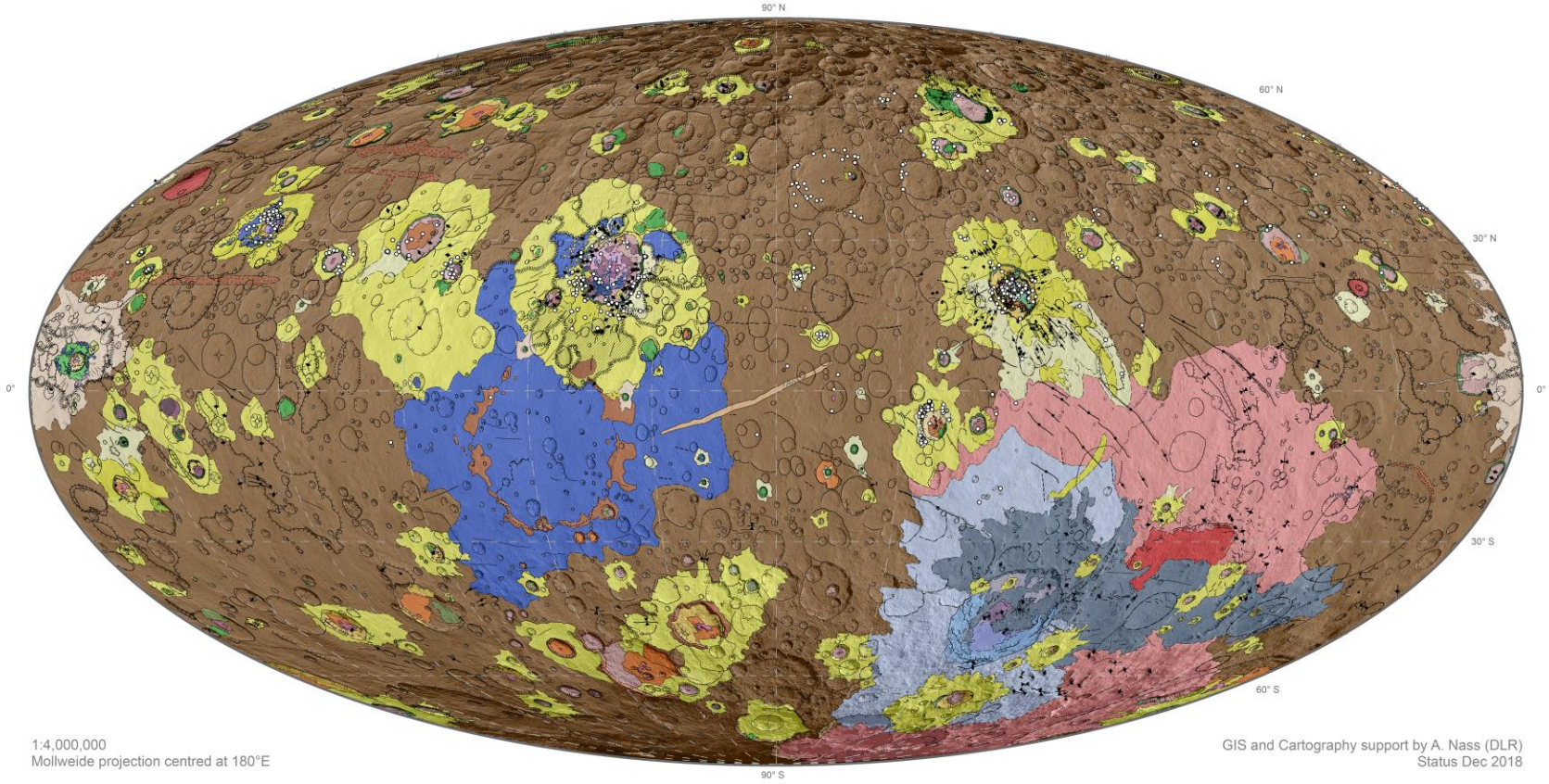

1:4,000,000
Mollweide projection centred at 180°E

Scale is true at equator

0 125 250 500 km

Background: LAMO mosaic, 35 m/pxl

for more information Roatsch et al., 2017, PSS 140, 74–79, doi:10.1016/j.pss.2017.04.008)

GIS and Cartography support by A. Nass (DLR)
Status Dec 2018

for more information
Nass, A. and the Dawn Mapping Team, 2017.LPSC #1892,
Williams, D. et al, 2017, LPSC, #1451, Williams, D. et al, 2018, LPSC, #1614

Figure 2-1. A 1:4,000,000 scale global geologic map of the dwarf planet Ceres in Mollweide projection. This map was created through the unification of the 15 LAMO-based quadrangle maps. The symbology and unit nomenclature for this map are presented in Figure 2-2. This image was adapted from the cover of *Icarus* (316). For more information, see Nass et al. (2017), Roatsch et al. (2017), Williams et al. (2017), and Williams et al. (2018a and 2018b). Image credit: Andrea Nass, DLR.

Legend for quadrangle-based Geologic Mapping of Ceres

POINT FEATURES

- central peak of impact crater (1st)
- central peak of impact crater (2nd)
- knob or central peak
- large, steep-sided shield, dome
- pit of impact crater floor (2nd)
- bright spot
- dark spot
- small cone, vent, cinder or spatter cone
- small crater
- small shield, dome, or volcanic construct
- small tholi
- very small tholi

LINEAR and AREAL FEATURES

- fault, accurate
- fault, approximate
- normal fault, accurate
- normal fault, approximate
- graben trace, accurate
- graben trace, approximate
- ridge crest (1st), accurate
- ridge crest (1st), approximate
- ridge crest (2nd), accurate
- ridge crest (2nd), approximate
- base of scarp
- fracture
- furrow
- trough or narrow depression
- sharp groove
- subdued groove
- pit chain
- impact crater chain
- lineament
- linear depression or valley
- lobate scarp
- narrow channel (possible lava)
- groove
- scarp
- channel
- channel (fluvial)
- channel (volcanic)
- crater ray
- raised rim of large impact crater
- raised rim of small impact crater
- degraded impact crater rim
- buried impact crater rim
- basin ring
- pit of impact crater floor (mapped to scale)
- depression
- dome, edifice, or circular scarp
- caldera
- topographic rise or hill

GEOLOGICAL UNITS

- cb — crater material bright
- c — crater material
- cd — crater material dark
- cfb — crater floor material bright
- cf — crater floor material
- cfd — crater floor material dark
- cfhb — crater floor material hummocky bright
- cfh — crater floor material hummocky
- cfhd — crater floor material hummocky dark
- cfsb — crater floor material smooth bright
- cfs — crater floor material smooth
- cfsd — crater floor material smooth dark
- ctb — crater terrace material bright
- ct — crater terrace material
- ctd — crater terrace material dark
- crdeg — crater rim material degraded
- crb — crater ray material bright
- cr — crater ray material
- crd — crater ray material dark
- ccp — crater central peak material
- lb — lobate material bright
- l — lobate material
- ld — lobate material dark
- lhb — lobate material hummocky bright
- lh — lobate material hummocky
- lhd — lobate material hummocky dark
- lsb — lobate material smooth bright
- ls — lobate material smooth
- lsd — lobate material smooth dark
- lkb — lobate material knobby bright
- lk — lobate material knobby
- lkd — lobate material knobby dark
- ta — talus material
- s — smooth material
- th — tholus material
- p — pitted material
- crt — cratered terrain
- Ye — Yalode ejecta material
- Yfh — Yalode floor material hummocky
- UYs — Urvara/Yalode smooth material
- Ue — Urvara ejecta material
- Ut — Urvara terrace material
- Ufh — Urvara floor material hummocky
- Ufs — Urvara floor material smooth
- Uccp — Urvara central peak material

CONTACTS

- accurate
- approximate
- inferred
- concealed
- gradational

SURFACE FEATURES

- secondary crater field
- ejecta light
- ejecta dark
- mantling material light
- mantling material dark
- terrace deposits

Figure 2-2. Symbology and unit legend for the 15 LAMO-quadrangle and unified LAMO global geologic maps of Ceres. This figure was adapted from Williams et al. (2018b).

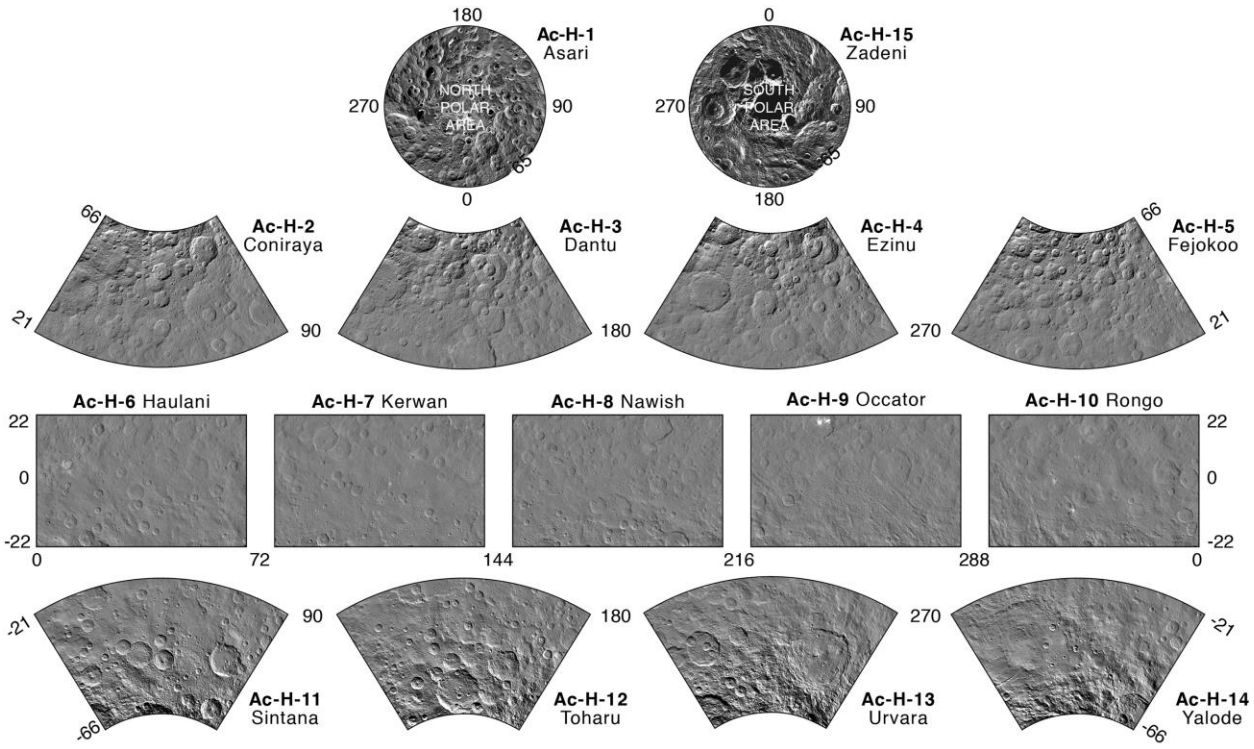

Figure 2-3. Layout of the 15 mapping quadrangles for the dwarf planet Ceres. The Fejokoo quadrangle is the subject of this chapter. This quadrangle is one of four mid-latitude northern hemisphere quadrangles (the others being Coniraya, Dantu, and Ezinu). This figure is adapted from Roatsch et al. (2016b).

In this chapter I present the detailed LAMO-based geologic map of the Ac-5 Fejokoo quadrangle of Ceres (21-66 °N and 270-360 °E), a description of its map units, and a simplified geologic history of the region. Additionally, during the mapping of the Fejokoo quadrangle it became obvious that, aside from impact craters, its geomorphology was dominated by mass wasting deposits and numerous tholi. The first confirmed detection of exposed H_2O on the surface of Ceres was also found to be in the Fejokoo quadrangle within Oxo crater. While mapping effort described in this chapter was predominantly limited to the Fejokoo quadrangle, the observations and interpretations of its composition and geomorphology have implications for the entire surface of Ceres. Through the geologic mapping I address the following questions:

1. What is the nature of the tholi and mass wasting features in the Fejokoo quadrangle?
2. What do the tholi and mass wasting features tell us about the global properties of Ceres?
3. What is the geological context of Oxo crater and its H_2O detection?

2.2 Datasets and Methodology

2.2.1 Base Data and Basemaps

The Ceres science segment of the Dawn mission started in March of 2015 and ended on November 1, 2018. During this science phase data were acquired in four progressively lower altitude stages: (1) Approach (≥13,600 km altitude), (2) Survey orbit (4,400 km altitude), (3) HAMO (1,470 km altitude), and (4) LAMO (375 km altitude). These data were collected using Dawn's FC (Sierks et al., 2011), VIR (De Sanctis et al., 2011), GRaND (Prettyman et al., 2011), and radio science instrument packages (Konopliv et al., 2011). The work in this chapter is predominantly based on clear and color filter FC images and mosaics along with stereophotogrammetrically (SPG) derived digital terrain models (DTMs) of Ceres (vertical

accuracy ~10 m) (Preusker et al., 2016). These FC data were acquired globally at ~140 m/pixel and ~35 m/pixel, from the HAMO and LAMO mission phases, respectively. FC color filter images were acquired with near global coverage during the HAMO mission phase, and of select features of interest during the LAMO phase. For details on the calibration of FC images see Schröder et al., (2013) and Schröder et al. (2014).

Photometrically corrected FC mosaics of the Fejokoo quadrangle were also used to determine albedo variations within the quadrangle (for details on the method used to produce the photometrically corrected mosaic see Schröder et al. (2013)). Compositional data acquired by VIR was used to inform the map, in particular the variations in the depth of the 2.70 and 3.06 μm absorption band associated with OH in phyllosilicates and ammoniated clay minerals, respectively and the H_2O detection at Oxo (Combe et al., 2016). Bouger gravity anomaly maps derived from radio science observations were also used in the interpretation of the geologic map (Ermakov et al., 2016; Ermakov et al., 2017; Konopliv et al., 2018.).

2.2.2 Mapping Methodology and Tools

Geologic mapping was completed using ArcMap 10.3 on a set of georeferenced, quadrangle wide, clear filter (panchromatic) FC mosaics and DTMs (Figure 2-4 and Figure 2-5a & 2-5b). In order to ensure cartographic consistency, a uniform set of GIS and map layout templates were employed over all 15 quadrangles. The maps were informed by ancillary data products mentioned in section 2.2.1. Topographic profiles and surface feature measurements for the Ac-5 geologic map presented here were obtained from the HAMO DTM and its derivative slope map (Figure 2-6). A particularly useful HAMO color composite mosaic was also used in the production of the Fejokoo quadrangle geologic map. Known as color composite R (Figure 2-7),

this mosaic assigns the FC color filter ratios $\frac{965\text{ nm}}{750\text{ nm}}$ to the red channel, $\frac{550\text{ nm}}{750\text{ nm}}$ to the green channel, and $\frac{440\text{ nm}}{750\text{ nm}}$ to the blue channel. In color composite R, materials with a positive spectral slope appear reddish, while materials with a negative spectral slope appear blueish.

Crater size-frequency distributions (CSFDs) of surface units in this quadrangle were derived using CraterTools 2.1 developed by Kneissl et al. (2011; 2014; 2015). CraterstatsII (Micheal & Neukum, 2010) was used to analyze and fit the CSFDs to the lunar and asteroid derived production functions. Absolute model ages (AMAs) were generated by craterstatsII using the lunar and asteroid derived chronology functions from Hiesinger et al. (2016). The error assigned to the AMAs is the standard error of N(1) (the number of counted craters > 1 km in diameter per unit area) calculated as follows:

$$\sigma = \pm \mathrm{N_{cum}} * \frac{1}{\sqrt{n}}$$

Where *n* is the total number of fitted craters (Arvidson et al., 1979; Michael & Neukum, 2010).

2.3 Initial Exploration and Geologic Map of the Ac-5 Fejokoo Quadrangle of Ceres

The geologic map of the Fejokoo quadrangle of Ceres is presented in Figure 2-8. The following subsections of section 2.3 describe the quadrangle's geologic setting, physical geography, and give a description of the employed map units.

FRAMING CAMERA BASE MAP OF THE AC-5 FEJOKOO QUADRANGLE OF CERES

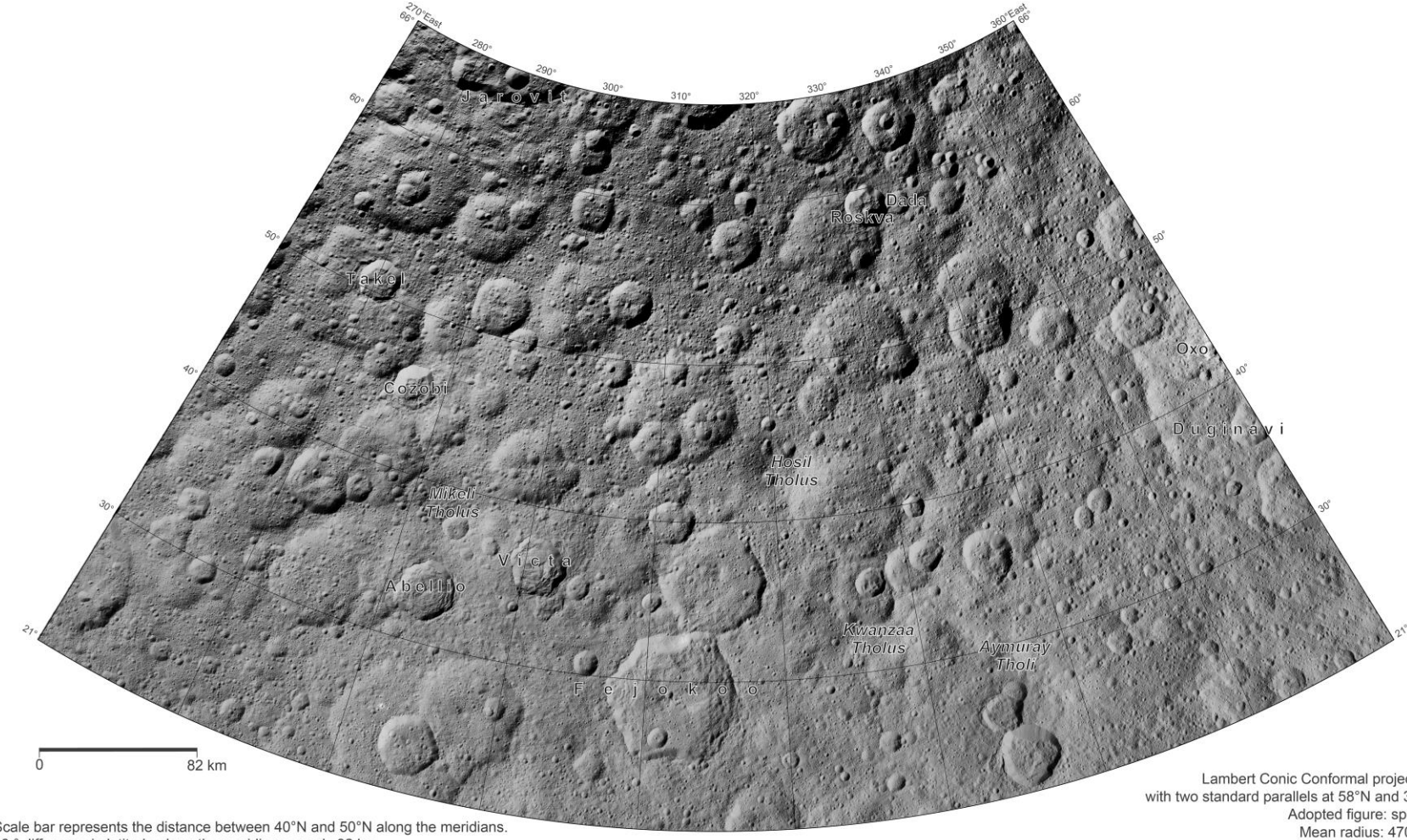

Scale bar represents the distance between 40°N and 50°N along the meridians.
10 ° difference in latitude along the meridians equals 82 km.

Lambert Conic Conformal projection
with two standard parallels at 58°N and 30°N
Adopted figure: sphere
Mean radius: 470 km
Grid: planetocentric lat./east long.

Figure 2-4. The Ac-5 Fejokoo Quadrangle: Dawn FC clear filter LAMO basemap mosaic in Lambert conformal conical projection (Figures 2-5, 2-6, 2-7, 2-8, 2-10, 2-12, and 2-13) also use this projection). Basemap mosaics, which have a resolution of ~35 m/pixel, were rendered following methods outlined in Roatsch et al. (2016b).

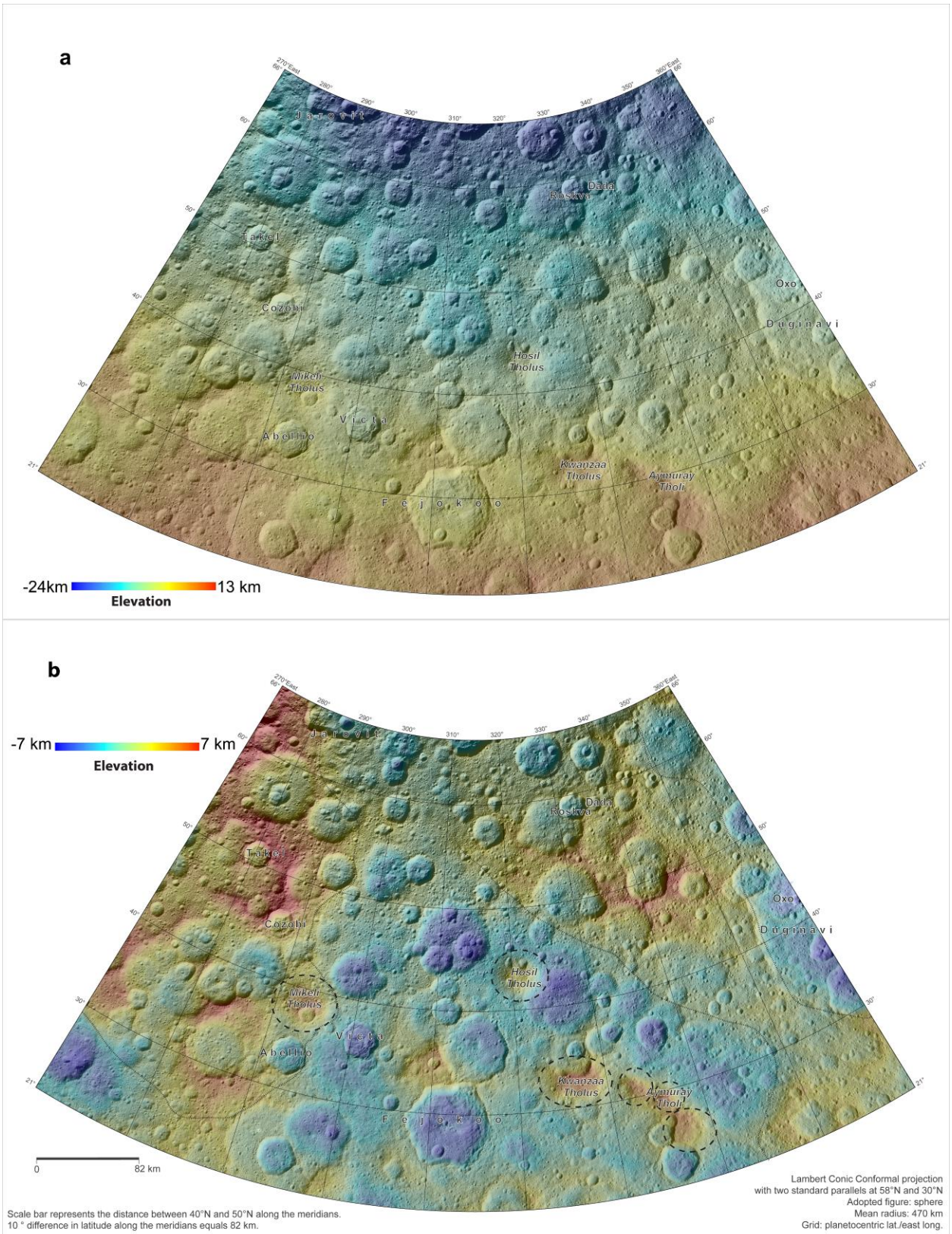
a
Jarovit
Dada
Roskva
Takel
Oxo
Cozobi
Dúginavi
Hasil
Tholus
Mikeli
Tholus
Victa
Abellio
Kwanzaa
Tholus
Aymuray
Tholi
Fejokoo
-24km
13 km
Elevation
b
-7 km
7 km
Elevation
Jarovit
Dada
Roskva
Takel
Oxo
Cozobi
Dúginavi
Hasil
Tholus
Mikeli
Tholus
Victa
Abellio
Kwanzaa
Tholus
Aymuray
Tholi
Fejokoo
0
82 km
Scale bar represents the distance between 40°N and 50°N along the meridians.
10 ° difference in latitude along the meridians equals 82 km.
Lambert Conic Conformal projection
with two standard parallels at 58°N and 30°N
Adopted figure: sphere
Mean radius: 470 km
Grid: planetocentric lat./east long.

Figure 2-5. Digital terrain models for the Ac-5 Fejokoo Quadrangle and surrounding area derived from HAMO images using stereophotogrammetry (Preusker et al., 2016). Surface elevations depicted in (a) are with respect to Ceres' mean geometric radius of 469.7 km. This panel emphasizes the oblateness of Ceres. Elevations depicted in (b) are with respect to Ceres' best fit biaxial ellipsoid (482 km × 482 km × 446 km). The locations of six named tholi in the Fejokoo quadrangle are indicated by dashed ellipses. The approximate boundaries between the central low topography province and the northeastern/western high topography provinces are shown with dashed lines.

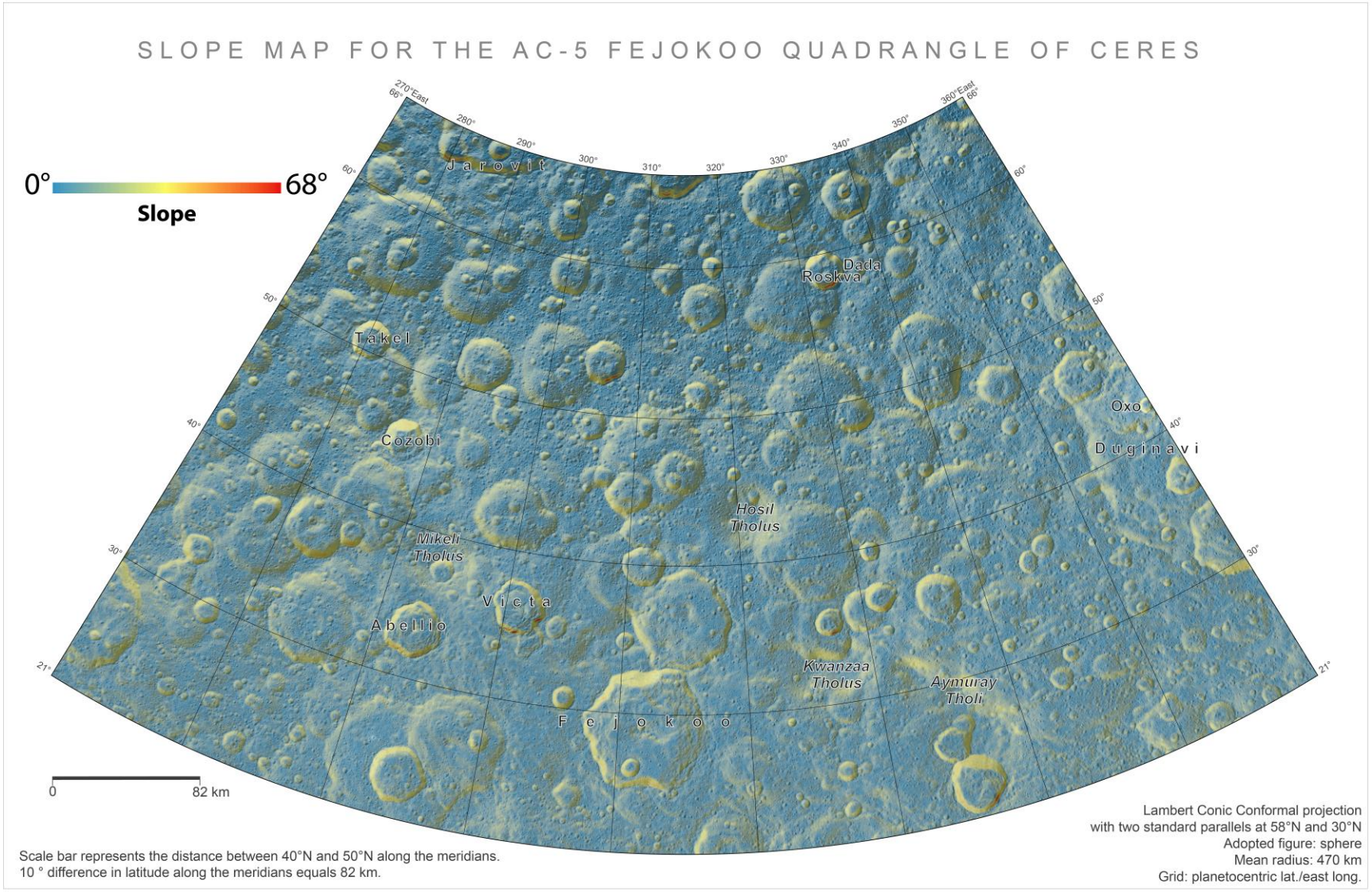
SLOPE MAP FOR THE AC-5 FEJOKOO QUADRANGLE OF CERES
0°
68°
Slope
Jarovit
Dada
Roskva
Takel
Oxo
Cozobi
Duginavi
Hosil
Tholus
Mikeli
Tholus
Victa
Abellio
Kwanzaa
Tholus
Aymuray
Tholi
Fejokoo
0
82 km
Scale bar represents the distance between 40°N and 50°N along the meridians.
10 ° difference in latitude along the meridians equals 82 km.
Lambert Conic Conformal projection
with two standard parallels at 58°N and 30°N
Adopted figure: sphere
Mean radius: 470 km
Grid: planetocentric lat./east long.

Figure 2-6. Slope map of the Ac-5 Fejokoo Quadrangle derived from the HAMO SPG DTM relative to the biaxial ellipsoid (see Fig. 2-5b).

COLOR COMPOSITE R IMAGE OF THE AC-5 FEJOKOO QUADRANGLE OF CERES

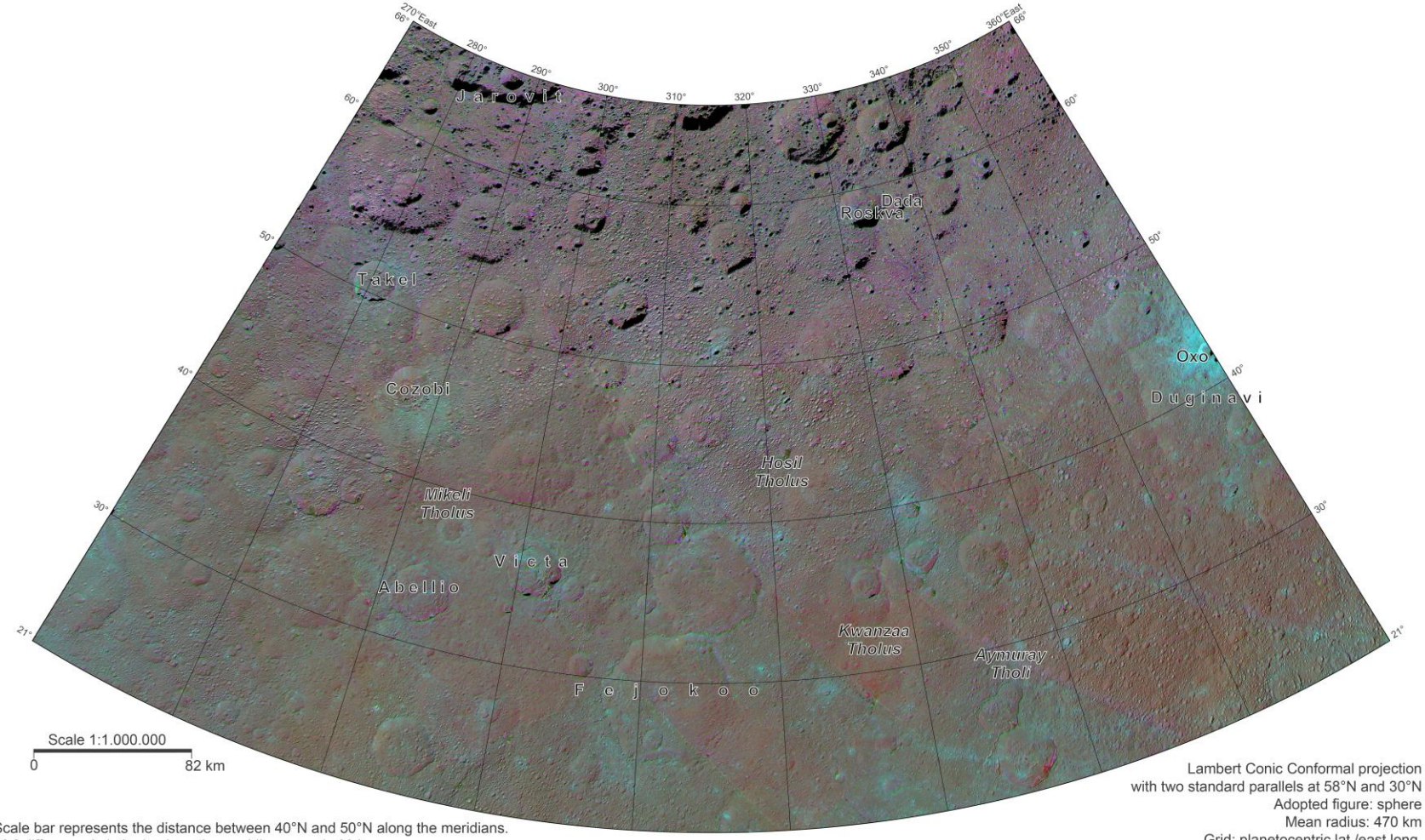

Scale bar represents the distance between 40°N and 50°N along the meridians.
10 ° difference in latitude along the meridians equals 82 km.

Lambert Conic Conformal projection
with two standard parallels at 58°N and 30°N
Adopted figure: sphere
Mean radius: 470 km
Grid: planetocentric lat./east long.

Figure 2-7. FC HAMO image derived color ratio mosaic known as color composite R overlain onto the FC LAMO clear filter mosaic of the Fejokoo quadrangle. Color composite R assigns the ratio $\frac{965\text{ nm}}{750\text{ nm}}$ to the red channel, the ratio $\frac{550\text{ nm}}{750\text{ nm}}$ to the green channel, and the ratio $\frac{440\text{ nm}}{750\text{ nm}}$ to the blue channel. Regions that appear red have a positive spectral slope in the visible and near IR, while regions that appear blue have a negative spectral slope in the visible and near IR. Note that there is little color variation in the Fejokoo quadrangle except around some fresh impact craters (which appear bluish) in the east central portion of the quadrangle, some ejecta rays originating from outside of Ac-5 seen in the southeast portion of the quadrangle (which appear bluish), and Oxo crater (which appears vibrantly blue).

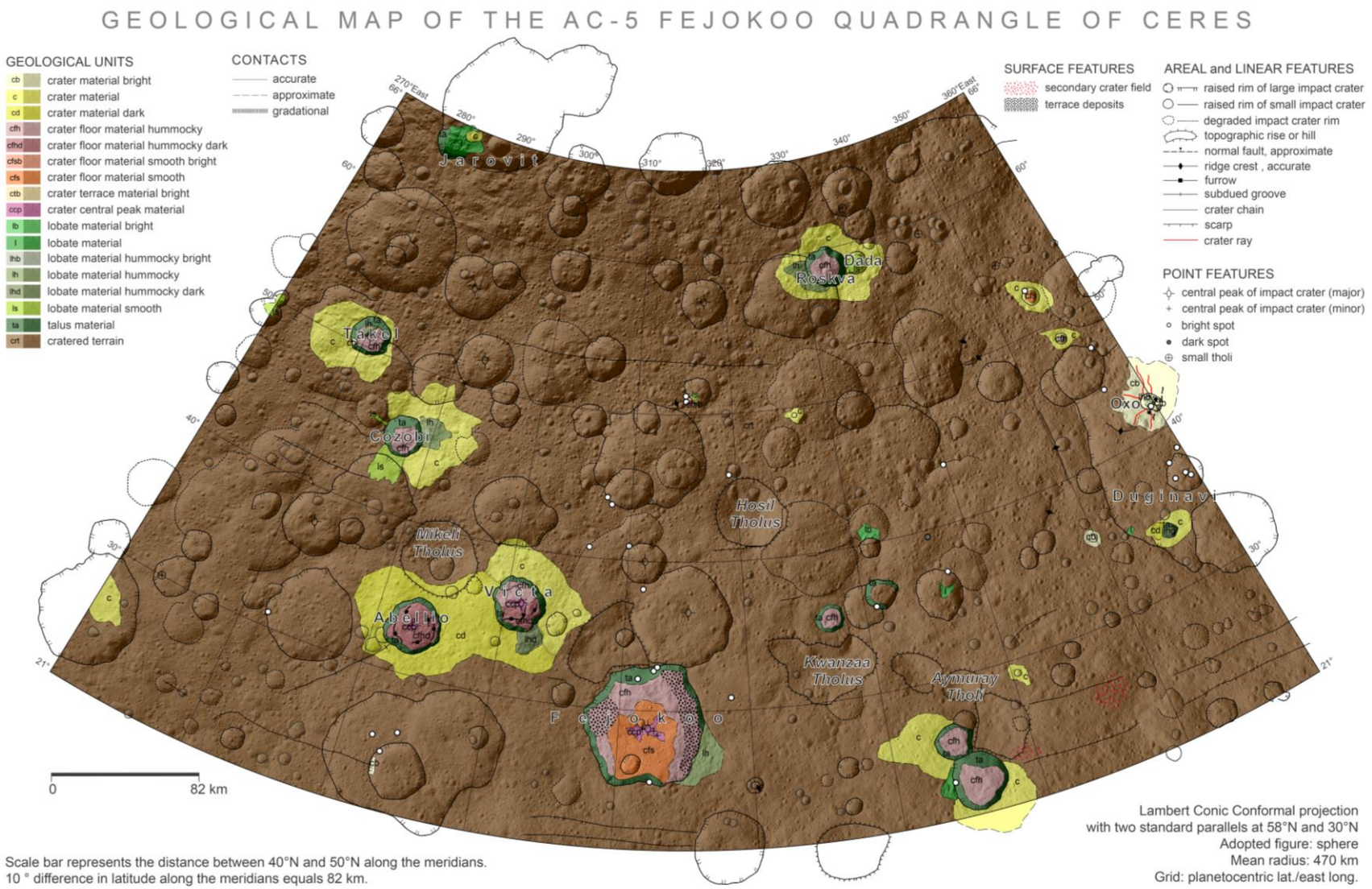
GEOLOGICAL MAP OF THE AC-5 FEJOKOO QUADRANGLE OF CERES
GEOLOGICAL UNITS
cb crater material bright
c crater material
cd crater material dark
cfh crater floor material hummocky
cfhd crater floor material hummocky dark
cfsb crater floor material smooth bright
cfs crater floor material smooth
ctb crater terrace material bright
ccp crater central peak material
lb lobate material bright
l lobate material
lhb lobate material hummocky bright
lh lobate material hummocky
lhd lobate material hummocky dark
ls lobate material smooth
ta talus material
crt cratered terrain
CONTACTS
accurate
approximate
gradational
SURFACE FEATURES
secondary crater field
terrace deposits
AREAL and LINEAR FEATURES
raised rim of large impact crater
raised rim of small impact crater
degraded impact crater rim
topographic rise or hill
normal fault, approximate
ridge crest , accurate
furrow
subdued groove
crater chain
scarp
crater ray
POINT FEATURES
central peak of impact crater (major)
central peak of impact crater (minor)
bright spot
dark spot
small tholi
Jarovit
Dada
Roskva
Takel
Cozobi
Oxo
Duginavi
Hosil Tholus
Mikeli Tholus
Victa
Abellio
Kwanzaa Tholus
Aymuray Tholi
Fejokoo
270°East
280°
290°
300°
310°
320°
330°
340°
350°
360°East
60°
50°
40°
30°
21°
0
82 km
Lambert Conic Conformal projection
with two standard parallels at 58°N and 30°N
Adopted figure: sphere
Mean radius: 470 km
Grid: planetocentric lat./east long.
Scale bar represents the distance between 40°N and 50°N along the meridians.
10 ° difference in latitude along the meridians equals 82 km.

Figure 2-8. Geologic map of the Ac-5 Fejokoo Quadrangle of Ceres. The geologic map is displayed on top of the FC clear filter basemap presented in Fig. 2 at 50% transparency. Descriptions of the geologic units displayed on this map are given in section 2.3.3.

2.3.1 Geologic Setting

The Ac-5 Fejokoo quadrangle is one of four mid-latitude northern hemisphere cartographic quadrangles on Ceres (Figure 2-3). The Fejokoo quadrangle's entire extent is dominated by heavily cratered terrain, like most other quadrangles on Ceres. This region represents a major fraction of the most densely cratered areas on Ceres, which implies it is one of the most ancient terrains on the surface (Hiesinger et al., 2016). The Fejokoo quadrangle is bordered on the west and southwest by the Ac-4 Ezinu (Scully et al., 2018) and Ac-9 Occator (Buczkowski et al., 2018) quadrangles, respectively. These adjacent regions are generally more sparsely cratered than the Fejokoo quadrangle. The dominant geological feature in the Ac-4/Ac-9 region is Occator crater and the surrounding topographic high, Hanami Planum. To the south of the Fejokoo quadrangle lies the topographically depressed, relatively sparsely cratered, Ac-10 Rongo quadrangle (Platz et al., 2018). Despite the general low lying nature of the Ac-10 Rongo quadrangle it contains numerous broad topographic rises and tholi (singular, tholus, meaning domical mountain or hill) including Ahuna Mons, a large, roughly symmetric, smooth sided edifice whose origin is possibly cryovolcanic (Ruesch et al., 2016). To the east is the Ac-2 Coniraya quadrangle (Pasckert et al., 2018), which is dominated by Coniraya, Omonga, and other large impact craters. The Fejokoo quadrangle is capped to the north by the Ac-1 Asari north pole quadrangle (Ruesch et al., 2018), whose geology is dominated by densely cratered terrain and a high degree of topographic variability.

2.3.2 Topography

The surface elevation of the Fejokoo quadrangle with respect to the best-fit biaxial ellipsoid (482 km × 482 km × 446 km) for Ceres is shown in Figure 2-5. The Fejokoo quadrangle displays three general topographic provinces: a long, quasi-wedge shaped region of considerably high

topography along the western margin, an irregular region of moderately high topography in the northeast, and a large central low lying area dominated by degraded impact craters and several large domical tholi that are not strongly associated with impact craters (Figure 2-5b).

The high-topography western province, which sits ~2,500 m above the best-fit ellipsoid, spans ~600 km in length from the north pole south towards Abellio crater and sweeps out an area westward to approximately 265 ºE. This province has an average width of ~150 km within the Fejokoo quadrangle.

The moderately high northeastern topographic province is located immediately west of Oxo crater and south of Roskva and Dada craters. It spans ~300km east-to-west and ~150 km north-to-south. This region, which sits ~1,900 m above the average ellipsoid, is broadly domical compared to the plateau like nature of the western high topography province.

The low lying central region of the Fejokoo quadrangle, which contains Victa and the namesake Fejokoo crater, is the northernmost extension of a large depressed province that dominates the topography of the Ac-10 Rongo Quadrangle. This region has been identified as a large, potential, degraded impact basin by Marchi et al. (2016). The extension of this low lying area in the Fejokoo quadrangle, which is on average ~2,000 m below the average ellipsoid, displays many of the same geologic and morphologic characteristics as the Rongo quadrangle; in particular, the presence of large quasi-symmetric domical tholi. These tholi provide significant positive relief of ~2-4 km above the background topography in an otherwise low-lying region. The tholi present in this low-lying province are discussed further in section 2.3.4.1.

2.3.3 Description of Map Units

Seventeen different geologic units are identified on the geologic map of the Fejokoo quadrangle presented in Figure 2-8. FC images of type locations for each major unit class are presented in Figure 2-9. Geologic units were defined primarily by textural and morphologic characteristics observed in FC clear filter images and the HAMO DTM. Reflectance and spectral features were also employed in the identification of map units.

2.3.3.1 Cratered Terrain

Cratered Terrain (crt) represents the background material of the Fejokoo quadrangle, and is found ubiquitously throughout the region. It is defined as area with a high concentration of impacts craters and no other distinguishing characteristics (Figure 2-9a). The craters in this unit are predominantly degraded and rarely have discernable ejecta. In the FC enhanced-color ratio image (color composite R: Figure 2-7), this unit appears a brownish-red color throughout the Fejokoo quadrangle with little variation. This unit does not cross-cut any other geologic units. *Interpretation:* This unit is interpreted to be the most ancient cerean material present in the Fejokoo quadrangle based on its relative uniformity and high density of degraded craters of all sizes less than 200 km in diameter (Hiesinger et al., 2016).

2.3.3.2 Crater Material

Crater Material (c) represents material external to an individual crater that has modified the background cratered terrain substantially in either texture or morphology (Figure 2-9b). These modifications are usually a softening of the underlying topography, sheeted, fluted, or furrowed layer deposits; and occasional linear to curvilinear material streaks. *Interpretation:* These units are the result of relatively recent impacts into the Fejokoo quadrangle, and appear to degraded quickly

over time. Typically, this material is excavated from the parent crater (ejecta), but it can also be non-lobate mass wasting on the outward facing rim of parent craters.

Crater Material Bright (cb) and Crater Material Dark (cd) are sub-types of the Crater Material unit group. The distinguishing criterion between these three units is the reflectance measured in photometrically corrected FC images (Figure 2-10). Crater material bright has a higher reflectance than the immediate surrounding units, crater material dark has a lower reflectance than the surrounding units, and crater material has generally the same reflectance as surrounding units.

2.3.3.3 Crater Floor Materials

Crater Floor Materials Hummocky (cfh) and Crater Floor Materials Hummocky Dark (cfhd) are both related sub-types of the Crater Floor Material unit. These units, found on the floors of impact craters, are characterized by concentric furrows, terraces, and/or occasionally bulbous mounds. Again, the distinguishing criterion between these units is their reflectance compared to proximal background material. *Interpretation:* These units are disproportionately present in young craters (at least relative to the age of the ubiquitous cratered terrain), which imply that they degrade significantly over geologic time. Examples of these units that contain concentric terraces and/or a 'pinwheel' like texture (e.g. Figure 2-9h) are interpreted as being similar to transient crater collapse features on the icy satellites of Jupiter, Saturn, and Uranus (Schenk, 1989; Hiesinger et al., 2016). Thus the geomorphology of *cfh* and *cfhd* units with concentrically and/or 'pinwheel' terraced floors may be an indication that the upper layer of Ceres is rheologically similar to those of outer solar system satellites; at least proximally to where these units occur. In the case of *cfh* or *cfhd* units that do not have 'pinwheel' structures or concentric terraces (e.g. Figure 2-9c) we interpret them as similar to slumps found in the interiors of lunar and mercurian craters.

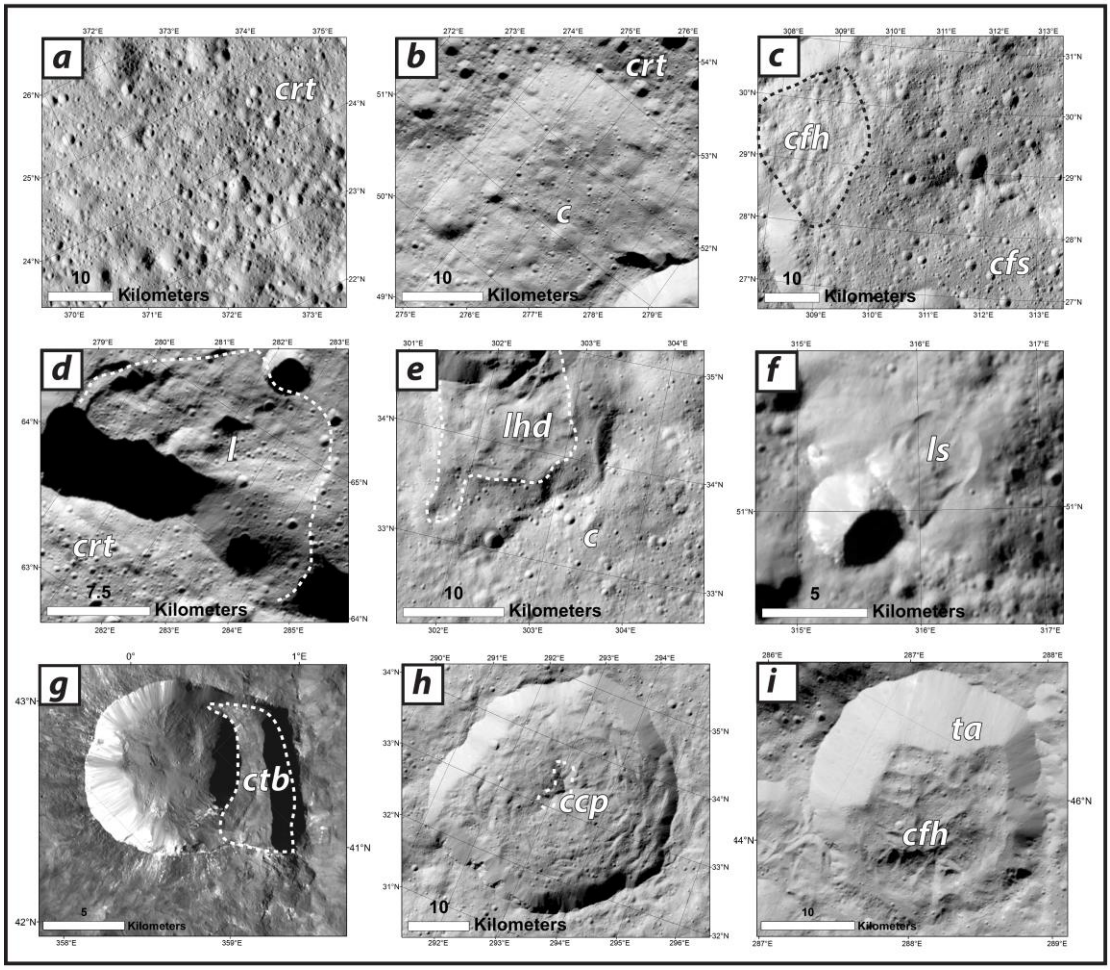

Figure 2-9. Type locales of the parent classes of geologic map units in the Fejokoo quadrangle. Image subsets are from FC clear filter LAMO mosaics or individual FC images: (a) cratered terrain, (b) crater material (seen in the center of the panel below the dashed black line), (c) crater floor material hummocky (inside black dashed line) and crater floor material smooth (right side of panel), (d) lobate material (inside white dashed line), (e) lobate material hummocky (in this case dark, see Figure 2-10 for an albedo enhancing photometrically corrected image of the Fejokoo quadrangle) is in the upper central portion of this panel (inside white dashed line), (f) lobate material smooth (center of panel), (g) crater terrace material (inside white dashed line; FC image number: FC1B0052044_16017012741F1E), (h) crater central peak material (inside white dashed line), and (i) talus material (upper portion of centrally located impact crater).

PHOTOMETRICALLY CORRECTED BASE MAP OF THE AC-5 FEJOKOO QUADRANGLE OF CERES

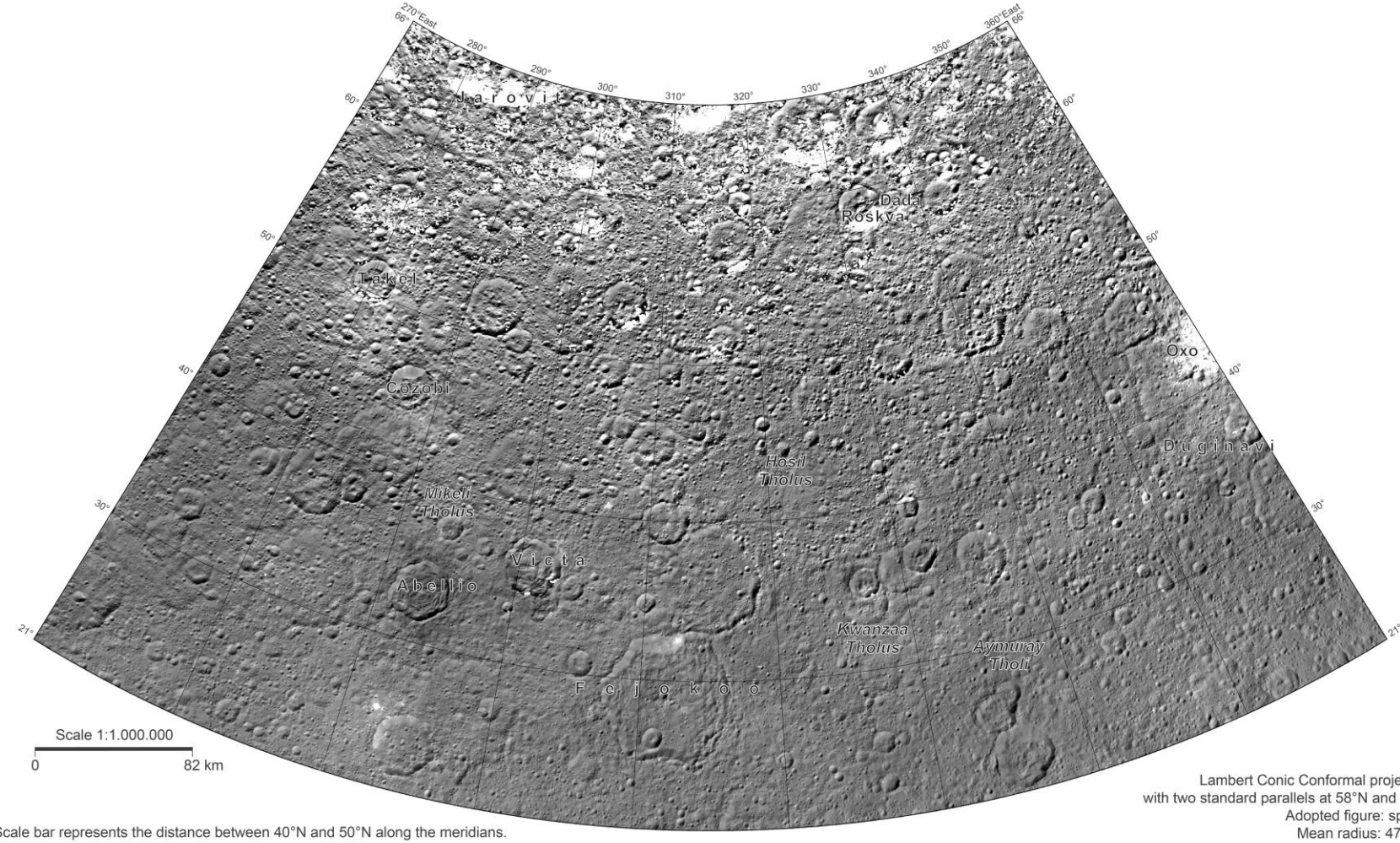

Scale bar represents the distance between 40°N and 50°N along the meridians.
10 ° difference in latitude along the meridians equals 82 km.

Lambert Conic Conformal projection
with two standard parallels at 58°N and 30°N
Adopted figure: sphere
Mean radius: 470 km
Grid: planetocentric lat./east long.

Figure 2-10. Photometrically corrected HAMO base map of the Ac-5 Fejokoo Quadrangle of Ceres. In this image stereotopography was used to help mitigate apparent brightness variations caused by different illumination conditions and topography. Brightness variations in this panchromatic image are predominantly due to reflectance differences in the surface material.

Crater Floor Material Smooth (cfs) and Crater Floor Material Smooth Bright (cfsb) are another pair of related units which are sub-types of Crater Floor Materials. These units are morphologically non-descript like the floors of craters found in the ubiquitous cratered terrain unit. The major differences between smooth crater floor material and cratered terrain are that smooth crater floor material is relatively less densely cratered, and is qualitatively less rough. Again, the distinguishing criterion between these units is their relative brightness compared to the immediate surrounding material. *Interpretation:* These units may represent an intermediate degradational state between hummocky crater floor material and cratered terrain; alternatively, they may represent rheological heterogeneities within the upper layer of Ceres.

2.3.3.4 Lobate Material (l)

This family of units are found both inside and outside of, but always associated with, impact craters. They are characterized by continuous deposits with well defined arcuate to linear margins, frontal lobes or snouts, and positive topographic relief relative to surrounding material (Figure 2-9d). The Lobate Material bright (lb) unit is differentiated from lobate material based on the relative brightness of the surrounding units. *Interpretations:* These lobate deposits are most frequently associated with distinctive scarps and appear to have down-slope directionality, as such they are predominantly interpreted as various forms of mass wasting such as debris flows, impact and/or gravitationally induced landslides, and ice-cemented flows. Occasionally these flows have no obvious head scarps, and in these cases are interpreted as a form of fluidized ejecta.

Lobate Material Hummocky (lh), Lobate Material Hummocky Dark (lhd), and Lobate Material Hummocky Bright (lhb) units are distinguished from lobate material by the presence of elongated mounds and rolls on their surface (Figure 2-9e). These hummocks typically have characteristic heights of several tens of meters, widths of hundreds of meters, and long-axis lengths

of hundreds to several thousands of meters. The long-axis of these features are typically aligned perpendicular to the downslope direction, except in Oxo crater. The lobate material hummocky dark and bright units are differentiated from the lobate material hummocky unit based on the relative brightness of the surrounding units. *Interpretation:* These features are interpreted as slumps and landslides within the Fejokoo quadrangle, and possibly fluidized ejecta for the incidence of hummocky lobate material to the east of Cozobi.

The Lobate Material Smooth (ls) unit has fewer surface features compared to other lobate material units, often starting from the rims of impact craters and running downslope (Figure 2-9f). They have a characteristic rounded appearance, and are often found with several superimposed deposits lying on top of one another. *Interpretation:* These units are likely formed directly or indirectly as impact triggered landslides. The Cozobi crater ls deposits are possibly a form of fluidized ejecta.

2.3.3.5 Crater Terrace Material Bright (ctb)

This unit, seen only within Oxo crater, demarks the unusual terrace block in the southeastern portion of the crater. Its surface is generally smooth and devoid of impact craters (Figure 2-9g). Notable surface features within this unit are open fissures and fault scarps (see section 2.3.4.2). *Interpretation:* This block is interpreted as a slump originating from the bounding ridge southeast of Oxo that collapsed towards its center. It was likely initiated post-impact during the collapse of the transient cavity.

2.3.3.6 Crater Central Peak Material (ccp)

This unit comprises the prominent central peaks of several complex craters in the Fejokoo quadrangle (Fig. 2-9h). Characteristic features of this unit include a distinctive break in slope at its

boundary, a conical topographic profile rising several hundreds of meters above the surrounding terrain, and a lower impact crater density than neighboring materials. *Interpretation:* These units are rebounded material created during the impact and post-impact collapse phases.

2.3.3.7 Talus Material (ta)

This unit is defined as non-descript slope material and otherwise unclassified slope related deposits. It is generally smooth, but in some cases displays a knobby texture (Figure 2-9i). It is always associated with the inward facing rims of impact craters. *Interpretations:* These talus slopes are likely highly unconsolidated granular materials resting at their angle of repose. They are interpreted as relatively young granular mass wasting and scree type deposits covering the walls of impact craters.

2.3.4 Geologic Features

2.3.4.1 Tholi

Six tholi of interest exist within the Fejokoo quadrangle (Figure 2-5b): South Aymuray (26ºN, 337ºE); Central Aymuray (29ºN, 336ºE); North Aymuray (31ºN, 334ºE); Kwanzaa (32ºN, 327ºE); Hosil (43ºN, 320ºE); and Mikeli (38ºN, 294ºE). These tholi share several common characteristics, including: prominence, diameter, profile, geographic affinity, and in some cases composition (see Table 2-1). These mounds have semi-major axes that fall in the range 13-24 km, an aggregate average mean quadratic radius of 19 km, and an average prominence of 3.3 km. In general, these tholi display broad circular to elliptical symmetry in their footprints with the exception of Kwanzaa and South Aymuray. These tholi have more irregular perimeters due to excavation by proximal impacts. The six tholi in the Fejokoo quadrangle are found only in the cratered terrain geologic unit, and all but the western-most tholus (Mikeli) exist in the south central

low topography province. In profile, these features are broadly domical (i.e. concave-down), have moderately steep slopes, and have plateau-like flat region near their summits (Figure 2-11). The flanks of the Fejokoo quad tholi have typical slopes of ~20º with a maximum measured slope of ~35º on Central Aymuray; for comparison, Ahuna Mons' smooth flanks have a typical slope of ~35º and a maximum slope of ~42º.

The four southeastern most tholi are also located within a regional positive Bouger gravity anomaly with a maximum value of ~140 mGal (Figure 2-12); although, they only appear weakly correlated with the center of the anomaly. This indicates that the region associated with the anomaly is isostatically overcompensated, which is consistent with the surrounding low topography province but unusual for such large edifices. The other prominent tholi in the Fejokoo quadrangle are not associated with any discrete gravity anomaly.

In addition to the aforementioned properties, Hosil, Mikeli, Central Aymuray, and to a lesser extent North Aymuray and Kwanzaa share similar spectral properties at 2.70 μm and 3.06 μm as observed by the VIR spectrometer (Figure 2-13). Increased band depth at 2.70 μm has been interpreted to represent an increased local abundance of phyllosilicate minerals in the regolith observable by VIR, whereas larger band depth at 3.06 μm has been interpreted to represent an increased abundance of ammoniated clay minerals in the regolith observable by VIR (De Sanctis, 2015). The aforementioned tholi are all distinguished as similar extreme points in the Fejokoo quadrangle with respect to their band depth values at 2.70 and 3.06 μm (Figure 2-13b). In general, these features are interpreted to have a lower concentration of ammoniated clays, and a slightly higher abundance of phyllosilicate minerals, than the average Fejokoo quadrangle background material. Factors like surface texture and grain size can also influence spectral properties, so if

these tholi are not compositionally related they are at the very least chemically and/or physically different than the average Fejokoo quadrangle.

2.3.4.2 Craters

At the time of this writing, the Fejokoo quadrangle has 10 impact craters with names recognized by the IAU (International Astronomical Union): Fejokoo, Abellio, Victa, Cozobi, Takel, Jarovit, Roskva, Dada, Duginavi, and Oxo.

Fejokoo: Centered at 29 ºN, 312 ºE within the low lying topographic province of the Fejokoo quadrangle, the 68 km mean diameter Fejokoo is the largest well preserved polygonal impact structure on Ceres. Its perimeter closely approximates an equilateral hexagon (Figure 2-14a). Like most craters on Ceres with diameters ≥ 20 km Fejokoo displays generally steep crater walls (slopes in some areas exceed 45º) and a largely flat floor. The smooth crater floor sits on average ~5 km below the surrounding terrain, and is disrupted only by the ~1km high central peak complex and collapsed crater wall material/terraces that are found near the northwestern and southeastern rims. In general, Fejokoo exhibits radially symmetric topography with minor departures from this symmetry around the collapsed southeast rim. Streaks of bright material hundreds of meters wide and ~5 km long are found on the inward facing slope of the north crater rim.

Tholus Name and Location	Semi-Major Axis (km)	Semi-Minor Axis (km)	Quadratic Mean radius (km)	Prominence (km)
South Aymuray: 26 ºN, 337 ºE	24	20	22	3.5
Central Aymuray: 29 ºN, 336 ºE	13	11	12	4.0
North Aymuray: 31 ºN, 334 ºE	17	11	14	3.1
Kwanzaa: 32 ºN, 327 ºE	35	19	28	3.0
Hosil: 43 ºN, 320 ºE	20	19	20	3.2
Mikeli: 38 ºN, 294 ºE	20	18	19	3.1
Ahuna Mons: 11 ºS, 316 ºE	21	13	17	4.2

Table 2-1. Approximate representative morphometric values for major tholi in the Fejokoo quadrangle and Ahuna Mons. Semi-major and semi-minor axes were determined using dominant breaks in slope around the tholi or Mons in question.

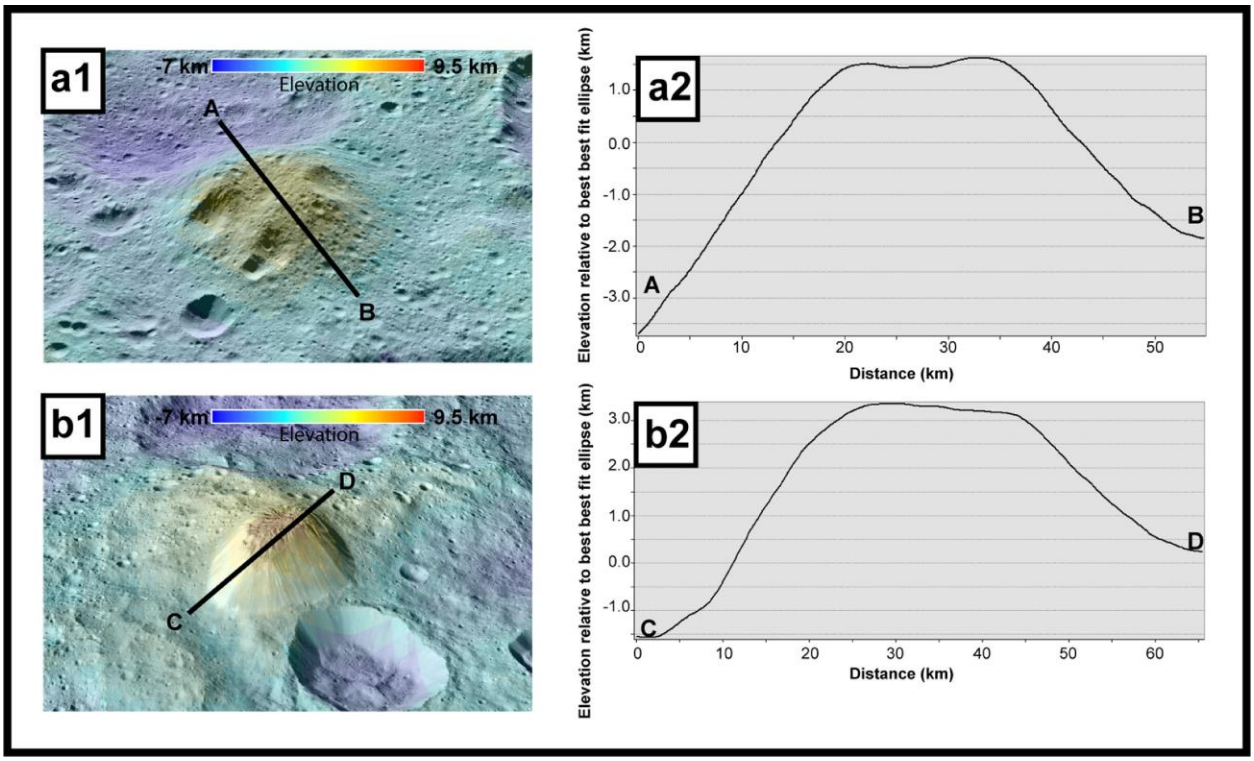

Figure 2-11. Perspective views and topographic profiles of Hosil tholus and Ahuna Mons (located in the Ac-10 Rongo Quadrangle). Hosil tholus, whose perspective view and profile are shown in panel (a1) and (a2), respectively, is the most morphologically similar example to Ahuna Mons found in the Fejokoo quadrangle. Ahuna Mons is depicted in panel (b1), and its profile is shown in panel (b2). The perspective views and profiles were created using the HAMO DTM. Vertical exaggeration in panels (a1) and (a2) is a factor of two. Panels (b1) and (b2) are vertically exaggerated by a factor of five.

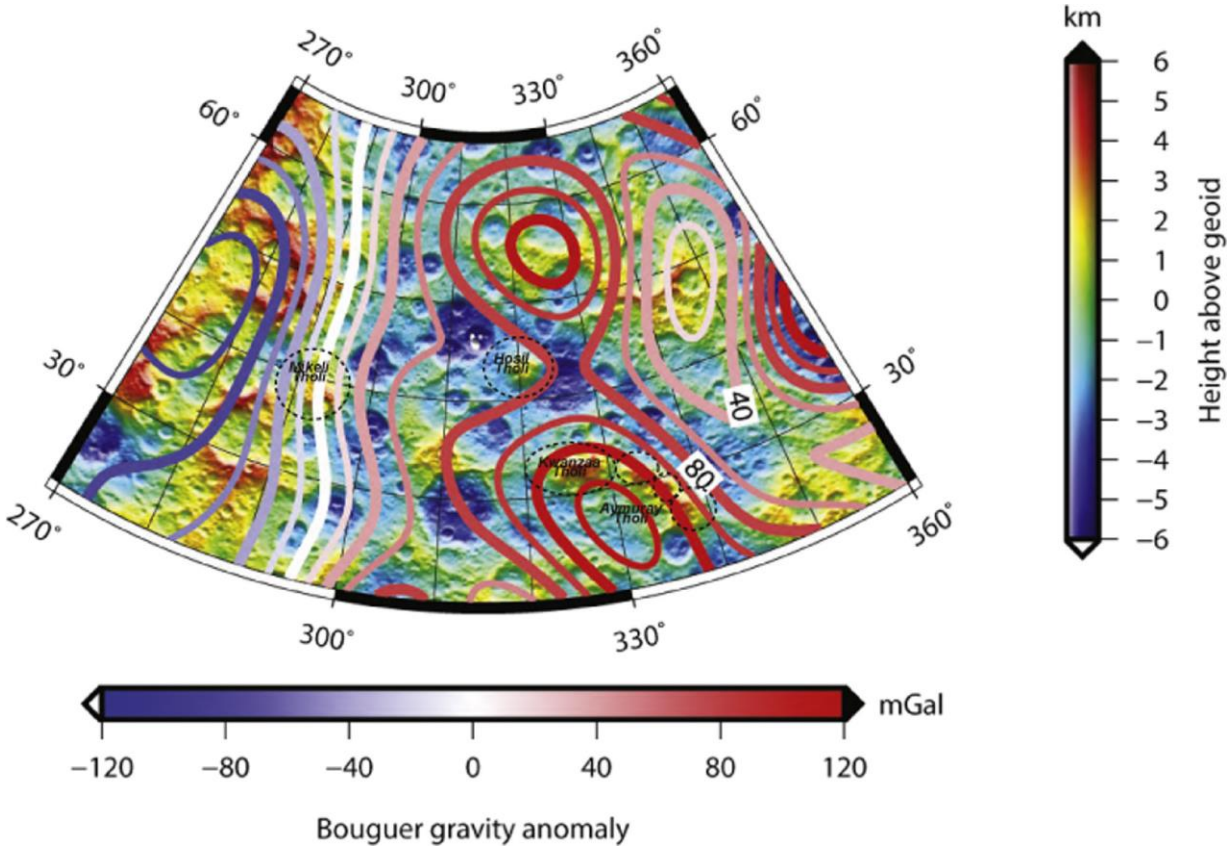

Figure 2-12. Bouger gravity anomaly map of the Fejokoo quadrangle. The location and approximate size of the Fejokoo quadrangle tholi are indicated by dashed ellipses. The gravity model used is computed to degree n = 16 for a two-layer model. The specific parameters for the model are presented in Ermakov et al. (2017).

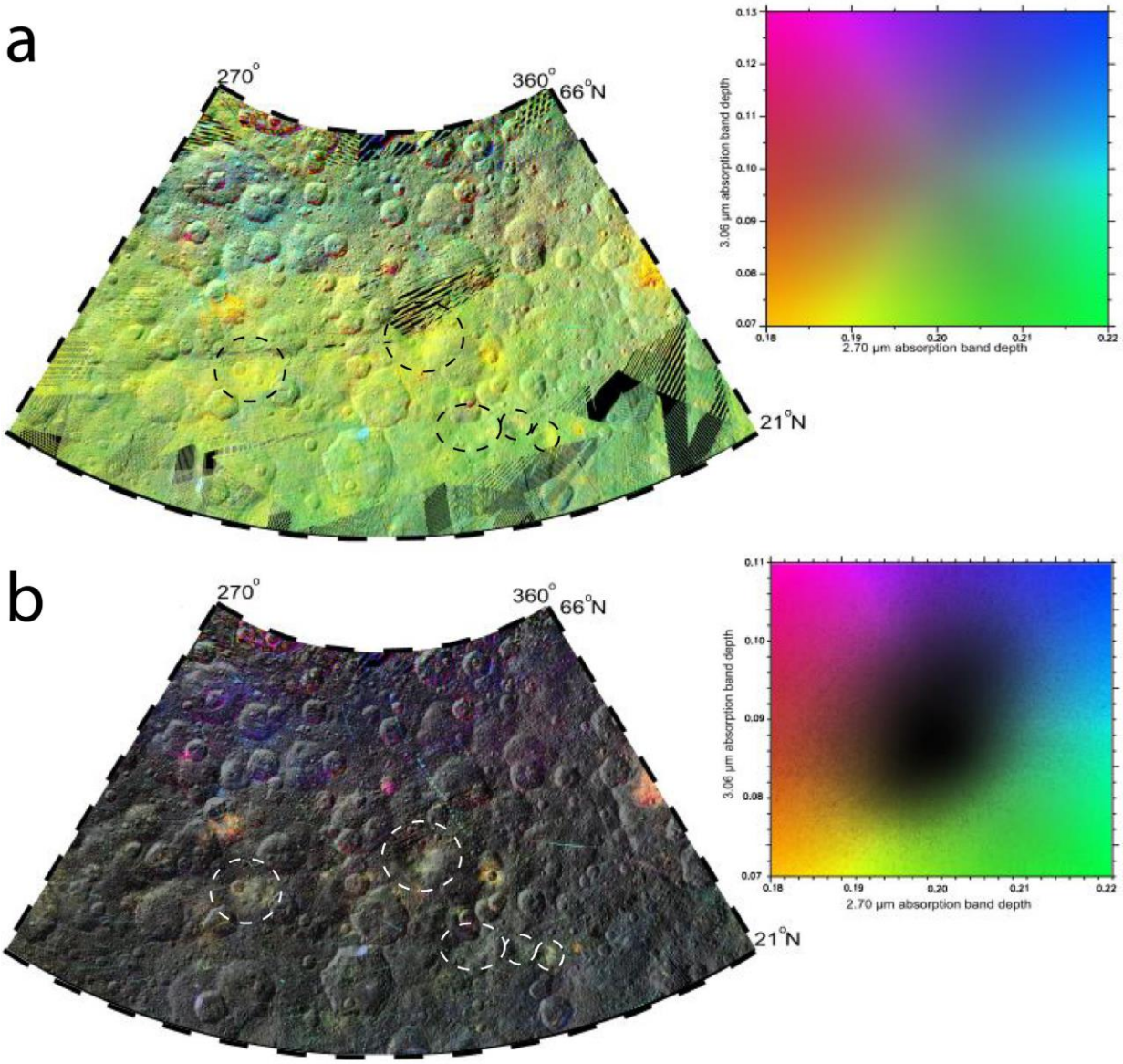

Figure 2-13. VIR spectral parameter map of the Fejokoo quadrangle. Panel (a) is a 2D color representation of the absorption band depth at 2.70 and 3.06 µm throughout the Fejokoo quadrangle. The upper palette displays the colors used in Panel (a). Panel (b) emphasizes the extreme values for both of the aforementioned bands throughout the Fejokoo quadrangle by masking out intermediate colors. The lower palette displays the colors used in Panel (b). Larger band depths at 2.70 µm have been interpreted to represent an increased local abundance of phyllosilicate minerals, whereas larger band depths at 3.06 µm have been interpreted to represent

an increased abundance of ammoniated clay minerals (De Sanctis, 2015). Note that the fidelity of VIR data deteriorates rapidly above 50ºN, so the systematic blue tones in the northern portion of both panels a) and b) are likely not real phenomena. Major tholi in the Fejokoo quadrangle are highlighted by dashed ellipses. The VIR spectral parameter maps are photometrically corrected for the effects of topography; the underlying FC base map is not. Fejokoo quad tholi that share similar spectral properties are indicated by dashed white ellipses.

Abellio: This 32 km diameter crater centered at 33 ºN, 293 ºE is located on the boundary of the western high and central low topography provinces. Abellio exhibits a topographically asymmetric floor that is systematically higher in the west and depressed in the east. This is likely because of its location in this transitional region (Fig. 2-5b & 2-14b). Like Fejokoo, Abellio exhibits a relatively flat crater floor (situated ~2,500 m below its mean rim height), a central peak (that rises ~500 m above the crater floor), and steep crater walls (~45º median slope). Abellio's floor also displays prominent concentric ridges and terraces that are morphologically similar to those found in craters on icy satellites (Schenk, 1989; Porco et al., 2005). Photometrically corrected FC images also identify Abellio and its surrounding ejecta as being composed of distinctly lower albedo material than the surrounding terrain (see Figure 2-10). Abellio's features appear only moderately degraded compared to the adjacent terrain; this coupled with a low crater density on the floor and surrounding ejecta blanket imply it is a relatively fresh crater in the Fejokoo quadrangle.

Victa: 32 km in diameter and located just east of Abellio (centered at 36 ºN, 301 ºE), Victa crater (Figure 2-14c) is similar in most ways to Abellio. Victa differs from Abellio in three distinct categories: (1) its floor and rim planes are much more parallel to the local tangent plane of the Ceres best-fit ellipsoid due to its location entirely within the low topography province, (2) it has far fewer concentric terraces and their spacing is much more irregular, and (3) although darker than the average background material in the Fejokoo quadrangle it displays a higher albedo on average than Abellio (see Figure 2-10). A large dark hummocky lobate deposit ~12 km long by ~8 km wide stretches radially outward from the southern rim of Victa into a local depression that is likely the remnant of a pre-existing impact crater. This deposit is interpreted as a combination of Victa ejecta whose collection was locally enhanced by the presence of a

depression and collapsed Victa crater rim material. Victa's ejecta darkens gradationally from east to west. Like Abellio, Victa also appears relatively fresh, but the cross-cutting relationships between Abellio, Victa, and their ejecta are ambiguous.

Cozobi: Centered at 45 ºN, 287 ºE, the 24 km diameter Cozobi crater displays a distinctly asymmetric rim profile (Figure 2-14d). The southern portion of the crater rim is almost completely collapsed displaying relief <1 km above the crater floor. This is in contrast with the northern rim, which rises ~6 km above the crater floor. This is a possible indication that the impact was into steep terrain, or that the impact itself was quite oblique. Cozobi's floor exhibits a bumpy texture consisting of several large domes. The floor also contains some curvilinear ridges and terraces. Cozobi has a continuous ejecta deposit to its north and east, which display radial furrowing, increased textural softness compared to the surrounding terrain, and gradational boundaries with no detectable topographic signature, but is lacking these features around the remainder of its circumference. Instead, three prominent lobate flows features are seen emanating radially away from the southern, eastern, and western rims. The western flow is ~12 km long by ~1.5 km wide with total drop height of ~2.6 km. It is morphologically smooth at LAMO resolution, and displays a mass concentration at its terminus in the form of a bulbous snout. The eastern flow is morphologically similar the previous flow, but is significantly larger. This flow extends ~18.5 km radially outward from the eastern rim, is ~12 km wide at its origin, and has a total drop height of ~3.5 km. The southern flow is considerably larger than the previous two cases measuring ~25 km long by ~18 km wide with a total drop height of ~4.1 km. The flow is structured into numerous small v-shaped superimposed lobes with smooth appearances and occasional ramparts similar to those found in martian fluidized ejecta (Mouginis-Mark, 1981). Although Cozobi is the only crater in the Fejokoo quadrangle

interpreted to have fluidized ejecta deposits, these types of flows are common on Ceres globally with the preponderance of them located between 60 ºS and 60 ºN (Schmidt et al., 2017). All of the flow features around Cozobi (Fig. 2-14d) have thicknesses on the order of a few 10s of meters as inferred from the DTM.

Takel: This 22 km diameter crater centered at 51ºN, 280ºE in the high topography province is the smallest well preserved complex crater in the Fejokoo quadrangle. It has a relatively asymmetric rim with the northeastern portion rising ~1 km higher than the average crater rim. Takel is ~2 km deep with respect to the average rim height. A moderately sized mass wasting feature (~7.5 km long by ~5.1 km wide) with pronounced lateral ridges up to ~30 m tall on the northern crater wall is the dominant geologic feature within Takel (Figure 2-14e). A larger bright material region associated with a blocky spine-like protrusion is located on the interior of the southern crater wall.

Jarovit: The 66 km diameter Jarovit, centered at 68 ºN, 285 ºE is the northernmost named feature to protrude into the Fejokoo quadrangle. This highly degraded and asymmetric crater displays significant recession of the crater rim in two main locations, one on the north rim and the other on the southwest rim. The recess on the southwest rim is also host to the most outstanding geologic feature in Jarovit, which is a large, broad, interior facing mass wasting feature (Figure 2-14f). This lobate deposit is ~22 km long, ~15 km wide, and ~200 m thick at its eastern terminus. The total drop high from the lobate deposit's scarp to its eastern toe is ~4.1 km. Unlike the rest of Jarovit, the scalloped recess where the mass wasting feature originates displays sharp undegraded morphologies suggesting it is relatively young compared to its host crater. The landslide's scarp does not display significant uplift relative to the remaining rim of Jarovit, nor does there appear to be any obvious ejecta or mass wasting exterior to this recess. Thus this

feature has been interpreted as being most likely an impact triggered landslide by a relatively small impactor, such that the triggering impact crater was eroded during the subsequent landslide.

Roskva and Dada: Roskva and Dada are two proximal craters centered at 59 ºN, 333 ºE and 59 ºN, 337 ºE, respectively (Figure 2-14g). The ~22 km diameter Roskva crater is roughly symmetrical in shape and in topography. Roskva has a generally flat floor that lies ~2.5 km below the average rim height. The floor itself is characterized by curvilinear ridges and large scale hummocks (100-200 m tall and 700-1000 m wide). A poorly developed central peak with a prominence of ~250 m is located in the center. Roskva crosscuts Dada along their shared rim indicating it is the younger of the two.

The 12 km diameter Dada crater is a simple bowl-shaped crater with a maximum depth ~1,000 m below the average rim height. The floor of Dada sits ~1,000 m above the average depth of Roskva, and the shared rim between the two craters rises only ~300 m above the floor of Dada. A sinuous scarp in the western portion of Dada indicates possible collapse of a section of the crater into Roskva. This observation is difficult to confirm as the downrange section of any mass wasting falls within a currently shadowed region as seen by Dawn.

Duginavi: Centered at 39 ºN, 4 ºE (Figure 2-14i), the 155 km diameter Duginavi crater only partially extends into the southeast/south central portion of the Fejokoo quadrangle, and is the host crater for the previously mentioned Oxo crater. Duginavi is highly degraded and heavily cratered. The crater floor extends to a maximum depth of ~5 km below the highest segment of the rim, and the center is dominated by a large degraded central peak. The northeastern portion of Duginavi contains a large unnamed tholus that appears unrelated to the subdued central peak.

Oxo: This crater (Figure 2-14h) is the most striking geologic feature in the Fejokoo quadrangle. With an absolute average reflectance of ~0.07 at 550 nm, Oxo is the second brightest feature on Ceres behind Cerealia Facula, the central bright dome in Occator (absolute reflectance ~0.3 at 550 nm wavelength); the average Ceres has an absolute reflectance of ~0.035 (Nathues et al., 2015). The ~10 km diameter crater, centered at 42.2 ºN, 359.6 ºE, is shared between the Ac-5 Fejokoo and Ac-2 Coniraya quadrangles with the preponderance of the feature lying within the former. The crater interior to the SE rectangular terrace is a simple bowl shape (maximum depth ~1,200 m below the average height of the undisturbed western rim) that rises towards the east (Figure 2-15) due mainly to the large bounding ridge trending NE-SW located at its southeastern margin. The large rectangular terrace slump block found in the southeastern half of the crater dominates the internal morphology of Oxo. The terrace, which measures ~8.2 km along strike and is ~2.1 km wide, sits ~1,000 m above the base of Oxo, which puts it at roughly the same elevation as the northwest rim. The main bounding scarp rises an additional ~1,000 m above the terrace block itself. The bulk of this elevation gain occurs over ~1,300 m equating to an average slope of ~38º (Figure 2-15c). This is significantly higher than 24º, which is representative of the slope of the northwestern rim.

Unlike most other craters in the Fejokoo quadrangle Oxo has a photometrically distinct and well-defined ejecta blanket surrounding it. The majority of the ejecta falls within a skewed rectangular region ~44 km long by ~31 km wide centered at 42.4 ºN, 359.7 ºE with the long axis trending NE-SW. Like the crater itself Oxo's ejecta is substantially brighter on average than the mean Ceres, yet it still displays a high degree of small scale structure on the order of hundreds of meters in the form of bright and dark material rays. The dark material rays are on average 10% less bright than the background cratered terrain, while the bright material rays can be up to 3

times as bright as the background terrain in some locations. These alternating curvilinear rays are found to radiate away predominantly from the western half of Oxo. Additionally, Oxo is the most spectroscopically variable feature in the Fejokoo quadrangle. Oxo and its surrounding ejecta appear strongly blue in color composite R (Figure 2-7) meaning it has a negative spectral slope in the visible wavelengths. This negative slope is in contrast to the majority of the Fejokoo quadrangle, which generally has a positive slope (i.e. reddish tinge in color composite R). Regions on Ceres with negative spectral slopes have been associated with younger surface ages (Jaumann et al., 2016; Schmedemann et al., 2016).

Initial VIR observations of Oxo detected significant water ice absorption bands at 1.65 μm and 2.00 μm (Combe et al., 2016), which partially motivated the detailed geological mapping effort presented here (Fig. 2-16). Two major detections were made in Oxo; the primary is centered at 359.8 ºE, 41.8 ºN (Figure 2-15, rectangle 1), and the weaker secondary detection is centered at 359.9 ºE, 41.4 ºN (Figure 2-15, rectangle 2) (Combe et al., 2016). This mapping campaign revealed four geologic/morphologic features in and around Oxo of particular noteworthiness: (1) an extensive boulder field, (2) a parallel to sub-parallel system of scarps, fissures, and normal faults; (3) lobate hummocky floor material associated with the primary H_2O detection (lobate material hummocky bright geologic unit in Figure 2-16), and (4) lobate mass wasting deposits associated with the secondary detection (lobate material geologic unit in Figure 2-16). A panchromatic base map image of Oxo and its ejecta is displayed in Figure 2-17.

Using LAMO resolution FC images 77 very large boulders (hereafter referred to as megablocks) ~100-140 m in diameter (which is the smallest scale that allows for reasonable interpretation) were identified in and around Oxo. The megablocks external to the crater are found only within ~4 km of the northern and northwestern portions of the rim indicating a

possible downrange direction for the Oxo forming impact. The megablocks in the crater's interior are found on all the constituent geologic units with a relative scarcity on the bright lobate hummocky material, which is associated with the primary H_2O detection. Boulders/megablocks have been observed around only a handful of other geologically fresh craters on Ceres (Schröder et al., 2016). In general, the scarcity of large blocks on the surface of Ceres appears broadly consistent with Basilevsky et al. (2015)'s prediction that the average lifetime of boulders on Ceres should be ~0.03 times that of boulders on the moon, assuming this scaling factor applies equally to all sizes of boulders/megablocks. However, other factors such as the observed lack of a cohesive cerean bedrock unit are not accounted for in this interpretation. This rapid degradation, if true, is likely driven by thermal cycling, micrometeorite bombardment, and potentially sublimation. The presence of megablocks at Oxo supports the relatively young crater counting model age estimates of ~3-4 Ma reported here (Figure 2-18). Crater counting at Oxo is particularly difficult due to its young age and morphology; it should be noted that its age has been reported as young as ~500 ka by other authors (Schmedemann et al., 2016).

The numerous linear fractures found parallel and sub-parallel to the main bounding scarp of Oxo's terrace block are located both exterior and interior to the crater. The exterior set of scarps and ridges are located to the south and southeast of the main bounding scarp along a broad ridge flanking Oxo, and are interpreted as normal faults. These faults range between 1-4 km in length, and have inferred vertical displacements of tens to approximately 100 meters. The most obvious fault located in the interior of Oxo is the main terrace bounding fault located along the SE margin of the crater. Based on the slump-like behavior of the main terrace block this fault, which has a vertical displacement of ~1,000 m, is likely a listric-style normal fault (Nathues et al., 2017). The remaining set of interior arcuate fissures and scarps are located exclusively on the

main terrace block. These features range in length from <1-3.5 km in length, and in the case of faults have vertical displacements on the order of tens of meters whereas the largest fissure open near the northern margin of the terrace is ~100 m wide. Vertical displacements were inferred from shadow measurement taken on individual FC frames, and informed by the DTM where the faults were resolved.

The lobate hummocky material unit is ~3.3 km wide along the widest part of its toe, and ~2.7 km long from the top of the inner most scarp to the edge of the toe; it faces towards the center of Oxo with a mean slope of ~21º, which is shallower than the surrounding crater walls. The primary H_2O detection is most closely associated with the high albedo bright unit near the southern end of the hummocky unit, but the VIR pixels showing the greatest H_2O absorptions are located immediately east of the bright unit within the shadow of the terrace block. The lobate hummocky unit appears covered with spatulate lobes hundreds of meters wide separated by numerous linear, and three major curvilinear and bifurcating grooves that run the length of the slope.

The secondary H_2O detection on the terrace block is mostly coincident with two lobate mass wasting features that are both ~1,300 m long by ~400 m wide with mean slopes of ~22º. These deposits are roughly as wide as their source and have broad steep-fronted toes with apparent terminal ramparts. The thickness of these toes is estimated to be on the order of tens of meters; however, the HAMO-based DTM is ambiguous at small scales in this region of high topographic contrast.

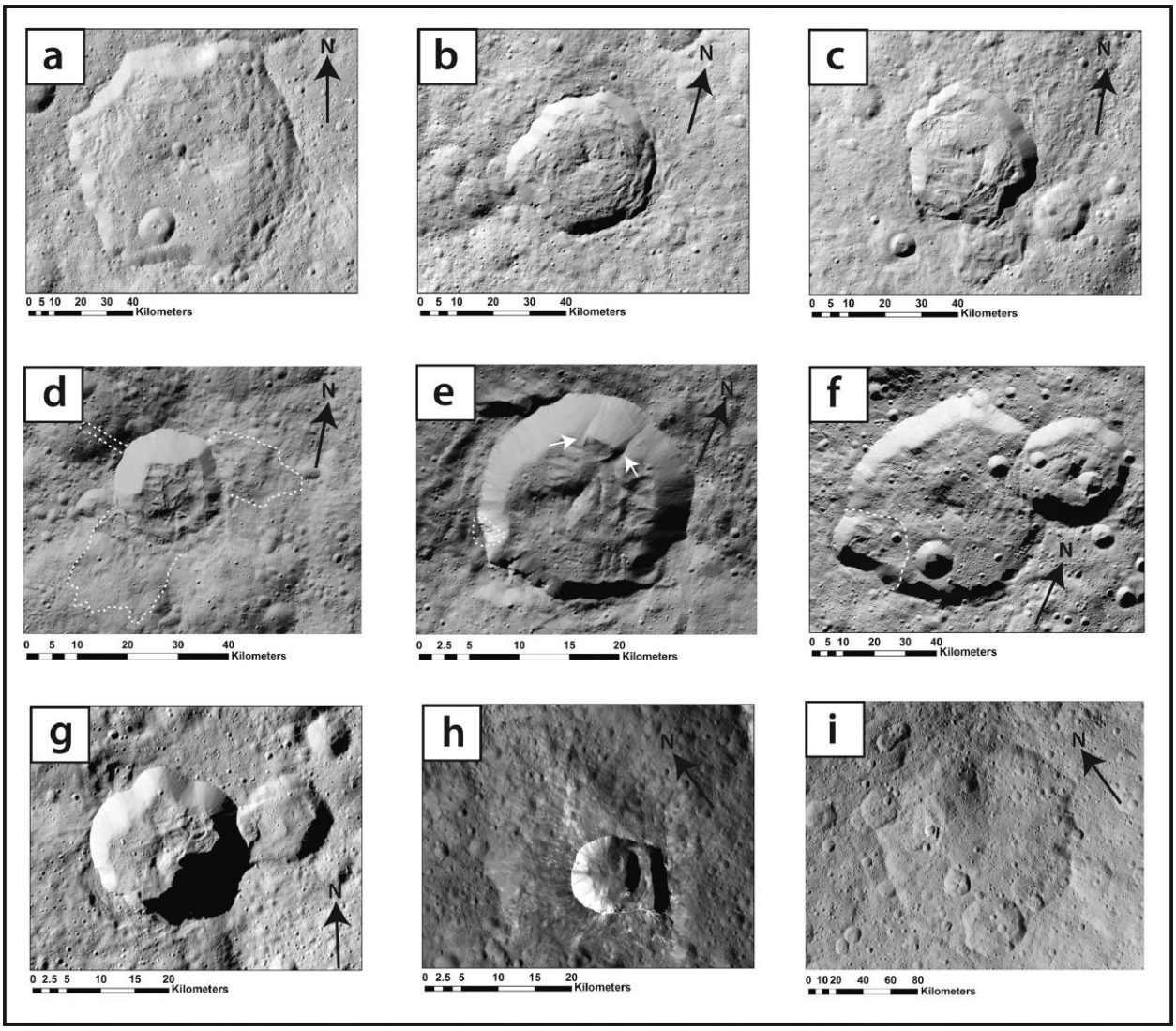

Figure 2-14. Named impact craters in the Fejokoo quadrangle; image subsets are from FC clear filter LAMO mosaics or individual FC images: (a) the namesake Fejokoo crater, which displays a distinctive hexagonal shape; (b) Abellio crater, which is characterized by its dark regularly ridged floor; (c) Victa crater, which is characterized by its mottled floor and dark external mass wasting deposit seen at the bottom of the frame (see Figure 2-10); (d) Cozobi crater, which is characterized by its bulbous external cuspate flow deposits (flow margins are indicated by dashed lines); (e) Takel crater, which is characterized by its internal mass wasting deposits (large ridges indicated by white arrows) and localized bright region (indicated by the dashed line); (f)

Jarovit crater, which is characterized by a large landslide-like feature emanating from the recess towards the left of the frame (the distal flow margin is approximately indicated by the dashed white line); (g) The joined Roskva (left) and Dada (right) craters, which are characterized by their recessed and sunken shared rim; (h) Oxo crater, characterized by its high albedo, negative spectral slope in the visible (see Fig. 6), and large internal slump block seem on the right side of the crater; and (i) Duginavi crater, which is characterized by its large diameter and high degree of degradation.

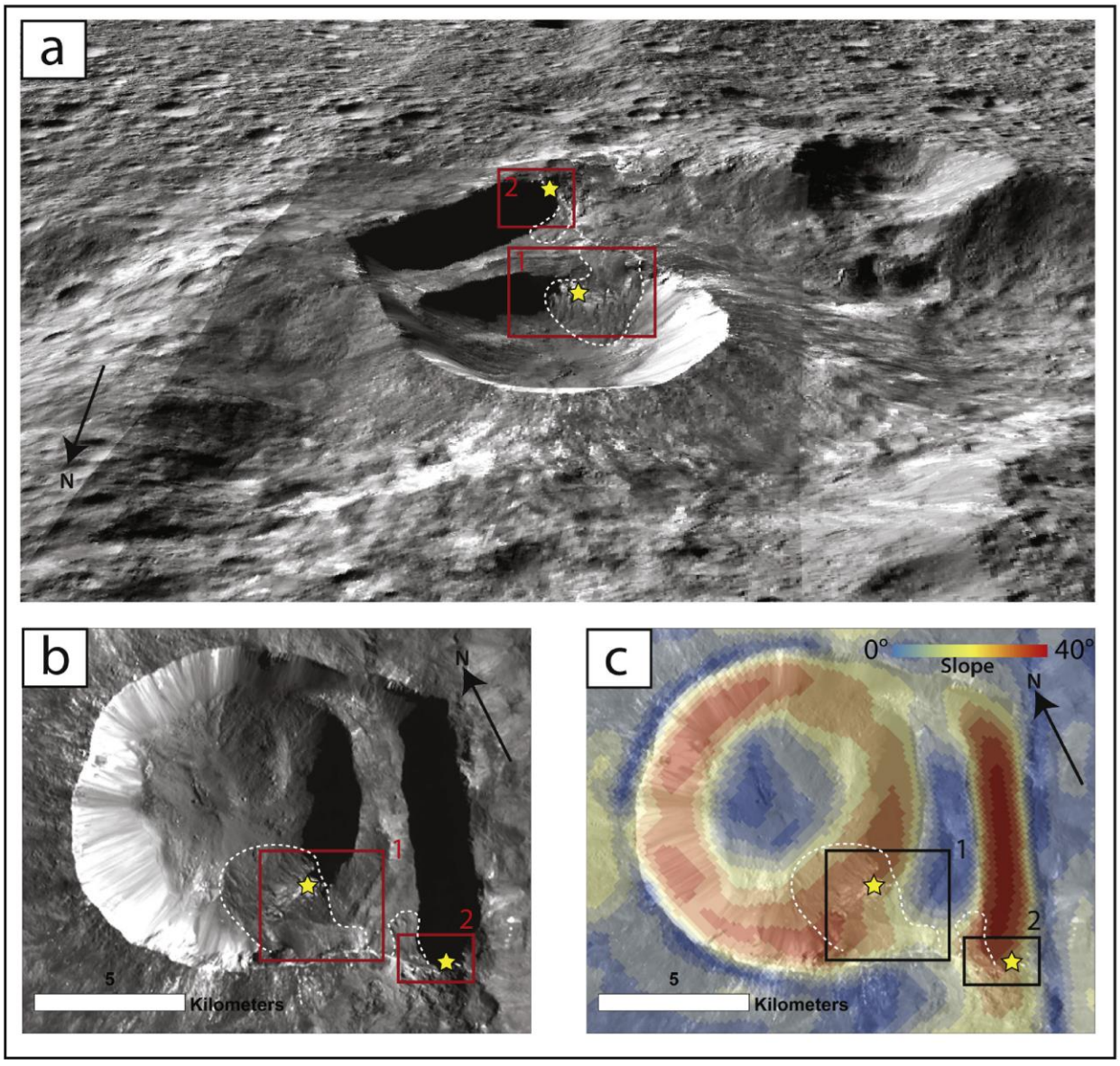

Figure 2-15. Morphology of the regions associated with the spectroscopic detections of H_2O in Oxo crater. In all panels the rectangles 1 and 2 refer to the primary and secondary detections of H_2O respectively; the yellow stars inside the rectangles indicate the location of the strongest signal within each locus of detection (see Combe et al., 2016), and the dashed white lines indicate the flow features associated with each detection. Panel (a) presents a perspective view of Oxo looking approximately southeast (vertical exaggeration is a factor of 1.5). Panel (b) presents

a plan view of Oxo. Panel (c) presents a slope map derived from the HAMO SPG DTM overlain onto the image in panel b). Note the hummocky and grooved terrain in rectangle 1 and the lobate material in rectangle 2.

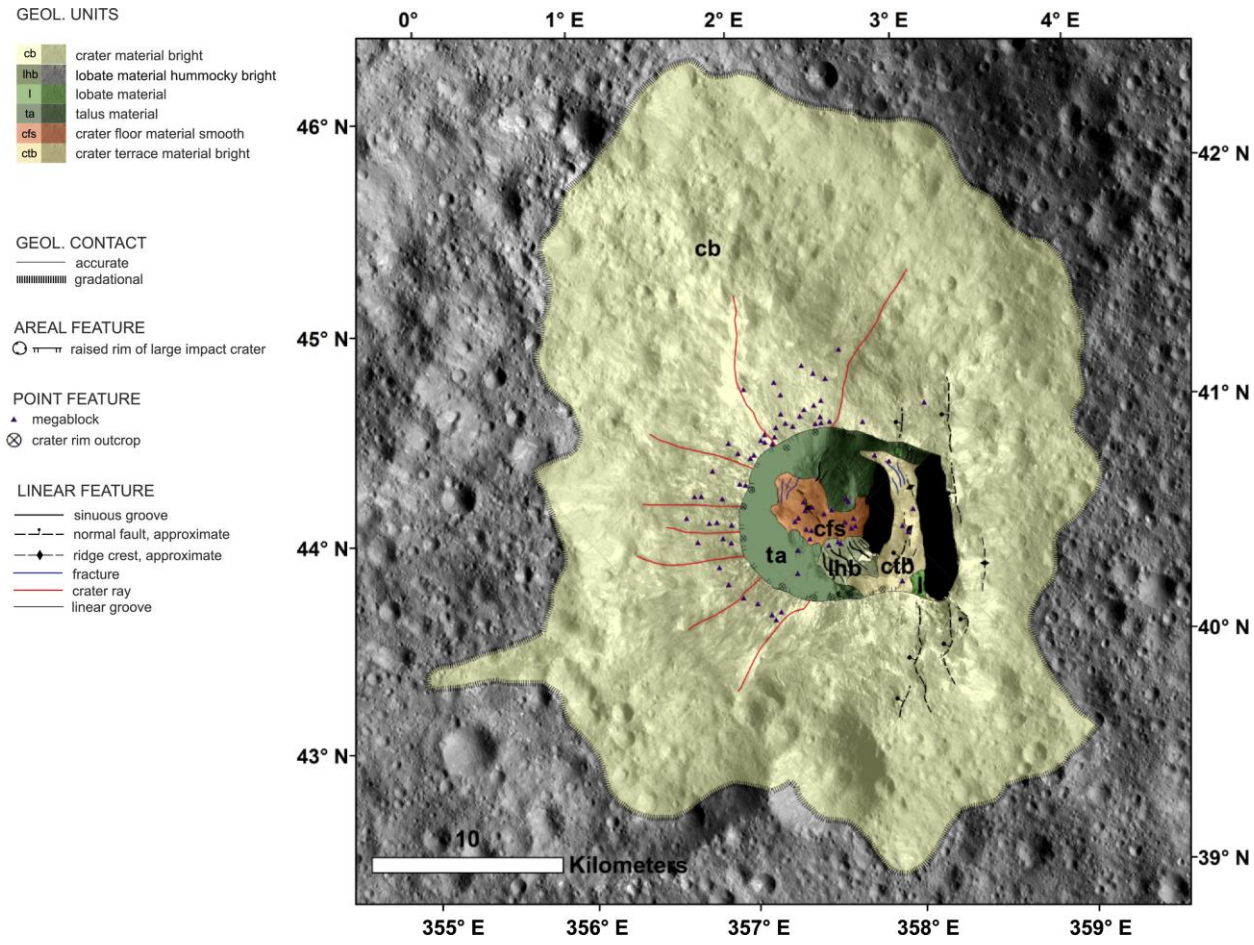

Figure 2-16. Geologic map of Oxo crater. The geologic map is shown is overlain onto a FC LAMO clear filter mosaic. The primary H_2O detection is located at 41.8 ºN, 359.8 ºE, which is nearly coincident with the crater floor material bright enclave within the crater floor material hummocky unit in the lower central region of the crater. The secondary H_2O detection is located at 41.4 ºN, 359.9 ºE, which is coincident with the lobate material unit in the lower right corner of Oxo's slump terrace. Both of these detections are discussed in detail in Combe et al. (2016). Crater rim outcrops indicate major rocky protrusions around Oxo. These outcrops are commonly situated at the origins of bright and dark material streaks.

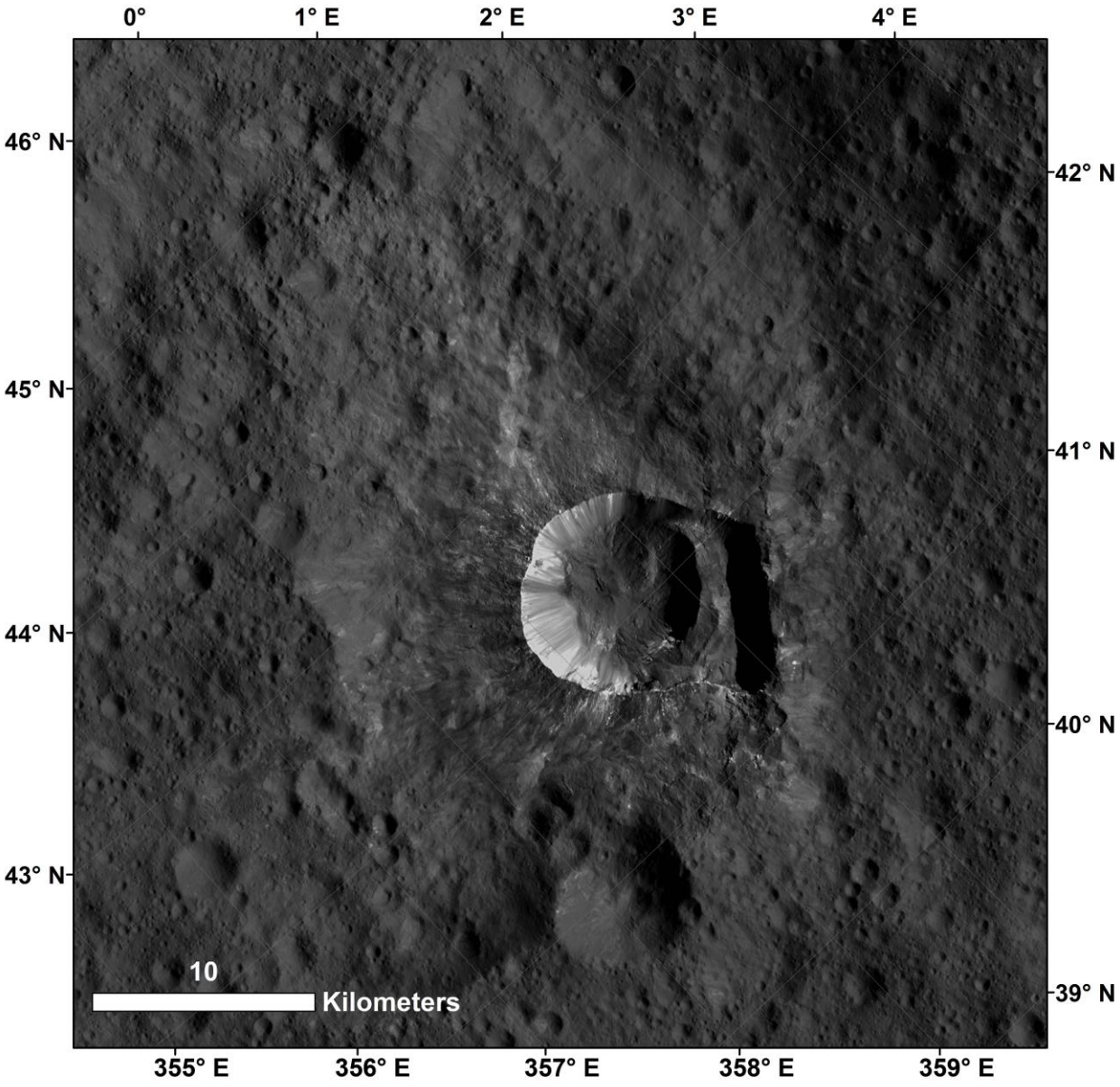

Figure 2-17. Panchromatic LAMO basemap of the Oxo crater region.

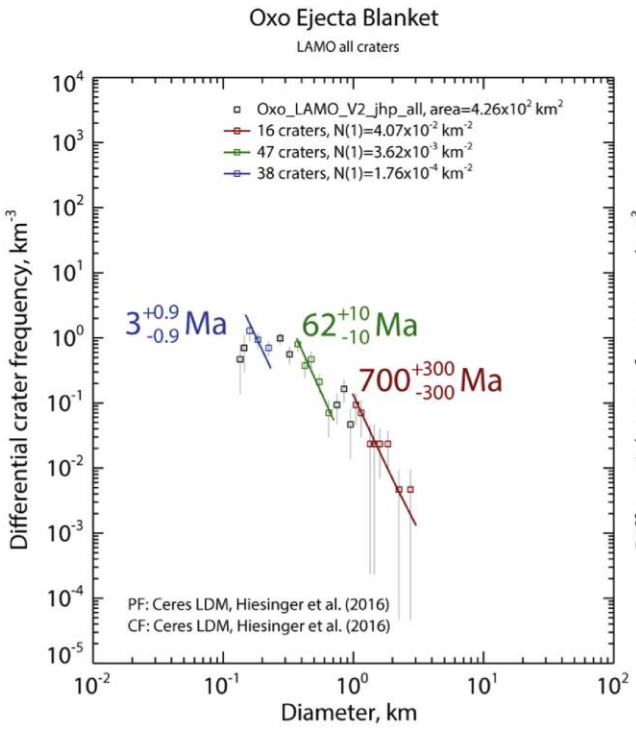
Oxo Ejecta Blanket
LAMO all craters
Oxo_LAMO_V2_jhp_all, area=4.26x10² km²
16 craters, N(1)=4.07x10⁻² km⁻²
47 craters, N(1)=3.62x10⁻³ km⁻²
38 craters, N(1)=1.76x10⁻⁴ km⁻²
3 +0.9 -0.9 Ma
62 +10 -10 Ma
700 +300 -300 Ma
PF: Ceres LDM, Hiesinger et al. (2016)
CF: Ceres LDM, Hiesinger et al. (2016)
Differential crater frequency, km⁻³
Diameter, km

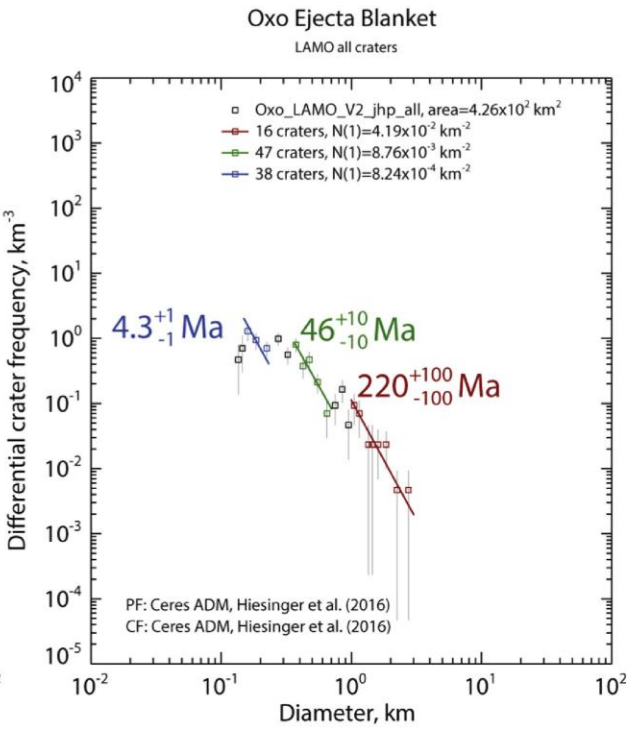
Oxo Ejecta Blanket
LAMO all craters
Oxo_LAMO_V2_jhp_all, area=4.26x10² km²
16 craters, N(1)=4.19x10⁻² km⁻²
47 craters, N(1)=8.76x10⁻³ km⁻²
38 craters, N(1)=8.24x10⁻⁴ km⁻²
4.3 +1 -1 Ma
46 +10 -10 Ma
220 +100 -100 Ma
PF: Ceres ADM, Hiesinger et al. (2016)
CF: Ceres ADM, Hiesinger et al. (2016)
Differential crater frequency, km⁻³
Diameter, km

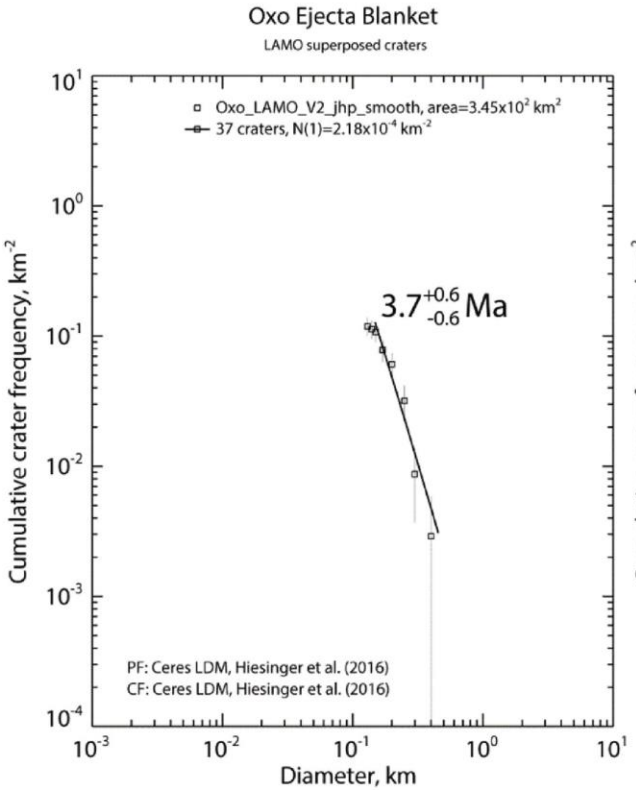
Oxo Ejecta Blanket
LAMO superposed craters
Oxo_LAMO_V2_jhp_smooth, area=3.45x10² km²
37 craters, N(1)=2.18x10⁻⁴ km⁻²
3.7 +0.6 -0.6 Ma
PF: Ceres LDM, Hiesinger et al. (2016)
CF: Ceres LDM, Hiesinger et al. (2016)
Cumulative crater frequency, km⁻²
Diameter, km

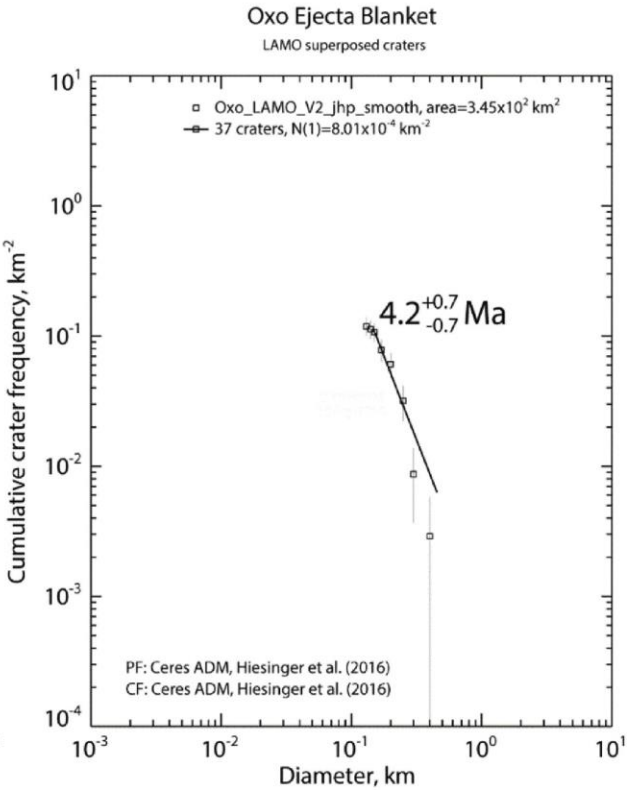
Oxo Ejecta Blanket
LAMO superposed craters
Oxo_LAMO_V2_jhp_smooth, area=3.45x10² km²
37 craters, N(1)=8.01x10⁻⁴ km⁻²
4.2 +0.7 -0.7 Ma
PF: Ceres ADM, Hiesinger et al. (2016)
CF: Ceres ADM, Hiesinger et al. (2016)
Cumulative crater frequency, km⁻²
Diameter, km

Figure 2-18. Absolute model ages (AMAs) for the ejecta blanket of Oxo crater derived using the lunar derived model (LDM) (left column) and the asteroid derived model (ADM) (right column) from Hiesinger et al. (2016). Best fits to resurfacing events were derived based on production function isochrones. Two approaches have been applied here. The differential plots (upper row) show crater size frequency distributions (CSFDs) with all craters measured within the counting area, including craters that are morphologically visible through the ejecta blanket, and thus consequently do not superpose it. Three different resurfacing events were identified. The youngest event at 3 Ma (LDM) or 4.3 Ma (ADM) likely represents the formation of Oxo crater, while the older ages represent two prior resurfacing events likely caused by underlying impact craters. The older of these events was likely caused by the emplacement of Duginavi or ejecta from one of the many nearby large impact craters. The cumulative plots (lower row) show the CSFDs of select craters which unambiguously superpose the ejecta blanket within the counting area. The derived AMAs are 3.7 Ma (LDM) and 4.2 Ma (ADM), which are nearly identical with the youngest resurfacing events of the differential plots. Consequently, we interpret them to represent the deposition of Oxo's ejecta blanket.

2.4 Discussion

2.4.1 Distribution and Implications of Tholi in the Fejokoo Quadrangle

The distribution of tholi in the Fejokoo quadrangle appears to be biased towards the low topography province in the southern portion of the quadrangle, which we recall from section 3.2 is essentially a northern extension of the smooth lowlands found ubiquitously in the Ac-10 Rongo quadrangle. Approximately 68% of all tholi and mons on Ceres identified by a global mapping campaign (Buczkowski et al., 2016) are found on the same hemisphere that includes the Ac-5 Fejokoo Quadrangle within a ~120º band of longitude and ~120º band of latitude centered at 0 ºN, 0 ºE. This portion of the surface accounts for only ~25% of the total surface area of Ceres. Most of these features exist within the aforementioned smooth lowlands (USGS: http://planetarynames.wr.usgs.gov/images/ceres.pdf).

Of Ceres' tholi/mons features Ahuna Mons (Figure 2-11) is the most striking, and the best studied. Located in the Ac-10 Rongo Quadrangle, it has been interpreted as an extrusive cryovolcanic edifice, and is morphologically similar to viscous lava domes on other planetary bodies (Ruesch et al., 2016). The tholi in the Fejokoo quadrangle have significantly more degraded surfaces and moderately shallower slopes than Ahuna Mons, but are morphometrically similar to it in prominence and areal extent (Table 2-1). Sori et al. (2017) postulated that the large tholi on Ceres may be viscously relaxed cryovolcanic edifices akin to ancient versions of Ahuna Mons. These authors argue that if these features are sufficiently ice rich (>40% by volume) they should viscously relax over geologic time; however, the high ice content and relatively short relaxation timescale of these features calculated by Sori et al. (2017) is at odds with the several hundred-million-year surface age of the cratered terrain in which they are found in the Fejokoo quadrangle (Hiesinger et al., 2016). The Sori et al. (2017) timescale can however

be increased by an order of magnitude by manipulating ice content, rheology, grain size, and thermal parameters.

Additionally, the spectral similarities between Hosil, Mikeli, Central Aymuray, North Aymuray, and Kwanzaa identified by VIR in the 2.70 μm and 3.06 μm region, although subtle, differentiate these tholi from the background cratered terrain (Fig. 2-13). The spectral similarities observed by VIR are independent of the tholi's illumination conditions. These spectral similarities imply similar local surface compositions and/or textures that differ from the average cratered terrain in the Fejokoo quadrangle, which would be unlikely if these tholi were created solely by impact cratering.

The four southeastern most tholi (Kwanzaa tholus and the Aymuray tholi) are also weakly associated with a significant positive Bouger gravity anomaly. In comparison, Ahuna Mons is strongly associated with a large positive regional Bouger gravity anomaly (Ermakov et al., 2016). The remaining tholi in the Fejokoo quadrangle are not associated with either positive or negative Bouger gravity anomalies.

Despite these similarities, the degradation states of the Fejokoo quad tholi, and their prominences on the order of the depths of the major impact craters in Ac-5, make it impossible to eliminate the possibility that they are residual topography created by impacting, rather than constructional features, using the methods employed in this mapping study. This is especially the case for South Aymuray, which has no outstanding spectral features. This leads to the open questions of whether they are genetically related, and how/if they relate to the regional low topography province. Further analysis of high-resolution LAMO DTMs and regional elemental/mineralogical composition data from GRaND and VIR will undoubtedly shed more

light onto these enigmas (e.g. determining if the broader low-lying regions has a unique elemental signature).

2.4.2 Morphological Interpretation of H_2O at Oxo Crater

Using a linear spectral mixing approach to model the VIR data, Combe et al. (2016) determined that H_2O ice best reproduced the spectral signature seen at Oxo; however, they did not conclude that this material is unambiguously water ice due to the fact that it should not be stable at this location on the surface over a time period greater than 10^4-10^5 years for a snow-like deposit, or 10^9 years for a deposit composed of cohesive blocks of ice (Hayne and Aharonson, 2015). The fact that a spectral mixing model derived from several different species of H_2O-bearing carbonate, sulfate, and chloride salts could also, albeit more poorly, emulate the results obtained by VIR further obfuscated a simple interpretation. However, at 3 Ma Oxo is young and ice preservation may occur. Here morphological observations are considered to further constrain this interpretation around the two major sites of H_2O detection at Oxo.

The primary detection falls within a bright crater material enclave within the bright hummocky lobate material unit in the south of the crater. The secondary detection lies partially over a lobate material unit, the shadow cast by the main terrace scrap, and a portion of the southern rim. Both of these regions are morphologically distinct within Oxo.

The broad lobate hummocky deposit (Figure 2-15 rectangle 1) associated with the primary detection has bulbous lobes separated by subdued grooves, no obvious source depression or scarp, and a slope of ~21º. From the morphology, we interpret this lobate feature as being similar to a debris avalanche and/or ice cemented flow as observed on both the Earth and Mars (e.g. De Blasio, 2011; Matsuoka et al., 2005; Barsch, 1992; Carr & Schaber, 1977). Given

the brightness and intensity of the primary H_2O detection situated on this deposit (Figure 2-15 rectangle 1, yellow star) it is likely that this small patch, while still a part of the main flow, was exposed by a recent local landslide.

We adopt the term ice cemented flow as a non-specific descriptor for flows whose morphology is most analogous to terrestrial and martian rock glaciers. Ice cemented flows typically have spatulate lobes with hummocks and concave-down morphologies (Figure 2-19a). In many terrestrial and martian cases, these features are formed through a combination of true creep (i.e. strain is accommodated by ice crystal deformation), basal sliding, and granular flow. All of which could plausibly be occurring at mid to high latitudes on Ceres at the present time (Savigny & Morgenstern, 1986). True rock glaciers and permafrost lobes in terrestrial environments have been observed to creep easily with ~50% ice by volume, but have been documented exhibiting some creeping behavior at as low as ~30% ice by volume (Darrow et al., 2016).

Due to Ceres' low obliquity the average diurnal surface temperature at Oxo remains relatively constant throughout the cerean year. This temperature, predicted by Hayne & Aharonson (2015) to be ~150 K, is warm enough such that it is plausible for ice-silicate mixtures to behave in a manner similar to those found on Earth. However, the poleward facing slope of Oxo, which hosts the mass wasting features of interest, is likely considerably colder than the estimated average temperature of ~150 K. Although the degree to which ice-rich martian deposits flow is still an open question, numerical simulations suggest that viscous flow plays a significant role in the morphological evolution of icy scarps near the north pole of Mars, where thermal conditions approach those found at Oxo (Sori et al., 2016). The scarps modeled by Sori et al. (2016) are notably steeper than the Oxo deposits with slopes measured between 60°-70°.

Unlike ice cemented flows, debris avalanches are a relatively rapid type of granular flow that can display a multitude of different morphological traits. They can be either monodirectional and cohesive, or fluid-like and dispersive. They typically originate from an obvious scarp and have a tongue or droplet-like shape. They sometimes have longitudinal furrows that terminate normal to the frontal toe. Usually debris avalanches have a relatively flat surface profile and lateral levees, but these traits are not universal (Fleming et al, 1989; Evans et al., 1993; Strom et al., 2006). Of particular relevance to the primary mass wasting feature in Oxo are spread debris avalanches that have compact proximal bodies which meld into the source scarp and have a continuously thinning distal margin (Strom et al., 2006).

Generic granular flows and debris flows throughout the solar system often produce features with similar characteristics to debris avalanches, ice cemented flows, and the cerean flows in question. In general, it is a non-trivial task to differentiate between these types of flows using remote sensing data, even at LAMO resolution and with spectrally derived compositional knowledge. This makes it beyond the capabilities of this study to explicitly determine the nature of these flow features, but we do use the available Dawn data to determine a preferred interpretation.

The lobate flows (Figure 2-15 rectangle 2) associated with the secondary detection also have characteristics similar to the feature found coincident with the primary detection. The illumination profile of these flows indicates that they have concave-down spatulate toes that are thick relative to the main trunks of the flows, and they have very little divergence along their lengths except towards the snouts. These traits, especially the concavity of the main flow and the presence of multiple spatulate toes that branch off from the main trunk near its terminus, are consistent with terrestrial and martian ice cemented flows, but uncommon in most types of debris

avalanches (Figure 2-19b and 2-19c) (Haeberli et al., 2006; Evans et al., 1993; Strom et al., 2006). The compact nature of this flow indicates a significant degree of internal friction that would be unlikely if its rheology was controlled by hydrated phyllosilicates (Watkins et al., 2015). This degree of cohesion is not noted in the flow associated with the primary detection. In particular, the presence of multiple cleft terminal snouts is most consistent with the interpretation that they are ice cemented flows not debris avalanches, but this possibility cannot be excluded.

In contrast, mass wasting on the gravitationally similar asteroid Vesta typically manifests as either large rotational slumps with well-developed terraces and whose scarps are wide compared to their run-out length, or as intra-crater deposits that have been interpreted as dry granular flows (Krohn et al., 2014). Rotational slumping is observed within the Fejokoo quadrangle (e.g. in Fejokoo and Oxo craters), but usually at smaller scales and without the same degree of terrace development found on Vesta. Most of the intra-crater granular flows on Vesta tend to be amorphous and reminiscent of terrestrial talus deposits rather than discrete landslides; although examples of well-developed landslides do exist (e.g. Figure 13c and Figure 17 from Krohn et al., 2014). In general, vestan landslides have diffusive and tapered margins as opposed to the more abrupt and texturally distinct morphologies associated with cerean examples. Where vestan landslides do exhibit a compact, concave-down morphology, with abrupt and texturally distinct margins it is typically due to topographic channeling. The cerean flows of interest in Oxo are minimally constrained by topography. Vestan flows do not exhibit multiple cleft snouts emerging from a single flow.

The aforementioned morphological properties of the cerean flows of interest in Oxo and the lack of similar morphological features on the predominantly anhydrous asteroid Vesta, which has multiple documented cases of lobate deposits interpreted as dry granular flows (Krohn et al.,

2014), indicate a fundamental compositional and/or mechanical difference between these two objects within their top few hundred meters. Based on this observation, their individual morphologies, and the Combe et al. (2016) H_2O detection we interpret the primary mass wasting feature within Oxo as similar to a granular debris flow and/or ice cemented flow as seen on the Earth and Mars, and the secondary mass wasting features as similar to an ice cemented flow or a highly modified debris avalanche where ground ice is significantly altering its mechanical and rheological properties. Furthermore, we conclude that the most plausible principal explanation for the morphological differences observed between the Oxo flows and vestan landslides is the presence of significant quantities of ground ice on Ceres; however, other compositional and mechanical differences such as the presence of hydrated silicates and various salt species on Ceres, or global grain size differences between Vesta and Ceres cannot be ruled out as major causative factors. This interpretation is further supported by GRaND results that predict the emergence of a pore-space-saturating surface ice table near Oxo's latitude (Prettyman et al., 2017). The interpretation that these features are analogous to ice bearing flows on other solar system bodies provides context and a framework for interpreting other similar features on Ceres, as well as placing a lower bound on their water ice volume fraction of ~30-50%. Their localized and discrete nature also implies that if these flows are ice controlled, ground ice is distributed inhomogeneously within the upper few hundred meters of Ceres with an enriched region coinciding with these features; at least in the vicinity of Oxo crater. Inhomogeneously distributed ground ice could also account for the limited evidence of viscously relaxed craters and slopes on Ceres, and has previously been suggested by Bland et al. (2016) as a possible explanation for the morphological discrepancy between Coniraya and Vinotonus craters in the Ac-2 quadrangle. Regardless of interpretation, the aforementioned observations demonstrate that despite similar

thermal, gravitational, and orbital environments there exist forms of mass wasting on Ceres that have no morphological equivalent on Vesta.

2.4.3 Distribution, Style, and Implications of Mass Wasting and Lobate Flow Features in the Fejokoo Quadrangle

A diversity of mass wasting and lobate flow features have been noted on the surface of Ceres, which have been broadly interpreted as belonging to a continuum composed of three archetypical endmembers (Buzckowski et al., 2016; Schmidt et al., 2017): Type 1 flows, which occur at high latitudes, have concave-down profiles, steep snouts, longitudinal and sometimes lateral groves, and high height-to-runout (H/L) ratios (generally 0.3-0.7) relative to Type 2 & 3 flows. Type 2 flows, which occur at all latitudes (but most abundantly in mid-latitudes), typically have a sheeted spatulate appearance, are generally smooth, have a lower degree of curvature, and lower H/L ratios than Type 1 flows (generally ~0.2). Schmidt et al. (2017) have suggested that Type 1 and 2 flows are possibly ground ice influenced landslides/ice cemented flows and long run-out landslides, respectively. Type 3 flows, which occur at low to mid latitudes and are interpreted as fluidized flows similar in appearance to martian fluidized ejecta. They typically have a thin sheeted appearance, are smooth and featureless on their surface, terminate in multiple small v-shaped lobes, and have H/L ratios between 0.1-0.3 (the majority of observed example are found at the lower end of this range). For a more detailed discussion on these flow types and their properties see Buzckowski et al. (2016) and Schmidt et al. (2017).

Based on the aforementioned properties, the Fejokoo quadrangle contains well-preserved examples of all three types of flows with nine unambiguously classified features (two Type 1 flows, six Type 2 flows, and one Type 3 flow). The majority (six) of these flows are associated with morphologically fresh appearing craters. A Type 1 flow at Oxo (the same feature that is

associated with the secondary H_2O detection; Figure 2-15 rectangle 2), a Type 3 flow at Cozobi (Figure 2-14d), and one Type 2 flow at each of Jarovit (Figure 2-9d), Cozobi (Figure 2-14d), and Takel (Fig. 2-14e). The remaining flows exist at 36 ºN, 337 ºE; 41 ºN, 331 ºE; 49 ºN, 270 ºE; and 51 ºN, 316 ºE. The former four flows are all Type 2. The affinity of these features towards apparently young craters implies that they degrade relatively quickly over geologic time.

2.4.4 Comparison of Surface Geology with Asteroid Vesta

The photogrammetric, spectroscopic, and physiographic analyses completed as part of the mapping campaign of the Fejokoo quadrangle are analogous to the investigations carried out during the geological mapping of the asteroid Vesta using Dawn spacecraft data. The similarity of these mapping campaigns allows for simple, direct, and meaningful comparisons between these two contrasting worlds in the main belt.

A first order result of the exploration of these two objects is that the surface geology of both Vesta and Ceres is dominated by impact craters and the impact cratering process (Williams et al., 2014; Hiesinger et al, 2016). While this result seems obvious in hindsight, due to Ceres' anomalously low density and potentially high water ice content, many investigators argued that Ceres' surface may have been significantly depleted in impact craters due to efficient viscous relaxation of a nearly pure water ice crust (Bland, 2013).

Despite the abundance of craters on Vesta and Ceres, their expression and morphologies differ greatly between these two bodies. On Vesta, craters were observed to be almost exclusively simple (i.e. bowl shaped), and the asteroid was estimated to have a simple to complex transition diameter of ~70 km (Schmedemann et al., 2014). By comparison, Ceres is observed to be ubiquitously covered in transitional and complex craters (i.e. craters with

modified, mottled, and/or terraced floors with evidence for a central uplift), and its simple to complex transition diameter is observed to be as low as ~7.5 km (Hiesinger et al., 2016). This contrast between two objects of nearly identical surface gravities implies that Ceres has a dramatically weaker surface relative to Vesta, at least at the strain rates associated with impact cratering.

From spectroscopy we know that hydrated and ammoniated phases, such as clay minerals and ionic salts, are abundant in the Fejokoo quadrangle and Ceres as a whole. Such highly evolved products of aqueous alteration were not seen on the basaltic, pyroxene dominated Vesta (McCord & Scully, 2015). Spectral features associated with primitive, unaltered minerals like olivine and pyroxenes are not appreciably detected in the Fejokoo quadrangle or on Ceres in general. The detection of water ice on the surface of Ceres within the Fejokoo quadrangle signifies another radical compositional departure from Vesta. On Vesta the global surface abundance of hydrogen is approximately ~250 μg/g, whereas nuclear spectroscopy suggests that on Ceres this value is at least 16 wt. % (Prettyman et al., 2017). This represents an increase of at least two orders of magnitude, which strongly implies that initial inferences about Vesta being a protoplanet that evolved anhydrously and Ceres being a water rich dwarf planet are correct. Furthermore, while the geomorphology of Ceres rules out a nearly pure ice upper crust, in combination with the aforementioned results from spectroscopy, it suggests that the upper layer of Ceres is an intimate mixture rich in both hydrated silicate phases and water ice.

The physical geography of the Fejokoo quadrangle indicates that Ceres supports a number of important morphological features besides impact craters. Specifically, lobate debris deposits and tholi. Unlike Vesta, where lobate deposits are associated only with slumping and granular mass wasting morphologies, lobate deposits on Ceres exist in a multitude of forms

ranging from frozen debris flow-like, to long run-out landslide-like, to fluidized ejecta-like. All of these morphologies strongly imply and abundant concentration of water ice in upper few hundred meters of Ceres, which is supported by the spectral observations. The presence of numerous kilometer scale tholi in the Fejokoo quadrangle alone raises the possibility that some form of diapirism or constructional process was, or is still, at work in the cerean subsurface. While Vesta's Aricia Tholus' appearance is suggestive of a constructional origin, there exist no other unambiguous examples of mountain-like topography on the asteroid which are unrelated to impact cratering.

2.4.5 Simplified Geologic History of the Ac-5 Fejokoo Quadrangle

Based on morphological freshness and impact crater densities, the Fejokoo quadrangle is broadly divided into four arbitrary geological periods which from oldest to youngest are termed the "Oldest period", "Intermediate period", "Young period" and "Youngest period" (Figure 2-20). These periods primarily serve to delineate the relative order in which the named craters within the Fejokoo quadrangle formed.

The Fejokoo quadrangle appears to evolve very little over the portion of Ceres' history it preserves in terms of active geologic processes. The dominant geologic process that shaped this quadrangle is undeniably impact cratering. This process has clearly been the major geomorphic force since the exposure of the surface to space up until the present. Mass wasting, whether spontaneous or impact induced, has also been a major geomorphic process throughout the history of the Fejokoo quadrangle. Examples of such features are present in all but the oldest demographic of impact craters.

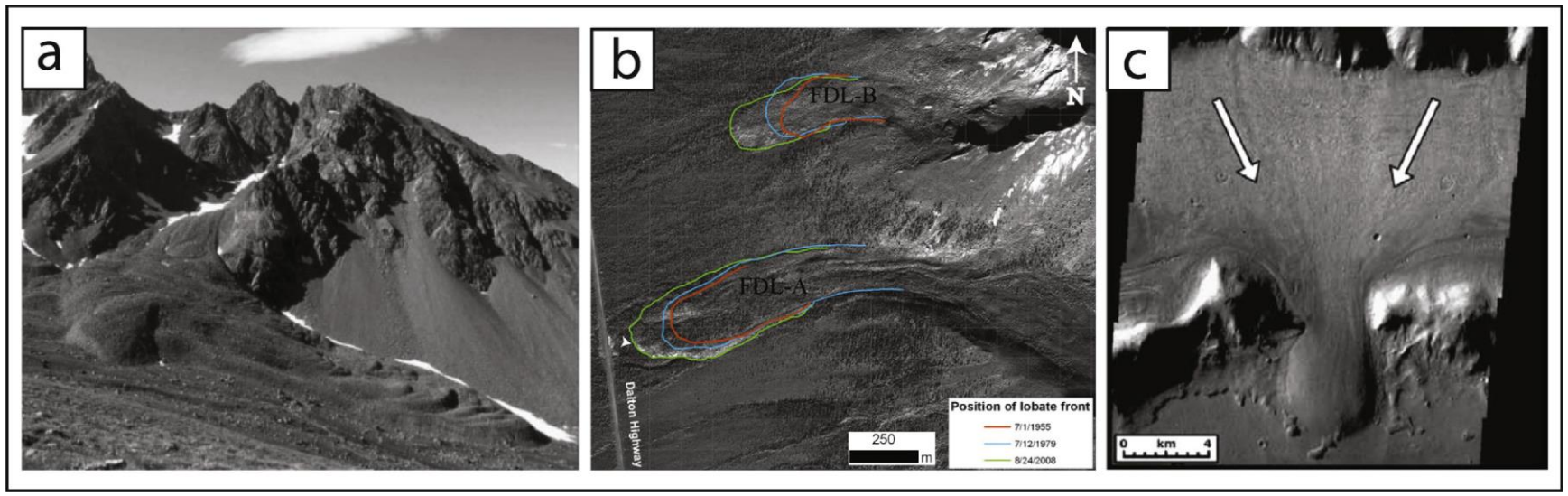

Figure 2-19. Possible planetary analogues for the hummocky grooved terrain and lobate flows seen in Oxo crater (Figure 2-15). Panel (a) shows a creeping alpine ground ice lobe with a mean width, length, and surface gradient of 180 m, 380 m, and 19º, respectively (adapted from Matsuoka et al. (2005)). Panel (b) illustrates a creeping ice cemented flow in northern Alaska with a surface gradient near its snout of ~18º. Note the longitudinal grooves and superimposed toe lobes (adapted from Daanen et al. (2012)). Panel (c) shows a debris covered glacier on Mars, arrows indicate direction of flow. Themis image V12057009 (adapted from Head et al. (2010)).

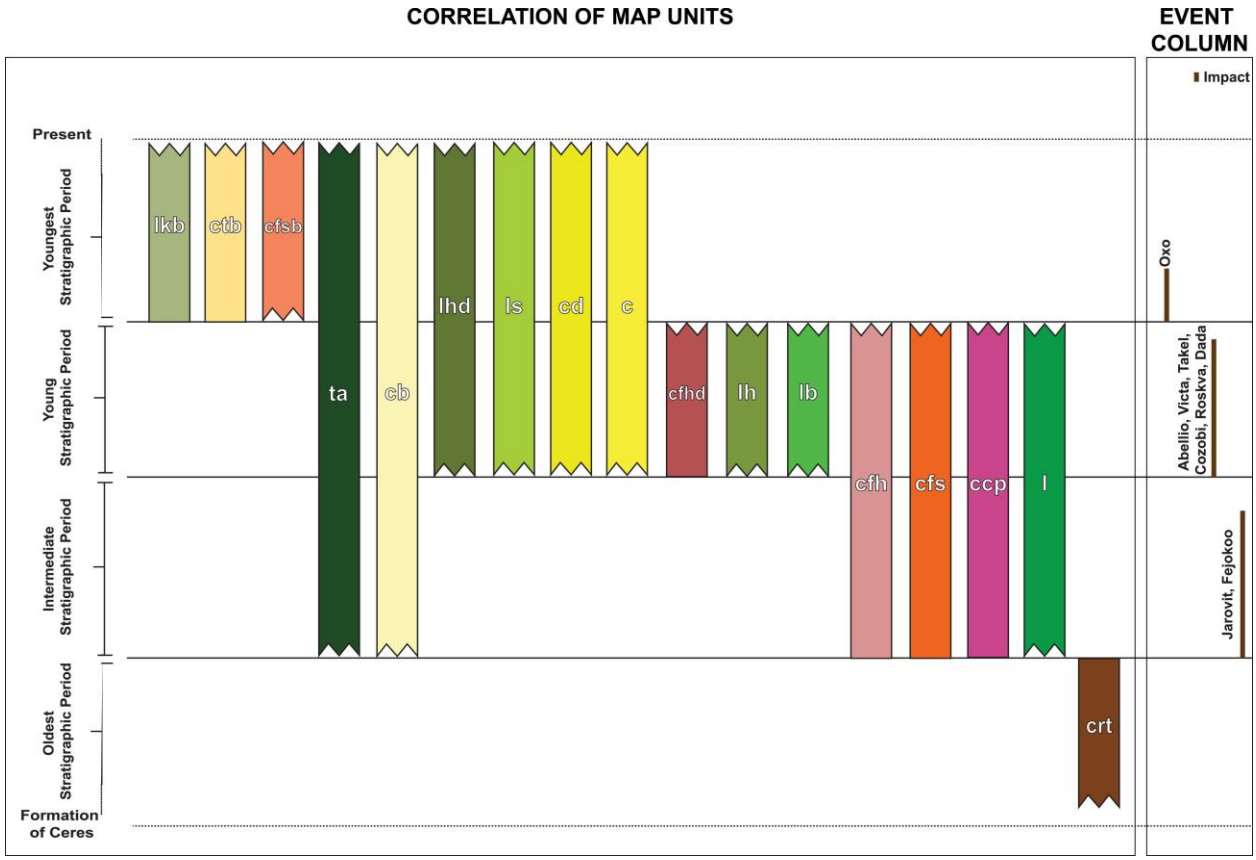

Figure 2-20. Correlation of map units. This diagram presents a simplified geologic history of the Ac-5 Fejokoo Quadrangle. The map units (see section 2.3.3 for unit abbreviations and descriptions) are horizontally stratified into four geologic periods of increasing age towards the bottom. The event column on the right indicates to which geologic period the named impact craters in Ac-5 belong.

Given the ambiguity of how the Fejokoo quadrangle tholi formed there are multiple possible timelines for their emplacement. Any tholi that may have formed as residual topography from impact cratering were likely created early on in the history of the quadrangle due to their generally rounded profiles and location within the ancient cratered terrain unit. Any tholi that may have been produced as constructional features are far less constrained with respect to their time of formation. Without more knowledge of how uplift affects the texture and the ability of the cratered terrain to retain topography it is very difficult to estimate when any such tholi formation mechanism may have been active. It may be possible that these features were formed very early on, very recently, or continuously throughout the history of the Fejokoo quadrangle.

2.5 Conclusions

The geologic mapping of the Ac-5 Fejokoo Quadrangle shows that this area contains some of the most ancient terrain on Ceres. It is ubiquitously covered in cratered terrain, and shows limited but important geologic variability. The diversity comes mainly in the form of crater material units and lobate deposits associated with fresh impact craters.

Tholi in the Fejokoo quadrangle share many physical, morphometric, and geographical similarities with the presumptive cryovolcanic structure Ahuna Mons. The majority of these tholi in the Fejokoo quadrangle also have similar surface compositions that differ from the surrounding cratered terrain, which makes it unlikely that they are residual topography derived from impacting.

Oxo crater is a feature of extreme importance on Ceres because of the presence of distinctive morphological units associated with water ice. The lobate deposit associated with the primary H_2O detection appears morphologically analogous to ice cemented flows and/or debris

avalanches seen on the Earth and Mars. The former of these analogies bolsters the interpretation that the spectroscopic detection of H_2O in Oxo is of water-ice; however, the latter does not. The lobate deposit associated with the secondary H_2O detection is extremely similar to terrestrial and martian ice cemented flows. This association provides a framework for interpreting other morphologically related flows and mass wasting features found throughout the Fejokoo quadrangle and Ceres as a whole. In particular, the presence of potentially ice controlled mass wasting features in Oxo demonstrates that while the upper layer of Ceres is more depleted in volatiles than expected, water ice is likely still present in the upper crust in abundances of at least a few tens of volume percent. Localized pockets of ground ice enriched beyond this background value likely exist throughout the Fejokoo quadrangle (and Ceres as a whole), and strongly influence surface processes. This stands in contrast to the strong, basaltic crust observed on the asteroid Vesta, where water played a miniscule role in shaping its surface.

3 Mass Wasting and Lobate Deposits: Geomorphological Evidence for Abundant Ground Ice on Ceres

3.1 Observations and Categorization of Ubiquitous Lobate Deposits on Ceres

Early results from the geologic mapping campaign of Ceres reported in the previous chapter revealed that lobate deposits suggestive of different forms of mass wasting and impact emplacement are common place, at least in the northern hemisphere, on Ceres. Furthermore, their particular morphologies implied that these deposits' origins might be tied to an abundance of ground ice in the near surface of Ceres. In order to test this hypothesis, a global identification and characterization campaign for lobate deposits on Ceres was undertaken. The results of this campaign and subsequent analyses are presented in this chapter, which is derived primarily from work published by Buczkowski et al. (2016), Schmidt et al. (2017), and Combe et al. (2019) to which the author of this dissertation contributed substantially.

The primary objectives of this identification campaign were to locate all potential kilometer scale lobate mass wasting deposits on Ceres, describe qualitatively their morphology, and to analyze their run-out distances and drop heights through morphometry. This was accomplished via a detailed search of Dawn FC global mosaics taken at both ~140 m/pixel (HAMO phase) and ~35 m/pixel (LAMO phase). The morphometry was done using the HAMO stereophotogrammetric DTM (Preusker et al., 2016). For the purposes of this investigation, lobate deposits were defined as contiguous geologic features that exist directly downslope from cliffs, escarpments, ridges, or other breaks in high standing topography; they must also have discrete (i.e. non-diffuse) boundaries, and an arcuate, cuspate, and/or bulbous terminus.

Mass wasting on Ceres is generally related to impact craters, as these are its primary topographic features. Material flows kilometers to tens of kilometers in scale are commonly

observed both interior and exterior to many of Ceres' craters at rates much higher to what is typical on other planetary objects (e.g. Krohn et al., 2014; Singer et al., 2012). At least 20% of craters greater than 10 km in diameter have one or more instances of a lobate landslide-like deposit. From the global search, 82 unambiguous instances of lobate deposits were identified on Ceres (Table 3-1). These features broadly fall into three morphologic classifications uncreatively named Type 1, Type 2, and Type 3 flows.

Type 1 flows (Figure 3-1) are a class of tongue-shaped, lobate, and voluminous (they are typically up to hundreds of metres thick) mass wasting features that form down-slope flows underneath failed interior-facing segments of crater rims. Type 1 flows occur at a wide range of scales, but always have single or multiple elongate trunks as wide as their source, often overprinted by parallel longitudinal furrows, and exhibit broad steep snouts and distal ramparts at their termini. The largest of these features form where small impact craters are emplaced into older crater walls, and material flows into the floor of the older crater. The feature (a) in Figure 3-1 emanates from an irregular, scalloped-rim small crater, and consists of one main trunk with two flanking flows that reach ~300 m thick at the toe. Superposed lobes are observed in the centre of the structure. A tall flanking ridge suggests that the flow may have left a levee as it displaced material. The feature (b) in Figure 3-1 is a series of short, steep flows formed from a complex of short trunks that terminate in steep, lobate toes of ~150 m thickness. This particular feature shows several similarities with the small lobate deposits associated with the secondary H_2O detection within Oxo (Figure 2-15), such as multiple terminal lobes, a high final angle of deposition, and superposition over pre-existing impact crater generated terrain. Thus, although some type 1 flows could be triggered during an impact, others may form later. The feature (c) in Figure 3-1 has a ~150-m-thick primary trunk with longitudinal and transverse furrows and

flanking ridges. The terminal rampart is thicker than the centre of the flow, indicating possible post depositional deflation or kinetic sieving (Gray et al., 2006).

Type 2 flows (Figure 3-2) are the most numerous mass wasting features observed on Ceres. With 47 confirmed examples they account for more than half of all the lobate deposits catalogued during the identification campaign. These long, spatulate, sheeted flows typically initiate near the crest of crater rims and often, but not always, flow down the exteriors of craters. These flows are characterized by circular to arcuate lobate toes, and can range in appearance from single broad or fan-shaped sheets to many sheets diverted or dispersed by even subtle topography into multiple directions. Type 2 flows generally blanket low-grade relief, but their paths are controlled by local topography, even becoming channelized, as shown in Figure 3-2. Type 2 flows typically traverse path lengths of tens of kilometers, on shallow slopes usually less than ten degrees. In comparison to Type 1 flows, Type 2 flows appear to be less cohesive, lack steep snouts, appear on shallower slopes and on outward- rather than inward-facing crater walls, and show no strong correlation with crater size. Despite Type 2 flows initiating predominantly at crater rims, they are always associated with head scarps and are morphologically distinct from ejecta. Superposition relationships with underlying ejecta deposits suggest that some Type 2 flows do not necessarily form contemporaneously with their host crater, suggesting landslide-like behavior post-impact.

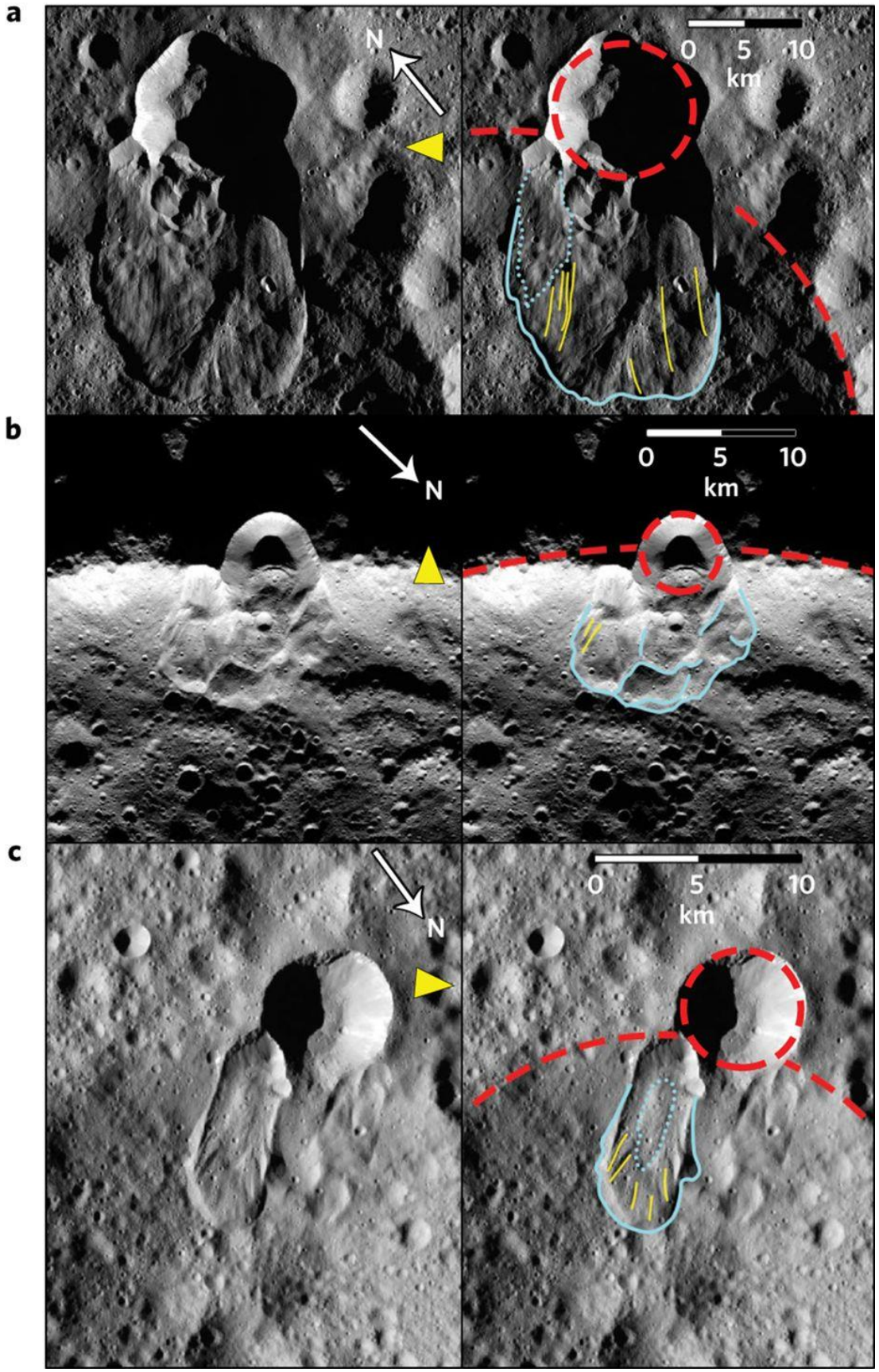
a
N
0 5 10
km
b
N
0 5 10
km
c
N
0 5 10
km

Figure 3-1. Type 1 flows occur primarily at Ceres' high latitudes. Yellow arrows indicate the direction of incident sunlight, light blue solid lines show flow margins, dotted light blue lines trace overprinting flows, red dashed lines delineate crater rims, and yellow lines indicate longitudinal furrows. (a) This Type 1 feature in Ghanan crater (79° N, 58° W) is the longest and most voluminous flow of its kind on Ceres. (b) This complex feature at 77° S, 181° W is composed of several superposed trunks that begin with a handful of slumped segments of the crater wall. (c) This feature at 50° N, 27° E displays a prominent rampart (i.e. a snout that thickens towards the end of the flow), which is suggestive of post-depositional deflation or kinetic sieving. Image adapted from Schmidt et al. (2017).

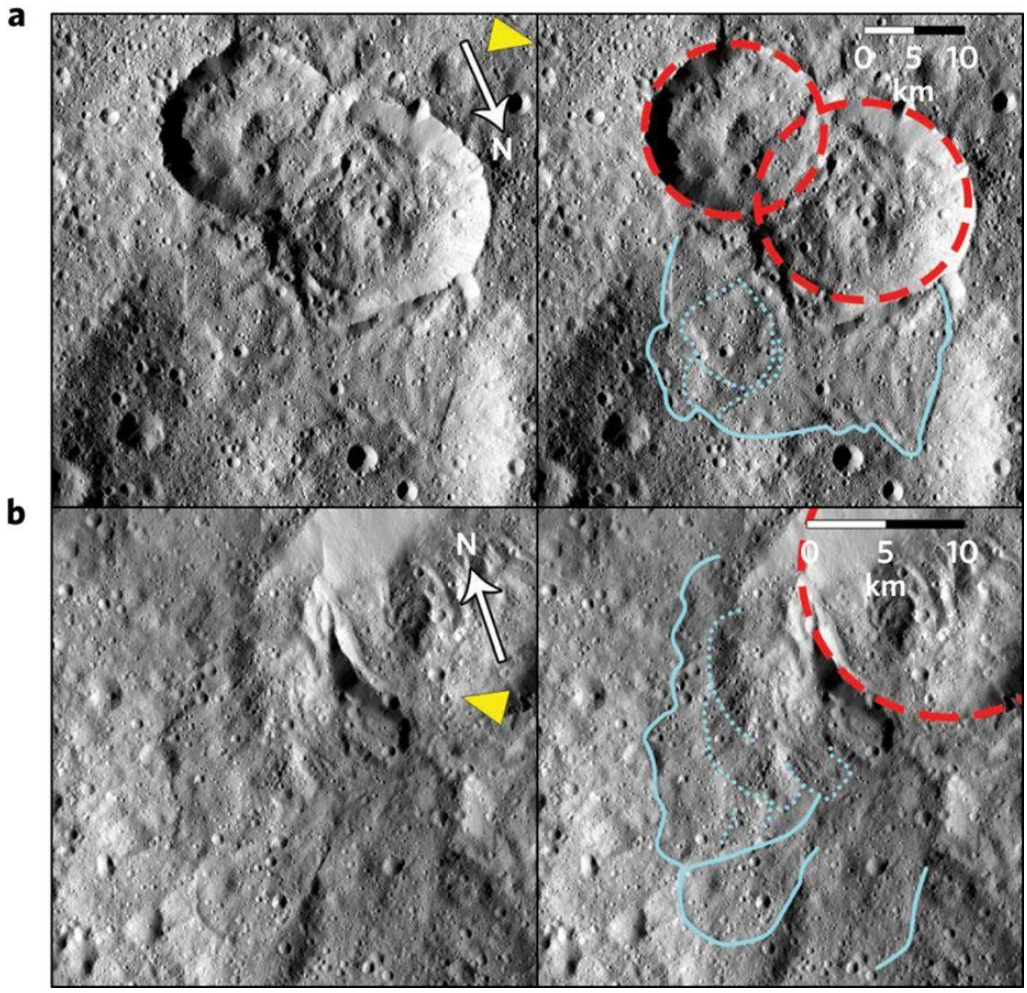

Figure 3-2. Example of Type 2 flows on Ceres. Yellow arrows indicate the direction of incident sunlight, light blue solid lines show flow margins, dotted light blue lines trace overprinting flows, and red dashed lines delineate crater rims. (a) Cerean Type 2 landslide at (53.9° N, 114° W) demonstrating typical, broad sheets with rounded (spatulate) toes up to ~15 km long. This feature formed after the impact on the left of the figure, but originates on the rim of both craters. (b) This Type 2 flow (18.9° N, 23.2° E) flows over a shallow ~8° slope. It has two prominent lobate sheets emanating from the host crater towards the southwest, extending ~19 km to the SW. This feature displays strong topographic control and channelization. The southern lobe is constrained by a ridge to the east and a crater to the south. Image adapted from Schmidt et al. (2017).

Type 3 flows (Figure 3-3) are cuspate, sheeted flows, which without exception extend radially outward from source crater rims. These features are collocated with or obscure ejecta blankets, and are characterized by thin broad sheets of smooth material that blanket local topography and terminate in layered sets of lobes or cusps. These flows are generally wider than Type 2 flows, but are similar in thickness (tens of meters). In contrast with Type 1 and Type 2 features, Type 3 flows often do not seem to originate from obvious head scarps or escarpments; they also have large source regions that typically account for at least a third of the circumference of the host crater. Type 3 flows have narrow to acute curvilinear toes, lack deep longitudinal furrows, and possess lahar-like smooth to striated or hummocky textures, giving the impression of fluidization. Additionally, terminal mass concentrations are common among Type 3 features, which implies that kinetic sieving or deflation generally affects these flows. Type 3 flows are associated with complex craters, and generally those whose diameters are greater than 20 km.

3.2 Distribution and Abundances of Cerean Lobate Deposits

The locations of all identified Type 1,2 and 3 flows are displayed in Figure 3-4. In general, these features are concentrated above absolute latitudes of ~30° and are noticeably rarefied near the equator (Figure 3-5). This distribution implies a gradient in near-surface material strength with a systematic increase in weak or mobilizable material towards the poles. There also exists a slight hemispherical asymmetry with more lobate deposits located at high northern latitudes relative to high southern latitudes. A reduction in near-surface hydrogen concentration is also observed by the GRaND instrument at high southern latitudes relative to the north polar area (Prettyman et al., 2017).

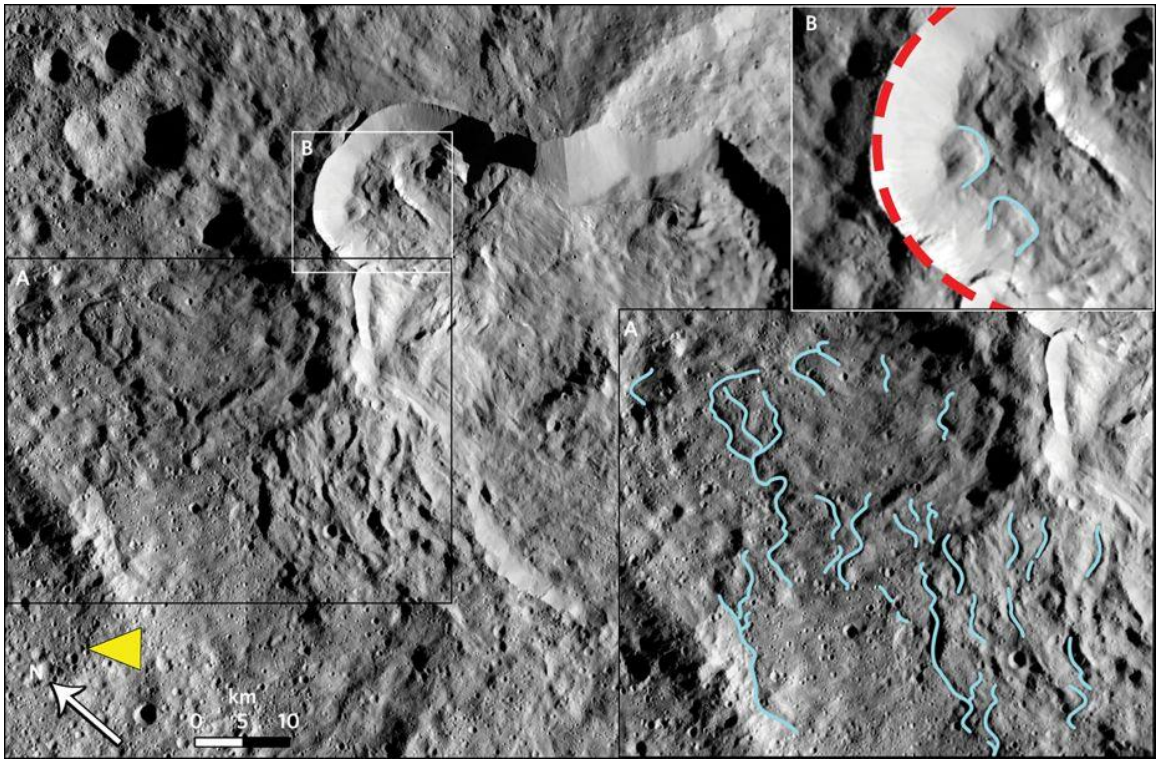

Figure 3-3. Example of a Type 3 lobate flow. These feature typically have a platy, smooth, lobate morphology with multiple superposed sheeted layers and numerous cuspate terminal lobes. The archetypical cerean Type 3 flow shown in this image is located in Datan crater (60° N, 250° W). The black inset shows the flows in detail. Yellow arrows indicate the direction of incident sunlight, light blue solid lines show flow margins, and red dashed lines delineate crater rims. The frontal flow margins trace v-shaped cuspate toes of the many flow sheets. The length of this flow ranges from ~17–32 km. The white inset shows terracing and two lobate flows on the interior of a presumably post-impact failed rim. These landslides could represent talus cones within the crater. Image adapted form Schmidt et al. (2017).

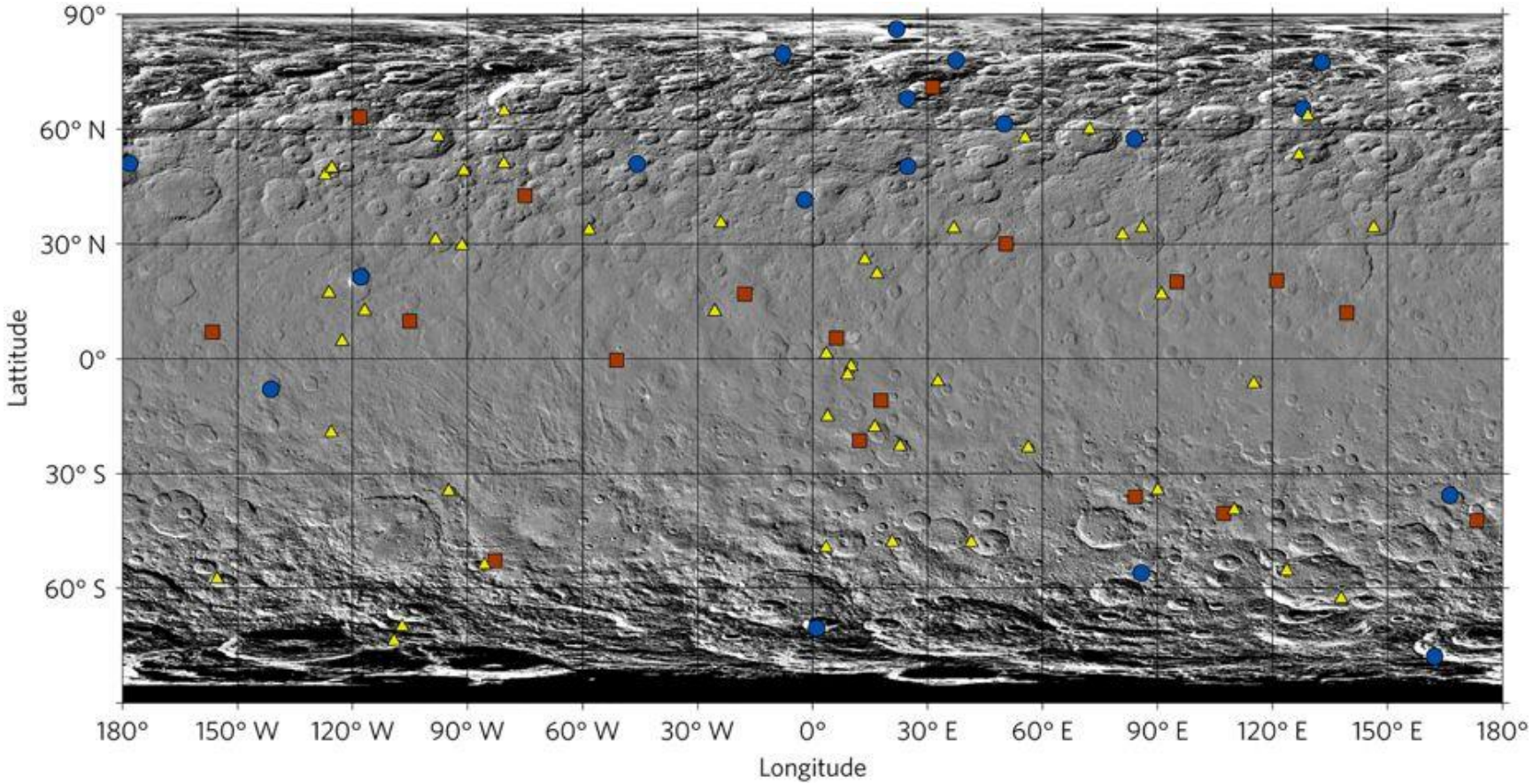

Figure 3-4. The global distribution of flow features on Ceres. The blue circles indicate the locations of the 19 identified Type 1 flows, the yellow triangles indicate the locations of the 47 identified Type 2 flows, and the red squares indicate the locations of the 18 identified Type 3 flows. The basemap for this image is the HAMO derived global panchromatic mosaic of Ceres, which is shown in equirectangular projection.

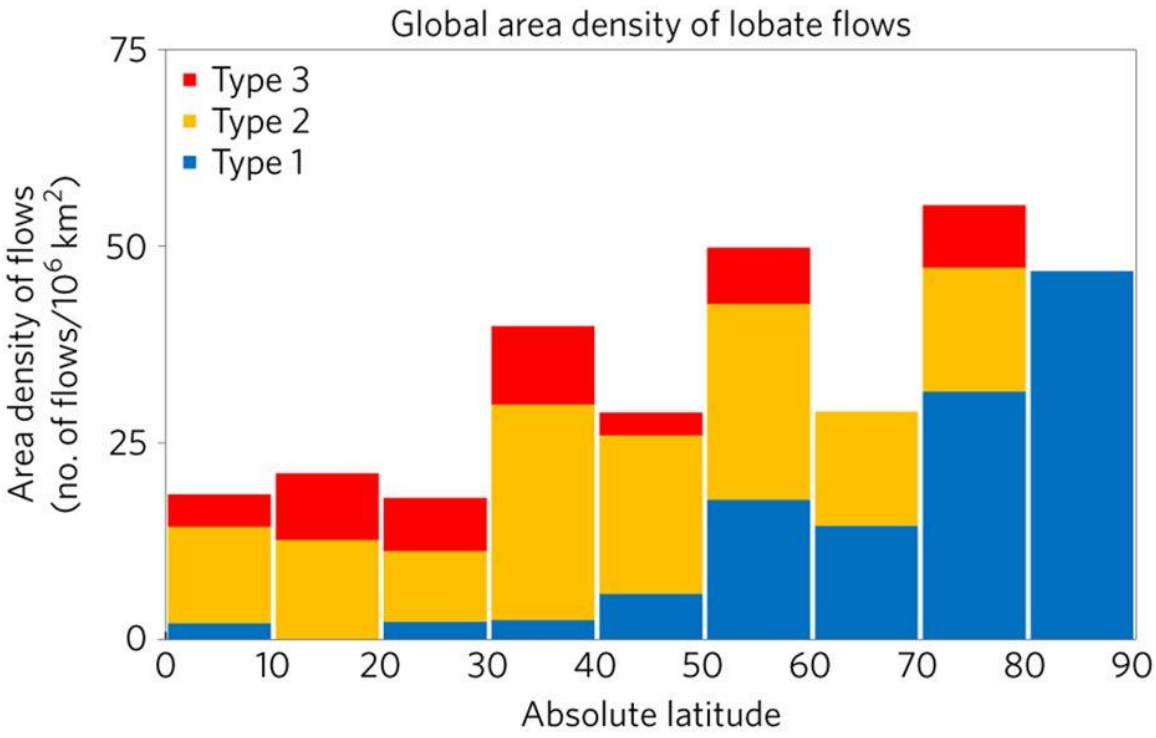

Figure 3-5. Global surface area density of lobate flows on Ceres. Note the general poleward increase in overall flow density. Type 1 flows exhibit a strong positive poleward enhancement in abundance, whereas Type 2 flows appear most abundant between ~30-60° absolute latitude, and Type 3 flows show no statistically significant trend with latitude.

The mapping campaign of lobate flow deposits on Ceres revealed that each of the three endmember types of flows discussed thus far have distinct latitudinal distributions (Figure 3-5). Of the 19 identified Type 1 cerean flows 14 are located polewards of ~50° latitude. Their relative abundance also increases dramatically with latitude with an overabundance of features near the poles, where they are the dominant form of mass wasting. Type 2 flows favor the mid-latitudes with their distribution peaking between 30°-60° latitude in both the northern and southern hemispheres, where they are the dominant form of mass wasting observed. However, Type 2 flows are seen at all absolute latitudes less than 80°. Type 3 flows are the least abundant form of lobate deposits observed on Ceres, with 18 unambiguous examples. These flows are found mostly in the low-mid latitudes, but were identified at latitudes as high as ~75°. The different morphologies and distributions of the different categories of lobate deposits suggests different mechanisms of formation and/or substantial latitudinal variability in the mechanical properties of the near-surface cerean regolith.

3.3 Comparison of Flows on Ceres and other Worlds

Mass wasting is a ubiquitous process on all solid planetary bodies, and the morphology of the resulting surface deposits provide first-order insights into the physical processes at work and the mechanical properties of the material in motion. As Ceres is the first world of its class to be explored in detail by an orbiting spacecraft, we employ comparative planetology to compare and contrast the observed lobate deposits with better understood analogues on other solar system bodies. This comparative process helps disentangle which known physio-geologic processes are at work within a framework of previously documented physics. Lobate flows on the Earth, Mars, Moon, Vesta, and icy satellites of Jupiter and Saturn were considered as possible analogues for Type 1, 2, and 3 cerean flows.

Additionally, mass flows transform gravitational potential energy into horizontal kinetic energy and heat. A first order method for estimating the efficiency of this potential energy to kinetic energy transformation is to measure the ratio of the run-out length (L) of a flow to the total vertical drop height it traverses (H). In this case the ratio H/L gives the apparent coefficient of internal sliding friction (e.g. Singer et al., 2012; Legros, 2002). The trend in H/L versus L is used to compare the efficiency of the movement among different flows. These measured values for Ceres' flows are plotted in Figure 3-6, along with reference flows on other solar system bodies. The H/L versus L trends reveals that there is no overall trend of H/L with L that defines all Cerean flows, but each sub type of flow exhibit their own unique behavior.

Type 1 flows on Ceres share morphological similarities with terrestrial and Martian rock glaciers and frozen debris flows in that these flows produce thick, rounded toes, longitudinal furrows, and occasional lateral levees (Daanan et al., 2012; Singer et al., 2012; Haeberli et al, 2006; White, 1976). However, with Ceres' low gravity, it is unlikely that conditions for glacial basal slip are met, so while deformation or non-Newtonian flow within these flows could explain their morphology, flow at the bed would require reduction in basal friction. The type 1 flows are consistent with other planetary landslides but generally form at unusually small length scales given their drop heights (Figure 3-6), and with high apparent values of internal friction. The apparent cohesive nature of Type 1 flows is consistent with their morphological likeness to ductile deposits like rock glaciers and frozen debris flows.

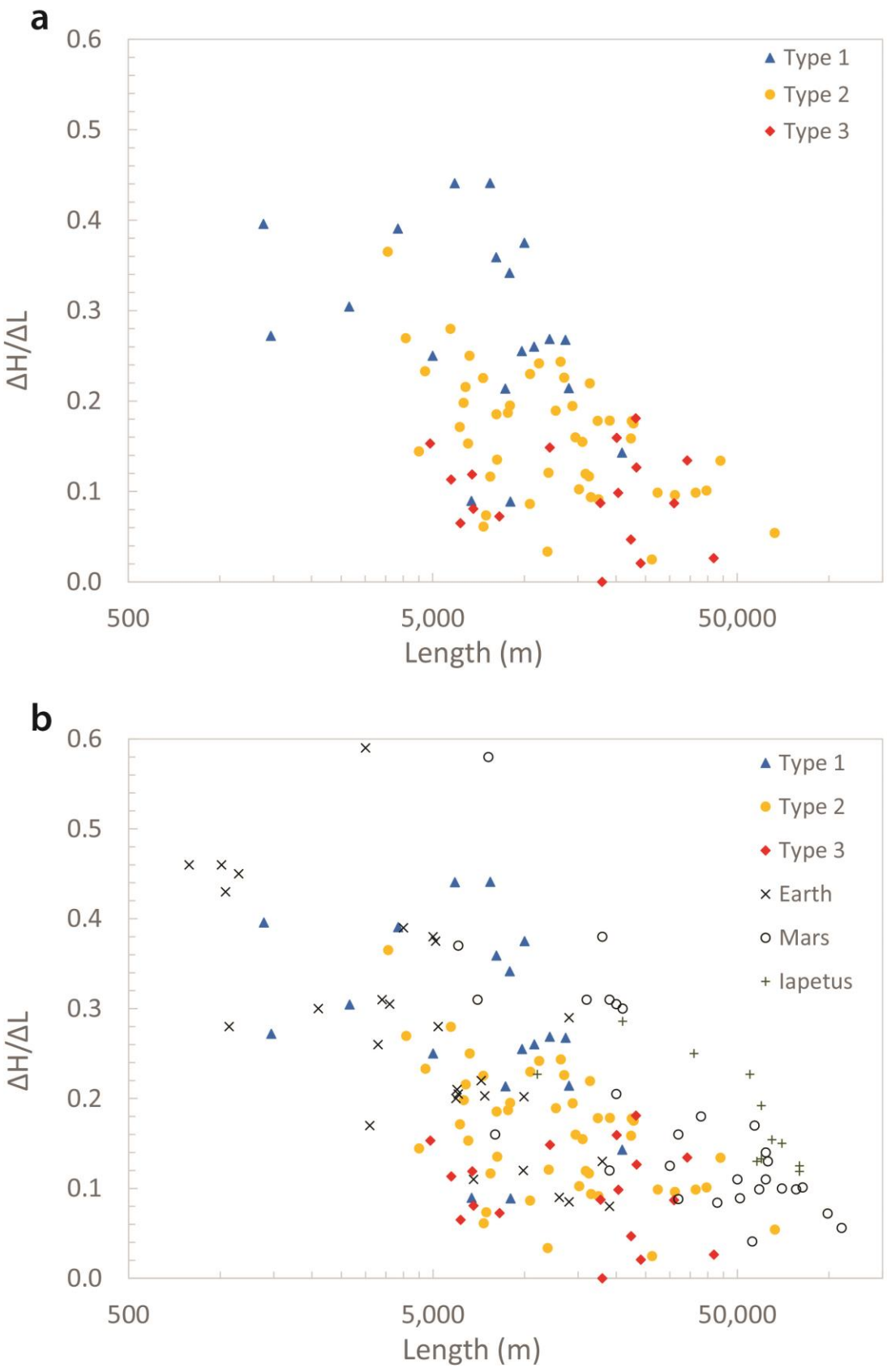
a
0.6
0.5
0.4
0.3
0.2
0.1
0.0
ΔH/ΔL
500
5,000
50,000
Length (m)
Type 1
Type 2
Type 3
b
0.6
0.5
0.4
0.3
0.2
0.1
0.0
ΔH/ΔL
500
5,000
50,000
Length (m)
Type 1
Type 2
Type 3
Earth
Mars
Iapetus

Figure 3-6. *H*/*L* versus *L* diagram for all lobate flows observed on Ceres. (a) and (b) are the same plot, but subfigure (b) includes data from mass wasting deposits on Earth (Malin, 1992), Mars (Malin, 1992), and Iapetus (Singer et al., 2012). Type 1 (blue triangles) and type 2 flows (yellow circles) have shallow *H*/*L* versus *L* trends, whereas type 3 flows (red diamonds) show no relationship. Ceres flows are most similar to the lobate landslides on Iapetus (+ symbols) and have generally lower $\Delta H/\Delta L$ values than those observed on Earth (× symbols) and Mars (open circles).

Type 2 flows share similarities to martian long runout landslides (e.g. Lucchitta, 1987), terrestrial supraglacial landslides (e.g. Shreve, 1966), and landslides on Iapetus (Singer et al., 2012), with thin rounded toes, relatively long extents along shallow slopes, and examples of channelization by local topography. The *H*/*L* versus *L* trend of Type 2 flows (Figure 3-6) are generally consistent with landslides found on Mars and Iapetus. However, their *H*/*L* values are generally smaller than terrestrial landslides, with the exception of snow avalanches and runout enhanced supra glacial landslides. These trends suggest that Type 2 cerean landslides are enabled by some form of basal friction reduction, such as frictional melting of volatile or sliding on a clay or ice rich substrate, as has been hypothesized for analogous flows on Mars and Iapetus (Watkins et al., 2015; Singer et al., 2012).

Type 3 flows are morphologically similar to fluidized ejecta in rampart craters on Mars (e.g. Mouginis-Mark, 1981; Senft & Stewart, 2008) and on Ganymede (Boyce et al., 2010), and are always found exterior to crater rims. Specifically, they are always found oriented radially away from a central source crater, they have smooth continuous surfaces unlike ballistically emplaced ejecta, they do not have a head scarp or obvious source region, and they terminate in multiple cuspate lobes which often have a layered appearance. However, on Ceres' these only occur around part of the crater, and so are not necessarily ejecta. No such flow morphologies were found on Vesta (Figure 3-7), which is incredibly insightful since Ceres and Vesta have similar surface gravity and impact rates due to their proximity within the main asteroid belt. Only Type 3 flows are strongly coupled to impact timing or size. The variation in the source and age of the flow material, and overprinting of trunks, lobes and sheets common in Type 1 and Type 2 flows demonstrates they do not only form immediately post-impact.

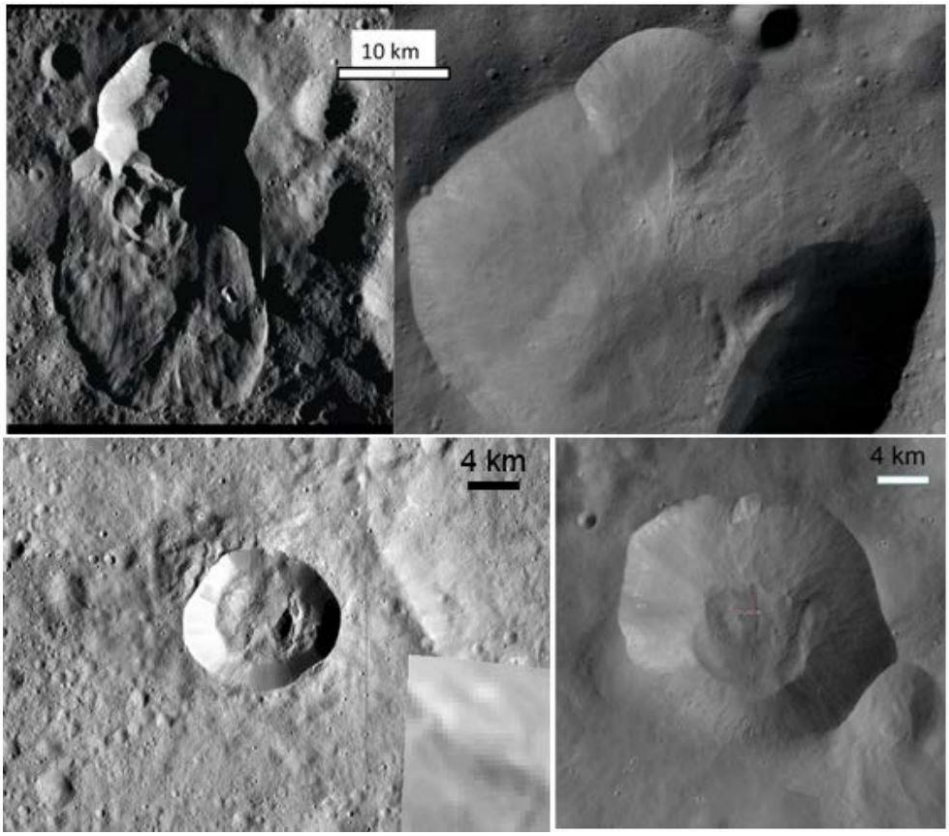

Figure 3-7. Comparison of typical mass wasting on Vesta (right, top and bottom) with examples from Ceres (left, top and bottom). Top: Similar scale and geometry of a large crater with a smaller crater located along the rim, from which the mass wasting occurs. Left is a Type 1 flow on Ceres (Figure 3-1), right is Vesta's Lepida Crater (53.39° S, 16.35° W). Note the absence of any trunk, distinct margins, or rounded snout for Vesta. Bottom: Left is a small Ceres crater with infilling material, right is an image Drusilla crater (98.8° S, 15.29° E) showing rim wasting on Vesta. The larger crater has several flows down its interior walls that lack discrete sources or slumping. The smaller crater to the lower right has broad wispy flows away from its rim. While these flows could be considered lobate, they lack the sharp boundaries, flow textures, and discrete toes of Ceres landslides; The Vesta mass wasting is here is more similar to Ceres' modified craters with interior rim collapse. Image adapted from Schmidt et al. (2017).

In general, flows on Ceres are thicker, more voluminous, and longer than those observed on Vesta. Vestan flows generally form flat conical deposits to the interior of craters, are rarely lobate, and never appear fluidized (Krohn et al., 2014). These contrasting morphologies indicate fundamentally different mechanisms; this is best explained by differences in rheology and likely composition, with Ceres flows containing weaker or lower melting point materials such as ices, clays or salts.

3.4 Discussion

3.4.1 Origins of Cerean Lobate Deposits

In general, these aforementioned data support the interpretation that there are distinguishable groups of surface flow behaviors on Ceres that define a continuum from Type 1 to Type 2 features, and Type 3 features represent instances of possible fluidized ejecta. The most consistent explanation for the mass wasting behavior we observe on Ceres is ice within its shallow subsurface materials, and that variation in the ice content, surface conditions, and triggering explain the observed variations.

Type 1 flows truncate at relatively shorter lengths than the other flows and display the least efficient down-slope transport. This suggests different mechanical behavior, such as a difference in rheology (i.e. increase in effective viscosity), deformation within the flow or non-Newtonian (e.g. Bingham) flow (Ancey, 2006). The first spectral detection of ice on Ceres was collocated with small Type 1 flows found in Oxo crater within the Fejokoo quadrangle of Ceres (see Chapter 2, subsection 2.3.4.2). Type 1 features have distinct geomorphology, and low mass transport efficiency relative to the other low types (see Figure 3-6) despite the fact that they occur on steep slopes that should promote longer flow. In particular, the rolled appearance of Type 1 flows, forming steep, concave-down, frontal snouts, is difficult to explain without

internal deformation. Ice can creep under a wide variety of conditions (Durham et al., 1997; Weertman. 1983), and such deformation or non-Newtonian flow is possible where ice content is high enough to overcome silicate grain friction (e.g. Legros, 2002). Crater rim collapse or rapid flow down steep scarps would create high strain rates under which an ice-silicate mixture would warm to high homologous temperatures and could plausibly flow or fail, explaining the observations of Type 1 flows. While the areal density of steep slopes is larger at high latitudes on Ceres, due to an increased concentration of small impact craters, the fractional abundance of Type 1 flows near the poles compared to near the equator is significantly larger than the equivalent ratio of slope abundances (Ermakov et al., 2019). Thus, we conclude that the contribution of steep slopes to the formation of Type 1 flows is minor relative to the effects of abundant near-surface ground ice. A minimum of 10% ice by volume is required for rock glaciers or frozen debris flows to move, although pore-filling ice is much more effective, and to flow as a fluid the volume of rock and ice must be similar, approaching 50% (e.g. Dannan et al., 2012; Darrow et al., 2016; Haeberli et al., 2006; Humlum, 2000; White, 1976), so ice in Ceres' upper layers proximal to Type 1 flows may range from 10–50 vol.%

Type 2 flows are most consistent with lubrication by ice, which can occur at temperatures above 250 K, within a few tens of kelvin of Ceres' surface temperatures. On Ceres, as on Mars and Iapetus, frictional heating of any ice grains during a landslide would raise the temperature within the flow and at its base, conditions that can cause ice to become slippery or melt. These warm grains and basal melt blebs reduce sliding friction and allow the flow to traverse long distances even along shallow slopes (Legros, 2002; Singer et al., 2012), resulting in long, thin flows with rounded, almost spatulate toes. Both salts and clays have lower melting points than anhydrous silicate; however, these are significantly higher than that of ice, by at least ~300 K.

Thus, ice provides the lowest temperature threshold for mobilizing flows. We also favor ice due to several observations: detections of local surface ice from visible and infrared, and ice in the upper meter of the surface by GRaND; the lack of both long runout landslides and ice on Vesta, whose surface differs from Ceres primarily in composition, including water content; and these flows appear geographically and morphologically intermediate between cold, high-ice-content flows (Type 1) and fully fluidized flows (Type 3). However, other long runout landslides on Earth and Mars have been attributed to an array of mechanisms, including lubrication by clay minerals (Watkins et al., 2015), acoustic fluidization (Legros, 2002), and ice in the substrate; thus, ice is not necessarily required to generate Type 2 landslides. Additionally, the Type 2 *H*/*L* trend is very similar to the behavior exhibited by landslides on Iapetus, and is shallower than terrestrial and Martian landslides. This also suggests that a reduction in basal friction could be occurring in Ceres flows

Type 3 flows are strongly correlated with impact events and they always originate at a crater rim. These flows show no obvious relationship between flow length and *H*/*L* and have universally low values for *H*/*L* relative to the other cerean flow types. Together with their collocation with impact ejecta, this suggests that Type 3 flows result from melting and/or vaporization during energetic impacts. However, they infrequently encircle the entirety of their source crater, which suggests that if they are fluidized impact ejecta, either only part of the ejecta is fluidized, only a portion of the subsurface is rich in mobilizable volatiles, and/or these flows occur in impacts that deposit ejecta asymmetrically. Conversely, they may be flows initiated by post-impact heating or triggering; however, this does not explain why most of the Type 3 flows lack significant head scarps or escarpments. The energy required to melt subsurface ice on Ceres

is easily met for most of its impactor velocity distribution, and rare faster impacts could eject up to half of this melted material as fluidized ejecta (Marchi et al., 2013).

3.4.2 Implications for Ground Ice on Ceres

The physiography and morphology of flows on Ceres are best explained by ice within its shallow subsurface; their distribution also suggests that their behavior is strongly influenced by latitude (Figure 3-5); due to Ceres' low obliquity, latitude is also the primary control on near-surface ground ice abundance (Prettyman et al., 2017). Type 1 flows, which are interpreted to be ice rich, generally exist above ~50° latitude, and are the dominant flows at the poles. Although their global distribution may not uniquely require ice, Type 2 flows peak between 30°–60°. Type 3 flows are found in low abundance, but mostly in low-mid latitudes. Thus the distribution of surface flows is consistent with a latitude-dependent depth to the ice table with an increasing abundance of shallow ground ice being made available towards the poles (Hayne & Aharonson, 2015; Prettyman et al., 2017). This latitude-dependent behavior would not be expected for salts or clays, nor has spatial variation in such compounds been observed (De Sanctis et al., 2015).

Our results suggest that ice exists across Ceres in its subsurface materials, with a sharp increase above ~50° latitude. This is consistent with observations by GRaND (Prettyman et al., 2017). Similar to the north–south asymmetry in the GRaND data, a north–south asymmetry is also seen in the abundance of Type 1 flows (Figure 3-4) suggesting the surface near the south pole of Ceres may be depleted in water ice relative to its north pole. Additionally, since the first spectral detection of surface ice was made on Ceres, eight more instances of this volatile have been documented (Combe et al., 2019). Of these nine total detections of surface ice, five are associated with lobate deposits that were identified during this identification campaign (Figure 3-

8). This further solidifies the link between the specific flow morphologies seen on Ceres and the presences of abundantly available near-surface ground ice.

3.5 Conclusions

Ceres' flows occur along a morphological spectrum consistent with the behavior and measured distribution of near-surface interstitial ground ice. High ice content is required for high latitude preferring Type 1 flows, enhanced basal gliding (likely derived from ground ice) is required to explain the ubiquitous Type 2 flows, and melting of that ice best explains Type 3 flows. Type 1 mass wasting also provides some constraint on the volume of ice possible in the near-surface. This is likely between ~10-50 vol. %. These observations make Ceres only the third planetary body where ground ice is confirmed and geographically widespread.

Ground ice also provides a context by which to understand other features on Ceres. There are many crater walls, floors and ejecta deposits that contain high-albedo features, which could be deposits left by sublimation and or evaporation (e.g. De Sanctis et al., 2016). Many craters have melted floors that could be produced by melting subsurface ice, and slumping or ponding of material may be another form of ice-driven mass wasting. Because Ceres is significantly warmer than icy moons, any melt reservoirs formed by impact will have a protracted lifetime, possibly promoting permafrost-style behavior. The presence of ice in Ceres' crust suggests that water ice may indeed be common in the as-yet unexplored outer asteroid belt, and this reservoir of water represents a potential source of Earth's primordial water and a possible resource for mining of asteroids. It also blurs the compositional distinction between (rocky) asteroids and (volatile-rich) comets.

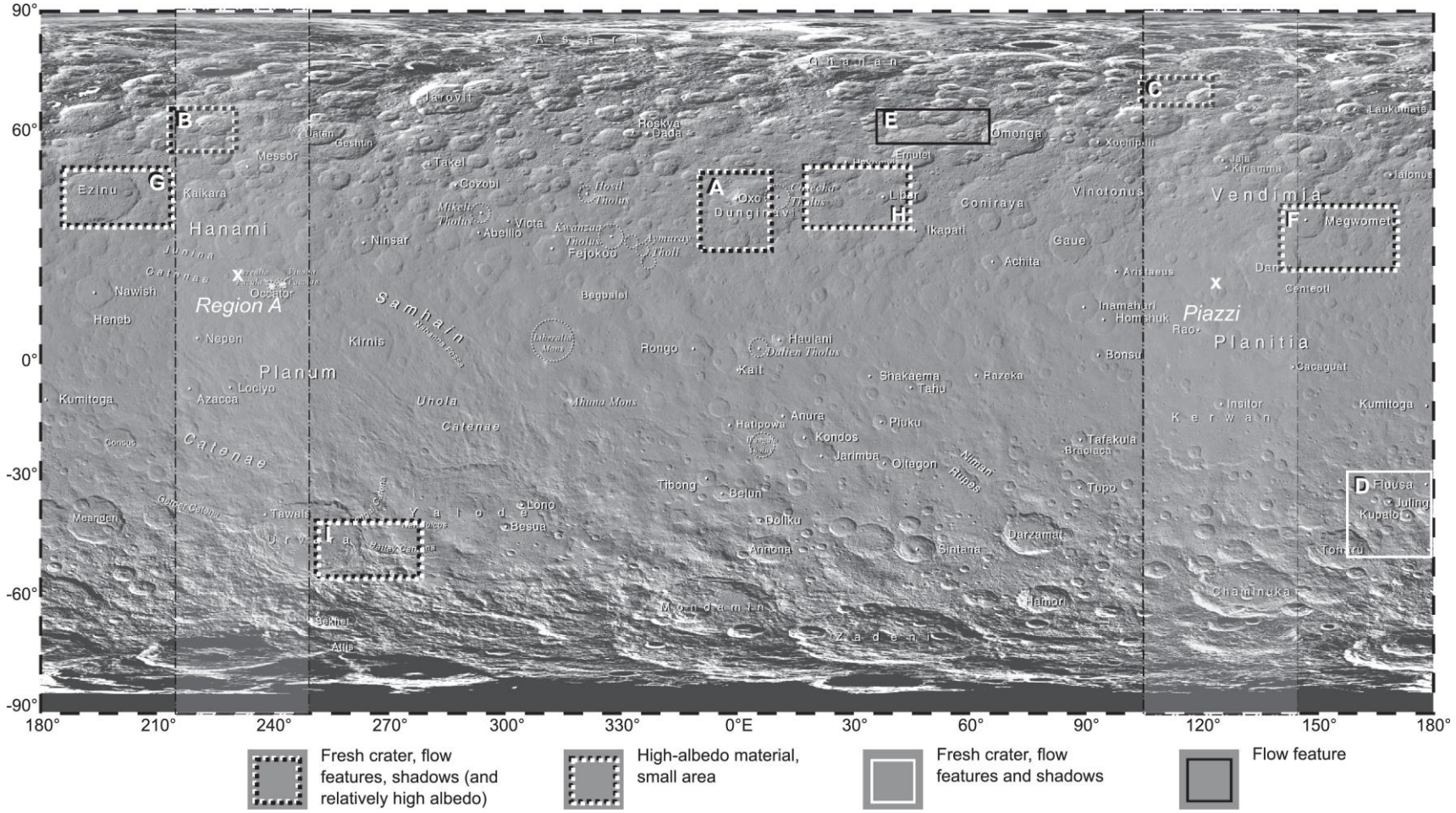

Figure 3-8. Locations of the nine exposed water ice rich areas on Ceres. Individual boxes outline the detection areas. Note that the black lined, white lined, and dotted black lined boxes indicate that the water detection was co-located with a lobate deposit of the types outlined in this chapter. The grey vertical bands and locations marked by an X labeled Region A and Piazzi refer to the two areas identified as possible sources of H_2O vapor outgassing by Küppers et al. (2014). Image adapted from Combe et al. (2019).

Flow Type:	longitude:	latitude:	ΔH (drop height, m):	ΔL (runout length, m):	ΔH/ΔL:
1	135.696	77.671	800	9000	0.089
1	27.233	86.03	600	6700	0.090
1	-5.208	80.209	3000	14000	0.214
1	26.159	68.043	2500	9800	0.255
1	52.142	61.848	3750	10000	0.375
1	85.952	57.76	1850	8660	0.214
1	-176.254	51.479	550	1390	0.396
1	-43.882	51.294	1250	5000	0.250
1	26.846	50.537	3250	12100	0.269
1	130.158	65.607	2600	5900	0.441
1	-0.452	41.838	810	2660	0.305
1	-0.194	41.426	400	1470	0.272
1	-115.964	21.71	2900	8080	0.359
1	168.191	-35.366	3050	8930	0.342
1	87.687	-55.681	1500	3840	0.391
1	3.341	-70.099	2800	10760	0.260
1	164.127	-77.494	3650	13640	0.268
1	-139.415	-7.572	3400	7710	0.441
1	38.252	78.164	2990	20920	0.143
2	-79.145	64.877	4000	22820	0.175
2	129.678	63.519	2800	14390	0.195
2	56.158	58.123	1380	6400	0.216
2	-79.676	51.484	3200	13140	0.244
2	-124.736	49.963	1900	15890	0.120
2	-23.294	35.746	1600	17500	0.091
2	-125.273	17.565	1300	3560	0.365
2	4.325	-49.169	3400	19070	0.178
2	-155.15	-57.935	1000	6530	0.153
2	72.288	59.813	4000	39600	0.101
2	-96.131	58.669	5900	44030	0.134
2	126.932	53.682	1900	16280	0.117
2	-90.588	49.128	1650	7320	0.225
2	-126.189	48.523	4000	22500	0.178
2	146.532	34.732	3600	66410	0.054
2	87.165	34.472	3050	13500	0.226
2	37.784	34.447	1100	4720	0.233
2	-57.53	34.143	400	11900	0.034
2	-4.245	33.849	450	7340	0.061
2	81.754	32.709	1500	8090	0.185
2	-97.541	31.514	3600	16400	0.220
2	-90.708	30.07	2400	12680	0.189

2	14.531	26.158	1550	15120	0.103
2	17.075	23.796	2700	27380	0.099
2	-24.782	13.042	1650	6600	0.250
2	-116.206	12.664	1750	8970	0.195
2	-121.891	4.883	1100	4080	0.270
2	4.472	1.517	1600	5720	0.280
2	10.911	-1.803	550	7480	0.074
2	-9.379	-3.187	1450	12000	0.121
2	10.171	-3.549	1100	8130	0.135
2	33.446	-5.321	2350	14700	0.160
2	116.109	-6.174	1650	8820	0.187
2	4.858	-14.795	1050	6130	0.171
2	16.957	-17.461	2700	11170	0.242
2	-124.786	-18.918	650	4500	0.144
2	23.871	-22.133	3100	17400	0.178
2	57.279	-23.299	900	7720	0.117
2	-95.469	-33.911	900	10420	0.086
2	90.974	-34.05	2400	10440	0.230
2	111.376	-40.008	2400	15500	0.155
2	19.534	-47.801	1250	6310	0.198
2	47.446	-48.475	3000	31210	0.096
2	125.009	-55.18	3600	36490	0.099
2	138.36	-62.275	3550	22380	0.159
2	-105.259	-70.293	650	26220	0.025
2	-109.025	-73.22	1550	16540	0.094
3	33.215	71.593	0	18000	0.000
3	-117.326	59.703	4600	34230	0.134
3	-73.353	42.87	4200	23210	0.181
3	51.673	30.997	1100	41850	0.026
3	122.57	20.374	500	24080	0.021
3	96.913	20.197	2000	20320	0.098
3	-16.226	17.214	650	5740	0.113
3	140.911	12.271	600	8270	0.073
3	-103.356	10.355	550	6800	0.081
3	-155.234	7.404	1550	17760	0.087
3	-49.513	-0.34	800	6730	0.119
3	19.643	-10.168	750	4900	0.153
3	14.186	-21.241	2950	23320	0.127
3	85.596	-35.729	1050	22370	0.047
3	176.999	-39.907	3200	20080	0.159
3	109.192	-39.965	400	6160	0.065
3	-84.143	-54.101	1800	12120	0.149
3	7.734	5.721	2700	31000	0.087

Table 3-1. Geographic locations and physical measurements for each of the identified Type 1, 2, and 3 flows on Ceres.

4 Fluidized Appearing Ejecta on Ceres: Implications for the Mechanical Properties, Frictional Properties, and Composition of its Shallow Subsurface

4.1 Fluidized Appearing Ejecta on Ceres and Throughout the Solar System

When the Dawn spacecraft began making detailed scientific observations of the dwarf planet Ceres it observed that a small but significant number of cerean craters exhibited ejecta morphologies that reflect a significant degree of fluidization, and suggest that they were emplaced as ground-hugging flows (Schmidt et al., 2017; Hughson et al., 2018). In contrast with most lunar and mercurian ejecta, which are predominantly emplaced by ballistic sedimentation and have limited runout distances (Shoemaker, 1962; Barnouin et al., 2012; Runyon & Barnouin, 2018), these cerean Fluidized Appearing Ejecta (FAE) commonly have one or many of the following characteristics: well-defined (i.e. non-gradational/abruptly terminating) margins, a sheeted or layered appearance, arcuate or cuspate terminal lobes, longitudinal grooves, channelized flows, and occasional mass concentrations at their distal margins. Although cerean FAE have no holistically perfect analogues on other solar system objects, the aforementioned morphological characteristics are also found among layered ejecta, abruptly terminating ejecta, and rampart craters on Mars, Ganymede, Europa, Dione, and Charon (e.g. Carr et al., 1977; Gault & Greeley, 1978; Schultz & Gault, 1979; Mouginis-Mark, 1979, 1981; Woronow, 1981; Horner & Greeley, 1982; Boyce & Mouginis-Mark, 2006; Jaumann et al., 2009; Boyce et al., 2010; Schenk, 2010; Li et al., 2015; Robbins et al., 2018) (Figure 4-1). There is currently no scientific consensus on the mechanisms of fluidization for martian and ganymedean layered ejecta; however, a plurality of investigators have interpreted the characteristics of these deposits to be due predominantly to the presence of volatiles, particularly water ice, in the upper layer of the target bodies (e.g. Carr et al., 1977; Mouginis-Mark, 1981, 1987; Barlow & Bradley. 1990;

Stewart et al., 2001; Barlow & Perez, 2003; Barlow, 2005; Boyce & Mouginis-Mark, 2006; Osinski, 2006; Senft & Stewart, 2008; Boyce et al., 2010; Weiss & Head, 2013, 2014, 2018). Other proposed factors that may contribute to the fluidized appearance of these deposits are: ejecta-atmosphere interactions in the case of Mars (e.g. Schultz & Gault, 1979; Schultz, 1992; Barnouin-Jha & Schultz, 1998; Barnouin-Jha et al., 1999a, 1999b; Barlow et al., 2005; Boyce & Mouginis-Mark, 2006; Boyce et al., 2010; Komatsu et al., 2007), base surges from the collapse of the main vertical ejecta column or near-rim ejecta (e.g. Boyce & Mouginis-Mark, 2006; Boyce et al., 2012; Barlow & Boyce; 2013), continuum fluid flow (e.g. Baloga et al., 2005; Barnouin-Jha et al., 2005; Mouginis-Mark & Baloga, 2006), and granular flow (e.g. Wada & Barnouin-Jha, 2006).

Ceres' low bulk density of 2162 ± 8 kg/m^3 (Park et al., 2016) has long been suggestive of a composition that is rich in water ice, hydrated materials, and/or organic compounds (Thomas et al., 2005; McCord & Sotin, 2005; Zolotov, 2009; Castillo-Rogez & McCord, 2010; Russell et al., 2016). The interpretation that Ceres' uppermost layer is rich in water ice is further strengthened by additional spectral observations of H_2O ice absorption features at geographically diverse locations on Ceres in spite of its thermodynamic instability (Combe et al., 2016, 2019), nuclear spectroscopy results that predict a thinly armored surface ice table at absolute latitudes greater than ~40° (Prettyman et al., 2017), and gravitational/topographic studies that predict ~25 vol.% ice in the upper ~40 km of Ceres (Fu et al., 2017; Ermakov et al., 2017). Despite these observations, the distribution and concentration of water ice in the upper layer of Ceres is still poorly constrained at the scale of several tens of kilometers and finer.

Layered ejecta craters on Mars and FAE on Ceres display significant variation in their ejecta mobility ratios (EM), which is defined as the ratio of a continuous FAE facies' mean distal

radius from the crater rim over the observed crater rim radius (R_e/R_f) (e.g. Carr et al., 1977; Mouginis-Mark, 1979; Barlow & Pollak, 2002; Barlow, 2005; Weiss & Head, 2014). In the case of Mars, these variations in EM values have variously been attributed to modulations in the abundance of near surface volatiles (Gault & Greeley, 1978; Barlow & Pollak, 2002; Weiss & Head, 2014), variations in the distribution of volatiles in the target material (Costard, 1989), variations in the mechanical properties of the near-surface (Wada & Barnouin-Jha, 2006), and ejecta-atmosphere interactions (Schultz, 1992). The three former factors are of particular interest in the case of FAE on Ceres.

This study tests the hypothesis that the morphologies and various EM values of cerean FAE deposits can be explained via impacting into a low-cohesion ice-silicate target material, and material sliding on a low-friction substrate. The aforementioned factors are directly controlled by the abundance and distribution of ground ice in the region immediately proximal to the impact. This is done by identifying and characterizing morphologically distinct cerean FAE through geologic mapping, analyzing their geographic distribution, measuring their EM values, and by comparing these values to a hybrid kinematic-dynamic sliding ejecta emplacement model moderately similar to the kinematic model developed by Weiss and Head (2014) for applications on Mars.

4.2 Datasets and Methodology

4.2.1 Basemaps and Photographic Data

The data used in the identification and quantification of cerean FAE were entirely photographic and stereophotogrammetric in nature. The analyzed images were collected during Dawn's High Altitude Mapping Orbit (HAMO: 1,470 km altitude) and Low Altitude Mapping

Orbit (LAMO: 375 km altitude) by the spacecraft's Framing Camera (FC) (Sierks et al., 2011). These clear and color filter FC data were acquired globally at ~140 m/pixel and ~35 m/pixel, from the HAMO and LAMO mission phases, respectively. Globally acquired FC images taken from HAMO were used to generate the stereophotogrammetric (SPG) digital terrain model (DTM) of Ceres (vertical accuracy ~10 m) (Preusker et al., 2016). For details on the calibration of FC images see Schröder et al., (2013) and Schröder et al. (2014).

4.2.2 Mapping of Fluidized Appearing Ejecta on Ceres

Previous global mapping campaigns by Buczkowski et al. (2016) and Schmidt et al. (2017) identified 18 landslide-like deposits that they termed "Type 3 flows" (see Chapter 3). Schmidt et al (2017) interpreted these Type 3 flows as possible instances of fluidized ejecta mainly by virtue of their thin sheeted appearance and anomalously low drop-height-to-runout-length (H/L) ratios that display no correlation with average flow length. These low H/L values are analogous to having high runout efficiencies (e.g. Barnouin-Jha & Buczkowski, 2007; Runyon & Barnouin, 2018). Inspired by the results of Chapter 3 (Schmidt et al., 2017), a global geomorphologic mapping campaign based on expanded criteria was conducted to identify and characterize prominent instances of FAE on Ceres. Specifically, ejecta facies that displayed at least one direct morphological indication of fluidization were mapped, namely: the presence of discrete cuspate or arcuate terminal lobes, a sheeted or multilayered appearance, abrupt or well defined margins, superimposed longitudinal grooves, or topographically controlled channelized flow (i.e. ejecta which has been confined to areas of relatively low topography and/or been focused or deflected by topographic obstacles). Ejecta facies that did not display any of the aforementioned characteristics were interpreted as dry runout flows, and not included in the

mapping. Distinct occurrences of landslides within or coincident with FAE are discussed in Duarte et al. (*Submitted to JGR: Planets*), and may be formed during or after FAE emplacement.

In total, 30 robust occurrences of FAE on Ceres were identified. These features were interpreted as belonging to two separate morphological populations: a channelized FAE population and a cuspate/lobate population. The 11 identified channelized FAE display multiple prominent instances of topographic control (e.g. pooling in depressions, formation of numerous small channels in low lying regions, and being easily diverted around isolated instances of high standing terrain), occasional flow banding, and have thin sheeted appearances; they do not exhibit well developed cuspate lobes, longitudinal grooves, or a multilayered appearance, and have well-defined terminal margins only intermittently around their distal margins. The remaining 19 cuspate/lobate FAE display prominent cuspate or arcuate terminal lobes, a layered or multilayered appearance, and have well-defined distal margins around the majority of their perimeter. These cuspate/lobate FAE also display occasional longitudinal grooves near the rims of their source craters, and mass concentrations near their distal margins. Typical examples of cerean channelized and cuspate/lobate FAE, their mapped facies, and their local topography are shown in Figure 4-2 (similar renderings for all 30 identified cerean FAE are given in Appendix A, Figures A-1 through A-28). In general, cerean FAE were found to be predominantly associated with morphologically fresh appearing impact craters. Specific morphological characteristics of cuspate/lobate and channelized cerean FAE are displayed in Figures 4-3 and 4-4, respectively. This mapping analysis, as well as the global search campaign, was completed using ArcMap 10.3.

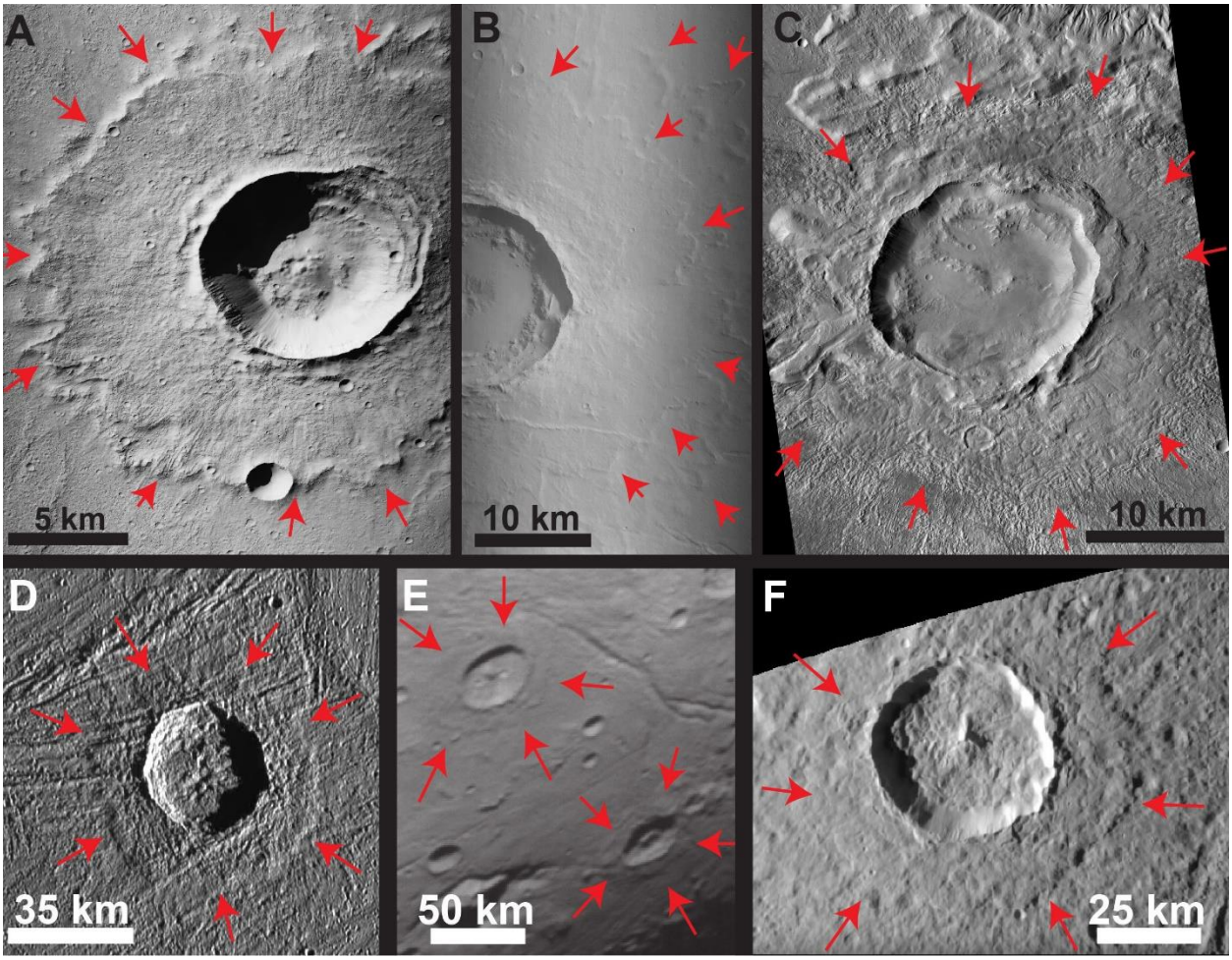

Figure 4-1. Examples of various types of fluidized ejecta throughout the solar system: (a) single-layer ejecta crater on Mars (25.9º S, 152.4º E; CTX image, Planetary Data System [PDS] ID P17_007554_2154), (b) multiple-layered ejecta on Mars (22º N, 146º E; CTX image, PDS ID P07_003624_2041), (c) double layer ejecta crater on Mars (30.4º N, -86.3º E; CTX image, PDS ID D22_035780_2101), (d) Achelous crater on Ganymede exhibiting a rampart morphology (61.8º N, 11.7º W; SSI image mosaic courtesy of Paul Schenk), (e) abruptly terminating ejecta on Charon, the identified crater in the top left is Spock (14.7º N, 25.7º E), the identified crater in the bottom right is unnamed (LORRI image, PDS ID lor_0299171413_0x636_sci), (f) Sagaris crater on Dione exhibiting abruptly terminating ejecta (25ºS, 79ºE; ISS image mosaic courtesy of Paul Schenk). Major terminal ejecta lobes and flow fronts are indicated by the red arrows.

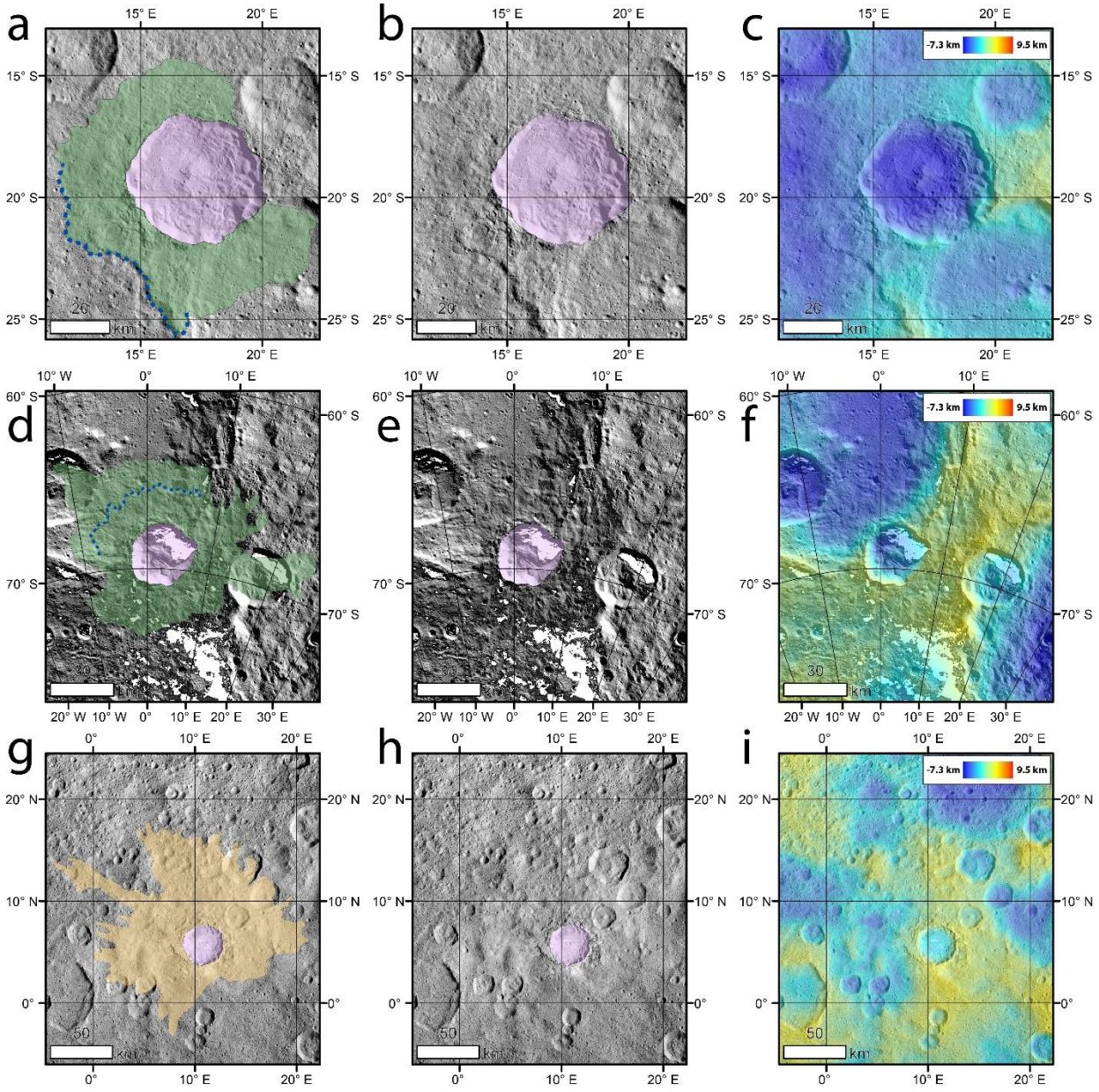

Figure 4-2. Three representative examples of cuspate/lobate and channelized FAE on Ceres. Mapped cuspate/lobate ejecta facies are represented by green overlays, channelized FAE are mapped with light orange overlays, and the source craters are mapped using light purple overlays. The dashed blue lines in (a) and (d) indicate regions of abruptly terminating ejecta similar to double layer ejecta on Mars and layered ejecta on icy satellites. (a) Kondo crater with mapped cuspate/lobate FAE deposit. (b) same image from (a) but with ejecta related map

overlays removed. (c) same image as (a) but with all mapping overlays replaced by color coded HAMO derived topography. (d) Jacheongbi crater with mapped cuspate/lobate FAE deposit and possible double layer behavior. (e) same image from (d) but with ejecta related map overlays removed. (f) same image as (d) but with all mapping overlays replaced by color coded HAMO derived topography. (g) Haulani crater with mapped channelized FAE deposit. (h) same image from (g) but with ejecta related map overlays removed. (i) same image as (g) but with all mapping overlays replaced by color coded HAMO derived topography.

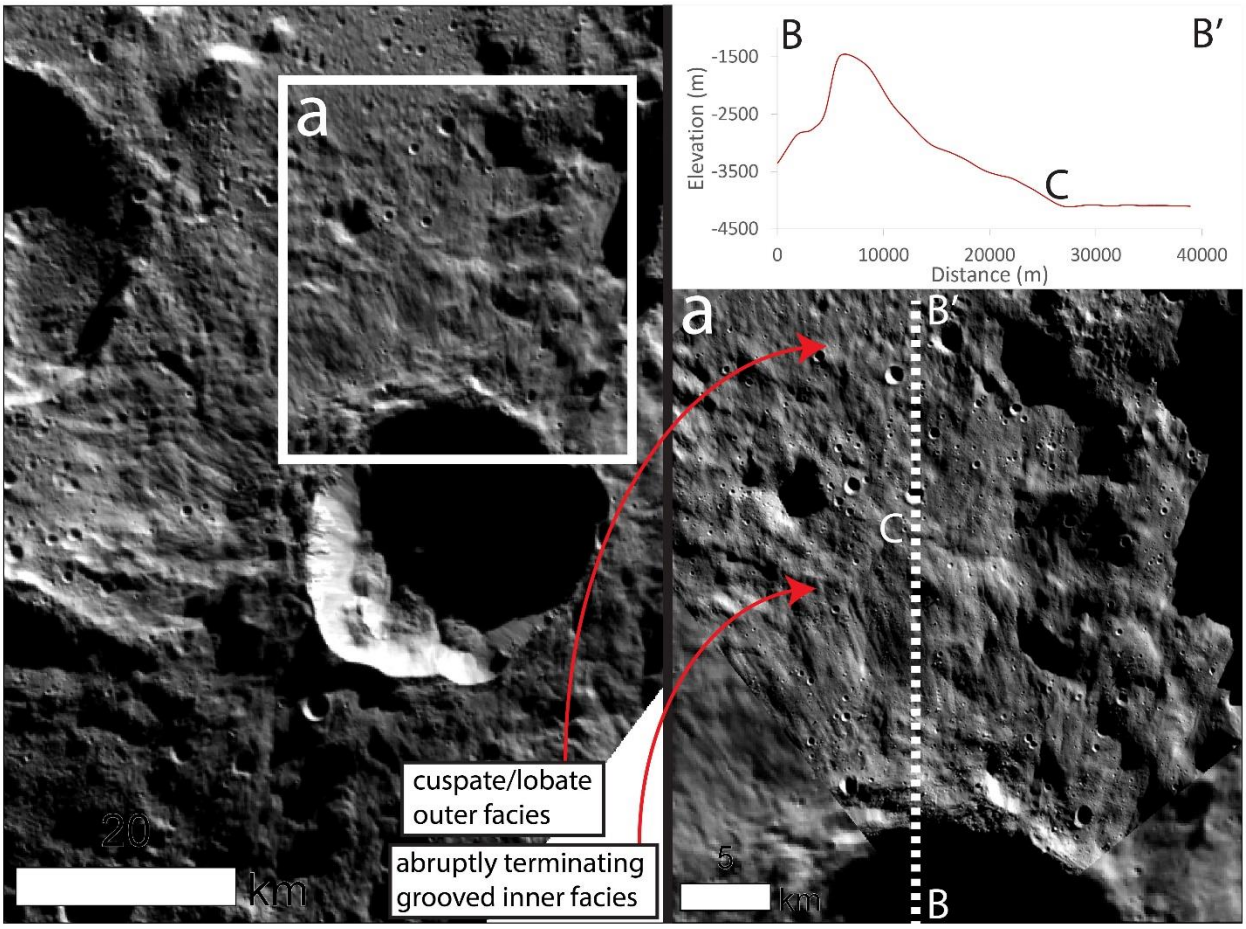

Figure 4-3. Expanded view of Jacheongbi crater and the northern portion of its cuspate/lobate FAE deposit as seen in Figures 4-2d, 4-2e, and 4-2f. In inset (a) note the arcuate-to-cuspate v-shaped lobes near the upper red arrow. This morphology is common among the outer facies of double- and multiple-layered ejecta on Mars as well as the other cuspate/lobate cerean FAE, and were used, in part, to help determine the outer margins of cuspate/lobate ejecta facies. The inner ejecta facies near the lower red arrow in inset (a) displays superimposed longitudinal grooves and an abruptly terminating margin, which is noticeable in the included topographic cross-section. These characteristic are often associated with the inner ejecta facies of martian double layer ejecta.

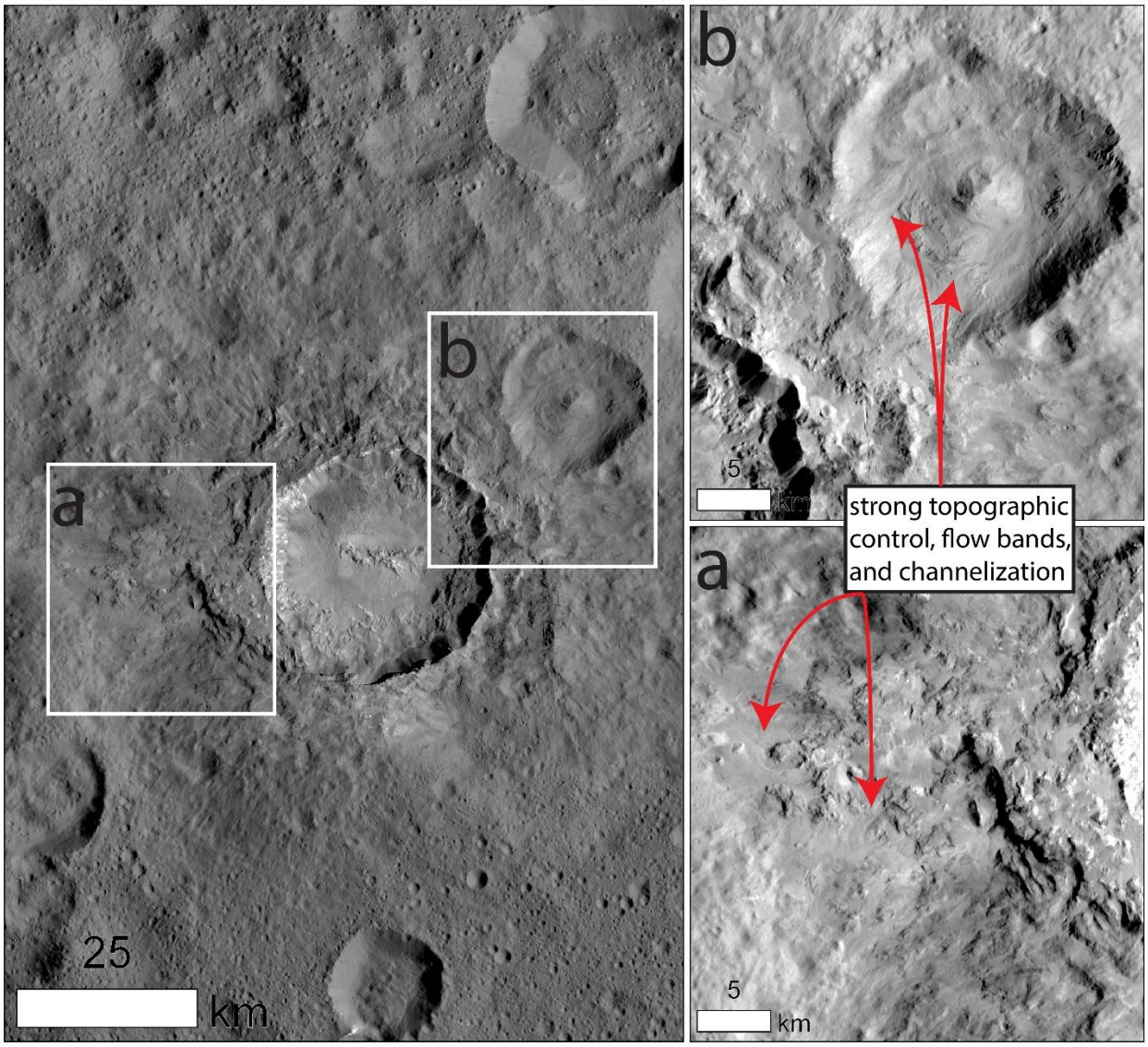

Figure 4-4. Expanded view of Haulani crater and the inner portions of its channelized FAE as seen in Figures 4-2g, 4-2h, and 4-2i. The thin sheeted appearance, susceptibility to topographic control, and flow banding of the channelized FAE is highlighted in insets (a) and (b). This behavior is also observed at greater distances from the center of Haulani, albeit less dramatically. These morphological characteristics are common among channelized FAE on Ceres, and were used to help delineate their boundaries.

Once FAE were identified geomorphically, both their source crater radii and rim-to-terminus ejecta emplacement distances were quantified. Due to the fact that many of the examined craters did not exhibit radially symmetric geometries, their radii were measured as the length-weighted mean distance from their rims to the centroid of their mapped polygon (see Figure 4-2 for examples of mapped polygons). Likewise, the rim-to-terminus ejecta emplacement distance was measured as the length-weighted mean distance from the distal margin of the outermost mapped FAE facies to the centroid of its source crater, minus the mean radius of the source crater itself. Beyond using length-weighted mean crater radii, the effects of elliptical crater geometries on measured EM values are not considered. This simplification is justified due to the generally low observed ellipticity of FAE source craters (see Appendix A). Although this geomorphic mapping, like all attempts at geologic mapping, suffers from a degree of subjectivity, the resultant values for FAE source crater radii, ejecta runout distance, and EM are fully self-consistent. They likely suffer from no more than (±) a few percent error.

Additionally, the spatial derivative of the HAMO SPG DTM was used to quantify the mean regional slopes radially away from the rims of FAE source craters. This exercise was completed in order to calibrate the measured EM values to a common slope gauge, so that the analysis of these values (albeit crudely) was independent of variations in the slope local to each instance of FAE. This was accomplished through the use of ArcMap's Zonal Statistics tool.

4.2.3 Geospatial Analysis and Distribution Modeling of Fluidized Appearing Ejecta

On Mars, fluidized ejecta craters display distinct latitudinal distribution trends based on their specific morphology (Weiss & Head, 2014). It is likely that these distributions are controlled primarily by the availability of near-surface/surface ground ice and its stratigraphic locations (Barlow & Perez, 2003). If latitudinal trends exist in the distribution of FAE on Ceres

they would most likely be caused by variations in the near-surface ground ice content (Schmidt et al., 2017) due to enhanced desiccation near the equator (Prettyman et al., 2017), and/or by decreased volatility of ice, clathrates, and hydrated salts in the very near-surface at the poles due to the ~50 K decrease in the mean annual surface temperature relative to the equator (Hayne & Aharonson, 2015).

In order to test for any latitudinal trends in the populations of cerean FAE their distribution functions were estimated using Kernel Density Estimation (KDE) (Rosenblatt, 1956; Parzen, 1962). KDE is a non-parametric method for estimating the probability density function (PDF) of a random variable. It is particularly useful in the case of cerean FAE as there is no *a priori* knowledge about their distribution, and given the relatively small amount of data traditional statistical parameters such as the mean and variance are of limited utility. The only subjective choices made in the KDE analysis were kernel form and bandwidth. Gaussian kernels were chosen for the KDE analysis, and a modified Silverman's rule of thumb (Eq. 1) was used to select a bandwidth that minimized the mean integrated squared error for each instance of this investigation.

$$h = 0.9 \cdot \sigma \cdot N^{-0.2} \quad (1)$$

Where in Eq. 1 h is the kernel bandwidth, σ is the standard deviation of the samples, and N is the number of samples (Silverman, 1986).

A complementary KDE analysis of the distribution of cerean FAE with respect to their EM values was also carried out. The results of the global identification campaign and distribution analysis are summarized in section 4.3.1. This statistical analysis was completed using the Scikit-learn module for Python 3 (Pedregosa et al., 2011).

4.2.4 The Hybrid Kinematic-Dynamic Ejecta Emplacement Model

After measuring EM values and source crater radii, the hypothesis that cerean FAE could develop due to the presence of an H_2O rich near-surface layer was tested by using an analytic hybrid kinematic-dynamic sliding ejecta emplacement model. This model is similar to the one developed by Weiss and Head (2014) to approximate the ejecta mobility for double layer and low-aspect-ratio layered ejecta craters in ground ice rich substrates on Mars, but with several key differences. Namely, full Newtonian gravity is utilized as opposed to the kinematic approximation, and the substrate is not assumed to be composed of a pure ice layer of variable thickness overlaying a rocky substrate, instead it is assumed to be an intimate mixture of silicates and water ice whose relative proportions are variable. Additionally, a uniformly sloped substrate onto which the ejecta is deposited is assumed rather than a purely horizontal surface. A schematic representation of the kinematic-dynamic sliding ejecta emplacement model is displayed in Figure 4-5.

Kraus et al. (2011)'s vaporization scaling law (Eq. 2) is used to confirm that ejecta fluidization via melted and vaporized water is plausible on Ceres. In Eq. 2, M_V is the total mass of ice melted and vaporized, M_i is the mass of the impactor, T is the target material's temperature in Kelvin, ψ is the impact angle measured from the horizontal, γ is the porosity, U is the average impact speed at Ceres, and $E_M(\gamma)$ is the specific internal energy for complete melting. Note that the results returned by Eq. 2 overestimate the mass of vapor produced by about a factor of two for impacts ~5 km/s (Kraus et al., 2011), which is the mean impact speed at Ceres (Marchi et al., 2016):

$$\log\left[\frac{M_{M+V}}{M_i}\right] = -0.53 + 0.0017 \cdot T + 0.7 \cdot \log[\sin\psi] + 0.46 \cdot \gamma + \frac{3\cdot(0.554-0.07\cdot\phi)}{2} \cdot \log\left[\frac{U^2}{E_M(\gamma)}\right] \quad (2)$$

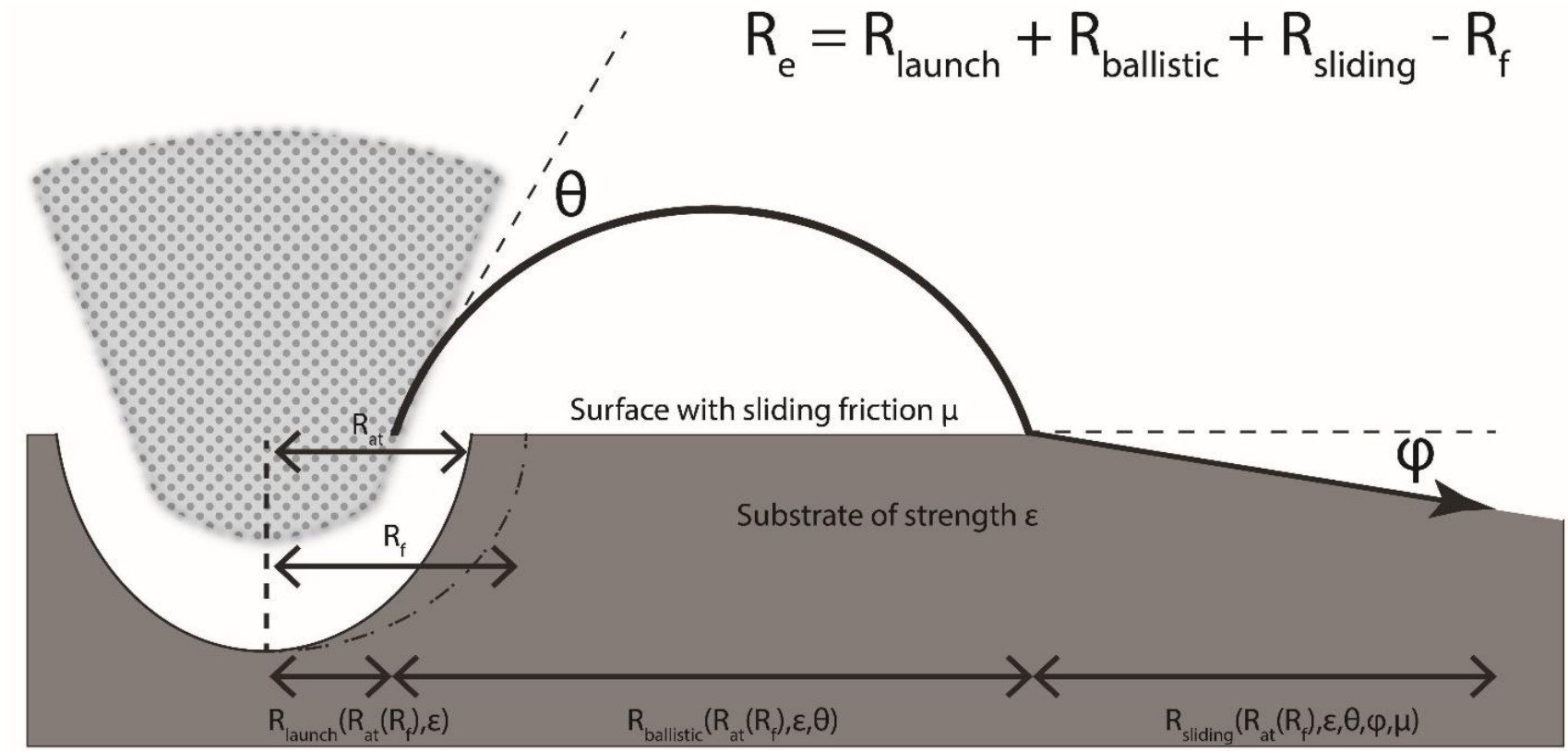

Figure 4-5. Schematic breakdown of the ejecta emplacement model (Eq. 3) described in section 2.4. Note that the model is radially symmetric about the center of the source crater. The ejecta excavation angle, θ, is measured upwards from the horizontal, while the mean surface slope, φ, is measured downwards from the horizontal.

In this model FAE are treated as ground-hugging continuous flows similar to landslides, debris flows, granular flows, or snow avalanches, which is consistent with how martian fluidized ejecta have been interpreted to have been deposited, and has been observed in laboratory ejecta experiments (e.g. Mouginis-Mark & Baloga, 2006; Jones et al., 2016; Runyon & Barnouin, 2018). In the model proposed here (Eq. 3), upper bound values for the coefficient of sliding friction encountered by FAE on Ceres are established by ignoring flow within the cohesive mass of ejecta. This approximation assumes that the cerean FAE deposits were emplaced primarily as basal-glides (i.e. flows that exhibit generally low velocity gradients throughout the entire depth of the flow, except at the sliding interface: Baloga et al., 2001). This assumption is justified by the morphological similarities between these cerean flows and martian layered ejecta, which along with martian and cerean long-runout landslides have been interpreted as basal-glide emplaced features (Barnouin-Jha et al., 2005; Schmidt et al., 2017; Chilton et al., 2019). It should be noted, however, that martian-style rampart ejecta are thought to require appreciable velocity gradients to form (Weiss & Head, 2018). These cases are not considered separately as unambiguous ramparts have not been detected on Ceres. While it remains unknown if martian layered ejecta or cerean FAE behave predominantly like flows emplaced by basal-gliding, the coefficient of sliding friction in the model remains a general proxy for dissipative forces. Thus even if basal-gliding does not play a significant role in the emplacement of these flows this model will still provide insight into the viscosity, degree of fluidization, and volatile content of these deposits (Wada & Barnouin-Jha, 2006; Weiss & Head, 2014). Since Ceres has no appreciable atmosphere the model does not take atmospheric effects into account.

From Newtonian gravity and Newton's second law it can be shown that the expected ejecta runout distance, R_e, is given by:

$$R_e = R_{flight} + R_{sliding} + R_{launch} - R_f \quad (3)$$

The leftmost term on the right side of Eq. 3 is the ballistic flight contribution to the overall ejecta runout distance, $R_{sliding}$ is surface sliding contribution, R_{launch} is the distance relative to the center of the crater where the volume averaged ejecta is effectively sourced from, and R_f is the observed source crater radius. The components of R_{flight} and R_{sliding} are further described below:

$$R_{flight} = 2 \cdot R_0 \cdot \left[\pi - \cos^{-1}\left(\frac{1}{\epsilon} \cdot \left\{\frac{R_0 \cdot (U_{VA} \cdot \cos\theta)^2}{G \cdot M} - 1\right\}\right)\right] \quad (4)$$

$$R_{sliding} = \frac{(U_{VA} \cdot \cos\theta \cdot \cos\varphi - U_{VA} \cdot \sin\theta \cdot \sin\varphi)^2}{2 \cdot g \cdot (\mu \cdot \cos\varphi - \sin\varphi)} \quad (5)$$

Here R_0 is the mean radius of Ceres, g is the mean surface gravitational acceleration on Ceres, μ is the coefficient of sliding friction of the surface, θ is the excavation angle, φ is the mean surface slope of the substrate, M is the mass of Ceres, G is the gravitational constant, ϵ is the eccentricity (Eq. 6) of the volume averaged ejecta's sub-orbit, R_{at} is the apparent transient crater radius (Eq. 7), and U_{VA} is the volume averaged ejecta velocity (Eq. 8). R_{launch} is calculated by applying the mean value theorem to Eq. 8 after U_{VA} has been determined for a given R_{at}.

$$\epsilon = \left[1 + \frac{\left(U_{VA}^2 - \frac{2 \cdot G \cdot M}{R_0}\right)(R_0 \cdot U_{VA} \cdot \cos\theta)^2}{(G \cdot M)^2}\right]^{\frac{1}{2}} \quad (6)$$

$$R_{at} = \frac{(R^*)^{\eta} \cdot R_f^{1-\eta}}{1.3 \cdot \kappa} \quad (7)$$

$$U_{VA} = \int_{R_b(R_{at})}^{R_{at}} v_i(r) \cdot \frac{1}{3} \cdot \frac{\pi \cdot r^2}{V(R_{at}) - V(R_b)}\, dr \quad (8)$$

In Eq. 7 for the apparent transient crater radius (Melosh 1989; Holsapple, 1993), R^* is the simple-to-complex transition radius on Ceres, which is approximately 5.15 km (Hiesinger et al.,

2016). Both η and κ are numerically determined constants found to be approximately 0.04 ± 0.02 and 1.19 ± 0.04, respectively, in ice at the temperature of the icy jovian satellites (Senft & Stewart, 2011; Kraus et al., 2011), which is broadly representative of the conditions at Ceres.

The relationship in Eq. 8 derives the volume averaged ejecta velocity over the expected excavated paraboloid, $V(R_{at})$ given by (Eq. 9) (Melosh, 1989), minus the paraboloidal core of ejecta, $V(R_b)$, that exceeds the escape velocity of Ceres. U_{VA} is generated by averaging the launch velocities of paraboloidal shells of ejecta at given radial distances away from the center of impact, as given by the Richardson et al. (2005) scaling relationship (Eq. 10), weighted by the volume of ejecta lofted at each specific velocity. The lower bound of integration in Eq. 8, R_b, is calculated by numerically solving Eq. 10 for R at $v_i = v_{escape}$ (for Ceres $v_{escape} \approx 510$ m/s).

$$V(R) = \frac{1}{9} \cdot \pi \cdot R^3 \tag{9}$$

$$v_i(R) = \frac{2 \cdot \sqrt{R_{at} \cdot g}}{1+\varepsilon} \left[\left(\frac{R}{R_{at}} \right)^{-\varepsilon} - \left(\frac{R}{R_{at}} \right)^{\lambda} \right] \tag{10}$$

In the above equations R is the radial coordinate away from the center of impact, ε is the experimentally determined target strength, and λ is an arbitrary large constant chosen such that v_i goes to zero as R approaches R_{at}.

For this investigation establishing the plausibility of generating FAE through the incorporation of melt and vapor phases, non-dimensionalized scaling from Melosh (1989) was used to determine the relationship between R_{at} and R_i, the impactor radius.

$$\pi_D = 1.24 \cdot \left(\frac{\rho_t}{\rho_p} \right)^{\frac{1}{3}} \cdot \frac{R_{at}}{R_i} \tag{11}$$

$$\pi_2 = \frac{3.22 \cdot g \cdot R_i}{U^2} \tag{12}$$

$$\pi_D = C_D \cdot \pi_2^{-\beta} \quad (13)$$

In Eq. 13 C_D and β are experimentally determined constants taken to be 2.5 ± 0.5 and 0.16 ± 0.02 in ice-like material at 150 K (Kraus et al., 2011). A complete list of model parameters and parameter ranges is given in Table 4-1.

Representative shock pressure, melt and vapor fraction, crater scaling, and volume averaged ejecta velocity relationships from Eq. 2, 7, 8, 11, 12, and 13 are shown in Figure 4-6.

The sliding ejecta emplacement model (Eq. 3) was implemented for a range of plausible Ceres parameters outlined in Table 4-1, and compared the results to the slope corrected EM behavior of the channelized and cuspate/lobate FAE. In order to best characterize the most probable values of ε and μ over the entire parameter space of observed slope corrected EM and R_f values, the emplacement model was evaluated using a Monte Carlo-style analysis at $\varphi = 7.5^{\circ}$ for R_e and EM values within the range 0 m $\leq R_e \leq$ 50,000 m and 0.5 $\leq$ EM $\leq$ 6 using randomly generated values for ε and μ confined to the ranges $1.8 \leq \varepsilon \leq 2.6$ and $0.01 \leq \mu \leq 0.8$. Coordinate pairs whose R_e values were a multiple of 1250 m and EM values were a multiple of 0.2 comprised the grid over which the model was implemented; the ε and μ values between grid-points were estimated using cubic interpolation. In this analysis, the acceptable deviation from a prescribed EM value on the model grid for a randomly generated $\varepsilon - \mu$ pair was ±1%. The $\varepsilon - \mu$ pairs returned by the model represent the mean values of all the Monte Carlo generated $\varepsilon - \mu$ values that satisfied the aforementioned tolerance for a given R_f – EM coordinate pair. This was done in order quantify the variance of ε and μ for given EM values, and to establish the sensitivity of the model to changes in ε and μ. For each R_f – EM coordinate pair within the model grid analyzed by the Monte Carlo-style analysis, 100,000 $\varepsilon - \mu$ pairs were considered. Increasing

the number of iterations by an order of magnitude in general only changed the returned values of ε and μ by 0.3% and 0.01%, respectively. The results of this analysis are presented in section 3.2. Additionally, this Monte Carlo technique was applied to the specific R_f – EM coordinate pairs of all the identified cerean FAE at their measured average local slope (Table 4-2).

While methane clathrate hydrates, which may compose a significant component of the upper layer of Ceres (Fu et al., 2017), display significantly higher material strength than pure water ice at low to modest strain rates (Choukroun et al., 2013), the overall magnitudes of their strengths likely becomes comparable at impact cratering strain rates (Jia et al., 2016). Unfortunately, the range of the coefficient of sliding friction for methane clathrate is poorly understood, as is the effect of clathrate dissociation during deformation on the runout efficiency of FAE (Durham et al., 2003). Thus, it remains unclear from the results of this model if and how methane clathrates contribute to the strength and frictional properties of the cerean near-surface.

4.3 Results

4.3.1 The Geospatial and Mobility Distributions of Cerean Fluidized Ejecta

In total 30 individual cerean ejecta blankets were found to exhibit morphologies suggestive of fluidization. These cerean FAE craters were observed between absolute latitudes of 70°. While FAE forming craters are generally distributed uniformly in this latitude range, they display a slight affinity for the mid latitudes on the southern hemisphere (Figure 4-7). This is especially true of the 19 cuspate/lobate FAE, which show a moderately peaked distribution centered over the southern mid latitudes, while displaying decreased abundance in the northern hemisphere. The 11 channelized FAE display a much more uniform distribution at absolute latitudes below ~50°, despite their slight preference for the northern hemisphere, but quickly

become sparser at higher latitudes. The FAE on Ceres do not display any systematic trends with longitude, nor are any preferred flow orientations observed with varying geographic location.

In order to compare the cerean FAE to each other as objectively as possible, the observed EM value of each instance of FAE was corrected to an effective EM value with a regional slope of $\varphi = 7.5^{\circ}$, the average regional slope away from the source crater rim for all measured FAE craters. This was done using Eq. 3, the average regional slopes for each instance of FAE measured from the DTM using the mapped polygons (e.g. Figure 4-2), and the $\varepsilon - \mu$ pairs for each FAE deposit determined from section 3.2. The full range of observed EM values among cerean FAE is 0.58 – 3.71, while the full slope corrected range is 0.58 – 4.9. Attributes of the cerean FAE craters are displayed in Table 4-2.

The latitudinal locations of each class of cerean FAE as a function of their mobility, and the distribution of their observed and slope corrected EM values are shown in Figure 4-8. Subfigures 4-8a and 4-8b show the latitudinal locations and KDE derived distributions for the observed EM values of the FAE. These plots show both a qualitative and quantitative difference in the observed EM behavior between the channelized and cuspate/lobate FAE populations on Ceres. From Figure 4-8b it is clear that both distributions are broadly Gaussian, but with significantly different widths. In the uncorrected data the channelized FAE appear to have generally higher mobilities than their cuspate/lobate counterparts with distributions peaked at EM values of approximately 2.3 and 0.9, respectively. Subfigures 4-8c and 4-8d show a recapitulation of 8a and 8b, but with all the FAE's EM values corrected to a uniform substrate slope angle of 7.5°. While both the channelized and cuspate/lobate FAE's slope corrected distributions in Figure 4-8d retain their broadly Gaussian shape, their separation is significantly reduced. The corrected channelized FAE distribution's peak is reduced to EM $\approx$ 1.4, while the

corrected cuspate/lobate FAE peak is increased to EM ≈ 1.1. Additionally, larger slope corrected EM values appear to correlate with higher latitudes (Figure 4-8c); however, this conclusion is based on only six data points. These FAE are also distinguishable as the six outlying EM data in Figure 4-8d.

4.3.2 Ejecta Emplacement Modeling

Figure 4-9 displays the slope corrected EM values for both populations of FAE superimposed on to the $\varepsilon - \mu$ parameter maps returned by the Monte Carlo-style analysis using the ejecta emplacement model. Specifically, the parameter spaces in this figure are constructed from the model generated ε and μ grids (see Supplementary Datasets S1 and S2). These grids were cubically interpolated to form continuous parameter spaces that were then discretized into the color ranges displayed in Figure 4-9 for ease of interpretation.

Inspecting Figure 4-9a, it is clear that the dependence of EM on ε is weak for FAE whose EM and source crater radii exceed one and 10,000 m, respectively. Additionally, the blotted texture of Figure 4-9a suggests that the variance in the expected value of ε for a given R_f – EM coordinate pair is significant. In comparison, Figure 4-9b reveals a strong dependence of EM on μ. This is especially true for EM values less than 3. There is also no indication that there is significant variance in the expected values of μ from this figure. The full range of both ε and μ for the channelized and cuspate/lobate FAE, as well the model mean variances of these parameters are summarized in Table 4-3. A 2-dimensional KDE analysis of the model derived ε and μ values for each population of cerean FAE is shown in Figure 4-10.

Parameter	Symbol	Value
Crater collapse constant	κ	1.19 (Ice at 150 K: Kraus et al., 2011) 1.0 (competent rock: Holsapple, 1993)
Crater collapse power	η	0.04 (Ice at 150 K: Kraus et al., 2011) 0.079 (competent rock: Holsapple, 1993)
Crater scaling constant	C_d	2.5 (Ice at 150 K: Kraus et al., 2011) 1.6 (competent rock: Melosh, 1989)
Crater scaling power	β	0.16 (Ice at 150 K: Kraus et al., 2011) 0.22 (competent rock: Melosh, 1989)
Coefficient of sliding friction	μ	0.01 - 0.8
Ejecta scaling power	λ	6 (Richardson et al., 2005)
Excavation angle	θ	70° (Senft & Stewart, 2008)
Gravitational constant	G	$6.674 \cdot 10^{-10}$ $m^3/(kg \cdot s^2)$
Impactor density	ρ_p	920 kg/m^3 (ice) 2800 kg/m^3 (CV chondrite: Consolmagno et al., 2008)
Impact speed	U	5.1 km/s (Ceres: Marchi et al., 2016)
Simple-complex transition radius	R^*	5.15 km (Ceres: Hiesinger et al., 2016)
Surface gravity	g	0.28 m/s^2 (Ceres)
Target density	ρ_t	1290 kg/m^3 (Ceres: Ermakov et al., 2017)
Target porosity	γ	0.0 - 0.6
Target strength parameter	ε	1.8 (rock: Melosh, 1989; Weiss & Head, 2014) 2.6 (ice: Melosh, 1989; Weiss & Head, 2014)
Target temperature	T	150 K (Hayne & Ahronson, 2015)

Table 4-1. Sliding Ejecta Emplacement Model Parameters. The parameters are listed alphabetically.

Longitude	Latitude	Observed crater radius (m)	Observed EM (R_e/R_f)	Mean regional slope (degrees)	Model derived ε	Model derived μ	EM values corrected to 7.5° mean slope	FAE type	Crater Name
-104.22	-66.37	22410	0.59	4.83	2.19	0.25	0.94	cuspate/lobate	Sekhet
-131.06	-6.54	17220	0.68	8.89	2.21	0.38	0.58	cuspate/lobate	Lociyo
21.07	-10.00	9070	0.68	6.70	2.26	0.41	0.73	cuspate/lobate	Unnamed
124.49	18.31	16730	0.73	7.12	2.23	0.31	0.77	cuspate/lobate	Kokopelli
-107.64	59.22	27290	0.77	5.91	2.21	0.23	1.11	cuspate/lobate	Datan
-72.72	45.37	12090	0.85	11.43	2.22	0.44	0.59	cuspate/lobate	Cozobi
17.29	-19.27	22050	0.90	6.75	2.23	0.24	1.05	cuspate/lobate	Kondos
97.66	23.43	18100	0.90	8.48	2.22	0.30	0.78	cuspate/lobate	Aristaeus
77.49	-67.29	9470	0.92	5.05	2.23	0.25	1.36	cuspate/lobate	Ratumaibulu
168.44	-35.88	11640	0.97	7.99	2.23	0.31	0.91	channelized	Juling
110.82	-39.29	11360	1.04	7.42	2.22	0.28	1.05	cuspate/lobate	Unnamed
-158.41	-54.39	16720	1.07	7.58	2.21	0.25	1.06	cuspate/lobate	Unnamed
-81.57	-34.76	4860	1.12	6.06	2.24	0.28	1.35	cuspate/lobate	Unnamed
46.04	-47.94	32340	1.15	5.40	2.22	0.17	2.78	cuspate/lobate	Sintana
-87.68	-54.06	12000	1.35	6.95	2.22	0.22	1.53	cuspate/lobate	Nunghui
-160.93	-11.39	7550	1.39	6.52	2.22	0.23	1.69	cuspate/lobate	Unnamed
88.38	-32.37	18350	1.41	7.85	2.22	0.23	1.29	channelized	Tupo
-93.93	-34.28	8610	1.58	8.38	2.24	0.25	1.34	cuspate/lobate	Unnamed
-0.24	42.01	6060	1.59	7.71	2.22	0.25	1.53	channelized	Oxo
-49.40	0.67	4170	1.63	9.23	2.23	0.30	1.29	channelized	Xevioso
-59.80	-42.35	10040	1.70	4.97	2.25	0.16	4.93	cuspate/lobate	Besua
-141.64	-6.71	23920	1.90	9.01	2.20	0.22	1.22	channelized	Azacca
2.31	-69.23	14820	2.02	6.04	2.20	0.16	4.07	cuspate/lobate	Jacheongbi
28.08	69.01	14060	2.31	7.06	2.18	0.18	2.77	channelized	Shennong
-107.88	63.09	9710	2.39	8.00	2.21	0.20	2.06	channelized	Unnamed
45.62	33.75	27070	2.52	7.98	2.25	0.18	2.04	channelized	Ikapati
-120.67	19.81	46060	2.58	8.83	2.21	0.19	1.40	channelized	Occator
173.19	-39.39	15750	2.63	8.95	2.23	0.21	1.63	channelized	Kupalo
-154.56	7.74	2310	2.74	10.30	2.21	0.27	1.70	cuspate/lobate	Unnamed
10.82	5.73	16100	3.71	9.31	2.22	0.20	1.81	channelized	Haulani

Table 4-2. Measured and model derived properties of the 30 identified cerean FAE. The FAE craters are listed in ascending order according to observed EM value. The slope corrected EM values were generated using Eq. 3, the model derived ε and μ values, observed crater properties, and a prescribed regional of 7.5° radially away from the source craters.

FAE class	ε range	Mean model variance of ε (σ^2)	μ range	Mean model variance of μ (σ^2)
Channelized FAE	2.18 - 2.25	0.052	0.176 - 0.305	$1.3 \cdot 10^{-5}$
Cuspate/lobate FAE	2.19 - 2.26	0.052	0.159 - 0.438	$1.3 \cdot 10^{-5}$

Table 4-3. Model derived parameter ranges and variances for ε and μ.

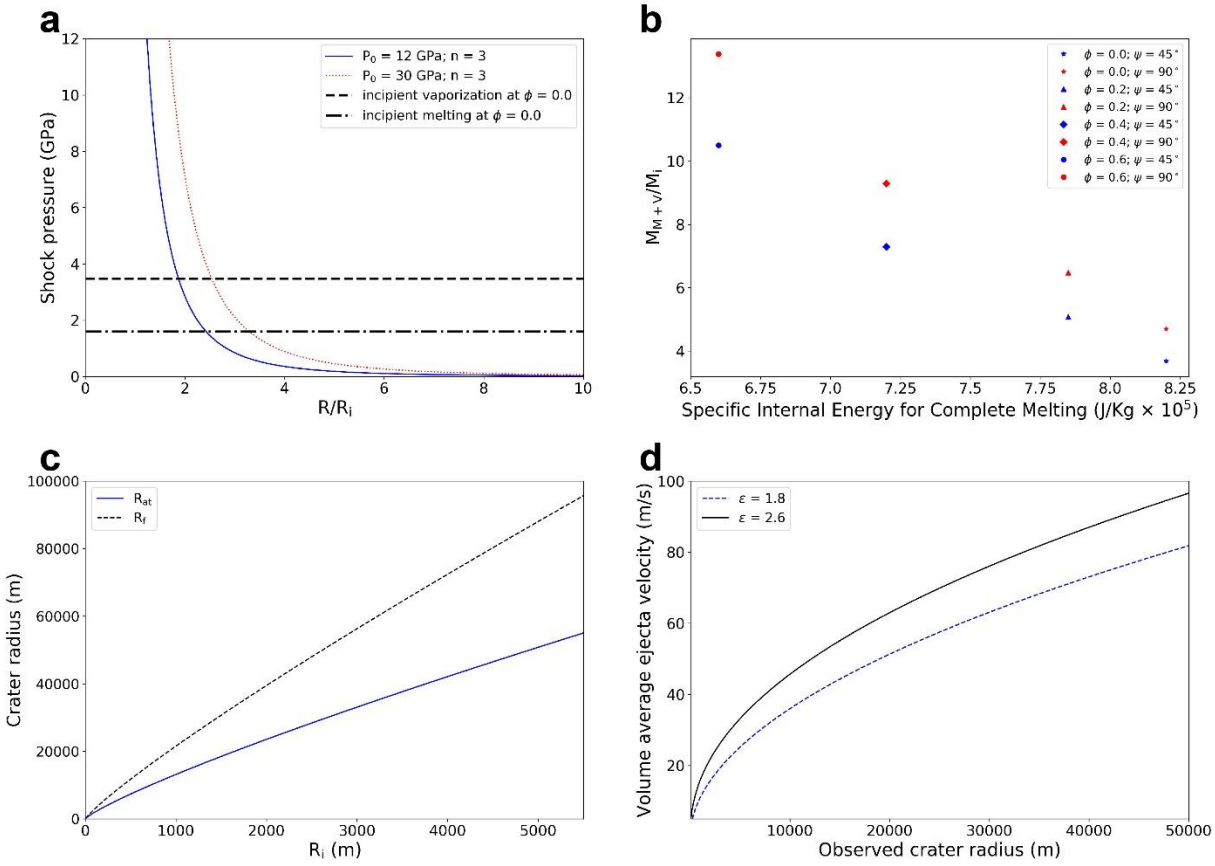

Figure 4-6. (a) Shock pressure as a function of the ratio of the radial distance away from the center of an impact over the impactor radius. The P_0 = 12 GPa curve is calculated for a pure ice impactor (ρ_p = 920 kg/m^3), whereas the 30 GPa curve is calculated for an average CV impactor (ρ_p = 2800 kg/m^3; Consolmagno et al., 2008). The incipient melting and vaporization pressures for water ice at approximate Ceres conditions (ϕ = 0.0 and T = 150 K) are 1.60 GPa and 3.48 GPa, respectively (Kraus et al., 2011). (b) Mass of water ice melted and vaporized relative to the impactor mass as a function of specific internal energy for complete melting using Kraus et al. (2011)'s scaling relationship. In this case the average impact speed at Ceres of 5.1 km/s is used such that the specific internal energy for complete melting is solely a function of porosity. The mass ratios plotted are reduced by a factor of two from Eq. 2 to reflect the departure from the scaling relationship observed at impact speeds less than 8 km/s (Kraus et al., 2011). (c) Final and

apparent transient crater radii as a function of impactor radius; the scaling relationships are taken from Melosh (1989) and Holsapple (1993), while the relevant proportionality constants are taken from Kraus et al. (2011). (d) Magnitude of the volume averaged ejecta launch velocity as a function of final crater radius for the limiting cases of $\varepsilon = 1.8$ and $\varepsilon = 2.6$. The aforementioned values of ε are for competent silicate rock and water ice, respectively.

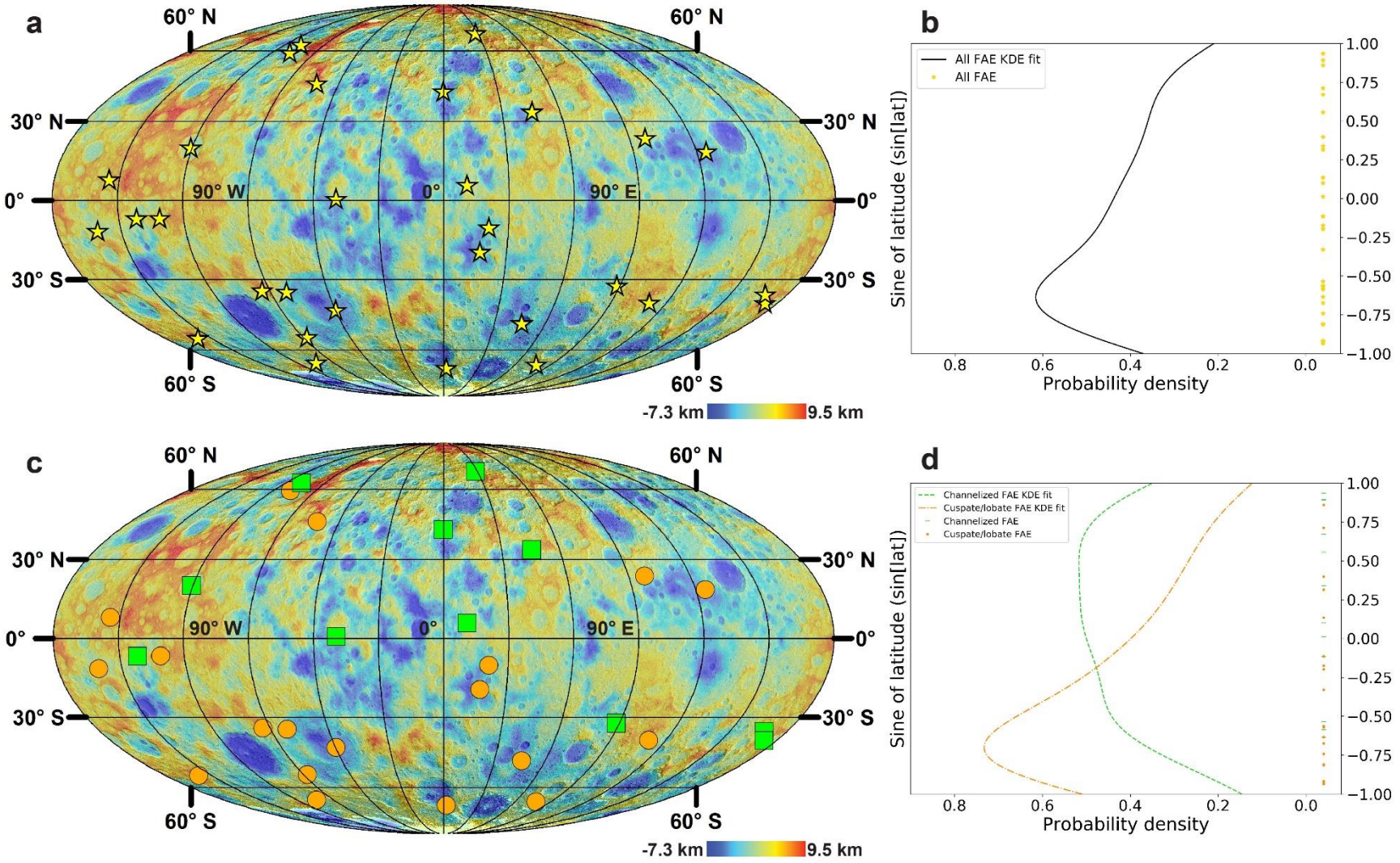

Figure 4-7. Global map and latitudinal distribution estimates for all FAE on Ceres. (a) Prime meridian centered Mollweide projection of Ceres, identified FAE are indicated by gold stars. (b) Normalized KDE latitudinal distribution function for all FAE on Ceres. Note

the peak in the distribution around the southern mid latitudes. (c) Recapitulation of subfigure (a) displaying the cerean FAE subdivided into their channelized (green squares) and cuspate/lobate (orange circles) populations. (d) Normalized KDE latitudinal distribution functions for the channelized and cuspate/lobate FAE populations. Note the preference for southern mid latitudes displayed by the cuspate/lobate FAE, and the more uniform distribution displayed by the channelized FAE. In subfigures (b) and (d) sine of latitude is used to correct for the decrease in area per latitudinal band towards the poles due to Ceres' spherical geometry.

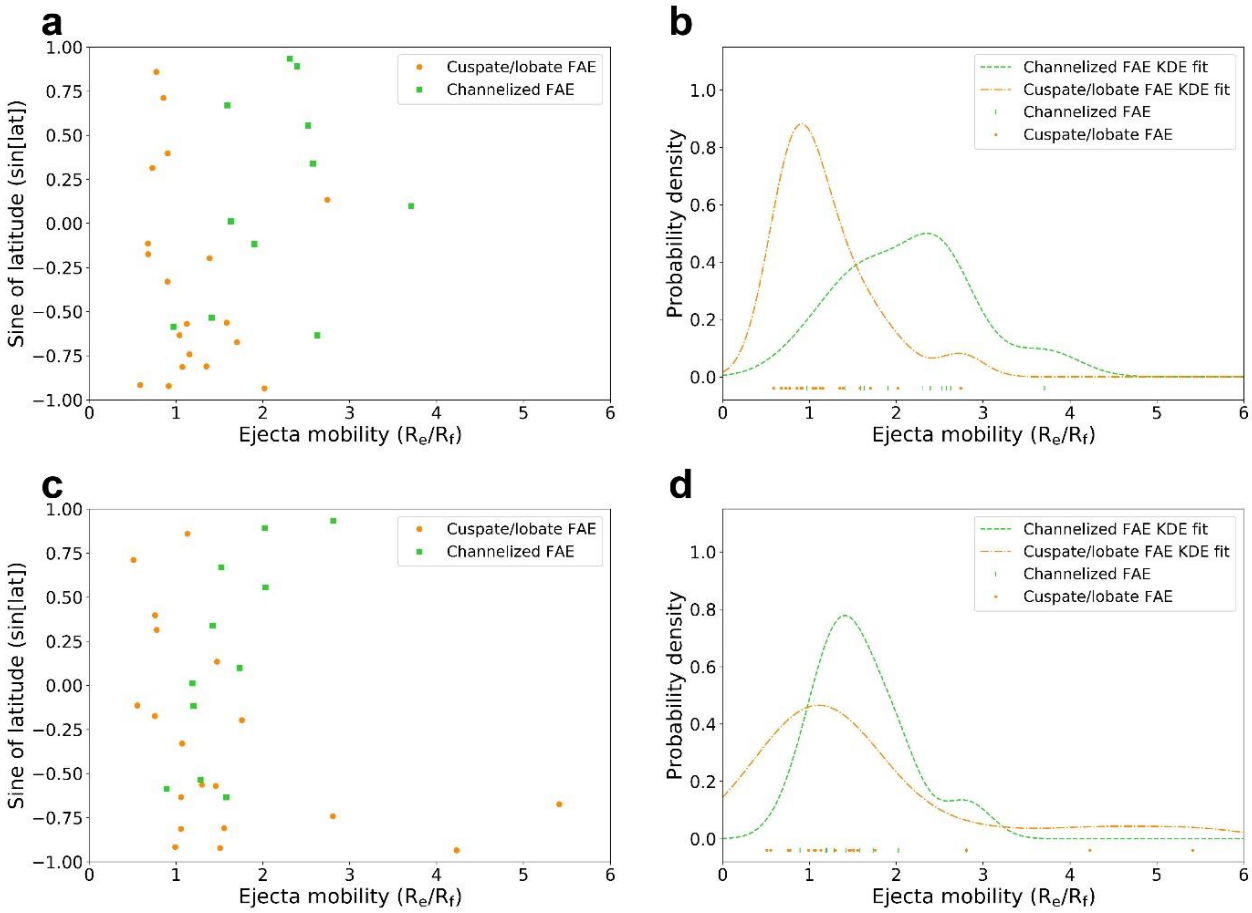

Figure 4-8. (a) Plot of the latitudinal distribution of the cuspate/lobate (orange circles) and channelized (green squares) cerean FAE as a function of their observed (i.e. non-slope corrected) EM values. (b) Normalized KDE analysis of the observed EM distribution functions for the cuspate/lobate and channelized FAE. (c) Plot of the latitudinal distribution of the cuspate/lobate (orange circles) and channelized (green squares) cerean FAE as a function of their 7.5° slope corrected EM values (i.e. the EM value for each FAE was adjusted using the model outlined in section 2.4 as if its mean regional radial slope was 7.5°). (d) Normalized KDE analysis of the slope corrected EM distribution functions for the cuspate/lobate and channelized FAE. Note the slight increase in mobility of FAE at higher latitudes in the slope corrected subfigure (c). The point markers in (b) and (d) indicate the locations of each individual FAE on the EM axis. In

subfigures (a) and (c) sine of latitude is used to correct for the decrease in area per latitudinal band towards the poles due to Ceres' spherical geometry. From subfigures (b) and (d) it can be seen that the process of slope normalization reduces both the systematic differences in EM values between channelized and cuspate/lobate FAE, and narrows the width of each populations' distribution function.

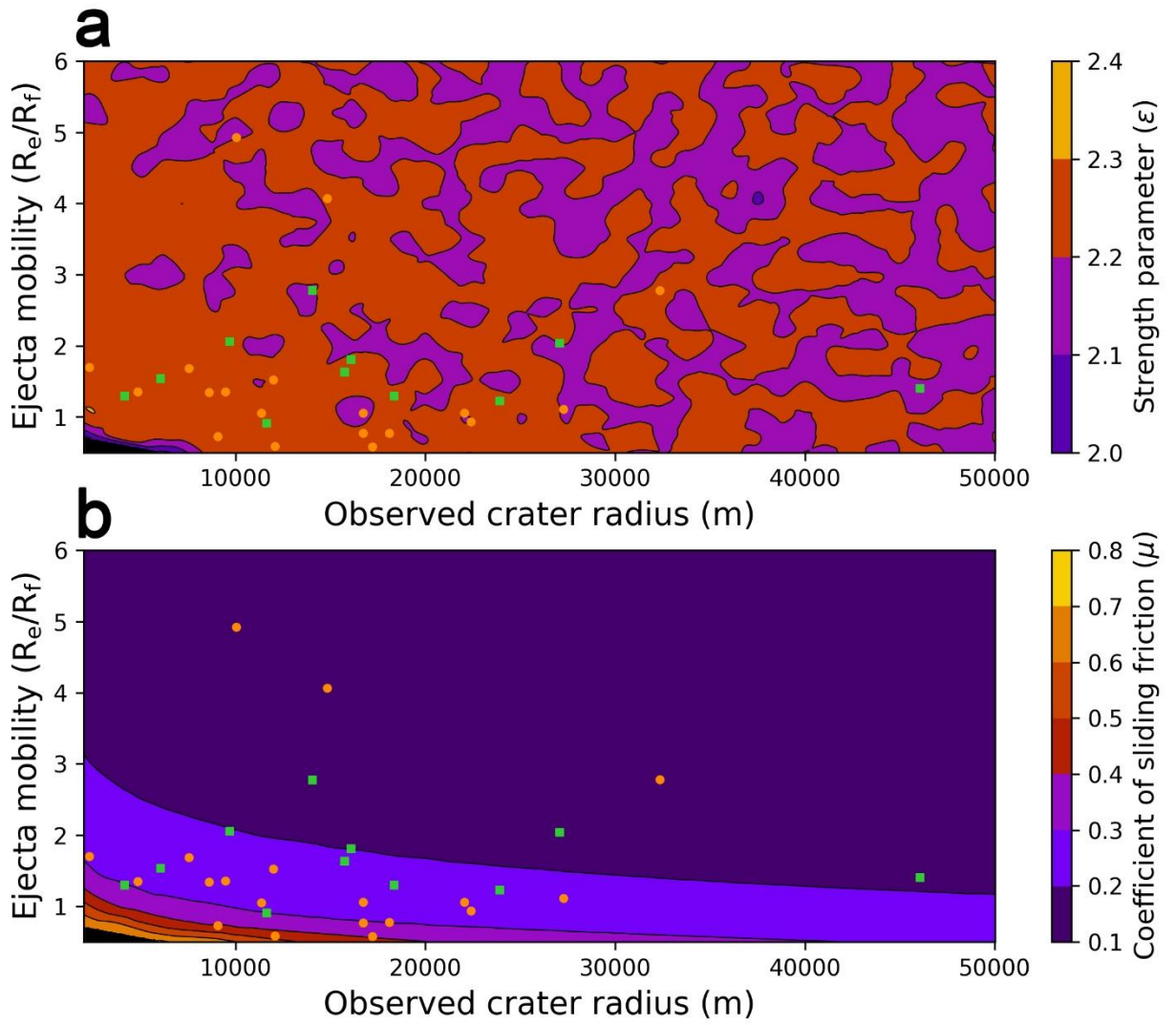

Figure 4-9. Results from the Monte Carlo-style analysis of the sliding ejecta emplacement model for cuspate/lobate (orange circles) and channelized (green squares) FAE. In both (a) and (b) observed final crater radius (R_f) is plotted on the horizontal axis, while slope corrected EM values are plotted against the vertical axis. The color contours in (a) indicate the model predicted values of the strength parameter, ε, as a function of R_f and slope corrected EM. The blotted texture in (a) suggests a weak dependence in the relationship between R_f and corrected EM on ε, and/or high variance in the model derived ε values for a given R_f – EM coordinate pair. (b) displays the model predicted values of the coefficient of sliding friction, μ, as a function of R_f

and slope corrected EM. The close to horizontal behavior of the contours in (b) suggests that μ strongly influences the mobility of cerean FAE. In (b), 80% of the identified FAE have μ less than 0.3. The black triangles in the bottom left of each plot represent parameter space that was not analyzed.

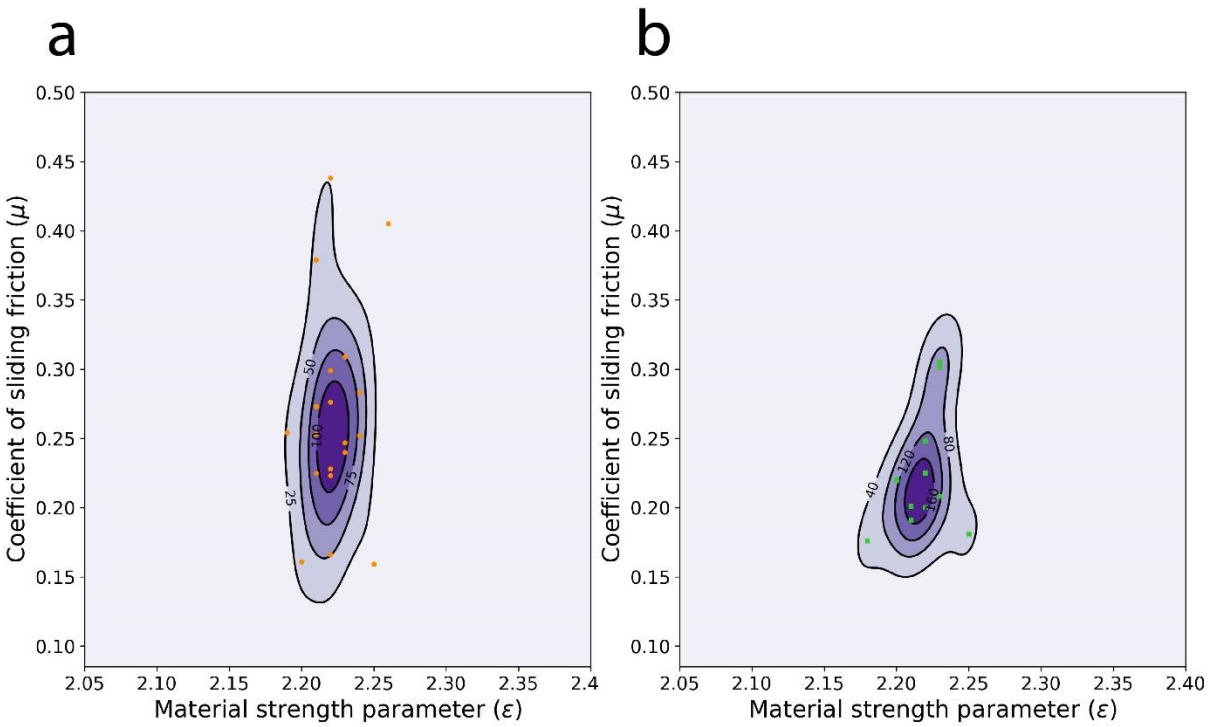

Figure 4-10. 2-Dimensional KDE analysis of the model derived ε and μ values for the cerean FAE. The labeled contour values are the probability density, with the color coding indicating increased probability with darkening color. Subplot (a) shows the cuspate/lobate FAE (orange circle), while (b) displays the channelized FAE (green squares).

4.4 Discussion

4.4.1 Interpretation of the Geospatial and Mobility Distributions of Fluidized Appearing Ejecta

The 30 FAE on Ceres identified in this study represent a substantial increase in described features from Schmidt et al. (2017)'s catalogue of Type 3 flows. This is not surprising given that the identification campaign presented in this study was conducted entirely at LAMO resolution. Additionally, the scope of this search was broadened to include morphological characteristics specific to fluidized ejecta/abruptly terminating ejecta. The two largest craters in the southern hemisphere of Ceres, Urvara and Yalode, as well as Dantu in the northern hemisphere were observed to have morphological elements consistent with the criteria for FAE. However, their characterization proved highly ambiguous due to the size of these craters and their ejecta blankets, their complex and varying morphologies, and their subsequent overprinting by younger impacts. Thus, they were excluded from the list of cerean FAE craters.

Duarte et al. (*Submitted to JGR: Planets*) completed a survey of all lobate deposits on Ceres with characteristics intermediate to the Type 1-3 endmembers discussed by Schmidt et al. (2017). In their analysis they identify a number of Type 3 and intermediate lobate deposits that share morphological similarities with both fluidized ejecta and long runout landslides that are only identified as FAE in this manuscript. While no attempt to characterize landslide behavior associated with FAE is made in this study, it is notable that some of the FAE on Ceres have superimposed layers interior to their main ejecta apron with landslide-like morphologies. These features are similar in form to double layer ejecta (e.g. Figure 4-3), but have much more muted morphologies than their martian counterparts (Weiss & Head, 2013 and 2018). These deposits seldom have well developed head scarps near the outside of their source crater rims, and have similar surface textures to their underlying ejecta layers. This suggests they were formed

contemporaneously with the formation of the FAE source crater, or shortly thereafter as part of the modification stage. The diversity of proximal and co-located landslide-like deposits with FAE on Ceres is consistent with the interpretation that they are mobilized by ground ice (Schmidt et al., 2017; Duarte et al., *Submitted to JGR: Planets*; Chilton et al., 2019).

From the latitudinal KDE analysis in Figure 4-7b it is apparent that the distribution of all cerean FAE is enhanced in the low to mid latitudes of the southern hemisphere. This is broadly consistent with the increased number density of Type 3 flows at low latitudes observed by Schmidt et al. (2017), but differs with respect to hemispherical preference of which they noted none. The subdivided channelized and cuspate/lobate FAE populations exhibit significantly different distributions with respect to latitude (Figures 4-7d); however, given the small number of FAE used in deriving these statistical class-specific distributions, they are not used to draw any specific conclusions. While there is no consistent pattern to how cerean FAE are distributed with respect to both latitude and longitude, these features are slightly clustered around Yalode crater (292.48 °E, 42.58 °S) and the high standing Hanami Planum (230 °E, 15 °N), both of these areas contain an abundance of surface features which indicate the presence of significant quantities of near-surface ground ice (Sizemore et al., 2018). Additionally, cerean FAE seem to be conspicuously absent from the low lying Vendemia Planitia (135 °E, 23 °N), Kerwan smooth material (124 °E, 11 °S), and much of the region composing the Ac-10 Rongo quadrangle (Platz et al., 2018). This supports the interpretation that near-surface ground ice on Ceres is distributed with a significant degree of heterogeneity (Bland et al., 2016, Sizemore et al., 2018).

The apparent association of cerean FAE with geologically fresh appearing morphologies suggests that these features degraded rapidly on the surface after emplacement. This could plausibly be due to disruption and overprinting by subsequent impacts, micrometeorite

bombardment and space weathering, sublimation of excavated volatiles, or any combination thereof. The preferred interpretation for the channelized FAE is that they are deposited with a relatively high abundance of liquid water and water ice that both act as basal lubricants, and reduce dissipative forces internal to the flow itself. Once re-frozen, these pervasively ice rich deposits are highly susceptible to degradation by all of the aforementioned weathering processes. This interpretation is supported by the highly fluid nature, relative paucity, and extremely fresh morphologies of the channelized FAE. With one exception, all of the observed channelized FAE are located in areas where the regional downhill slope exceeds the average cerean circum-crater slope of 7.5°. This behavior is not seen among cuspate/lobate FAE, who are observed to generally favor emplacement on downhill slopes shallower than this average. While this preference for different emplacement angles is largely subtle, it implies that reducing the effective coefficient of sliding friction and/or increasing the amount of expendable gravitational potential energy may favor the production of channelized FAE.

The cuspate/lobate FAE, which are generally more morphologically similar to abruptly terminating ejecta and martian layered ejecta, are interpreted to be deposited predominantly as basal glides whose mobility is primarily governed by the lubricating effects of near-surface ground ice in the region immediately proximal to the FAE forming impact. A consequence of this interpretation is that the flow material itself need not necessarily have a high water content if there exists an ample supply in the near-surface. If cuspate/lobate FAE flows are depleted in water compared to channelized FAE they would be relatively more resistant to volatile-loss driven degradation processes such as deflation and impact induced sublimation. In general, cuspate/lobate FAE are observed in a multitude of degradation states across numerous source craters of varying relative ages, which supports the interpretation that they have a longer

geologic lifetime than channelized FAE. The cuspate/lobate FAE are also observed to generally have qualitatively thicker deposits whose morphology is less frequently modified by preexisting topography relative to channelized FAE. This implies that cuspate/lobate FAE have high effective viscosities relative to their channelized FAE counterparts. This may be caused by increased interparticle friction due to reduced ice content of the material in motion relative to channelized FAE. Additionally, the thicker nature of cuspate/lobate FAE deposits likely helps preferentially preserve them relative to channelized FAE, at least at the resolution used to identify them.

It is important to note that the morphologically based interpretation that channelized FAE have a higher bulk water content relative to cuspate/lobate FAE at the time of their deposition does not necessarily indicate a higher substrate ground ice volume fraction proximal to their source craters. This predicted increase in the water content of channelized FAE may be due to greater incorporation of warm ice or liquid water from infrequent but exceptionally energetic impacts, rather than an increase in the ground ice content of the target materials. Since the mobility of cuspate/lobate FAE is interpreted to be dominated by basal friction, a ground ice rich substrate would still greatly reduce the friction experienced by these relatively drier flows.

4.4.2 Interpretation of the Ejecta Emplacement Model

The results presented in Figure 4-9 show that there is no robust distinction between the channelized and cuspate/lobate FAE populations in R_e – slope corrected EM space. Additionally, there are no robust clusters or families of FAE seen within this space.

It is clear from inspection of Figure 4-9a that for the R_e – slope corrected EM parameter space relevant to cerean FAE their mobility is only weakly dependent on ε. The entire ε mean

range of all forms of cerean FAE is estimated from the model to be $2.18 \leq \varepsilon \leq 2.26$, while the mean model standard deviation (σ) for a given ε is 0.23 (Table 4-3). The mean value of ε for each population is 2.22, which is almost exactly intermediate behavior between competent rock ($\varepsilon = 1.8$) and water ice ($\varepsilon = 2.6$). The weak dependence of the model on ε manifests in the intermediate values and blotted texture of the entire ε parameter space. The intermediate values of the ε parameter space combined with its high variance suggest that a large range of material strengths could lead to similar EM values for a given crater radius and well constrained μ value. Thus, the blotted texture in Figure 4-9a results from statistical noise in the Monte Carlo analysis due to the small amount of control ε exerts on the model derived EM values relative to μ, which is the dominant factor in determining its behavior. From the measurement and deviation of ε alone it is difficult to estimate the ground ice content of the substrate, but it is evident that the substrate near these FAE, under impact cratering strain rates, behaves more mechanically akin to a ground ice rich ice-silicate mixture, and/or an extremely unconsolidated material, than competent rock. This is consistent with the low flexural rigidity reported by Hughson et al. (2019), for the cerean crust near Nar Sulcus, and the low simple-to-complex transition diameter for impact craters observed by Hiesinger et al. (2016), which have been interpreted to make Ceres more mechanically akin to outer solar system icy satellites than terrestrial planets.

Unlike ε, inspection of Figure 4-9b shows a strong correlation between μ and slope corrected EM value. While the lower bounds on the range of μ values are similar for both the channelized and cuspate/lobate FAE, the upper bound μ value for the cuspate/lobate ejecta is significantly higher than its channelized FAE counterpart (see Table 4-3). The mean μ values for the channelized and cuspate/lobate FAE are 0.223 and 0.267, respectively, while the mean model

standard deviation for a given μ is 0.0037. This implies higher amounts of sliding friction are acceptable for the formation of cuspate/lobate FAE compared to the channelized variety.

On Earth, supraglacial landslides typically have effective μ values between 0.015 and 0.2 (Weiss & Head, 2018). While this range is somewhat comparable to cerean FAE, the upper bounds of their effective μ ranges are still larger by approximately a factor of two. This is in part possibly due to the increase in sliding friction coefficient expressed by polycrystalline ice with decreasing temperature. At 263 K, the coefficient for ice-on-ice sliding friction is typically 0.01-0.15 (this value is strongly a function of sliding velocity), whereas at a Ceres appropriate 150 K this value is approximately 0.45 (Schulson & Fortt, 2012; De Blasio, 2014). In contrast, the typical values for the coefficients of sliding friction for common terrestrial silicate materials lie between 0.5 and 0.8 (e.g. Ramana & Gogte, 1989). From the ice-like range of μ values expressed by the cerean FAE in combination with the expectation of a pore saturating ice layer within a few meters of the surface, even at the equator, inferred from nuclear spectroscopy (Prettyman et al., 2017), it is interpreted that the low model derived μ values for the observed FAE are most likely due to a combination of sliding on a ground ice rich substrate and by fluidization due to the incorporation of impact melt fluids and/or basal lubrication due to melted near surface water ice. This is especially likely for the 80% of FAE whose μ values are under 0.3. This is also consistent with the melt/vapor productions volumes estimated from Eq.2 shown in Figure 4-6b, and the morphological interpretations made in section 4.1. Due to a lack of experimental understanding, in formulating the previous interpretation it is assumed that any clathrates present near the surface have similar frictional properties to pure water ice.

Alternatively, some craters on dry airless bodies, such as the Moon's King crater, have ejecta morphologies suggestive of some degree fluidization (Howard, 1972; Heather & Dunkin,

2003), and it has been postulated that lateral sliding of dry ejecta materials from purely ballistic sedimentation could lead to lobate morphologies (Oberbeck, 1975). Strong vibrational motions from the initial impact shock may also help mobilize ejected material via acoustic fluidization (Melosh, 1979). Recent laboratory experiments by Runyon and Barnouin (2018) have further shown that dry ejecta deposited via ballistic sedimentation extensively shears the subsurface, embeds itself within the regolith, and exhumes regolith material via saltation all while sliding along the surface. Runyon and Barnouin (2018) go on to demonstrate that these interactions slightly increase the runout efficiency (which is the reciprocal of the drop height to runout length ratio: H/L) of dry ejecta relative to terrestrial rock avalanches. However, their measured runout efficiency values are broadly Earth-like in the context of mass wasting throughout the solar system. Since the reported runout efficiencies of putative cerean FAE are generally higher than those of comparable terrestrial or martian debris flows (see Chapter 3) the preferred interpretation continues to be that the enhanced mobility of FAE on Ceres is due to ground ice mediated friction reduction.

Using a simple areal mean approximation for the coefficient of sliding friction, similar to the method employed by De Blasio (2014) when analyzing terrestrial rock avalanches travelling on glaciers, an upper bound of ~30-50 vol. % water ice is estimated at a depth scale of at least 1 – 5 km proximal to each FAE source crater (depending on the size of the source crater). This range is derived from linearly mixing the μ value of ice, which is taken to be of order 0.01 at ejecta emplacement velocities, with μ values for common silicate materials, which are taken to be between ~0.5-0.8. The mixing model is constrained by the mean μ values derived for both classes of cerean FAE, and the resulting fractional contribution of water ice to the overall coefficient of sliding friction is taken to be representative of its volumetric abundance in the

near-surface. This estimate is broadly consistent with the composition suggested by Fu et al. (2017); however, accurately including the effects of melt water lubrication would certainly reduce this estimate. It remains ambiguous as to whether this estimated near-surface ground ice content is ubiquitously true across Ceres, or if it only applies selectively to heterogeneous regions of enhanced ground ice content, but the slight affinities and aversions for certain geographical regions combined with the variable range of model estimated μ values displayed by cerean FAE suggest that the latter is more representative of reality. This possibility was first postulated by Bland et al. (2016) to explain the radically different relaxation states of similar craters on Ceres. The physical properties and geographic distribution of FAE are interpreted to be indicative of a modest global reservoir of pore filling ground ice in the upper few meters to kilometers on Ceres, which is subject to significant regional enrichment and depletion.

An underlying assumption in this model is that the volume averaged ejecta is effectively excavated at an angle of 70° from the pre-impact surface (Senft & Stewart, 2008). This assumption is considered appropriate for the bulk properties of ejecta sourced within 80% of R_{at}, which the volume averaged ejecta well approximates, for impacts into a substrate rich in buried water ice (Senft & Stewart, 2008). This is likely the case on Ceres. Nevertheless, accurately accounting for the effects of changing excavation angle, particularly how it decreases with increasing R_{at}, by incorporating numerical impact simulations for potential Ceres-like substrates would further increase the fidelity of this model.

4.5 Conclusions

Thirty instances of FAE were identified on Ceres that display morphological elements (such as a sheeted or layered appearance, arcuate or cuspate terminal lobes, superimposed longitudinal grooves, and channelized deposits) commonly associated with fluidization. Two

distinct morphological populations of FAE were identified: a channelized FAE population, and a cuspate/lobate population. While both of these FAE types are distinctly cerean, the channelized FAE display morphological characteristics common among fluid rich debris flows, and the cuspate/lobate FAE share many morphological similarities with layered ejecta craters on Mars, Ganymede, Dione, and Charon. After mapping and quantifying the identified FAE a detailed investigation for trends in their geographical and EM distributions was conducted. Additionally, the hypothesis that the morphologies and various EM values of cerean FAE can be explained by a combination of impacting into a low-cohesion target material, and sliding on a low-friction partially icy substrate was explored using a hybrid kinematic-dynamic ejecta emplacement model. These investigations show that:

1. Two morphological classes of FAE exist on Ceres: channelized, and cuspate/lobate. Both the channelized and cuspate/lobate cerean FAE have similarly distributed slope corrected EM values, with distributions peaked at EM = 1.4 and EM = 1.1 respectively. Despite their distinctive physical appearances, both channelized and cuspate/lobate FAE have similar model derived ε and μ values.

2. FAE on Ceres are abundant at absolute latitudes less than 70°, above which their density rapidly decreases. The cuspate/lobate FAE display a slight affinity for the mid latitudes on the southern hemisphere. The channelized FAE display a more uniform distribution with respect to latitude.

3. The low model derived μ values for the majority of cerean FAE are likely due to a combination of sliding on an intimate mixture of rock and ice, and by friction reduction caused by both fluidization through the incorporation of impact melt fluids and basal lubrication via melted near surface volatiles.

4. The vast majority of FAE source craters are modeled to have material strengths that are more ice-like than rock-like under impact cratering strain rates. This is consistent with previous observations of the low simple-to-complex transition diameter, and the reported low flexural rigidity of Ceres. This aligns Ceres more closely with icy satellites than terrestrial planets with respect to the mechanical properties of its outermost layer.

5. The widespread distribution of FAE in combination with results from nuclear spectroscopy suggest that pore filling ground ice is present only a few meters below the surface to at least 1 – 5 km based on crater ejecta excavation depths.

The sliding ejecta emplacement model, despite its usefulness as a simple preliminary investigation tool, would be improved by higher fidelity constraints on the material strength and frictional properties of the shallow subsurface/surface. Laboratory experiments that better constrain these properties in Ceres regolith analogues would allow the model to better predict the composition of the near-surface of Ceres.

The identification and modeling of FAE on Ceres further cement its position as a volatile rich and geologically interesting world. The association of cerean FAE with weak, volatile rich material makes them of particular interest for future *in situ* exploration of Ceres, and further suggests that the geologic history of the cerean near-surface was significantly influenced by both physical and chemical water-rock interactions.

5 Normal Faults on Ceres: Insights into the Mechanical Properties and Thermal History of Nar Sulcus

5.1 Identification and Observations of Nar Sulcus

Upon arriving at the dwarf planet Ceres, Dawn discovered an intensely fractured region near its southern pole now named Nar Sulcus (Crown et al., 2018). The Nar Sulcus fractures (Figures 5-1 and 5-2), which are centrally located at 280.11 °E, 41.86 °S within the Yalode impact crater (Figure 5-3), display morphologies similar to those of imbricated listric normal faults on the Earth. These characteristics manifest as asymmetric fault block slopes, and systematic increases in scarp steepness from regionally low to high topography. They also have topographic profiles suggestive of elastic flexure, with characteristic flanking bulges and depressions. Modeling the shape of elastically flexed topography allows for the estimation of the elastic thickness of the mechanical layer being faulted. When this elastic thickness is combined with an assumed strength profile and a range of strain rates, the mechanical thickness and heat flux present at the site of the newly formed topography can be estimated. Estimates of these parameters through the analysis of flexurally supported topography have previously been done on the Earth (e.g. Weissel & Karner, 1989; Kusznir et al., 1991; Lowry & Smith, 1994), Venus, (e.g. O'Rourke & Smrekar, 2018), Mars (e.g. Grott et al., 2005; Ruiz et al., 2006), Ganymede (Nimmo et al., 2002; Nimmo & Pappalardo, 2004), Europa (Ruiz, 2005; Nimmo & Schenk, 2006), Tethys (Giese et al., 2007), and Enceladus (Giese et al., 2008). Despite a plethora of evidence suggesting Ceres' upper layer is rich in water ice (e.g. Buczkowski et al., 2016; Combe et al., 2016; Combe et al., 2019; Fu et al., 2017; Hughson et al., 2018; Prettyman et al., 2017; Schmidt et al., 2017; Sizemore et al., 2017; Sizemore et al., 2018; and Chapters 3 and 4 of this dissertation), the exact concentration and distribution of this material throughout its crust

remains enigmatic. Flexural analysis of Nar Sulcus presents a unique opportunity to better understand the role of water ice on the surface geology of Ceres, at least locally to this distinctive landform.

Unlike the previous two chapters that focused on different forms of surface flows present on Ceres, this chapter presents new material constraints on the upper mechanical layer of Ceres proximal to Nar Sulcus by examining instances of elastically supported topography. In this investigation, stereophotogrammetrically derived elevation models (Roatsch et al., 2016c) are used to identify two sets of possible normal faults on Ceres, analyze them for topography that is flexurally supported, and use that topography to obtain estimates of the effective elastic thickness and surface heat flux range proximal to Nar Sulcus at the time of their formation. In order to better constrain the role of ice in the upper layer of Ceres this exercise is repeated at strengths and rheologies approximating ice-rock mixtures with 0, 30, and 56 volume percent rock. Additionally, estimates for the time at which these parameter approximations are valid are generated by applying a Buffered Crater Counting (BCC) analysis (Fassett & Head, 2008; Kneissl 2015), which is specifically designed to derive crater-based absolute model ages of narrow linear features.

5.1.1 Geology and Geologic Setting

Nar Sulcus was extensively imaged by Dawn's framing cameras throughout its mission at resolutions as fine as ~35 m/pixel. This region consists of two mutually perpendicular sets of fractures located just north of a large (~2 km tall) tholus (Figure 5-3). The larger of these sets trends approximately east-west, is ~50 km long, and ~10 km wide. The smaller set trends approximately south-north, is ~15 km long, and ~10 km wide. The genetic relationships of these sets to each other and the underlying tholus represent outstanding science questions that are

beyond the scope of this dissertation. Stereo-topography (Roatsch et al., 2016c) revealed the major fractures in both sets to have characteristic vertical displacements (throws) between 400-550 m, horizontal displacements (heaves) between 800-1,000 m (estimated using a fixed fault dip at depth method further discussed in section 5.2), and spacings of ~1.5-2 km. The morphology of these well-defined sets of sub-parallel ridges and troughs are consistent with an origin due to extensional faulting. The consistent concave down shape of the downthrown fault blocks, and concave up shape of the upthrown fault blocks further suggests flexurally supported topography (Giese et al., 2007; 2008).

5.1.2 Chronology

Previous studies reported a model age of 580 Ma for Yalode ejecta, and 420 Ma for the Urvara/Yalode smooth material unit which hosts Nar Sulcus, using a lunar-like impact chronology (Crown et al., 2018). However, this smooth material may have a model age as young as 190 Ma (Crown et al., 2018). In this investigation, a BCC analysis of Nar Sulcus and its surrounding terrain was conducted for craters with diameters ≥200 m using both a Lunar Derived and Asteroid Derived chronology model (Hiesinger et al., 2016) in order to establish their chronostratigraphic relationship (Figure 5-4). The derived model age ranges for Nar Sulcus and the background material are 98-173 Ma and 165-478 Ma, respectively. This analysis determined that Nar Sulcus is temporally distinct from its immediate surroundings, and is considerably younger than Yalode; however, the temporal relationship between the two perpendicular fracture sets proved unresolvable.

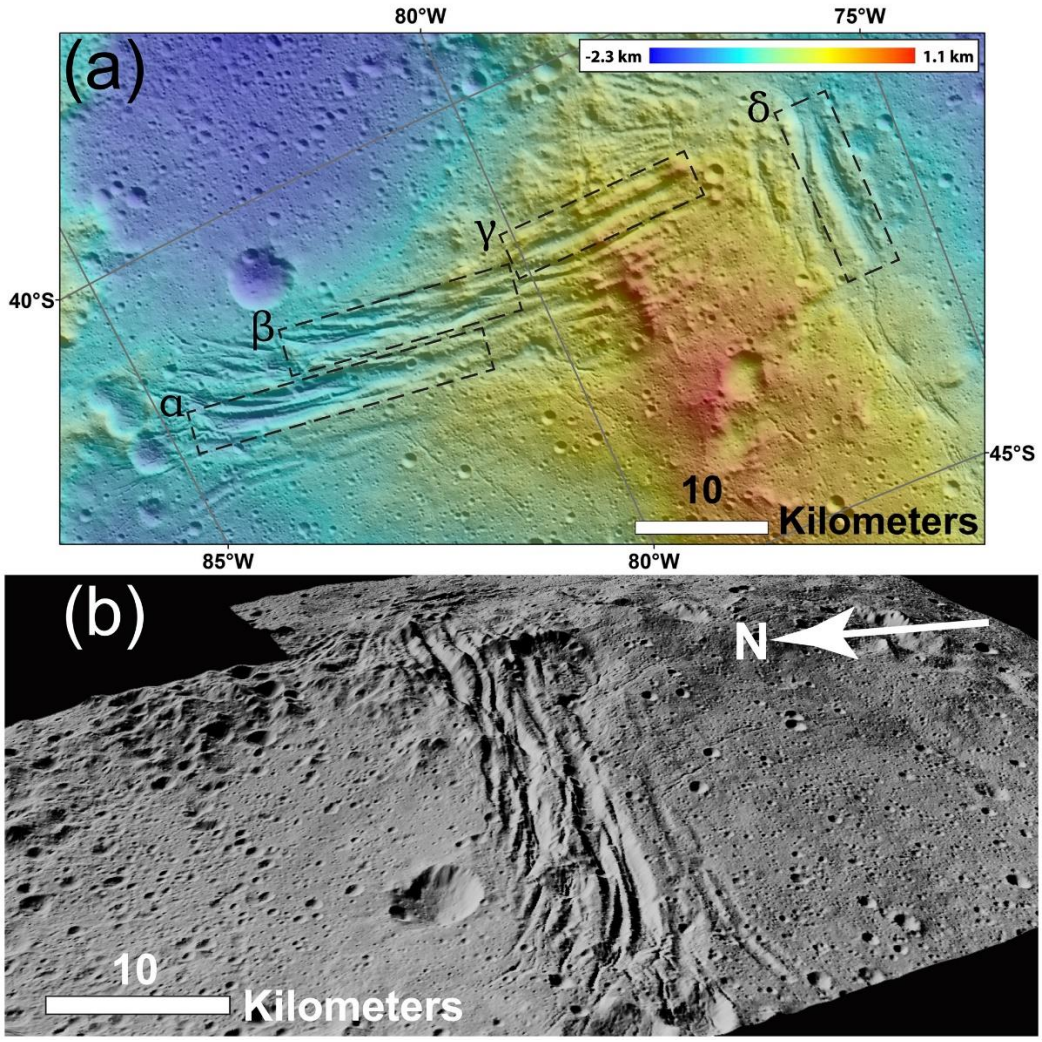

Figure 5-1. (a) Plan view of the Nar Sulcus fractures (from the Ceres Low Altitude Mapping Orbit Clear Filter Mosaic, resolution ~35 m/pixel; Roatsch et al., 2016b) overlain by color-coded stereo-topography relative to the 482 km by 446 km oblate best-fit bi-axial ellipsoid (vertical accuracy <10 m). The dashed boxes indicate the largest faults examined in this study. These valleys were unofficially named α, β, γ, and δ valles. Stacked topographic profiles for each valley were created from transects spaced 1 km apart oriented perpendicular to the long axis of each rectangle (see supplementary material for more information). (b) Perspective view of the largest faulted set at Nar Sulcus from the west looking east. The vertical exaggeration in this view is a factor of 1.5.

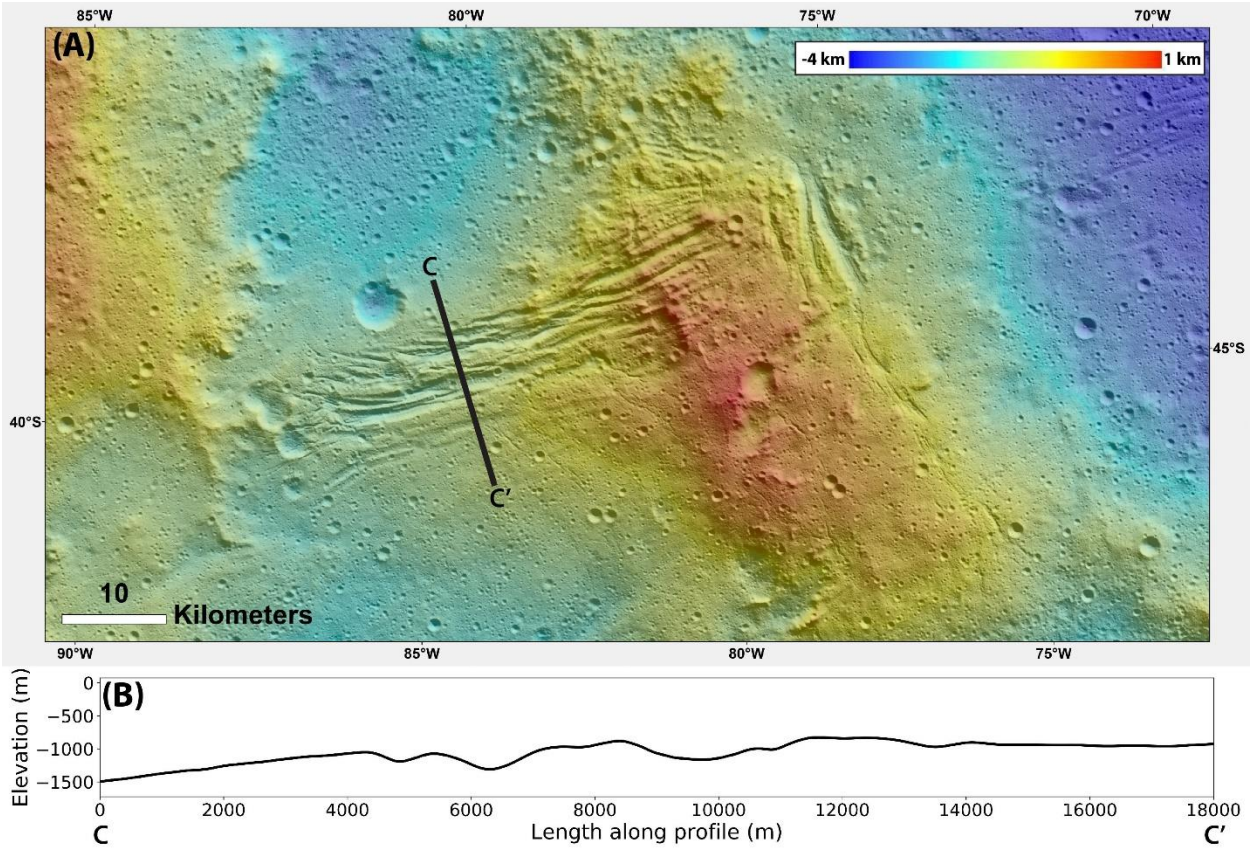

Figure 5-2. Representative topography across the primary fracture set at Nar Sulcus. Panel (a) is a plan view image of Nar Sulcus expanded from Figure 5-1a. Panel (b) displays a non-exaggerated topographic profile across β valles (located at ~6000 m) and the eastward margin of α valles (located at ~10,000 m).

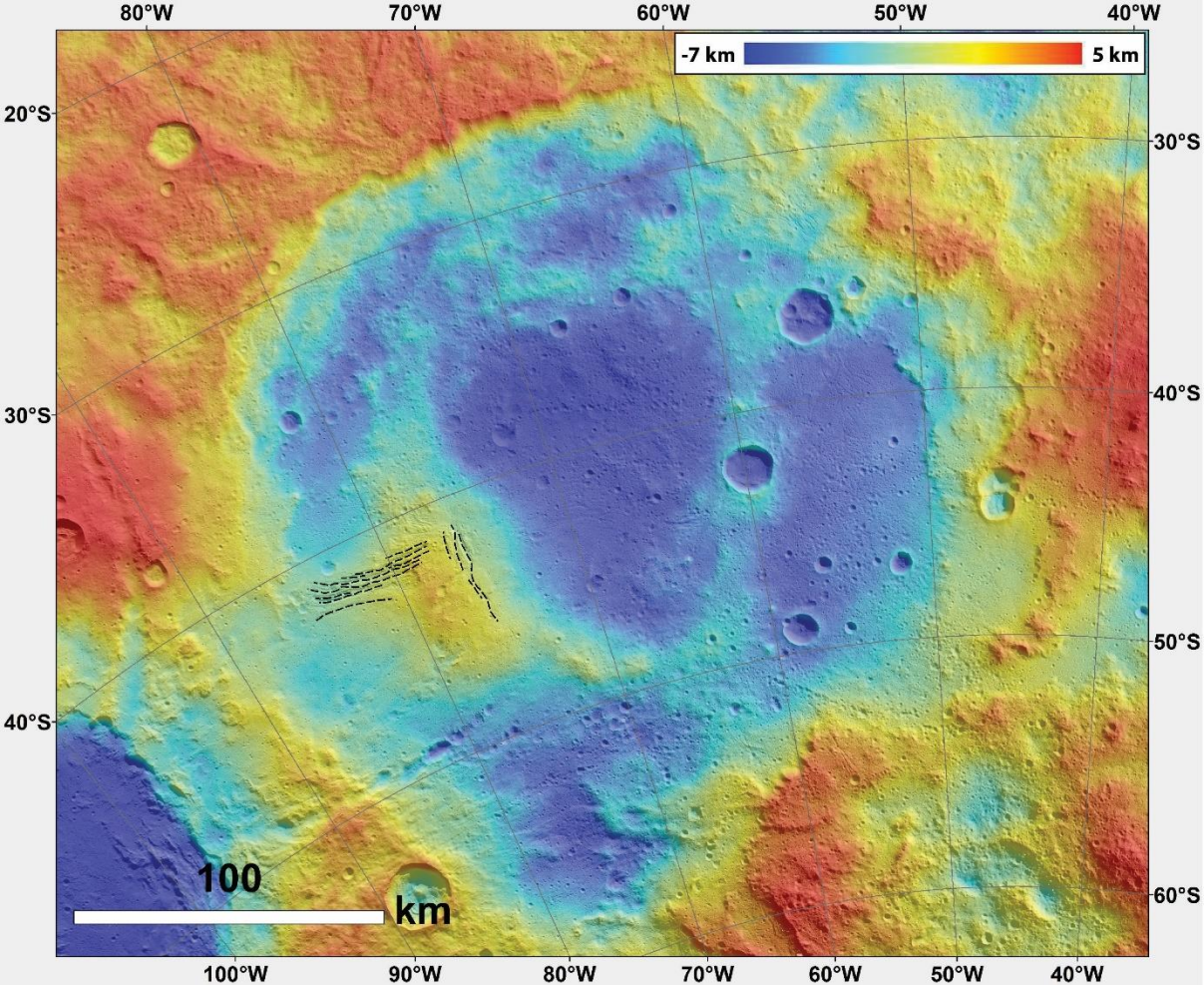

Figure 5-3. Further geologic context for Nar Sulcus. The large circular depression that occupies the majority of the image is the ~260 km diameter Yalode impact crater, which is the second largest confirmed impact structure on Ceres. Prominent fractures within Nar Sulcus are indicated by dashed black lines. Note the prominent elliptical tholus located coincidentally, and due south of, Nar Sulcus. While this tholus is clearly a unique structure within Yalode, it also appears to be co-located with an elevated, quasi-peak ring structure that sits within the crater.

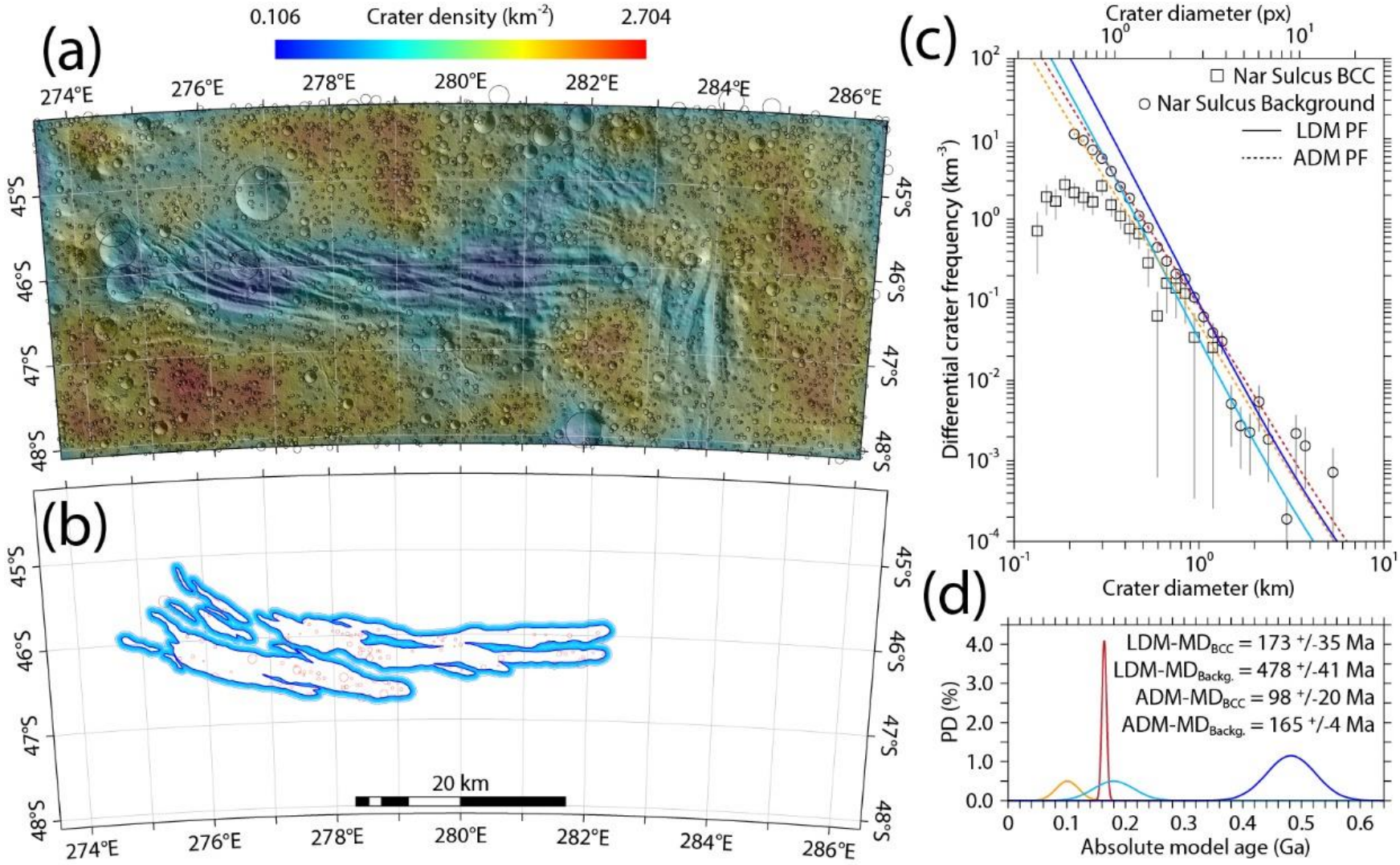

Figure 5-4. BCC analysis of Nar Sulcus and its immediate surroundings. (a) Identified craters and color-coded spatial crater density. (b) Count area (dark blue) and craters (red) used in the BCC analysis. Bright blue lines represent the calculated buffers used in

the BCC analysis. The remaining area beyond the outer buffer was used for extracting the differential crater size-frequency distribution (CSFD) of the background. (c) Differential CSFD of Nar Sulcus and the surrounding terrain plotted alongside the Lunar Derived chronology model (LDM) and asteroid derived chronology model (ADM) production functions (PF). The PFs represent the Poisson-calculated (Michael et al. 2016) median absolute model ages. The solid blue and dashed red curves are the fits to the background CSFD. The solid cyan and dashed yellow curves are the fits to the Nar Sulcus CSFD. (d) Probability density functions for the age of the Nar Sulcus (BCC) and background (Backg.) CSFDs for both the LDM and ADM. Values in the key represent the median absolute model ages (MD) and their +/-34 percentiles. The cyan, blue, yellow, and red curves correspond to the LDM_{BCC}, $LDM_{Backg.}$, ADM_{BCC}, and $ADM_{Backg.}$ age probability distributions, respectively.

5.2 Methodology

Estimates of the elastic thickness, T_e, for the upper mechanical layer proximal to Nar Sulcus are generated by applying a single layer flexural cantilever model similar to the one developed by Kusznir et al. (1991) to stacked topographic profiles of the four largest fault-bound valleys in Nar Sulcus (see Figure 5-1a for context). The details of this model are described below.

In the flexural cantilever model used to investigate Nar Sulcus, a planar normal fault places an asymmetric load on the elastic layer in question, which responds flexurally in accordance with the equations (2, 3, 4, and 5) for a thin elastic plate (e.g. Nadai, 1963; Lambeck, 1983).

The initial surface elevation profile, $u(x)$, of the fault as a function of the horizontal coordinate is given by:

$$u(x) = \begin{cases} \frac{-H \cdot \tan\theta}{2}, & x \leq \frac{-H}{2} \\ x \cdot \tan\theta, & \frac{-H}{2} < x < \frac{H}{2} \\ \frac{H \cdot \tan\theta}{2}, & x \geq \frac{H}{2} \end{cases} \quad (1)$$

where H is the observed heave and θ is the fault dip angle. Following Kusznir et al. (1991), the vertical deflection of the elastic plate, $w(x)$, is given by Eq. 2

$$D \cdot \frac{d^4 w(x)}{dx^4} + \rho_c \cdot g \cdot w(x) = l_b(x) \quad (2)$$

where ρ_c is the average crustal density of Ceres, g is its surface gravity, D is the flexural rigidity as described by Eq. 6. The right hand side of Eq. 2 is the buoyancy force, which is described by Eq. 3.

$$l_b(x) = -\rho_c \cdot g \cdot u(x) \quad (3)$$

The flexural uplift $w(x)$ is then computed in the wavenumber domain by

$$W(k) = \frac{1}{\rho_c \cdot g + D \cdot k^4} \cdot L_b(k) \quad (4)$$

where $W(k)$ and $L_b(k)$ are the Fourier transforms of $w(x)$ and $l_b(x)$ respectively. The resultant surface topography is given by $s(x)$, and is schematically summarized in Figure 5-5.

$$s(x) = u(x) + w(x) \quad (5)$$

T_e at Nar Sulcus is inferred from model derived values of the flexural rigidity (D), and from imposed values of the material's Young's modulus (E), and Poisson's ratio (υ). The relationship between these material properties is given by Eq. 6 (Nadai, 1963).

$$D = \frac{E \cdot T_e^3}{12 \cdot (1 - \nu^2)} \quad (6)$$

The heat flux and mechanical thickness, T_m, of the surface near Nar Sulcus was estimated by implementing McNutt's (1984) model of the vertical structure of the lithosphere. In this formalism strain is accommodated through brittle sliding in an upper fractured layer, through flexure of an underlying elastic layer, and finally by ductile flow within the bottommost region. The mechanical thickness is defined as the high strength region of Ceres from its surface down to where viscously supported stresses at geologically relevant strain rates are negligible. On Earth this is taken to be ~50 MPa (McNutt, 1984). This limiting stress on Ceres was chosen to be 1 kPa, which is small compared to the average maximum modeled differential stress of several hundred kPa. The dependence of T_m on the limiting stress is weak given that material strength falls off rapidly with increasing temperature. The relationship between T_m and T_e was established by using Giese et al. (2007; 2008) thermomechanical model given by Eq. 7.

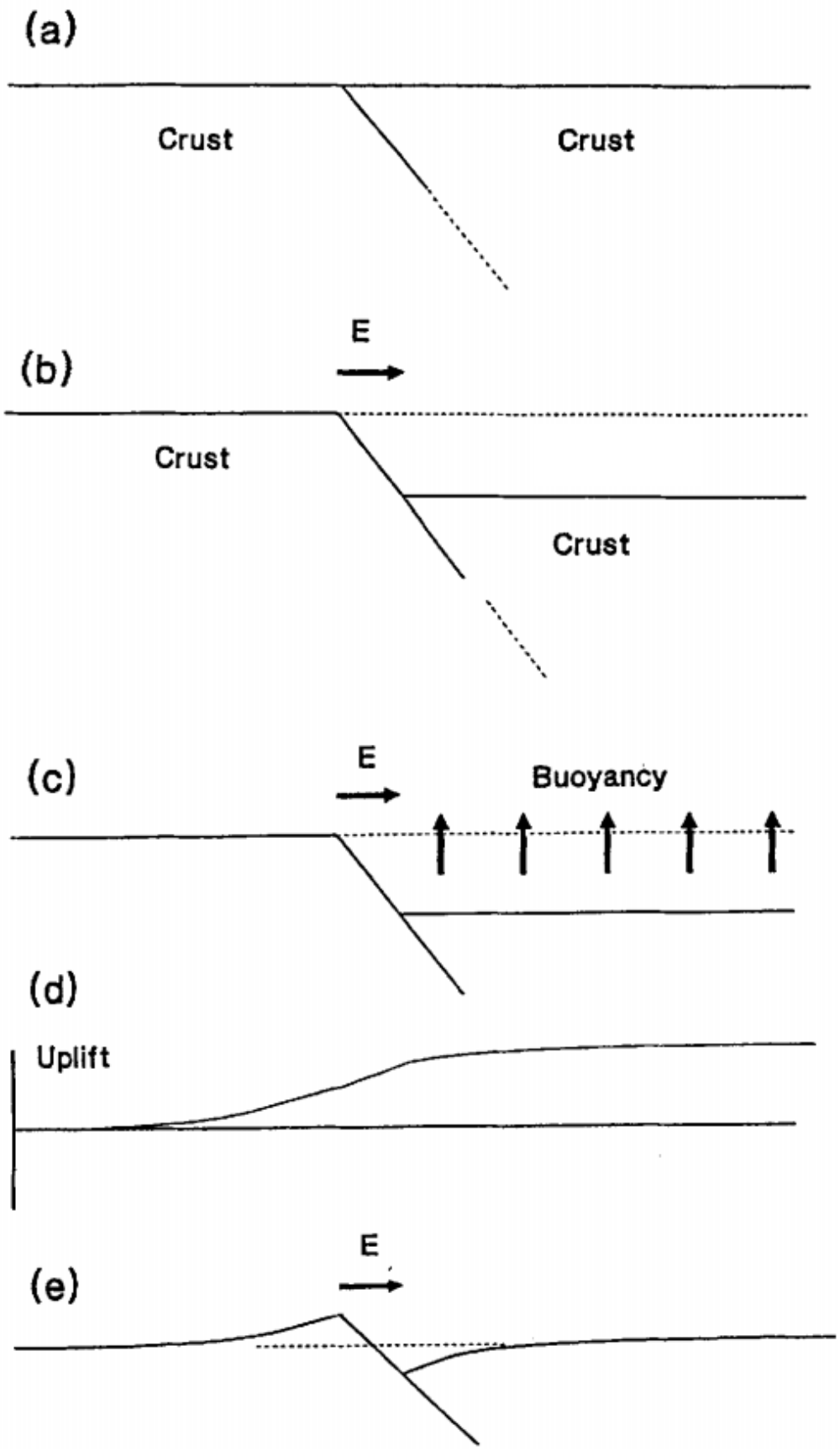
(a)
Crust
Crust
E
(b)
Crust
Crust
E
(c)
Buoyancy
(d)
Uplift
E
(e)

Figure 5-5. Schematic diagram summarizing the flexural isostatic interaction of normal fault blocks during extension along a planar fault. Panel (a) depicts the initial topography before extension. Panel (b) illustrates displacement along the planar fault and represents the starting profile, $u(x)$, for the flexural cantilever model. Panel (c) illustrates the buoyancy force (Eq. 3) acting to restore the hanging wall to its initial state. Panel (d) depicts the elastic response, $w(x)$, of the unified plate. Panel (e) shows the final, elastically flexed, topography given by Eq. 5. This image is adapted from Kusznir et al. (1991).

$$T_e = \left\{\frac{12\cdot(1-\nu^2)}{E\cdot K_{max}} \cdot \int_0^{T_m}[\sigma(z)\cdot(z-z_n)]dz\right\}^{\frac{1}{3}} \quad (7)$$

where $\sigma(z)$ is the differential stress at a depth z taken to be the least of the aforementioned brittle sliding stress, elastic stress, and ductile stress of the mechanical layer. K_{max} is the maximum curvature of either the upthrown or downthrown fault block's profile derived from the flexural cantilever model, and z_n is the depth to the neutral axis (i.e. the depth where the stress changes from compressional to extensional in a bent plate with positive curvature) such that the stress profile integrates to zero.

The stress profiles, $\sigma(z)$, were generated by adopting the brittle strength relationships for cold ice given by Beeman et al. (1988) with a slope of 0.69 and an intercept equal to zero. Changing the slope to 0.85, which is representative of most competent silicate materials (Byerlee, 1978), changes the value of T_e for a given heat flux by only ~1%. For the ductile strengths, grain boundary sliding and dislocation creep were considered via the following equation

$$\dot{\varepsilon} = \dot{\varepsilon}_{gbs} + \dot{\varepsilon}_{disl} \quad (8)$$

where $\dot{\varepsilon}$ is the average strain rate during the formation of Nar Sulcus and $\dot{\varepsilon}_{gbs/disl}$ are the specific strain rates associated with grain boundary sliding (gbs) and dislocation creep (disl). These strain rates can be written generally as the following (Giese et al., 2007; Giese et al., 2008; Goldsby & Kohlstedt, 2001; Ranalli, 1995)

$$\dot{\varepsilon} = A \cdot \left(\frac{\sqrt{3}}{2}\right)^{n+1} \cdot \left(\frac{1}{d}\right)^{m} \cdot \sigma_{ductile}(z)^n \cdot e^{\left(\frac{-Q}{R\cdot T(z)}\right)} \quad (9)$$

where R is the gas constant, $T(z)$ is the temperature at depth z, d is the grain size, and Q is the process dependent activation energy. A, n, and m are all process and material dependent constants. $T(z)$ is related to the heat flux, F, via Eq. 10

$$F = k_m \cdot \frac{\partial T}{\partial z} \tag{10}$$

where k_m is the thermal conductivity of the mechanical layer, which is assumed to behave in the manner described by McCord and Sotin (2005) for an ice-silicate mixture

$$k_m = 4.2 \cdot f_s + (1 - f_s) \cdot \left(0.4685 + \frac{488.12}{T(z)}\right) \tag{11}$$

where f_s is the silicate volume fraction, and k_m is measured in $W \cdot m^{-1} \cdot K^{-1}$. This model does not include the effects of porosity due to its unknown and likely complex structure; however, its potential influence on these results is discussed in section 5.4.

Throughout all the above calculations, the following values were employed: E_{ice} = 1.0 GPa (Giese et al. 2007; Giese et al., 2008; Nimmo & Pappalardo, 2004; Nimmo & Schenk, 2006), g = 0.28 $m \cdot s^{-2}$ (Russell et al., 2016), ρ_c = 1,287 $kg \cdot m^{-3}$ (Ermakov et al., 2017), υ = 0.33 (Giese et al., 2008), d = 0.1-1.0 mm, surface temperature T_s = 150 K (Hayne & Aharonson, 2015), n_{gbs} = 1.8, n_{disl} = 4, m_{gbs} = 1.4, m_{disl} = 0, Q_{gbs} = 49 kJ/mol, Q_{disl} = 60 kJ/mol, A_{gbs} = 3.9 $\cdot 10^{-3}$ $MPa^{-n} \cdot m^{m} \cdot s^{-1}$, and A_{disl} = 4.0 $\cdot 10^{5}$ $MPa^{-n} \cdot m^{m} \cdot s^{-1}$ (the latter eight values are from Goldsby & Kohlstedt, 2001).

To test mechanical layer compositions with rock volume fractions of f_s = 0.30 and f_s = 0.56 the Young's modulus of the modeled mechanical layer is increased by factors of 1.5 and 3.5 respectively relative to that of pure ice (Durham et al., 1992; Yasui et al., 2017). Additionally, the effective viscosity for f_s = 0.30 and f_s = 0.56 mixtures is increased by factors of 5 and 150

respectively relative to the rheology of pure ice (Durham et al., 1992). This is accomplished by multiplying the ductile stress component of $\sigma(z)$ by the previous factors when solving Eq. 7.

Finally, in order to estimate the geologically plausible strain rates at Nar Sulcus, the total strain each set of fracture is estimated by using equations 12 and 13.

$$\varepsilon = \frac{L_f - L_0}{L_0} \tag{12}$$

Where ε is the total strain, L_f is the profile length after extension, and L_0 is the profile length prior to extension.

$$L_0 = L_f - \frac{H}{\tan\delta} \tag{13}$$

In Eq. 13 H is the cumulative vertical offset along a profile, and δ is the dip angle of the faults at depth, which is taken to be 60°, in accordance with the assumptions adopted by Giese et al. (2007). This value was also chosen due to the lack of constraints on the behavior of the Nar Sulcus faults at depth provided by Dawn data. Additionally, the start/end points of the L_f segments were limited to be just before/after the first/last faults with an apparent vertical offset of at least 100 m across the examined fracture set perpendicular to strike.

5.3 Results from Elastic and Thermal Modeling

Figure 5-6 displays the results of applying the flexural cantilever model to stacked topographic profiles of the four largest valleys in Nar Sulcus (see Figure 5-1a). The minimum misfit models return D values ranging from $2.0^{+1.5}_{-0.9} \cdot 10^{15}$ (β valles) to $1.8^{+8.0}_{-1.0} \cdot 10^{16}$ N·m (γ valles). The reported uncertainties in the range of D values are representative of model fits whose root-mean-square (RMS) misfits for a given D are within 5% of the minimum misfit value for that particular valley at the best fit value for θ, which is analogous to the error reporting approach

adopted by Nimmo et al. (2002). Model misfit curves for each analyzed valley are shown in Figures 5-7 and 5-8. The maximum absolute curvatures of the valleys derived from model profiles range from $7.6 \cdot 10^{-6}$ (γ valles) to $3.1 \cdot 10^{-5}$ m^{-1} (β valles).

Using the above bounding values for the flexural rigidity, Eq. 6 predicts elastic thicknesses proximal to Nar Sulcus within the range of 280^{+70}_{-40} - 590^{+900}_{-110} m, 250^{+60}_{-40} - 500^{+800}_{-100} m, and 190^{+50}_{-30} - 390^{+600}_{-70} m for a pure ice, f_s = 0.30, and f_s = 0.56 mechanical layer, respectively. The quoted uncertainties in the above values for T_e are propagated from the uncertainties in D using Eq. 6. The lower bounds on both D and T_e are well constrained, whereas the upper bounds are less certain.

Analysis of the profiles in Figure 5-6 using Eq. 12 estimates of the strain in both of Nar Sulcus' fracture sets to be between 5-8%. Assuming that Nar Sulcus formed over no less than 0.1 Ma, and that it formed over a period of time no longer than the maximum model age estimate of 98-173 Ma, the inferred the geologically relevant strain rates in this region are 10^{-17}-10^{-14} s^{-1}. Results from applying the above bounding values of T_e/K_{max} and the aforementioned rheological parameters to Eq. 7 are shown in Figure 5-9. The total range of near-surface heat fluxes that satisfy the mechanical and geological constraints is 9-201 mW/m^2, with associated mechanical thicknesses 2.9-9.5 km. As expected, both the mechanical thickness and the heat flux exhibit considerable dependences on grain size and strain rate.

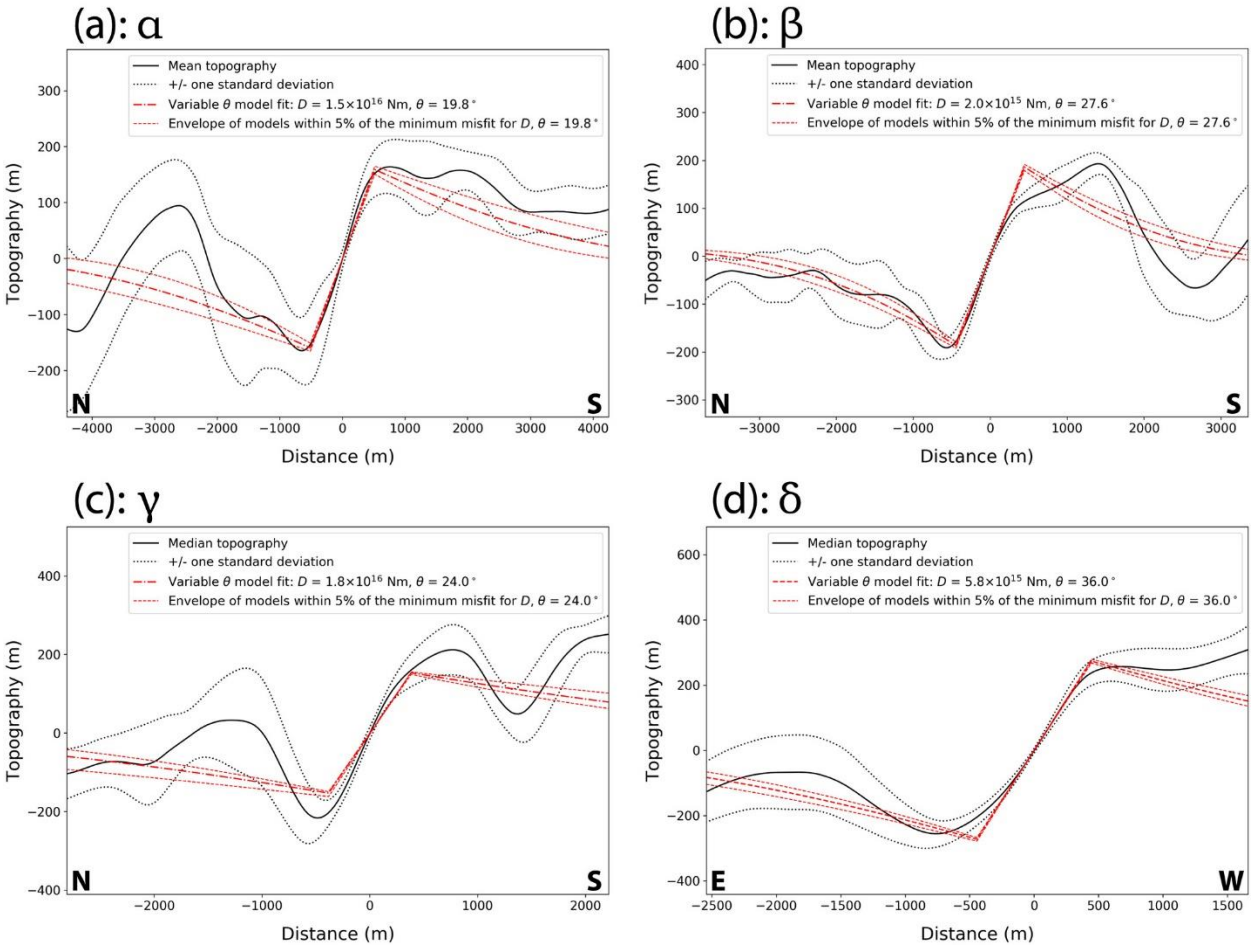

Figure 5-6. Stacked topographic profiles across the four valleys identified in Figure 5-1a. Solid black lines depict mean topographies, dotted black lines are ± one standard deviation from the mean topographies, reported θ values are the minimum RMS misfit dip angles for the faults, and the dash-dotted red lines depict best fit profiles from the flexural cantilever model. All model solutions at the given θs whose misfits are within 5% of the minimum misfit cases exist between the dashed red lines in each subfigure (see Figure 5-7 and 5-8). The magnitude of the model misfits is comparable to what has been reported for other solar system bodies (e.g. Nimmo & Schenk, 2006). Bold letters represent the approximate cardinal direction along each profile. (a) Depicts α valles, $D = 1.5^{+3.0}_{-1.0} \cdot 10^{16}$ N·m; (b) depicts β valles, $D = 2.0^{+1.5}_{-0.9} \cdot 10^{15}$ N·m; (c) depicts γ valles, $D = 1.8^{+8.0}_{-1.0} \cdot 10^{16}$ N·m; and (d) depicts δ valles, $D = 5.8^{+4.0}_{-2.0} \cdot 10^{15}$ N·m.

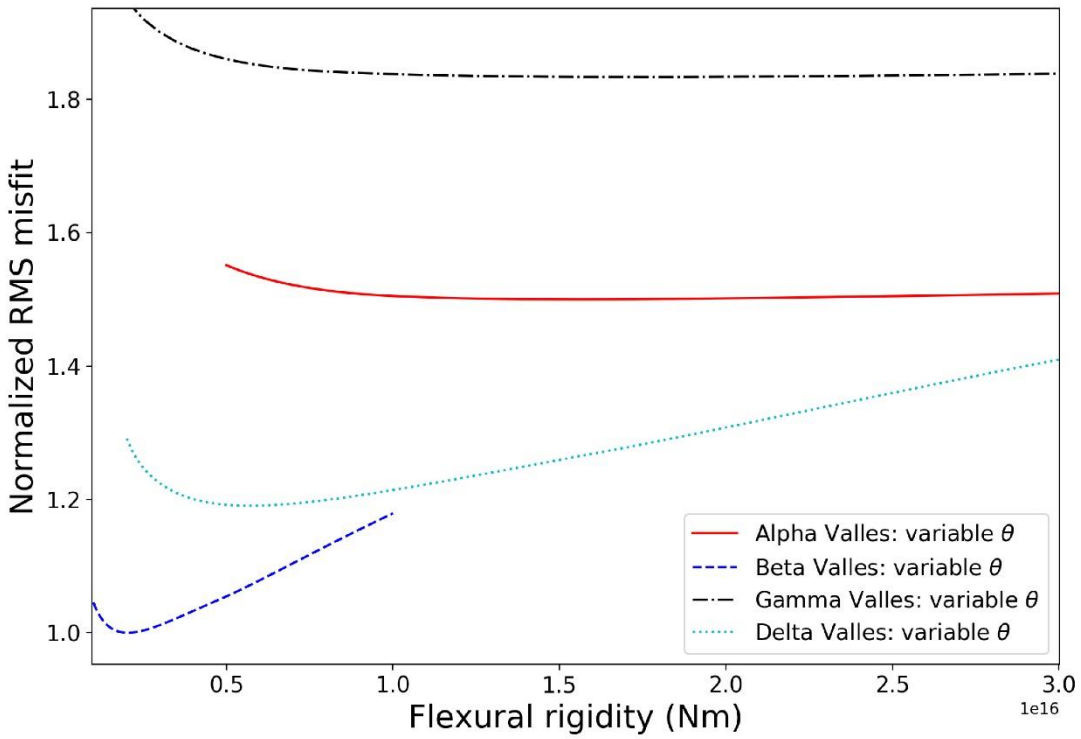

Figure 5-7. Normalized RMS misfits as a function of flexural rigidity for the flexural cantilever model fits depicted in Figure 5-6. The curves are normalized to the minimum RMS misfit derived from the β valles model: 42 m. The minimum RMS misfits for α, γ, and δ valles are 63 m, 77 m, and 53 m respectively. The minimum misfit model derived surface dip angles, θ, for each of the faults are: 19.8° (α valles), 27.6° (β valles), 24.0° (γ valles), and 36.0° (δ valles).

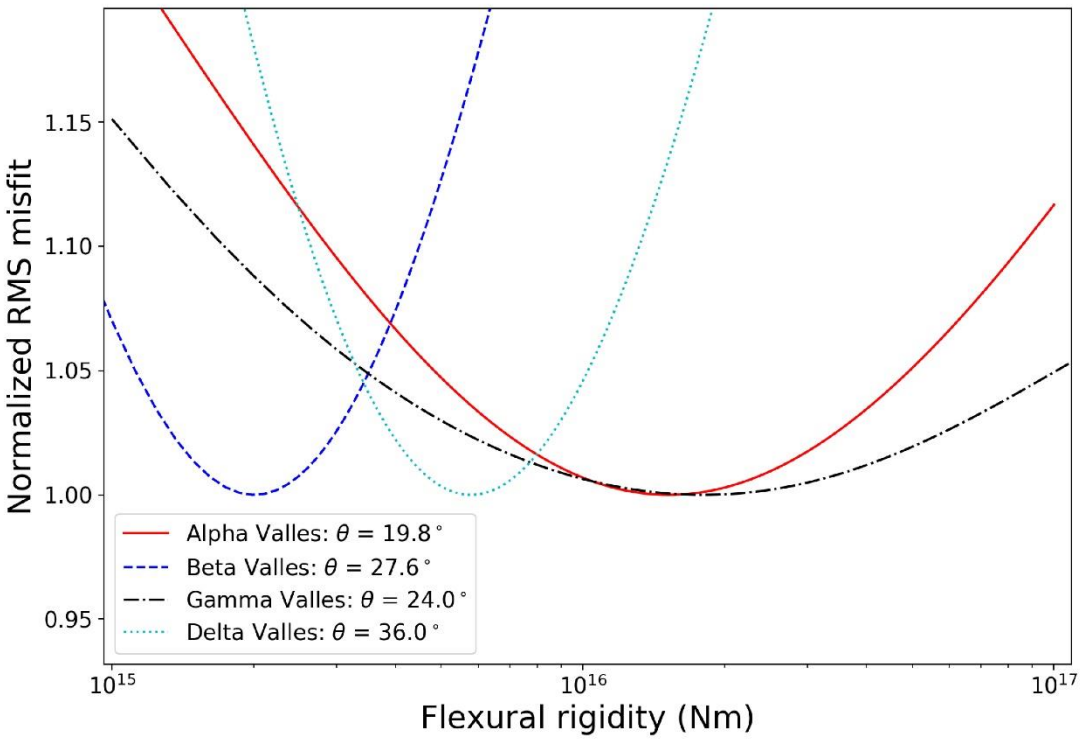

Figure 5-8. RMS misfits as a function of flexural rigidity for the flexural cantilever model fits depicted in Figure 5-6 at the minimum misfit values for θ reported in the caption for Figure 5-7. The curve for each valley is normalized to its own minimum misfit describe in the caption for Figure 5-7. The reported uncertainties in the minimum misfit D values for each valley ($D_\alpha = 1.5^{+3.0}_{-1.0} \cdot 10^{16}$ N·m; $D_\beta = 2.0^{+1.5}_{-0.9} \cdot 10^{15}$ N·m; $D_\gamma = 1.8^{+8.0}_{-1.0} \cdot 10^{16}$ N·m; and $D_\delta = 5.8^{+4.0}_{-2.0} \cdot 10^{15}$ N·m) at the 5% level are taken from the intersections of the misfit curves with the line Normalized RMS misfit = 1.05. Note that the flexural rigidity axis is a log scale.

5.4 Discussion

The average near surface heat flux on Ceres over the past ~800 Myr was likely no greater than ~1 mW/m^2 (Travis et al., 2018). This is in contrast to the results at Nar Sulcus, which are one to two orders of magnitude larger. However, it is possible that eutectic brines currently exist at shallow depths of 30-50 km below the surface (Travis et al., 2018). Stein et al. (2017) postulated that subsurface brines could be brought to the surface or near-surface of Ceres following large impact events. Laccolith formation from these fluids could plausibly raise the local heat flux by a few tens of mW/m^2. Similarly, it has been suggested that tholi on Ceres, like the one at Nar Sulcus, may have been formed through solid-state diapirism (Bland et al., 2018), which may have produced a small increase in the local surface heat flux. The emplacement of large quantities of excavated and/or impact heated Urvara/Yalode Smooth Material from the Urvara-forming impact (as suggested by Crown et al., 2018) could have plausibly raised the heat flux at Nar Sulcus by several tens of mW/m^2 for potentially a few Myr (see Biren et al. (2014), and Bowling et al. (2018) for relevant examples). On this geological basis, the local heat flux present at Nar Sulcus during the formation of the faults is interpreted to have most likely fallen within 10-100 mW/m^2.

The heat flux analysis presented in Figure 5-9 shows that the only curves which completely satisfy the preferred heat flux range over all geologically relevant strain rates belong to the family f_s = 0.0, with the exception of a single f_s = 0.3 curve. Based on this measured 5-8% strain, $\dot{\varepsilon} = 10^{-15}$ s^{-1} corresponds to deformation on the million-year timescale, which is the relevant heat dissipation timescale for large quantities of material disturbed by the Urvara-forming impact (Biren et al., 2014; Bowling et al., 2018). At this strain rate all but one of the f_s = 0.3, and only one of the f_s = 0.56 curves in Figure 5-9 fall below F = 100 mW/m^2. A silicate-

dominated rheology at Nar Sulcus is deemed highly unlikely as it would require both an extremely thin elastic layer, and an implausibly high heat flux. On this basis, an upper bound of ~30 vol. % mechanically silicate-like phases within the mechanical layer at Nar Sulcus is interpreted to be the most consistent with the thermal and mechanical model results presented in this chapter. This is broadly consistent with Fu et al. (2017)'s and Ermakov et al. (2017)'s estimate of the global rock volume fraction within the upper layer of Ceres. However, the remaining ~70 vol. % of the mechanical layer in this model is composed of mechanically ice-like phases, which is considerably more than the upper bound of ~25 vol. % ice estimated by Fu et al. (2017). This result is consistent with the variations in ice content in Sizemore et al. (2018) with more ice observed in association with large craters and basins.

5.4.1 Comparison of Ceres to other Solar System Bodies

Direct comparison of the model derived range of flexural rigidities at Nar Sulcus to other solar system objects firmly characterizes it as mechanically similar to most outer solar system icy satellites (Table 5-1). In contrast, silicate dominated bodies like the Earth and Mars have typical flexural rigidities at least four orders of magnitude greater than what are estimated at Ceres in this investigation. While no formal measurements have been made of the flexural rigidity of the vestan crust, the large scale of its topography combined with the small observed curvature of fault blocks in the Saturnalia and Divalia Fossae (Schafer et al., 2014; Scully et al., 2014) strongly suggest that it is similar to, or even greater than, those of the terrestrial planets. Given Ceres' intermediate surface thermal environment between that of the inner and outer solar system, the similarity between the flexural rigidity of Nar Sulcus and those of Ganymede, Europa, and Enceladus suggests that the faulted layer on Ceres is likely a mixture of water ice and denser, more rigid phases, but whose mechanics is dominated by the ice component.

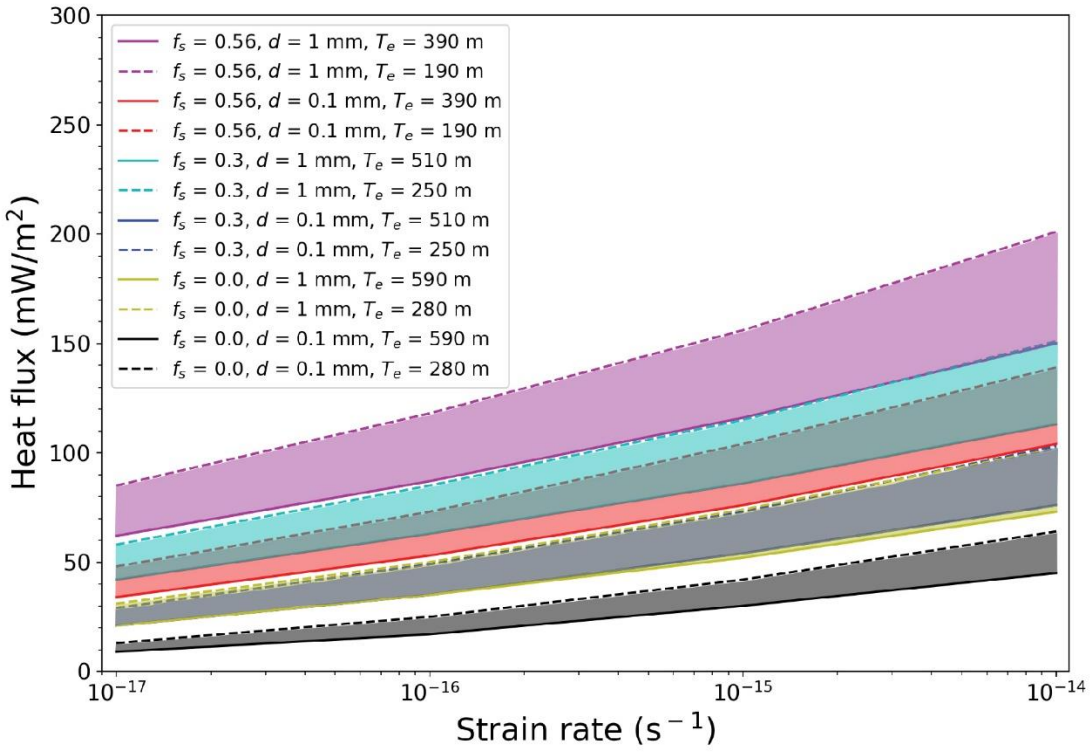

Figure 5-9. Surface heat flux as a function of strain rate derived from Eq. 7 for different combinations of f_s, T_e, and d. The dashed and solid lines of a given color represent the bounding values of T_e measured at Nar Sulcus for the chosen values of f_s and d, thus they encapsulate the full range of possible heat fluxes at a given strain rate for those parameter choices, as is illustrated by the color coded shaded regions.

Object	D (N·m)	Reference
Ceres (Nar Sulcus)	$2.0^{+1.5}_{-0.9} \cdot 10^{15}$ - $1.8^{+8.0}_{-1.0} \cdot 10^{16}$	This study
Ganymede	$5.5 \cdot 10^{14}$ – $1.6 \cdot 10^{17}$	Nimmo and Pappalardo (2004)
Europa	$3.0 \cdot 10^{14}$ – $1.5 \cdot 10^{17}$	Nimmo and Schenk (2006)
Enceladus	$2.5 \cdot 10^{15}$ - $3.9 \cdot 10^{16}$	Giese et al. (2008)
Tethys	$1.1 \cdot 10^{19}$ – $3.5 \cdot 10^{19}$	Giese et al. (2007)
Mars	$9.7 \cdot 10^{21}$ – $1.7 \cdot 10^{22}$	Grott et al. (2005)
Earth	Typically > 10^{20}	e.g. Lowery and Smith (1994); Walcott (1970)

Table 5-1. Flexural Rigidities of Various Solar System Objects.

Curiously, of the planetary objects listed in Table 5-1, Tethys (mean diameter 1062 km) is closest in size to Ceres (mean diameter 946 km), yet of the icy satellites its flexural rigidity is the most unlike Ceres. Ganymede, Europa, and Enceladus, whose flexural rigidities are Ceres-like, are all either much larger or much smaller than the dwarf planet. Additionally, these icy moons are all known to have subsurface oceans, and believed to have relatively high (tens to hundreds of mW/m^2) modern and/or historical heat fluxes (Bland et al., 2017; Ruiz, 2005; Giese et al., 2008). Tethys likely has no such ocean (Matson et al., 2009).

The similarity of Nar Sulcus to these ocean worlds is most likely due to a combination of its warm thermal environment in the main belt and the peculiar "dirty ice" composition of its surface layer. The average surface temperature on Ceres relative to Enceladus and Tethys is nearly 100 K greater. This dramatically reduces the depth to the ductile layer, which in turn limits the brittle thickness at Nar Sulcus compared to these icy moons for a given heat flux (assuming an ice dominated rheology). Giese et al. (2008) reported heat fluxes in the range 200-270 mW/m^2 for extensionally faulted terrain on Enceladus, so while the elastic properties of Nar Sulcus and Enceladus are very similar, their required formational heat fluxes likely are not. The opposite is true for Tethys, where Giese et al. (2007) reported heat fluxes in the range 18-30 mW/m^2, which are plausibly similar to the historical heat flux at Nar Sulcus, but whose cold, frozen elastic layer is inferred to be between 4.9-7.2 km thick. The increased ductility on Ceres is only partially compensated by the increased strength of the cerean near-surface due to its silicate component. The potential presence of brines and other salty ice phases near their homologous temperatures within the mechanical layer below Nar Sulcus may further limit the depth to the ductile layer.

Giese et al. (2008) found that including a porosity estimate in their calculations of the heat flux at Harran Sulci, Enceladus, decreased the derived values by a maximum of around one order of magnitude compared to the non-porous cases. However, they cautioned against interpreting their result as being reflective of the true effect of porosity on the thermal conductivity of Enceladus. This reduction in heat flow is due to the insulating effects of increased void space, which in general apply to all solar system objects. If the reduction in thermal conductivity due to porosity on Ceres is proportionally similar to that of what Giese et al. (2008) estimated for Enceladus, then all the parameter combinations in Figure 5-9 would become geologically plausible in the context of achievable surface heat fluxes on Ceres. The main implications of this would be that the upper layer of Ceres could contain much more silicate-like material than currently expected, or that the ancient surface heat flux at Nar Sulcus was no more than a few times the current global average.

Finally, unlike terranes observed on icy satellites such as Ganymede and Europa, the valleys investigated at Nar Sulcus appear to have rounded, smooth floors (e.g. Nimmo & Schenk, 2006). This morphological distinction implies an increased degree of sedimentary infilling has taken place at Nar Sulcus relative to similar features observed on icy moons. Since Nar Sulcus appears stratigraphically younger than most of the large neighboring impact craters, it is unlikely that ejecta is the sole source of this apparent infill. However, this observation is consistent with the high water ice content of the subsurface interpreted from the analyses performed in section 5.3. Unlike on outer solar system satellites, exposed or shallowly buried (within a handful of meters from the surface) water ice is thermodynamically unstable on Ceres and sublimates away over short geological timescales (Hayne & Aharonson, 2015). Sublimation of ice from consolidated regolith and near-surface materials has been shown to trigger mass wasting and

sediment transport in laboratory experiments undertaken at martian conditions (Sylvest et al., 2016). Faulting at Nar Sulcus would expose and induce sublimation in large portions of previously armored icy materials close by to the faults. A natural consequence of this would likely be sublimation triggered sedimentation and infill of the valleys at Nar Sulcus.

5.5 Conclusions

Through the application of flexural techniques developed for terrestrial settings, Nar Sulcus was determined to be mechanically much more similar to extensional structures on many icy satellites than to their counterparts on the silicate dominated planets. The characteristics of the faults in Nar Sulcus are consistent with a thin/weak elastic layer approximately 190-590 m thick. The corresponding mechanical layer is 2.9-9.5 km thick. Based on the modeled T_e range, geologic context, and genetic thermal models, the surface heat flux at Nar Sulcus during its formation is interpreted to have been ~10-100 mW/m^2. This range is between one and two orders of magnitude larger than the predicted average surface heat flux during the last ~800 Myr, although accurately including the effects of porosity could significantly reduce these values. In combination with the observed variability of the heat flux with changing grain size, this further underscores the importance of knowing both the porosity structure and grain size distribution for thermal modeling of Ceres. This interpreted heat flux range is consistent with a mechanical layer that contains no more than ~30 vol. % mechanically silicate-like phases. If the higher than expected historical heat flux at Nar Sulcus is true, it may plausibly be explained by solid-state diapirism, laccolith formation from cryomagma sourced from either endogenic reservoirs or impact melt, and/or residual heat from the emplacement of Urvara/Yalode Smooth Material from the Urvara-forming impact.

6 Summary and Conclusions

6.1 Summary

The small bodies of our solar system, such as asteroids, comets, and dwarf planets, represent the last remaining vestiges of the feedstock that birthed the terrestrial planets. As the only remaining dwarf planet in the inner solar system, Ceres is the largest surviving protoplanet that was likely forged during the nebular phase of our solar system's history. Understanding the geology, composition, and structure of Ceres is paramount for developing a deeper understanding of the processes that govern terrestrial planet formation, the compositional environment of the early solar system, and how volatiles, particularly water ice, are distributed and preserved within the inner solar system. Thus, NASA's Dawn spacecraft was selected to undertake a mission of exploration that would characterize the geology, surface composition, and internal structure of Ceres at an unprecedented level of detail (Russell & Raymond, 2011). The Dawn mission went on to be an overwhelming success. Beyond exceeding all of its originally stated data return goals at both Vesta and Ceres, Dawn discovered unexpected alien landscapes on Ceres such as the enormous natrite deposits that compose the Cerealia and Vinalia faculae, the towering Ahuna Mons and associated tholi, widespread lobate landslides that exhibit a wide spectrum of runout efficiencies, fluidized appearing ejecta, and the enigmatic fractures at Nar Sulcus. This dissertation contributes to the Dawn mission's goals of characterizing the geology, composition, and structure of Ceres by: (1) aiding in the global geologic mapping of Ceres and characterizing sites of geological and compositional interest (see Chapter 2), (2) identifying the numerous forms of mass wasting on Ceres and investigating their morphological link to ground ice (see Chapter 3), (3) classifying and modeling the emplacement dynamics of fluidized appearing ejecta on Ceres (see Chapter 4), and (4) estimating the mechanical and elastic

thickness of the upper layer of Ceres through flexural-cantilever modeling of the Nar Sulcus fractures (see Chapter 5).

Results from the regional geologic mapping campaign of the Ac-5 Fejokoo quadrangle, as well as the global mapping effort, are presented in Chapter 2 and in Hughson et al. (2018). This investigation revealed that impact craters dominate the morphology of Ceres' surface, a result that is contrary to predictions of a viscously relaxed ice-rich shell (e.g. Bland, 2013). Despite this observation, the direct detection of water ice exposed at the surface (such as at Oxo crater) as well as the identification of a multitude of forms of lobate material deposits and tholi from geologic mapping suggest that Ceres' crust is indeed rich in water-ice, but that its distribution and mechanical properties are far more complicated than what was predicted. On the basis of morphological analogues, the cerean lobate deposits within the Fejokoo quadrangle are interpreted to be similar to long run-out landslides, frozen debris flows, and martian-style fluidized ejecta; the observed tholi are interpreted to be ancient constructional features and not remnant topography created by impact cratering. Additionally, the geologic mapping revealed that the majority of the geomorphologic diversity on Ceres is concentrated within the freshest appearing craters. This implies that the surface geologic processes are primarily driven by cratering, and that the morphologic and photometric properties of cerean surface materials degrade rapidly over geologic time in their current environment at scales greater than ~100 m. Possible mechanisms for this apparent degradation include space weathering, sublimation driven deflation, and impact mixing.

In Chapter 3, as well as in Buczkowski et al. (2016) and Schmidt et al. (2017), the search for lobate material deposits is expanded globally. From this global identification campaign three unique morphological types of lobate deposits are ubiquitously identified on Ceres: Type 1, Type

2, and Type 3 flows. Type 1 flows are typically thick, have low runout efficiencies, bulbous and concave-down terminal snouts, and frequent longitudinal grooves; they are interpreted to be similar to terrestrial cohesive landslides and frozen debris flows. Type 2 flows are typically thin, have high runout efficiencies, and a spatulate appearance; they are interpreted to be similar to terrestrial supraglacial landslides, martian long run-out landslides, and iapetian long run-out landslides. Type 3 flows are typically thin, controlled by local topography, have high runout efficiencies that are independent of the scale of the deposit, and have superimposed layers that terminate in multiple cuspate lobes; they are interpreted to be similar to fluidized ejecta observed on other solar system bodies such as Mars, Ganymede, and Charon. The area density of these features increased significantly with increasing latitude, which is consistent with their origin being tied to the concentration of near-surface ground ice. Based on morphological analogy, these mass wasting and lobate features, which were not observed on the largely anhydrous asteroid Vesta, imply near-surface ground ice concentrations of between ~10-50 vol. % within the upper few hundred meters proximal to each deposit.

Chapter 4 and Hughson et al. (2019a) further explore the relationship between the composition and mechanical properties of the near-surface of Ceres and the presence of fluidized appearing ejecta (FAE), which are a broad morphological class of flow features whose definition is based on the Type 3 flows defined in Chapter 3. In this investigation 30 instances of cerean FAE were identified, which were subdivided into two morphological classes: cuspate/lobate FAE and channelized FAE. Cuspate/lobate FAE typically have multiple cuspate terminal lobes and a sheeted often multi-layered appearance, whereas channelized FAE are typically single layered, exhibit flow banding, and are strongly influenced by local topography. Through numerical analysis of the geographic and ejecta mobility (EM) distributions of cerean FAE it was

determined that they are effectively uniformly distributed throughout the low- and mid-latitudes, with the channelized FAE exhibiting ~30% greater mobility on average than their cuspate/lobate counterparts. Emplacement modeling of cerean FAE using the hybrid kinematic-dynamic sliding ejecta model revealed that the generalized strength of the impacted substrate is slightly more ice-like than silicate-like, but variations in this parameter do not appear to significantly affect FAE mobility, at least at the empirically determined strengths of competent silicate rocks and cryogenic water ice. Contrariwise, it was found that the coefficient of sliding friction of the substrate tightly controls ejecta mobility, and that the mobilities of cerean FAE are consistent with a combination of sliding on an intimate mixture of rock and ice, and by friction reduction caused by both fluidization through the incorporation of impact melt fluids and basal lubrication via melted near surface volatiles. The degree of friction reduction suggests that pore filling ground ice, accounting roughly for 30-50 vol. % of the substrate, is present only a few meters below the surface to at least 1 – 5 km based on crater ejecta excavation depths.

Chapter 5 and Hughson et al. (2019b) examine elastically supported topography within the fractured Nar Sulcus region on Ceres' southern hemisphere. In this investigation, it was determined that the Nar Sulcus fractures are an extensional system of normal faults whose topographic profiles are characteristic of elastic flexure. By applying a flexural-cantilever similar to one created for terrestrial applications it was found that the flexural rigidity of Ceres' mechanical layer is similar to that of many icy worlds of the outer solar system such as Europa, Ganymede, Enceladus, and Tethys. Consequently, the rigidity of the Ceres' crust, at least proximal to Nar Sulcus, is several orders of magnitude weaker than those of the terrestrial planets. Using the model derived flexural rigidities and laboratory derived values for the brittle, elastic, and ductile behavior of ice-silicate mixtures the historic heat flux at Nar Sulcus during

the formation of the fractures was estimated. Based on numerical and geological constraints this heat flux was interpreted to be between ~10-100 mW/m^2, a range which is approximately one to two orders of magnitude greater than the predicted global average for Ceres' during the past ~800 Myr. This interpreted heat flux range is consistent with a mechanical layer that contains no more than ~30 vol.% mechanically silicate-like phases, and may plausibly be explained by solid-state diapirism, laccolith formation from cryomagma sourced from either endogenic reservoirs or impact melt, and/or residual heat from the emplacement of Urvara/Yalode Smooth Material from the Urvara-forming impact.

6.2 Implications

The geologic mapping of its surface, presence of variable runout landslides, mobility of its FAE, and low flexural rigidity of its crust all indicate that Ceres' near-surface environment is rich in water ice despite the low number of surface H_2O detections. While water ice is not specifically stable on the surface of Ceres, these results demonstrate that large quantities of this material can be stored within modestly sized main-belt protoplanets over long geological timescales. This is consistent with the emerging understanding that water is more pervasively distributed throughout the inner solar system than what was predicted before the advent of powerful Earth- and space-based observatories. For example, Hsieh and Jewitt (2006) discovered cometary-like objects embedded within the main-belt, termed main belt comets, that frequently exhibit comae likely driven by the sublimation of near-surface ice. In addition to Ceres other large main-belt C-type asteroids, such as 24 Themis, have been found to have surfaces suggestive of water ice and organic compounds (Campins et al., 2010). In light of the geomorphic evidence for abundant water ice near the surface of Ceres presented in this dissertation, a substantial reservoir of water sequestered within modern main-belt C-type

asteroids seems increasingly likely. This reservoir of water-rich chondritic material is rapidly becoming an area of intense scientific interest as evidence mounts that it may be the most likely source of the Earth's water (Figure 6-1).

Based on the major findings presented in this dissertation, it is plausible that a substantial portion of Earth's water may have been delivered by ice-rich protoplanets such as Ceres. Additionally, organic-bearing asteroids such as Ceres could have delivered the pre-biotic materials necessary for life to flourish on Earth, and may even be currently habitable provided that liquid brines exist deep below their exteriors. Future landed missions on Ceres capable of making detailed geological, geophysical, and geochemical measurements represent the critical next step in understanding the origins of rocky planets, as well as the source of Earth's abundant water.

A water-rich Ceres also represents an incalculably valuable resource asset for future deep space exploration (Figure 6-2). *In situ* resource utilization of Ceres' large reserves of easily accessible ice is an attractive alternative to utilizing large, heavy-lift rockets launched from Earth. Efficient conversion of cerean ice into consumables and propellants such as liquid water, O_2, and H_2 could usher in a golden age of outer solar system exploration, enabling large orbital missions to the gas/ice giant systems and even Kuiper belt objects.

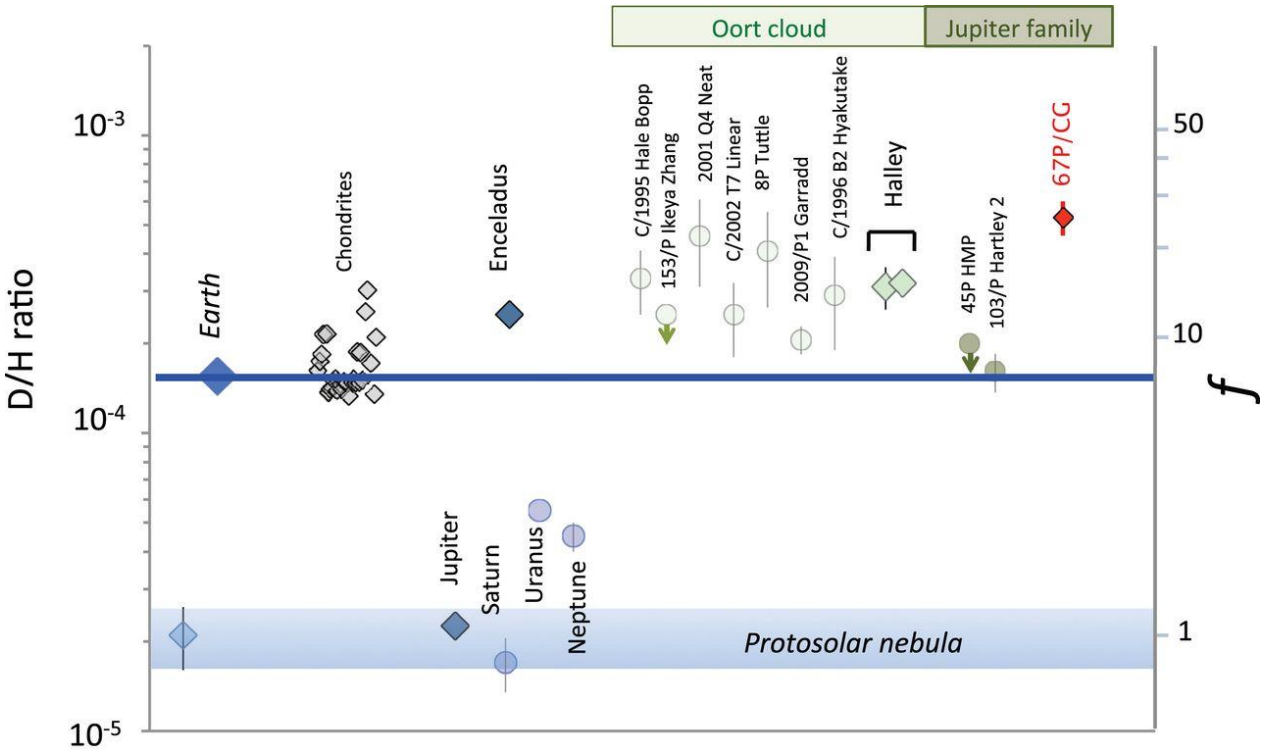

Figure 6-1. The deuterium/hydrogen (D/H) ratios of water in different solar system objects. Observations by the Rosetta spacecraft of the Jupiter family comet 67P/CG indicated that it had a substantially higher D/H ratio than the Earth's oceans; although, this may not be representative of all Jupiter family comets. No direct measurement of the D/H ratio of Ceres' ice has been made, but Dawn's spectroscopic observations suggest that it is compositionally similar to CI/CM chondrites. These meteorites are known to have D/H ratios very similar to the Earth's oceans. Image adapted from Altwegg et al. (2015).

Figure 6-2. Artistic rendering of *in situ* resource utilization on a near-Earth asteroid. Although human exploration of the solar system beyond the Earth-Moon system remains at least several decades away, much of the technology required for in situ resource utilization by semi-autonomous robotic vehicles already exists. Image credit: Denise Watt/NASA.

Appendix A: Identified Fluidized Appearing Ejecta on Ceres

Supporting figures A-1 through A-28 illustrate the mapped ejecta facies of the cerean FAE identified in Chapter 4, the clear filter images used to identify them, and the HAMO DTM derived local topography. Mapped cuspate/lobate ejecta facies are represented by green overlays, channelized FAE are mapped with light orange overlays, and the source craters are mapped using light purple overlays. The dashed blue lines in some of the supplementary figures indicate regions of abruptly terminating ejecta similar to double layer ejecta on Mars and layered ejecta on icy satellites.

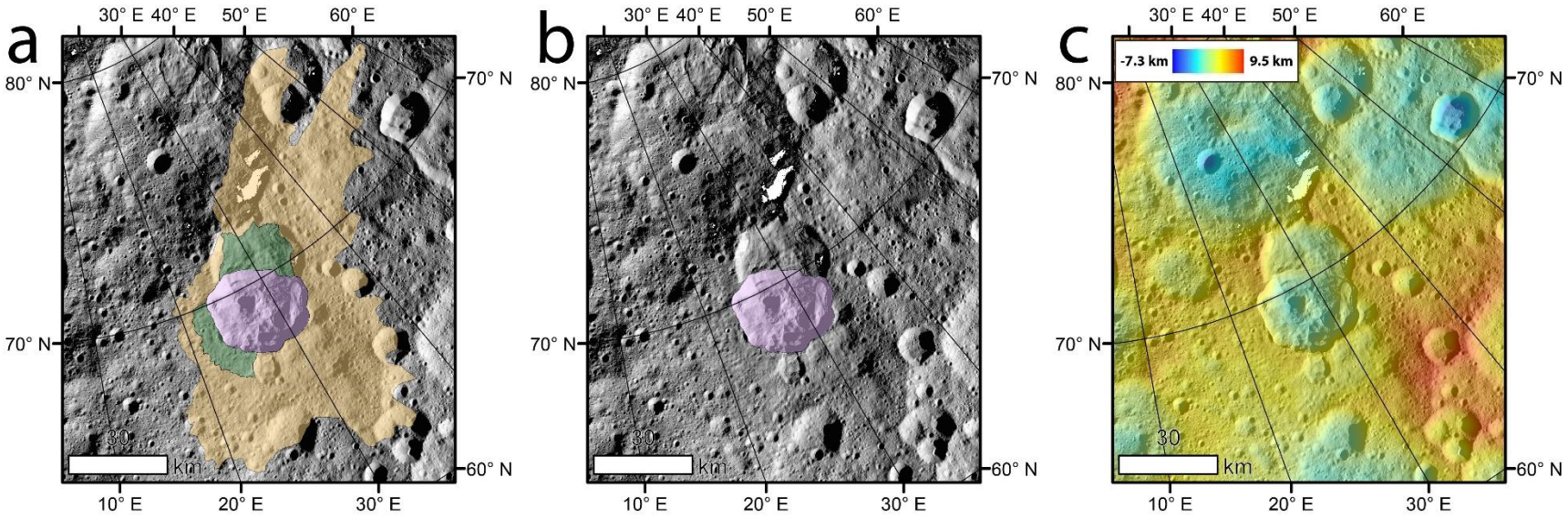

Figure A-1. (a) Shennong crater with mapped cuspate/lobate and channelized FAE deposits. (b) same image as (a) but with ejecta related map overlays removed. (c) same image as (a) but with all mapping overlays replaced by color coded HAMO derived topography.

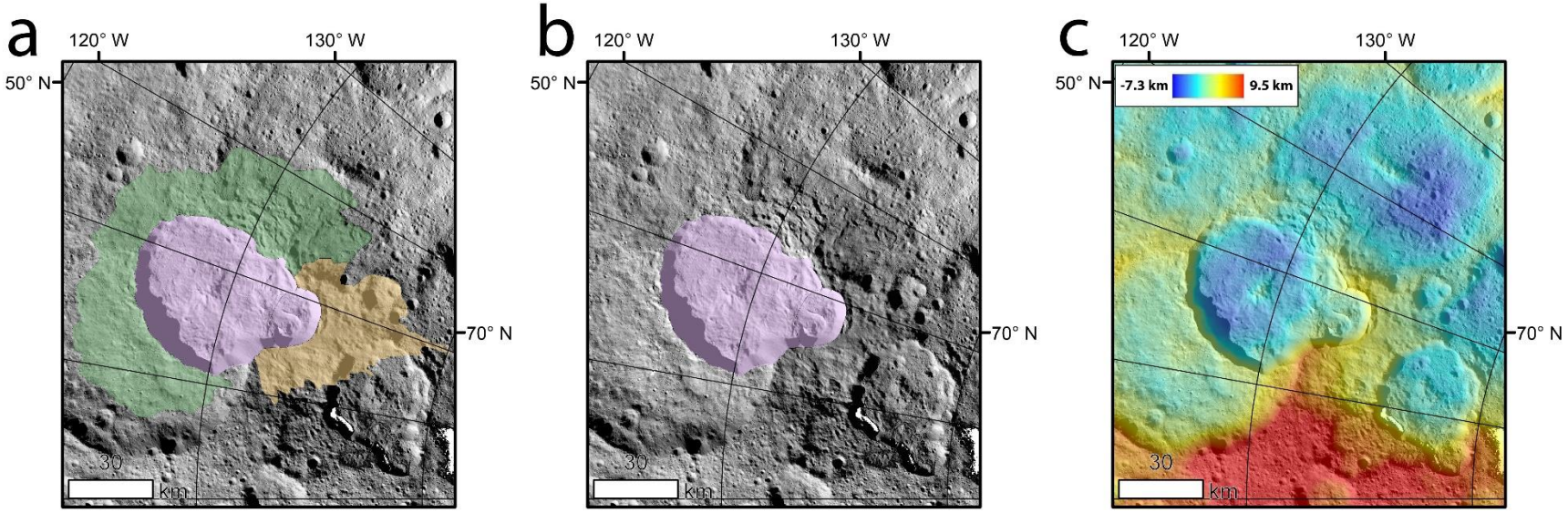

Figure A-2. (a) Datan and a small unnamed crater to its north (-107.88° E, 63.09° N) with mapped cuspate/lobate and channelized FAE deposits. (b) same image as (a) but with ejecta related map overlays removed. (c) same image as (a) but with all mapping overlays replaced by color coded HAMO derived topography.

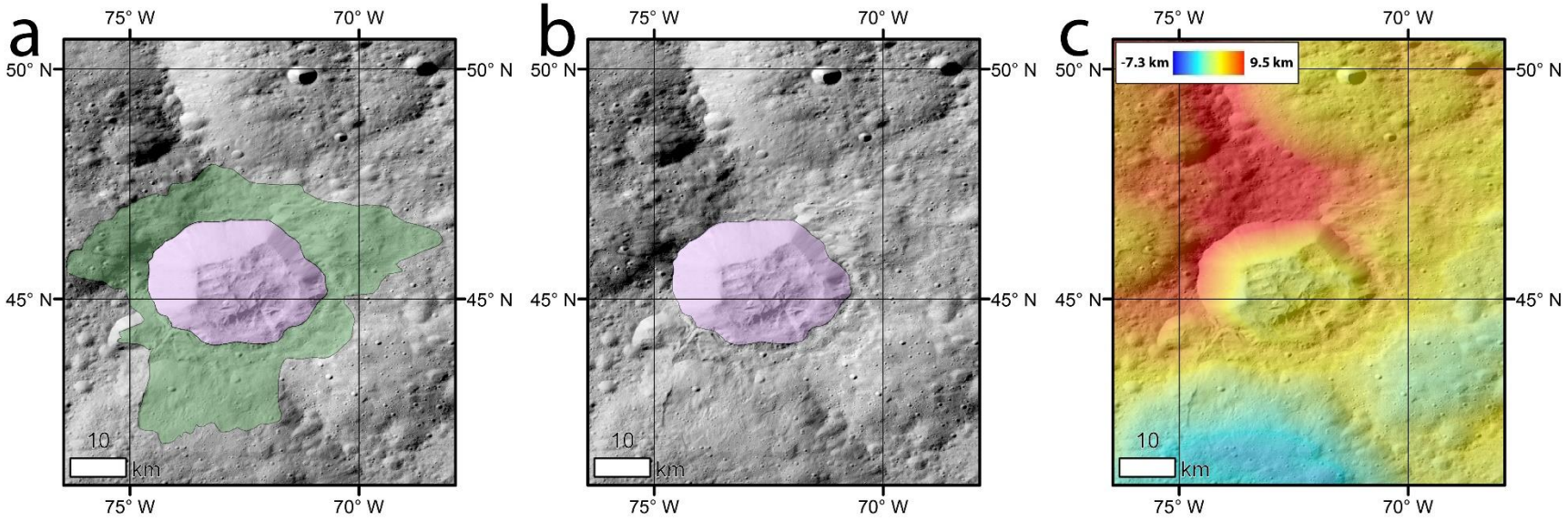

Figure A-3. (a) Cozobi crater with mapped cuspate/lobate FAE deposit. (b) same image as (a) but with ejecta related map overlays removed. (c) same image as (a) but with all mapping overlays replaced by color coded HAMO derived topography.

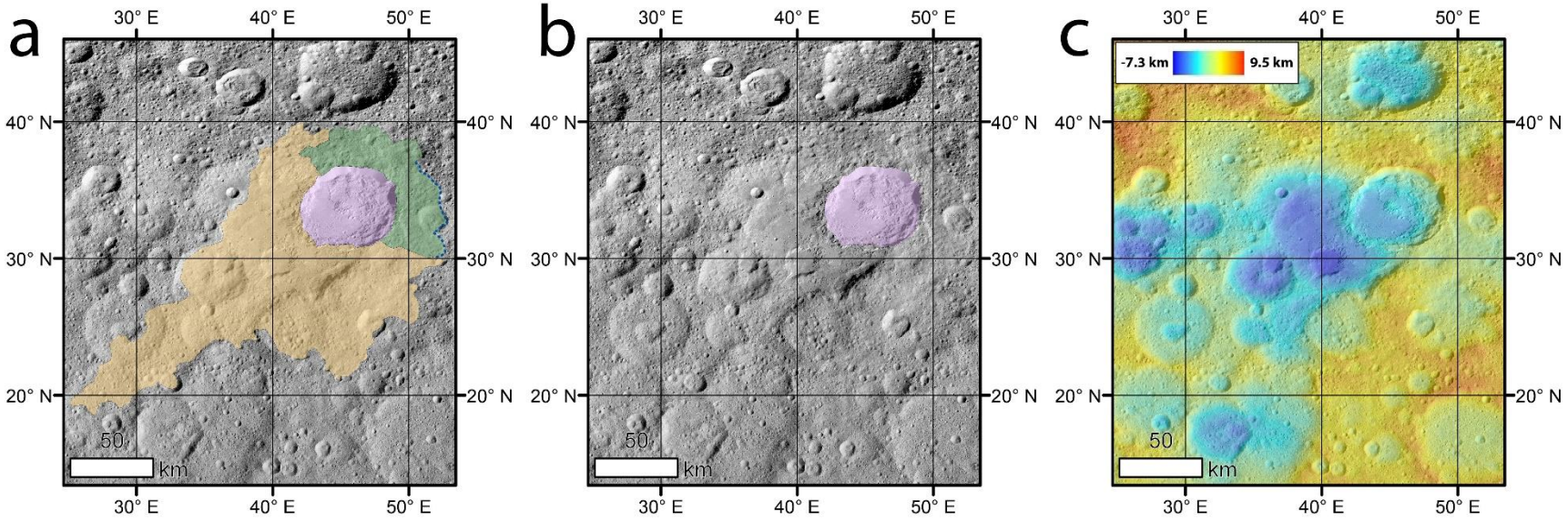

Figure A-4. (a) Ikapati crater with mapped cuspate/lobate and channelized FAE deposits. (b) same image as (a) but with ejecta related map overlays removed. (c) same image as (a) but with all mapping overlays replaced by color coded HAMO derived topography.

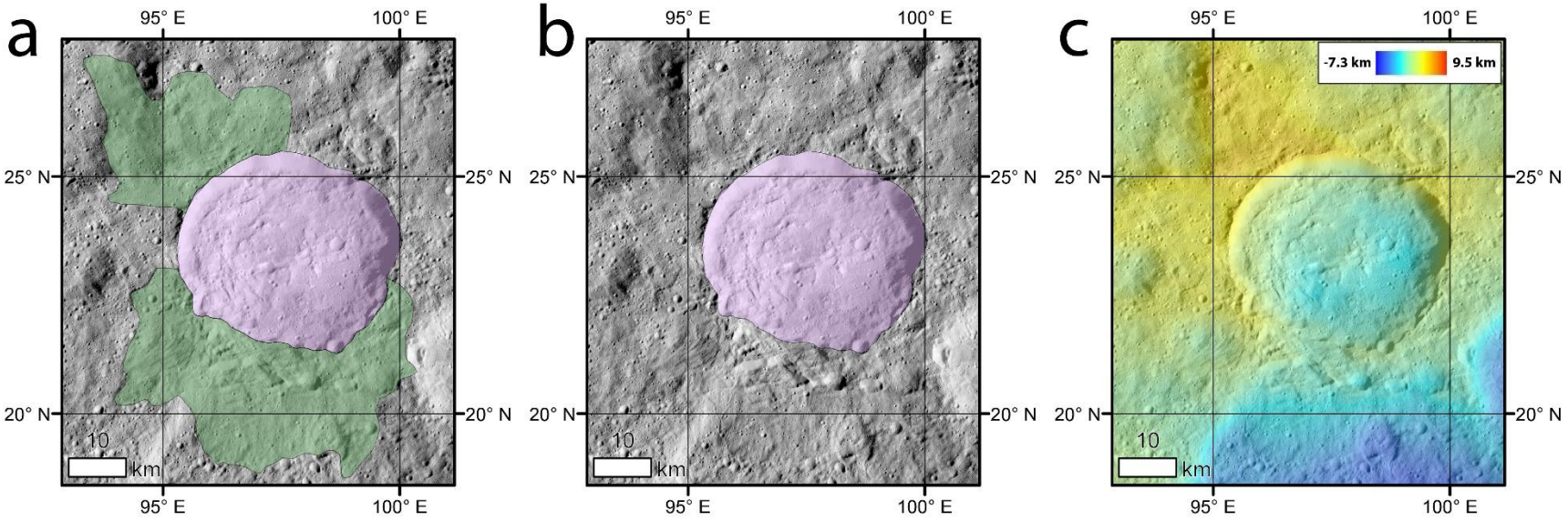

Figure A-5. (a) Aristaeus crater with mapped cuspate/lobate FAE deposit. (b) same image as (a) but with ejecta related map overlays removed. (c) same image as (a) but with all mapping overlays replaced by color coded HAMO derived topography.

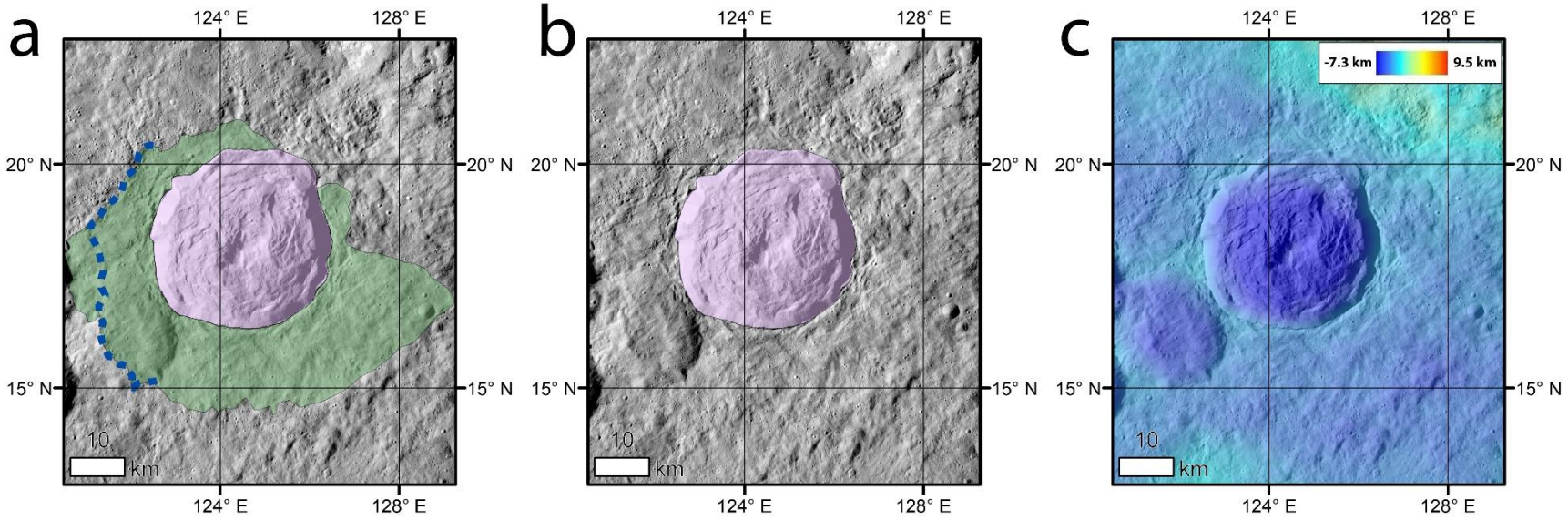

Figure A-6. (a) Kokopelli crater with mapped cuspate/lobate FAE deposit. (b) same image as (a) but with ejecta related map overlays removed. (c) same image as (a) but with all mapping overlays replaced by color coded HAMO derived topography.

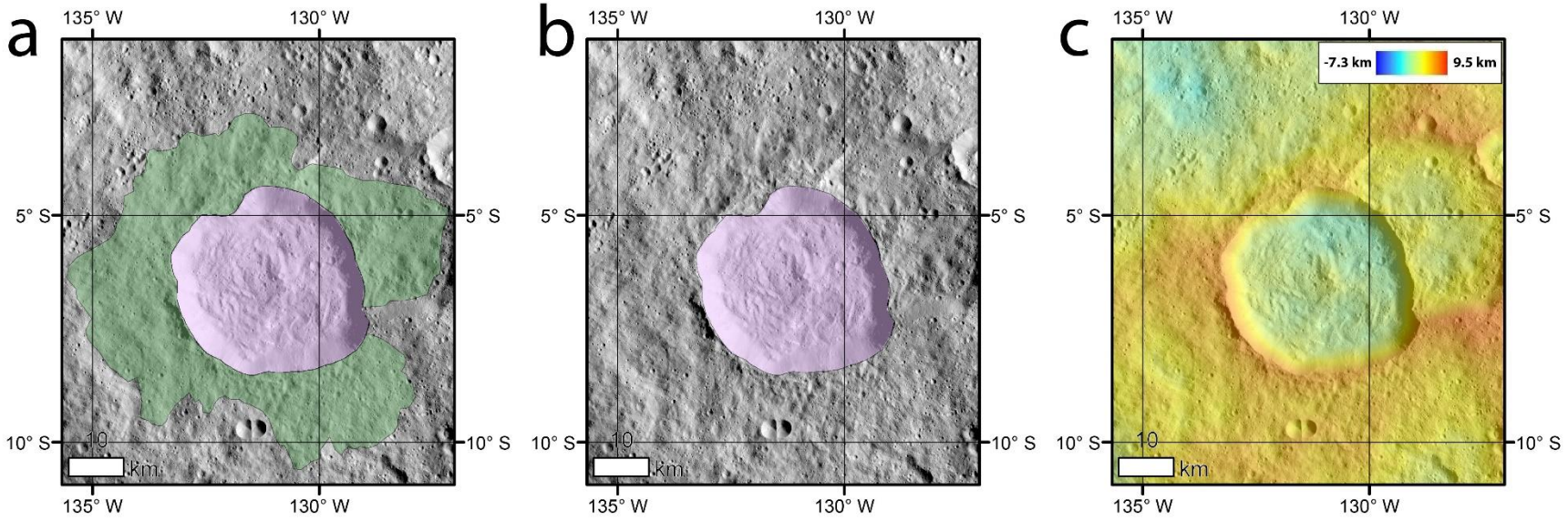

Figure A-7. (a) Lociyo crater with mapped cuspate/lobate FAE deposit. (b) same image as (a) but with ejecta related map overlays removed. (c) same image as (a) but with all mapping overlays replaced by color coded HAMO derived topography.

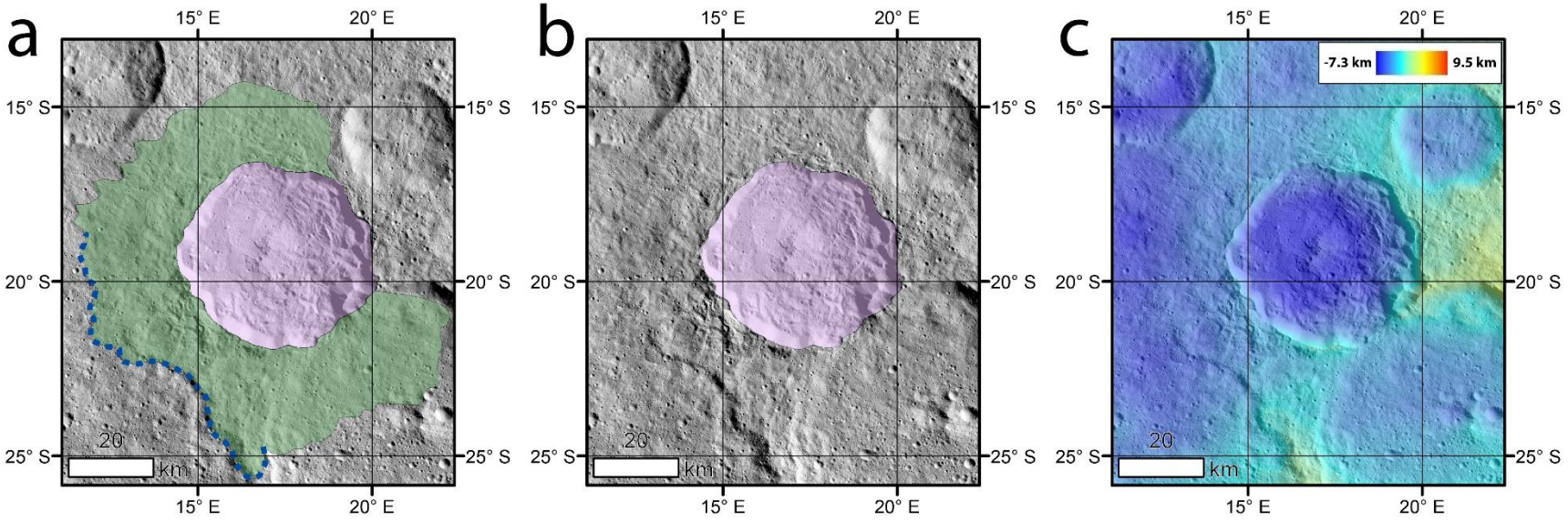

Figure A-8. (a) Kondos crater with mapped cuspate/lobate FAE deposit. (b) same image as (a) but with ejecta related map overlays removed. (c) same image as (a) but with all mapping overlays replaced by color coded HAMO derived topography.

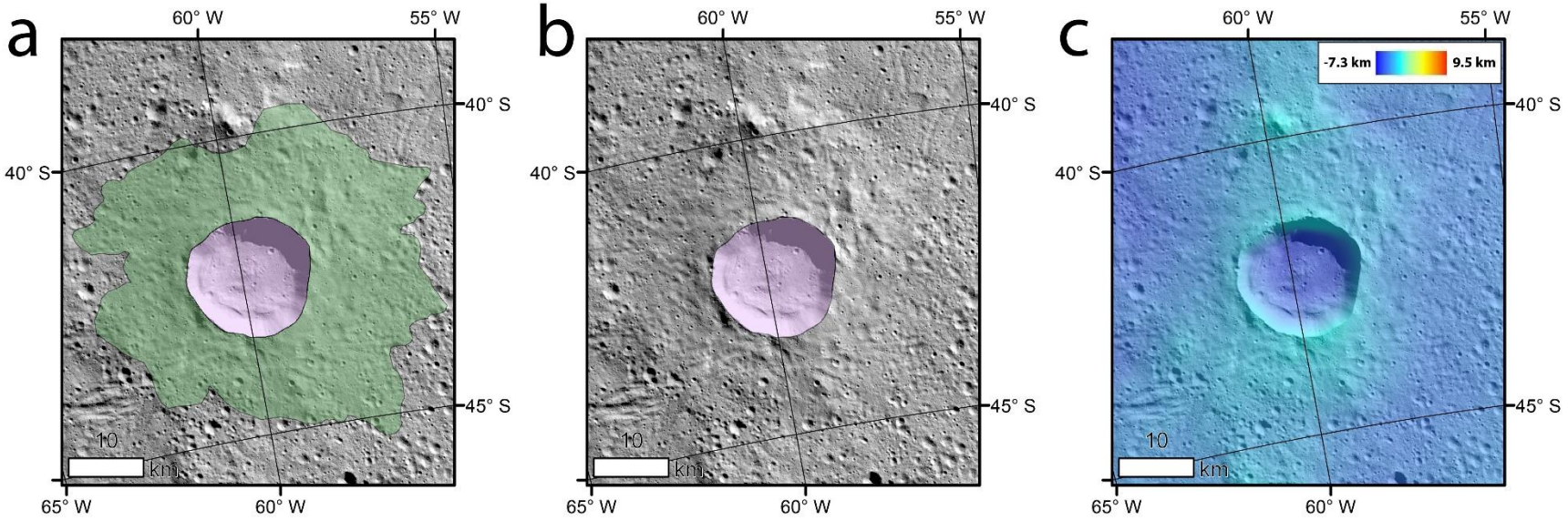

Figure A-9. (a) Besua crater with mapped cuspate/lobate FAE deposit. (b) same image as (a) but with ejecta related map overlays removed. (c) same image as (a) but with all mapping overlays replaced by color coded HAMO derived topography.

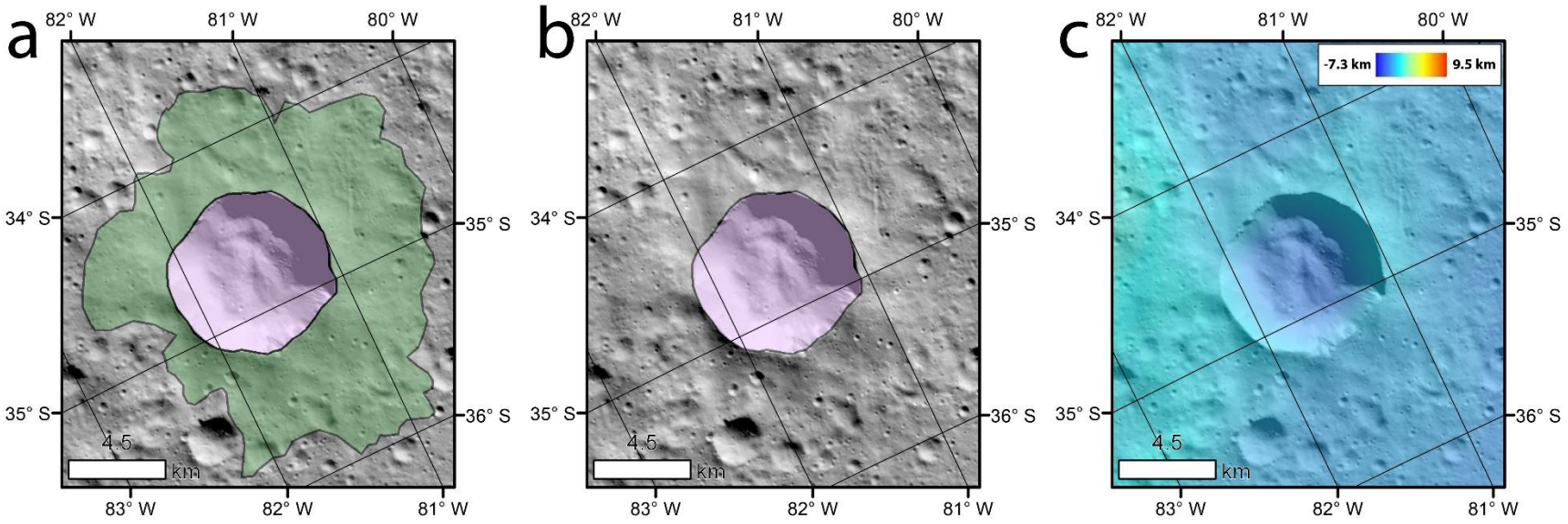

Figure A-10. (a) Unnamed crater (-81.57° E, -34.76° N) with mapped cuspate/lobate FAE deposit. (b) same image as (a) but with ejecta related map overlays removed. (c) same image as (a) but with all mapping overlays replaced by color coded HAMO derived topography.

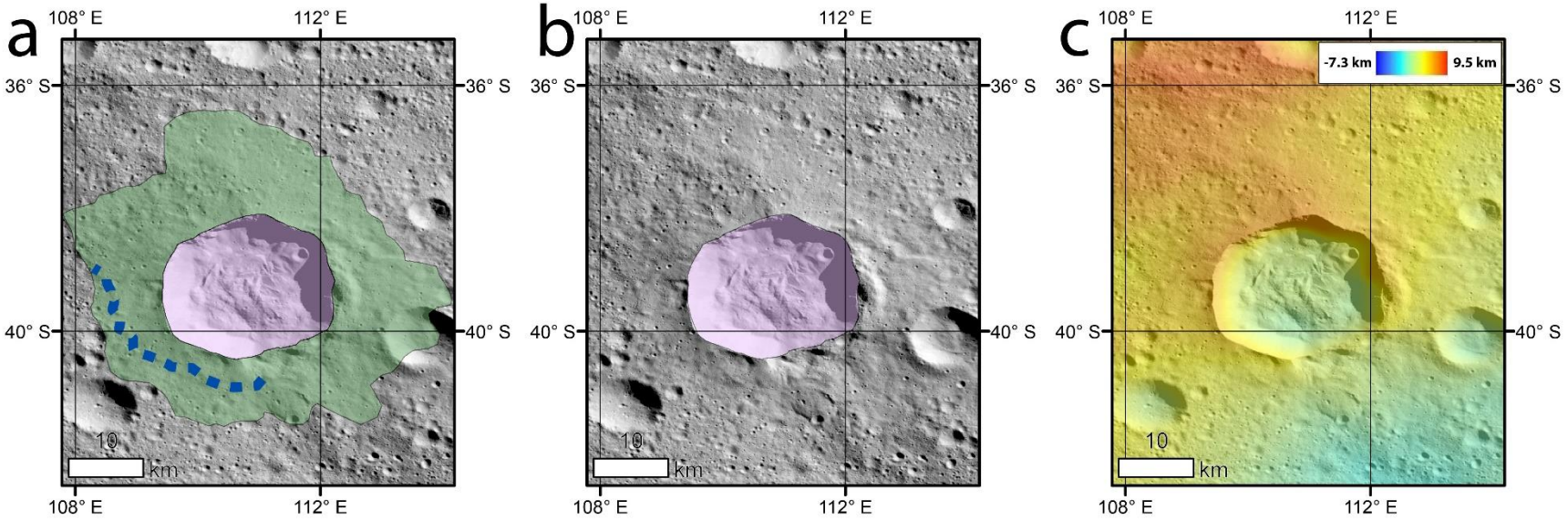

Figure A-11. (a) Unnamed crater (110.82° E, -39.29° N) with mapped cuspate/lobate FAE deposit. (b) same image as (a) but with ejecta related map overlays removed. (c) same image as (a) but with all mapping overlays replaced by color coded HAMO derived topography.

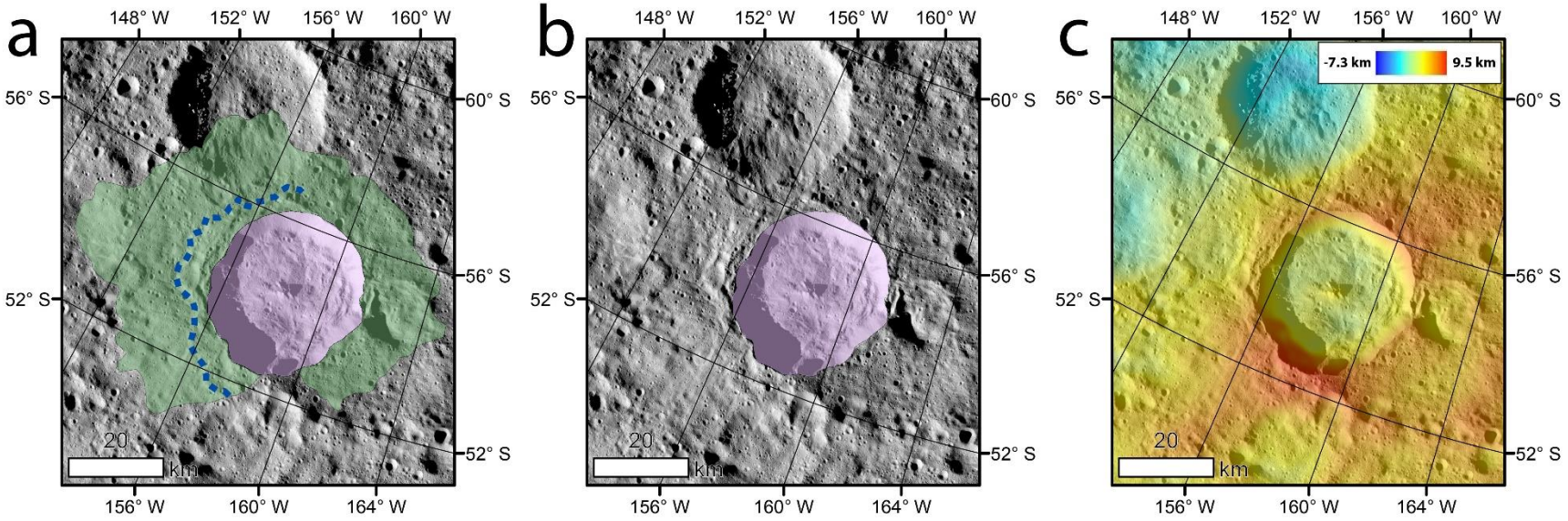

Figure A-12. (a) Unnamed crater (-158.41° E, -54.39° N) with mapped cuspate/lobate FAE deposit. (b) same image as (a) but with ejecta related map overlays removed. (c) same image as (a) but with all mapping overlays replaced by color coded HAMO derived topography.

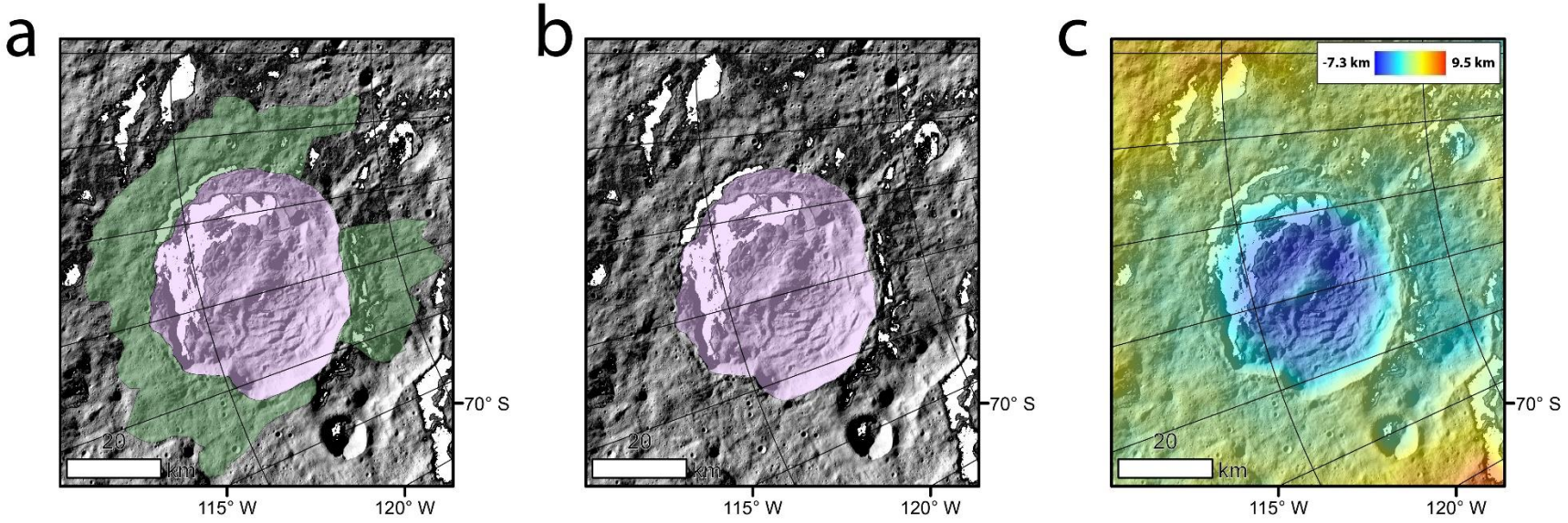

Figure A-13. (a) Sekhet crater with mapped cuspate/lobate FAE deposit. (b) same image as (a) but with ejecta related map overlays removed. (c) same image as (a) but with all mapping overlays replaced by color coded HAMO derived topography.

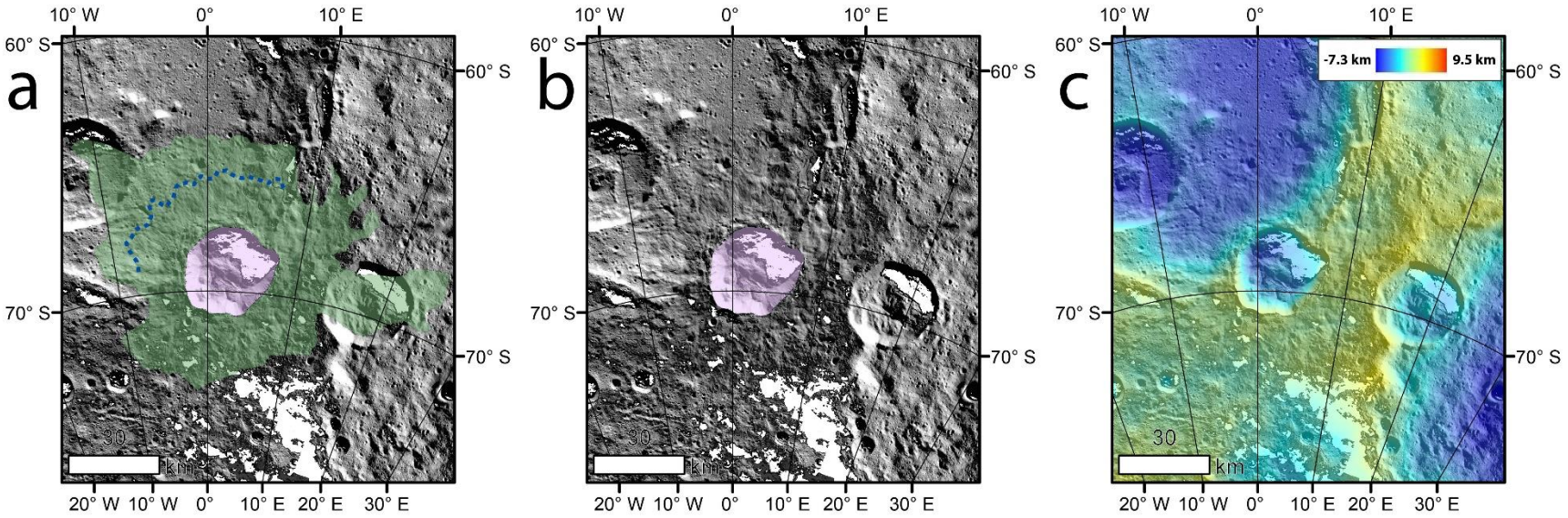

Figure A-14. (a) Jacheongbi crater with mapped cuspate/lobate FAE deposit. (b) same image as (a) but with ejecta related map overlays removed. (c) same image as (a) but with all mapping overlays replaced by color coded HAMO derived topography.

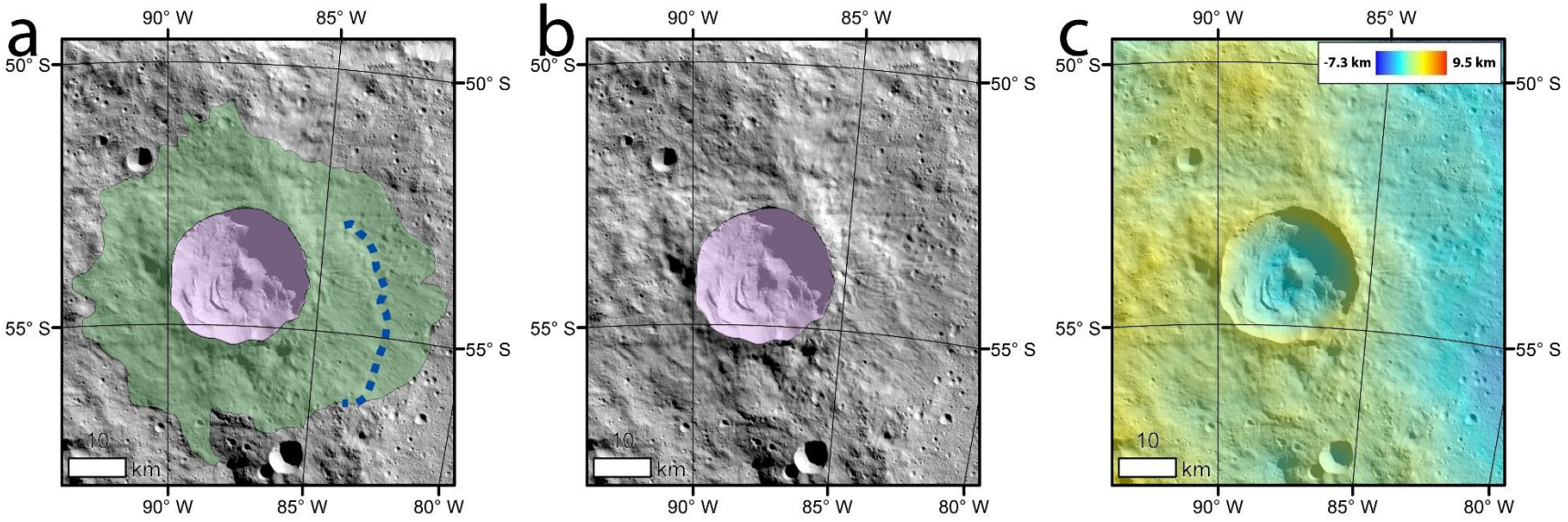

Figure A-15. (a) Nunghui crater with mapped cuspate/lobate FAE deposit. (b) same image as (a) but with ejecta related map overlays removed. (c) same image as (a) but with all mapping overlays replaced by color coded HAMO derived topography.

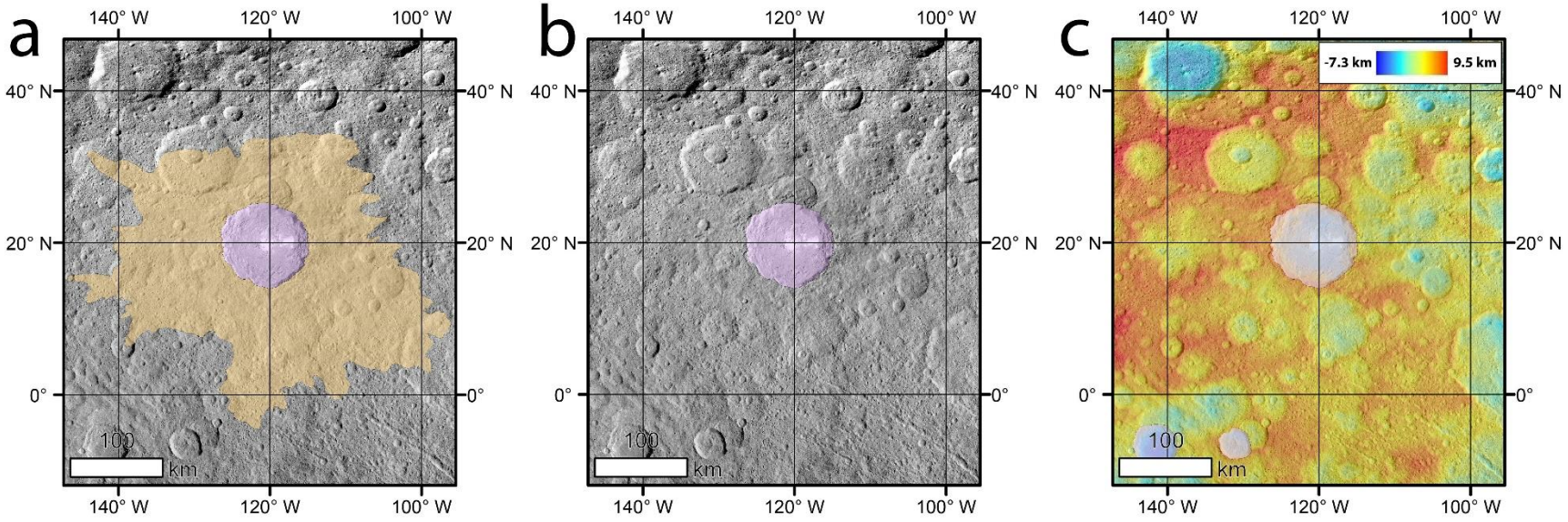

Figure A-16. (a) Occator crater with mapped channelized FAE deposit. (b) same image as (a) but with ejecta related map overlays removed. (c) same image as (a) but with all mapping overlays replaced by color coded HAMO derived topography.

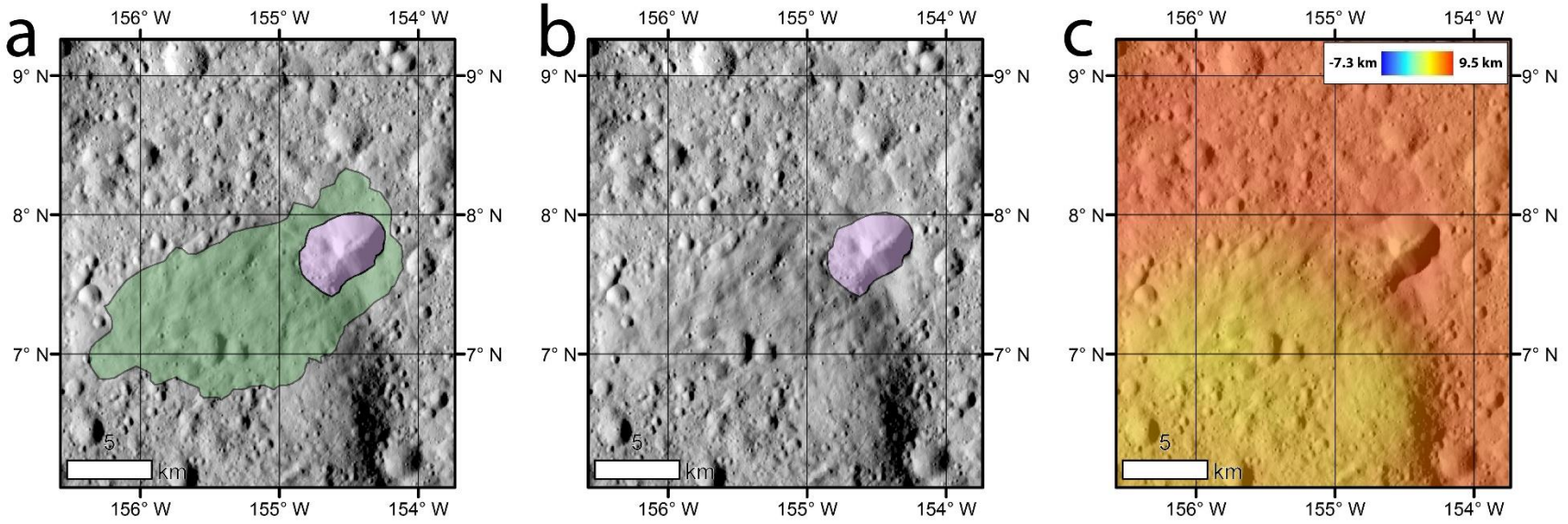

Figure A-17. (a) Unnamed crater (-154.56° E, 7.74° N) with mapped cuspate/lobate FAE deposit. (b) same image as (a) but with ejecta related map overlays removed. (c) same image as (a) but with all mapping overlays replaced by color coded HAMO derived topography.

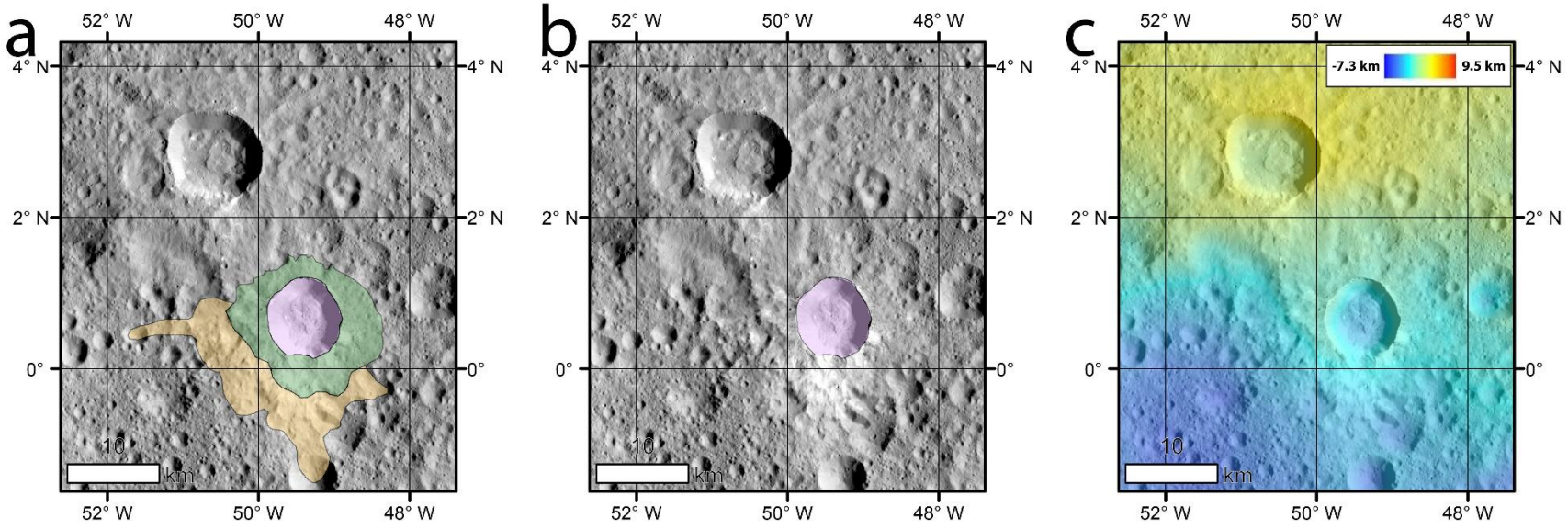

Figure A-18. (a) Xevioso crater with mapped cuspate/lobate and channelized FAE deposits. (b) same image as (a) but with ejecta related map overlays removed. (c) same image as (a) but with all mapping overlays replaced by color coded HAMO derived topography.

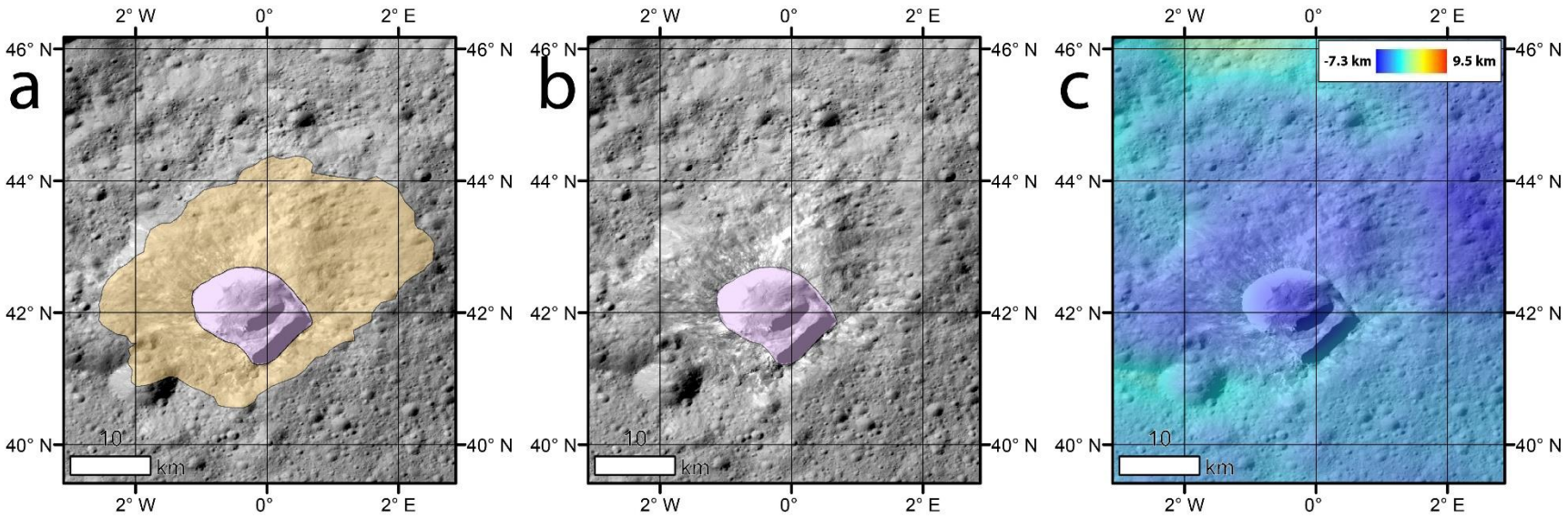

Figure A-19. (a) Oxo crater with mapped channelized FAE deposit. (b) same image as (a) but with ejecta related map overlays removed. (c) same image as (a) but with all mapping overlays replaced by color coded HAMO derived topography.

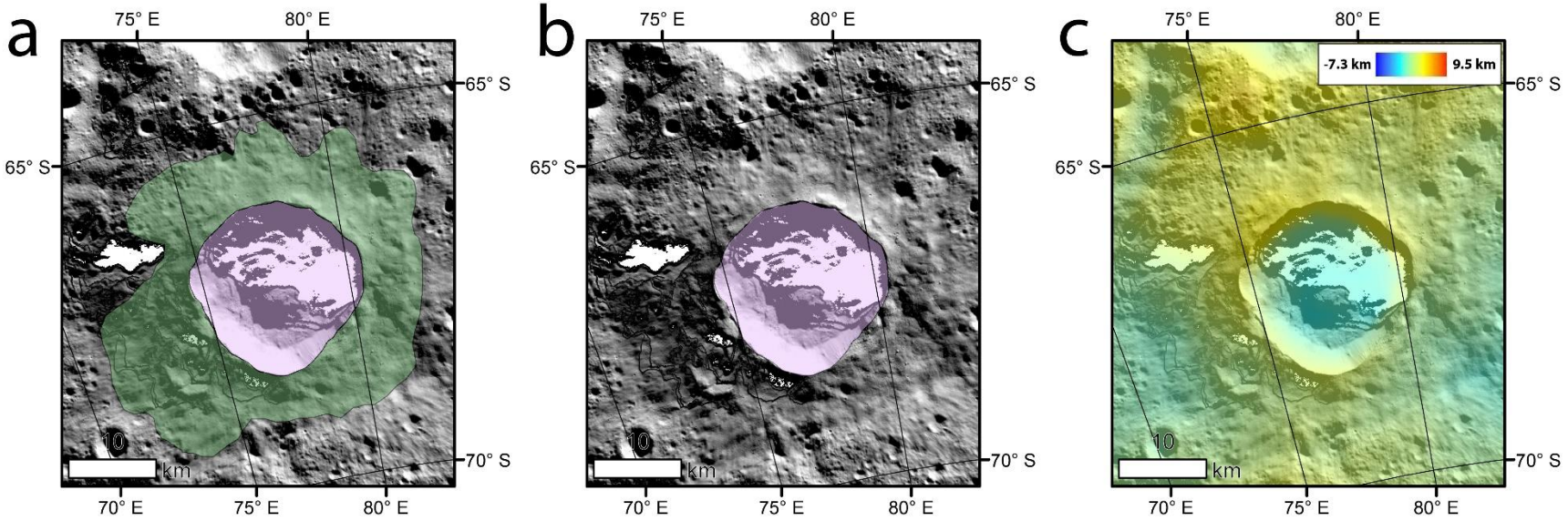

Figure A-20. (a) Ratumaibulu crater with mapped cuspate/lobate FAE deposit. (b) same image as (a) but with ejecta related map overlays removed. (c) same image as (a) but with all mapping overlays replaced by color coded HAMO derived topography.

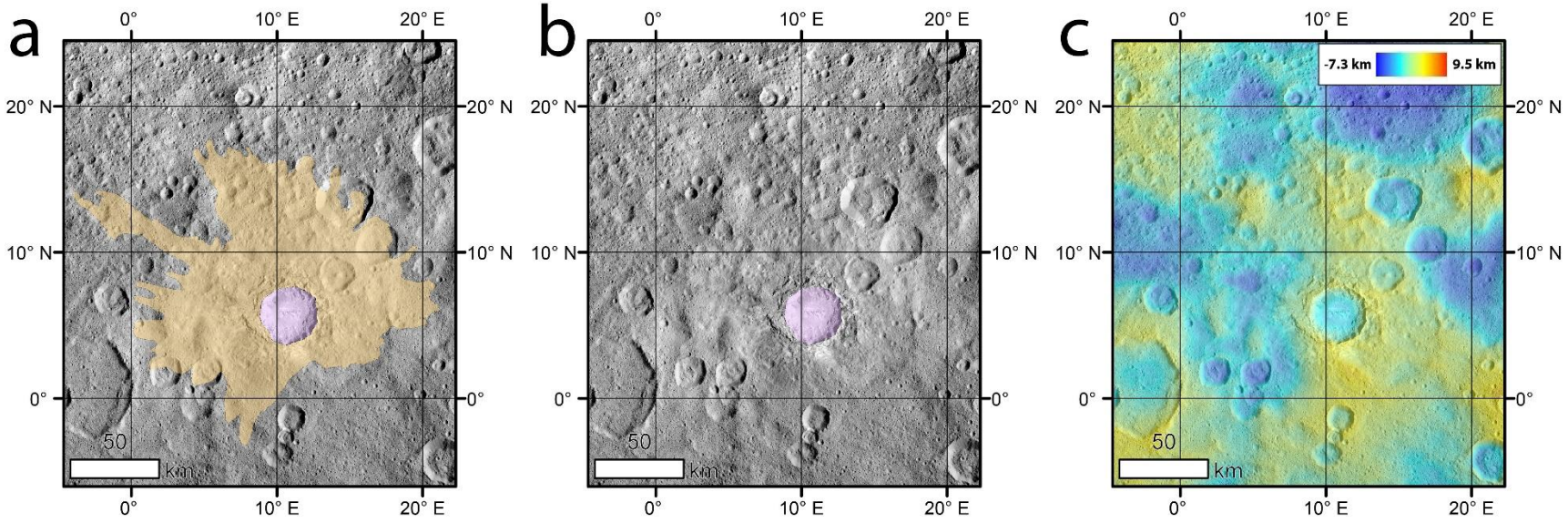

Figure A-21. (a) Haulani crater with mapped channelized FAE deposit. (b) same image as (a) but with ejecta related map overlays removed. (c) same image as (a) but with all mapping overlays replaced by color coded HAMO derived topography.

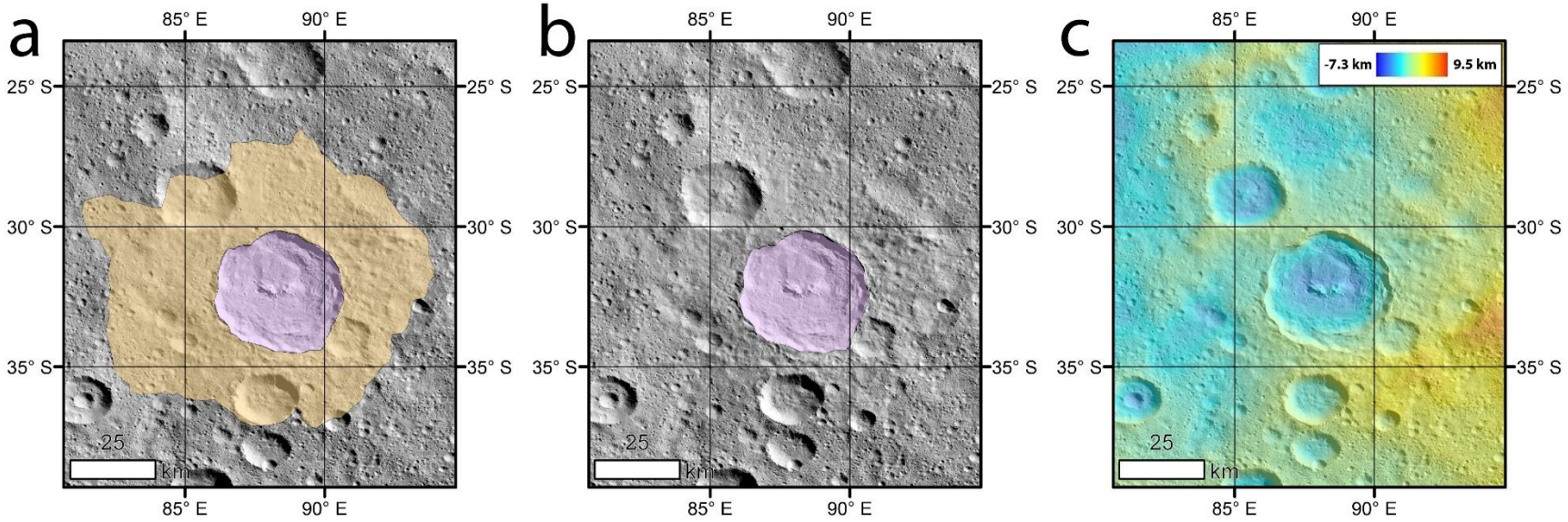

Figure A-22. (a) Tupo crater with mapped channelized FAE deposit. (b) same image as (a) but with ejecta related map overlays removed. (c) same image as (a) but with all mapping overlays replaced by color coded HAMO derived topography.

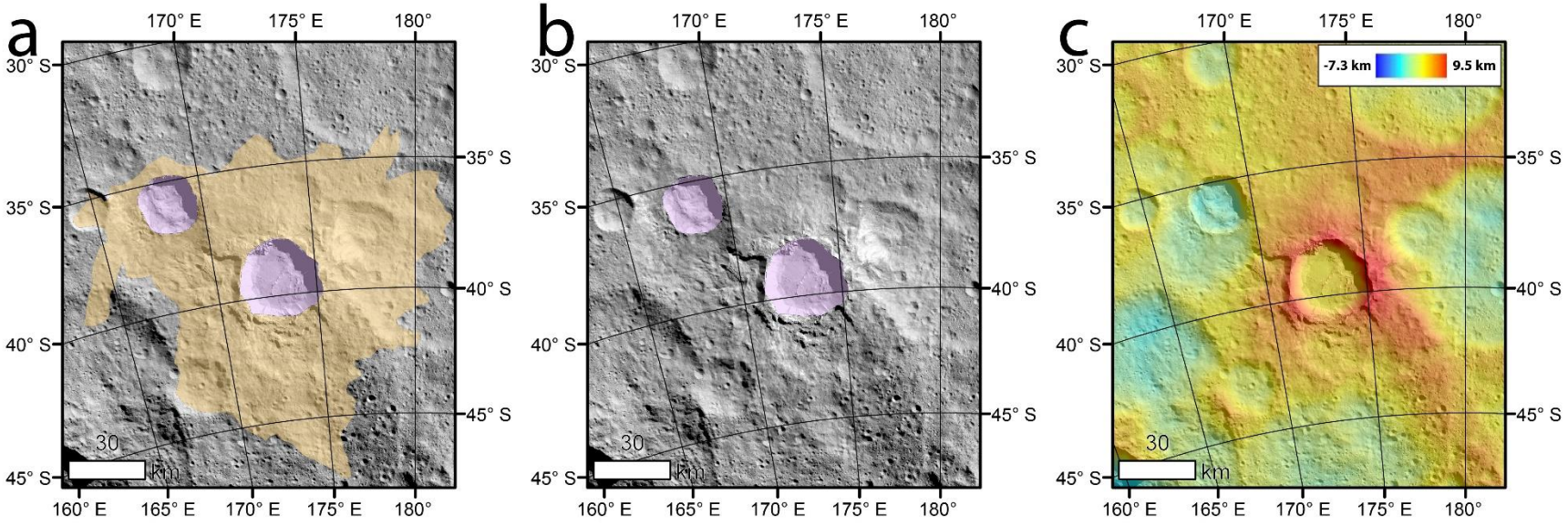

Figure A-23. (a) Juling and Kupalo craters with mapped channelized FAE deposits. (b) same image as (a) but with ejecta related map overlays removed. (c) same image as (a) but with all mapping overlays replaced by color coded HAMO derived topography.

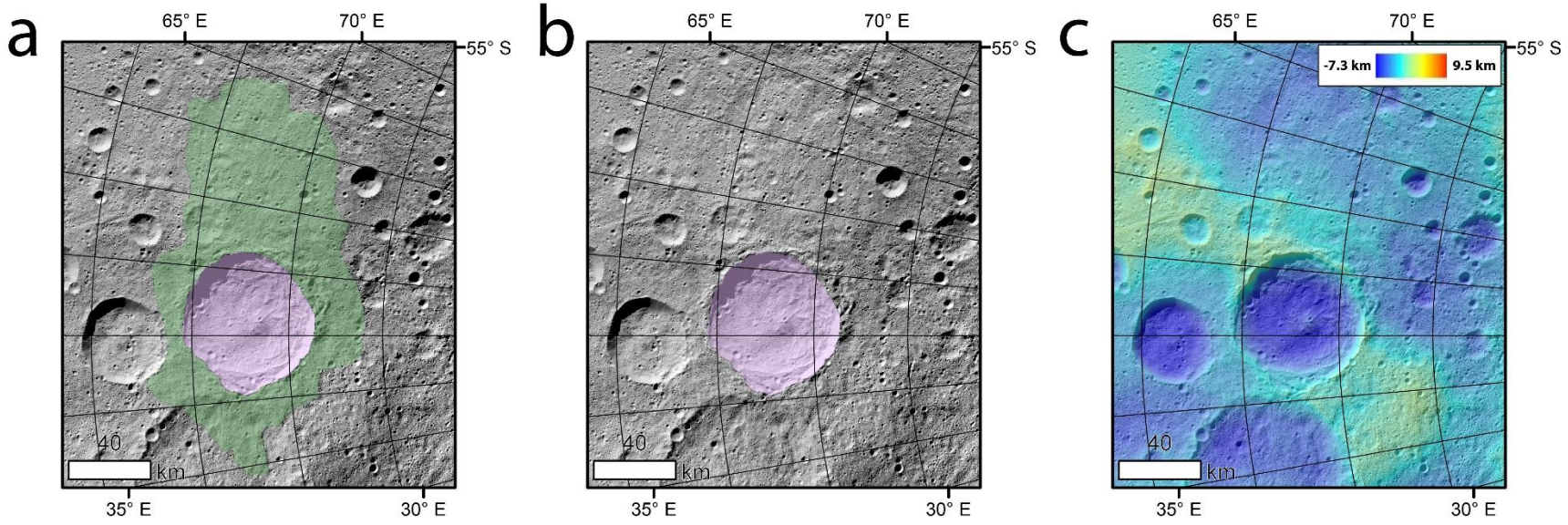

Figure A-24. (a) Sintana crater with mapped cuspate/lobate FAE deposit. (b) same image as (a) but with ejecta related map overlays removed. (c) same image as (a) but with all mapping overlays replaced by color coded HAMO derived topography.

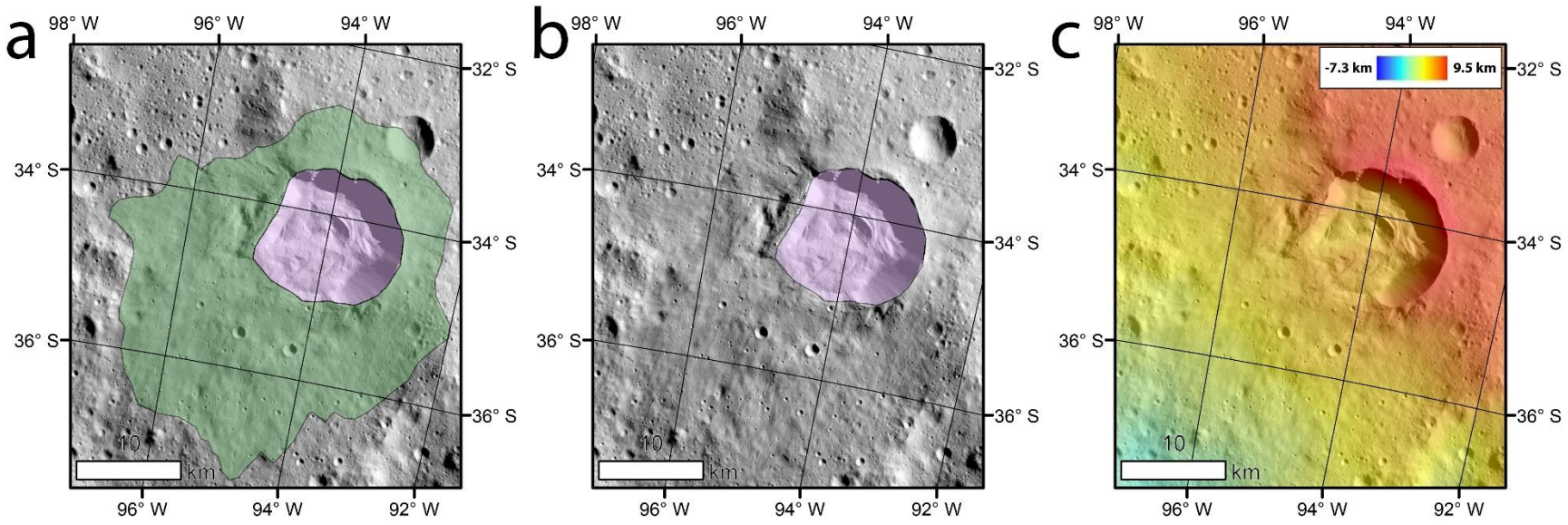

Figure A-25. (a) Unnamed crater (77.49° E, -67.29° N) with mapped cuspate/lobate FAE deposit. (b) same image as (a) but with ejecta related map overlays removed. (c) same image as (a) but with all mapping overlays replaced by color coded HAMO derived topography.

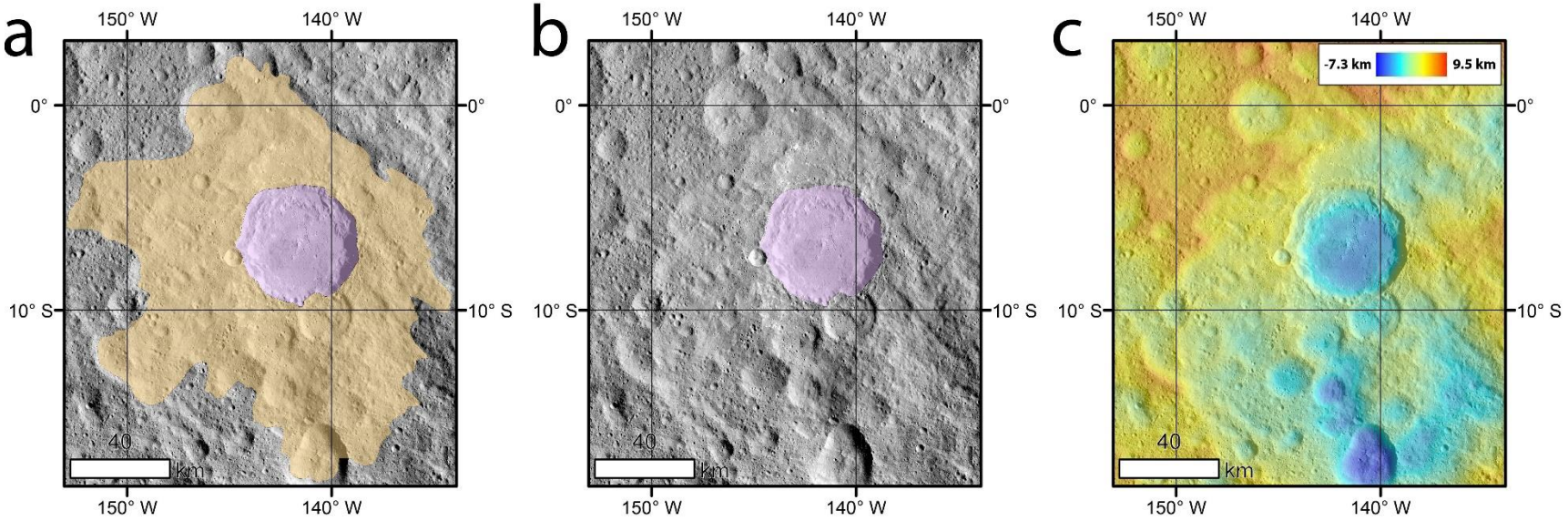

Figure A-26. (a) Azacca crater with mapped channelized FAE deposit. (b) same image as (a) but with ejecta related map overlays removed. (c) same image as (a) but with all mapping overlays replaced by color coded HAMO derived topography.

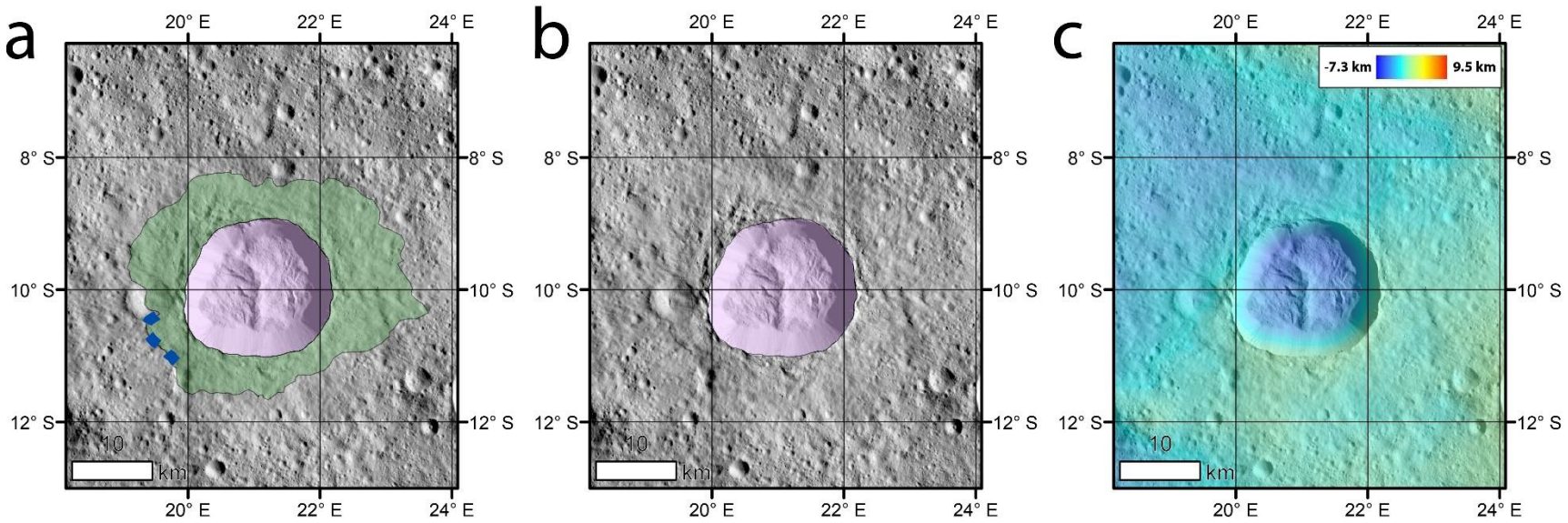

Figure A-27. (a) Unnamed crater (21.07° E, 10.00° N) with mapped cuspate/lobate FAE deposit. (b) same image as (a) but with ejecta related map overlays removed. (c) same image as (a) but with all mapping overlays replaced by color coded HAMO derived topography.

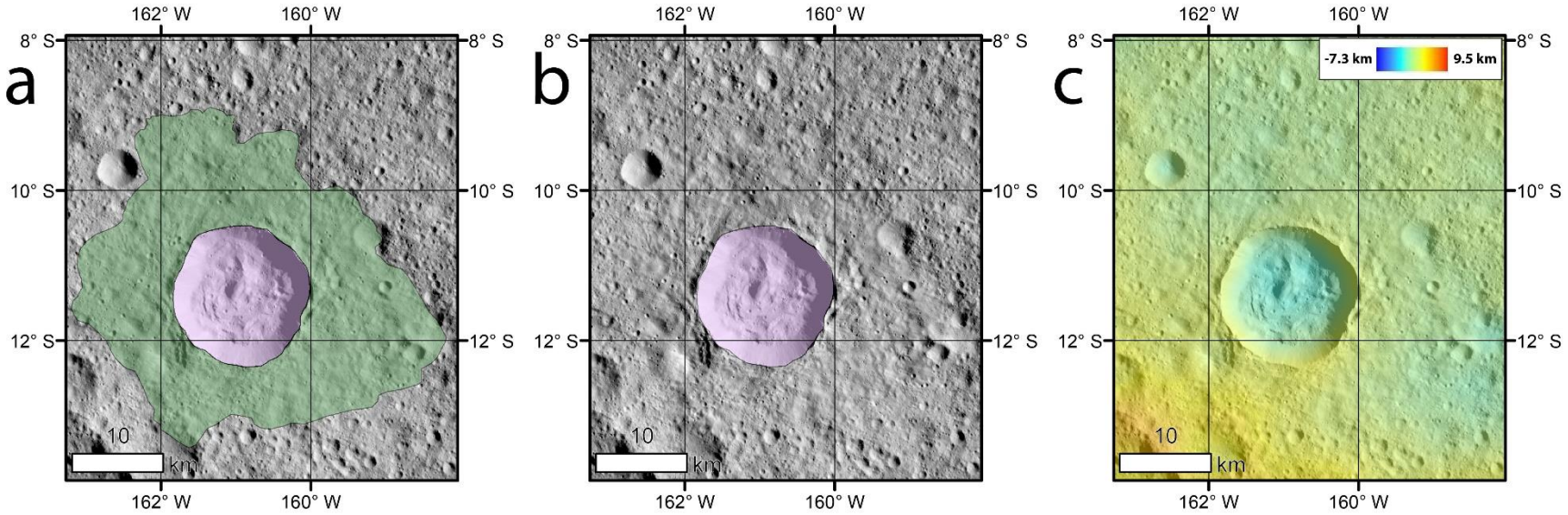

Figure A-28. (a) Unnamed crater (-160.93° E, -11.39° N) with mapped cuspate/lobate FAE deposit. (b) same image as (a) but with ejecta related map overlays removed. (c) same image as (a) but with all mapping overlays replaced by color coded HAMO derived topography.

Bibliography

Altwegg, K., Balsiger, H., Bar-Nun, A., Berthelier, J. J., Bieler, A., Bochsler, P., Briois, C., Calmonte, U., Combi, M., De Keyser, J., Eberhardt, P., Fiethe, B., Fuselier, S., Gasc, S., Gombosi, T. I., Hansen, K. C., Hassig, M., Jackel, A., Kopp, E., Korth, A., LeRoy, L., Mall., U., Marty, B., Mousis, O., Neefs, E., Owen, T., Reme, H., Rubin, M., Semon, T., Tzou, C.-Y., Waite, H., Wurz, P., (2015). 67p/Churyumov-Gerasimenko, a Jupiter family comet with a high D/H ratio. *Science* 347, Issue 6220, 1261952. DOI: 10.1126/science.1261952

Ammannito, E., De Sanctis, M. C., Ciarniello, M., Frigeri, A., Carrozzo, F. G., Combe, J. –Ph., Ehlmann, B. L., Marchi, S., Mcsween, H. Y., Raponi, A., et al., (2016). Distribution of phyllosilicates on the surface of Ceres. *Science* 353, Issue 6303, aaf4279. DOI: 10.1126/science.aaf4279

Ancey, C., (2006). Plasticity and geophysical flows: A review. *Journal of Non-Newtonian Fluid Mechanics* 142. 4-35. https://doi.org/10.1016/j.jnnfm.2006.05.005

Arvidson R., J. Boyce, C. Chapman, M. Fulchignoni, H. Moore, G. Neukum, P. Schultz, L. Soderblom, R. Strom, A. Woronow, R. Y., (1979). Standard techniques for presentation and analysis of crater size-frequency data. *Icarus* 37, 467-474. https://doi.org/10.1016/0019-1035(79)90009-5

Baloga, S. M., Fagents, S. A., and P. J. Mouginis-Mark, (2005). Emplacement of martian rampart crater deposits. *J. Geophys. Res.: Planets* 110 (E10). http://dx.doi.org/ 10.1029/2004JE002338

Baloga, S. M., Glaze, L. S., Peitersen, M. N., Crisp, J. A., (2001). Influence of volatile loss on thickness and density profiles of active basaltic flow lobes. *J. Geophys. Res.: Solid Earth* 106 (B7), 13395–13405. http://dx.doi.org/10.1029/2000JB900475

Barlow, N. G. (2005). *A review of martian impact crater ejecta structures and their implications for target properties*. Large Meteorite Impacts III, Kenkmann, T., Hörz, F., Deutsch, A. 433–442.

Barlow, N. G., and J. M. Boyce, (2013). *Martian low-aspect-ratio layered ejecta (LARLE) craters: Constraints on formation models from analysis of LARLE distribution and characteristics*. Paper presented at Lunar Planet. Sci. XLIV. Abstract 1196.

Barlow, N. G., and T. L. Bradley, (1990). Martian impact craters: Correlations of ejecta and interior morphologies with diameter, latitude, and terrain. *Icarus* 87 (1), 156– 179. http://dx.doi.org/10.1016/0019-1035(90)90026-6

Barlow, N. G., and C. B. Perez, (2003). Martian impact crater ejecta morphologies as indicators of the distribution of subsurface volatiles. *J. Geophys. Res.* 108 (E8), 5085. http://dx.doi.org/10.1029/2002JE002036

Barlow, N. G., and A. Pollak, (2002). *Comparisons of ejecta mobility ratios in the northern and southern hemispheres of Mars*. Paper presented at Lunar Planet. Sci. XXXIII. Abstract 1322.

Barnouin, O. S., Zuber, M. T., Smith, D. E., Neumann, G. A., Herrick, R. R., Chappelow, J. E., Murchie, S. L., Prockter, L. M., (2012). The morphology of craters on Mercury: Results from MESSENGER flybys. *Icarus* 219, 414-427. doi.org/10.1016/j.icarus.2012.02.029

Barnouin-Jha, O. S., Baloga, S., and L. Glaze, (2005). Comparing landslides to fluidized crater ejecta on Mars. *J. Geophys. Res.* 110 (E4), E04010. http://dx.doi.org/10.1029/2003JE002214

Barnouin-Jha, O. S. and D. L. Buczkowski, (2007). *Comparing the runout distances of fluidized ejecta on Mars with mass movements on Earth*. Paper presented at Lunar Planet. Sci. XXXVIII. Abstract 1304.

Barnouin-Jha, O. S., and P. H. Schultz, (1998). Lobateness of impact ejecta deposits from atmospheric interactions. *J. Geophys. Res.: Planets* 103 (E11), 25739–25756. http://dx.doi.org/10.1029/98JE02025

Barnouin-Jha, O. S., Schultz, P. H., and J. H. Lever, (1999a). Investigating the interactions between an atmosphere and an ejecta curtain: 1. Wind tunnel tests. *J. Geophys. Res.* 104 (E11), 27105. http://dx.doi.org/10.1029/1999JE001026

Barnouin-Jha, O. S., Schultz, P. H., and J. H. Lever, (1999b). Investigating the interactions between an atmosphere and an ejecta curtain: 2. Numerical experiments. *J. Geophys. Res.* 104 (E11), 27117. http://dx.doi.org/10.1029/1999JE001027

Barsch, D., (1992). Permafrost creep and rockglaciers. *Permafrost and Periglacial Processes* 3, 175-188. https://doi.org/10.1002/ppp.3430030303

Basilevsky, A.T., Head, J.W., Hörz, F., Ramsley, K., (2015). Survival times of meter-sized rock boulders on the surface of airless bodies. *Planetary and Space Science* 117, 312-328. https://doi.org/10.1016/j.pss.2015.07.003

Beeman, M., Durham, W. B., and S. H. Kirby (1988). Friction of ice, *J. Geophys. Res.* 93, 7625–7633. https://doi.org/10.1029/JB093iB07p07625

Bernknopf, R. L., Brookshire, D. S., Soller, D. R., McKee, M. J., Sutter, J. F., Matti, J. C., Campbell, R. H., (1993) Societal Value of Geologic Maps. *USGS Circular* 1111.

Bland, M, T., (2013). Predicted crater morphologies on Ceres: Probing internal structure and evolution. *Icarus* 226, 510-521. http://dx.doi.org/10.1016/j.icarus.2013.05.037

Bland, M.T., Raymond, C.A., Schenk, P.M., Fu., R.R., Kneissl, T., Pasckert, J.H., Hiesinger, H., Preusker, F., Park, R.S., Marchi, S., King, S.D., Castillo-Rogez, J.C., Russell, C.T., (2016). Composition and structure of the shallow subsurface of Ceres revealed by crater morphology. *Nature Geoscience* 9, 538-542.

Bland, M. T., Sizemore, H. G., Buczkowski, D. L., Sori, M. M., Raymond, C. A., King, S. D., Russell, C. T., (2018). *Why is Ceres lumpy? Surface deformation induced by solid-state subsurface flow*. Paper presented at Lunar Planet. Sci. XLIX. Abstract 1627.

Biren. M. B., van Soet, M., Wartho, J. -A., Spray, J. G., (2014). Dating the cooling of exhumed central uplifts of impact structures by the (U–Th)/He method: A case study at Manicouagan. *Chemical Geology* 377, 56-71. https://doi.org/10.1016/j.chemgeo.2014.03.013.

Boehnke, P., and M. T. Harrison, (2016). Illusory Late Heavy Bombardments. *PNAS* 113, 10802-10806. https://doi.org/10.1073/pnas.1611535113

Bowling, T. J., Ciesla, F. J., Davison, T. M., Scully, J. E. C., Castillo-Rogez, J. C., Marchi, S., Johnson, B. C., (2018). Post-impact thermal structure and cooling timescales of Occator crater on asteroid 1 Ceres. *Icarus* 320, 110-118. https://doi.org/10.1016/j.icarus.2018.08.028.

Boyce, J., Barlow, N., Mouginis-Mark, P. & Stewart, S., (2010), Rampart craters on Ganymede: Their implications for fluidized ejecta emplacement. *Meteoritics & Planetary Science* 45, 638-661. doi:10.1111/j.1945-5100.2010.01044.x

Boyce, J. M., Barlow, N. G., and L. Wilson, (2012). *Model for the emplacement of the outer ejecta layer of low-aspect-ratio layer ejecta craters by turbulent flow*. Paper presented at Lunar Planet. Sci. XLIV. Abstract 1196.

Boyce, J. M., and P. J. Mouginis-Mark, (2006). Martian craters viewed by the Thermal Emission Imaging System instrument: Double-layered ejecta craters. *J. Geophys. Res.* 111 (E10). http://dx.doi.org/10.1029/2005JE002638

Buczkowski, D. L., Williams, D. A., Scully, J. E. C., Mest, S. C., Crown, D. A., Schenk, P. M., Jaumann, R., Roatsch, T., Preusker, F., Platz, T., Nathues, A., Hoffman, M., Schaefer, M., Marchi, S., De Sanctis, M. C., Raymond, C. A., Russell, C. T., (2018). The geology of the Occator Quadrangle of dwarf planet Ceres: Floor-fractured craters and other geomorphic evidence of cryomagmatism, *Icarus* 316, 128-139. https://doi.org/10.1016/j.icarus.2017.05.025.

Buczkowski, D. L., Schmidt, B. E., Williams, D. A., Mest, S. C., Scully, J. E. C., Ermakov, A., Preusker, F., Schenk, P., Otto, K., Hiesinger, H., O'Brien, D., Marchi, S., Sizemore, H., Hughson, K. H. G., Chilton, H., Bland, M. T., Byrne, S., Schorghofer, N., Ruesch, O., Platz, T., Jaumann, R., Roatsch, T., Sykes, M. V., Nathues, A., De Sanctis, M. C., Raymond, C. A., Russell, C. T., (2016). The geomorphology of Ceres. *Science* 353, Issue 6303. https://doi.org/10.1126/science.aaf4332

Buratti, B. J. and P. A. Dalba, (2013). Vesta, vestoids, and the HED meteorites: Interconnections and differences based on Dawn Framing Camera observations, *J. Geophys. Res. Planets* 118, 1991–2003. doi:10.1002/jgre.20152.

Burbine, T.H., (1998). Could G-class asteroids be the parent bodies of the CM chondrites? *Meteoritics & Planetary Science* 33, 253-258. https://doi.org/10.1111/j.1945-5100.1998.tb01630.x

Byerlee, J., (1978). Friction of Rocks. *Pure and Applied Geophysics* 116, 615-626. https://doi.org/10.1007/BF00876528.

Campins, H., Hargrove, K., Pinilla-Alonso, N., Howell, E. S., Kelly, M. S., Licandro, J., Mothe-Diniz, T., Fernandez, Y., Ziffer, J., (2010). Water ice and organics on the surface of the asteroid 24 Themis. *Nature* 464, 1320-1321. DOI: 10.1038/nature09029

Carr, M. H., Crumpler, L. S., Cutts, J. A., Greeley, R., Guest, J. E., Masursky, H., (1977). Martian impact craters and emplacement of ejecta by surface flow. *J. Geophys. Res.* 82 (28), 4055–4065. http://dx.doi.org/10.1029/JS082i028p04055

Carr, M. H., Kirk, R. L., McEwen, A., Veverka, J., Thomas, P., Head, J. W., Murchie, S., (1994). The geology of Gaspra. *Icarus* 107, 61-71. DOI: 10.1006/icar.1994.1006

Carr, M. H. and G. G. Schaber, (1977). Martian permafrost features. *Journal of Geophysical Research* 82, 4039-4054. https://doi.org/10.1029/JS082i028p04039

Carrozzo, F. G., De Sanctis, M. C., Raponi, A., et al., (2018). Nature, Formation, and Distribution of Carbonates on Ceres. *Science Advances* 4, no. 3, e1701645 DOI: 10.1126/sciadv.1701645

Castillo-Rogez, J.C., Bowling, T., Fu, R.R., McSween, H.Y., Raymond, C.A., Rambaux, N., Travis, B., Marchi, S., O'Brien, D.P., Johnson, B.C., King, S.D., Bland, M.T., Neveu, M.,

De Sanctis, M.C., Ruesch, O., Sykes, M.V., Prettyman, T.H., Park, R.S., Russell, C.T., (2016). *Loss of Ceres' icy shell from impacts: Assessment and implications*. Paper presented at Lunar Planet. Sci. XLVII, Abstract 3012.

Castillo-Rogez, J.C. and T. B. McCord, (2010). Ceres' evolution and present state constrained by shape data. *Icarus* 205, 443–459. https://doi.org/10.1016/j.icarus.2009.04.008

Castillo-Rogez, J. , Neveu, M. , McSween, H. Y., Fu, R. R., Toplis, M. J. and Prettyman, T., (2018). Insights into Ceres's evolution from surface composition. Meteorit Planet Sci, 53: 1820-1843. doi:10.1111/maps.13181

Chambers, J., (2014). Forming terrestrial planets. *Science* 344, Issue 6183, 479-480. DOI: 10.1126/science.1252257

Chilton, H. T., Schmidt, B. E., Duarte, K., Ferrier, K. L., Hughson, K. H. G., Scully, J. E. C., Wray, J. J., Sizemore, H., Nathues, A., Platz, T., Schorghofer, N., Schenk, P. M., Landis, M., Bland., M., Byrne, S., Russell, C. T., Raymond, C. A., (2019). Landslides on Ceres: Inferences into ice content and layering in the upper crust. *Journal of Geophysical Research: Planets*, 124. https://doi.org/10.1029/2018JE005634

Choukroun M., Kieffer S. W., Lu X., Tobie G., (2013). Clathrate Hydrates: Implications for Exchange Processes in the Outer Solar System, pp 409-454. In: Gudipati M., Castillo-Rogez J. (eds) *The Science of Solar System Ices*. Astrophysics and Space Science Library, vol 356. Springer, New York, NY

Combe, J. -P., McCord, T. B., Tosi, F., Ammannito, E., Carrozzo, F. G., De Sanctis, M. C., Raponi, A., Byrne, S., Landis, M., Hughson, K. H. G., Raymond, C. A., Russell, C. T., (2016). Detection of local H_2O exposed at the surface of Ceres. *Science* 353, Issue 6303, aaf3010. https://doi.org/10.1126/science.aaf3010

Combe, J. -P., Raponi, A., Tosi, F., De Sanctis, M. C., Carrozzo, F. G., Zambon, F., Ammannito, E., Hughson, K. H. G., Nathues, A., Hoffmann, M., Platz, T., Thangjam, G., Schorghofer, N., Schroder, S., Byrne, S., Landis, M. E., Ruesch, O., McCord, T. B., Johnson, K., Singh, S., Raymond, C. A., Russell, C. T., (2019). Exposed H_2O-rich areas detected on Ceres with the dawn visible and infrared mapping spectrometer. *Icarus* 318, 22–41. https://doi.org/10.1016/j.icarus.2017.12.008

Consolmagno, G. J., Britt, D. T., and R. J. Macke, (2008). The significance of meteorite density and porosity. *Chemie der Erde* 68, 1-29. doi:10.1016/j.chemer.2008.01.003

Coradini, A., Magni, G., and D. Turrini, (2010). From gas to satellitesimals: Disk formation and evolution. *Sapce Sci. Rev.* 153, 411-429. 10.1007/s11214-009-9611-9

Coradini, A., Turrini, D., Federico, C., Magni, G., (2011). Vesta and Ceres: Crossing the history of the solar system. *Space Sci. Rev.* 163, 25-40. https://doi.org/10.1007/s11214-011-9792-x

Costard, F. M., (1989). The spatial distribution of volatiles in the martian hydrolithosphere. *Earth Moon Planets* 45, 265–290. http://dx.doi.org/10.1007/BF00057747

Crown, D. A., Sizemore, H. G., Yingst, R. A., Mest, S. C., Platz, T., Berman, D. C., Schmedemann, N., Buczkowski, D. L., , D. A., Roatsch, T., Preusker, F., Raymond, C. A., Russell, C. T., (2018). Geologic mapping of the Urvara and Yalode Quadrangles of Ceres. *Icarus* 316, 167-190, https://doi.org/10.1016/j.icarus.2017.08.004

Daanan, R. P., Grosse, G., Darrow, M. M., Hamilton, T. D., Jones, B.M., (2012). Rapid movement of frozen debris-lobes: Implications for permafrost degradation and slope instability in the south-central Brooks Range, Alaska. *Nat. Hazards Earth Syst. Sci.* 12, 1521-1537. DOI: 10.5194/nhess-12-1521-2012

Darrow, M.M., Gyswyt, N.L., Simpson, J.M., Daanen, R.P., Hubbars, T.D., (2016). Frozen debris lobe morphology and movement: an overview of eight dynamic features, southern Brooks Range, Alaska. *The Cryosphere* 10, 977-993. https://doi.org/10.5194/tc-10-977-2016

De Blasio, F. V., (2011). Introduction to the Physics of Landslides. Springer. https://doi.org/10.1007/978-94-007-1122-8

De Blasio, F. V., (2014). Friction and dynamics of rock avalanches travelling on glaciers. *Geomorphology* 213, 88-98. https://doi.org/10.1016/j.geomorph.2014.01.001

DeMeo, F. E. and B. Carry, (2014). Solar System evolution from compositional mapping of the asteroid belt. *Nature* 505, 629-634. https://doi.org/10.1038/nature12908

De Sanctis, M.C., Ammannito, E., Raponi, A., Marchi, S., McCord, T.B., McSween, H.Y., Capaccioni, F., Capria, M.T., Carrozzo, F.G., Ciarniello, M., Longobardo, A., Tosi, F., Fonte, S., Formisano, M., Frigeri, A., Giardino, M., Magni, G., Palomba, E., Turrini, D., Zambon, F., Combe, J.-P., Feldman, W., Jaumann, R., McFadden, L.A., Pieters, C.M., Prettyman, T., Toplis, M., Raymond, C.A., Russell, C.T., (2015). Ammoniated phyllosilicates with a likely outer Solar System origin on (1) Ceres. *Nature* 528, 241-244. https://doi.org/10.1038/nature16172

De Sanctis, M.C., Raponi, A., Ammannito, E., Ciarniello, M., Toplis, M. J., McSween, H. Y., Castillo-Rogez, J. C., Ehlmann, B. L., Carrozzo, F. G., Marchi, S., Tosi, F., Zambon, F., Capaccioni, F., Capria, M. T., Fonte, S., McCord, T. B., Capria, M. T., Formisano, M., Frigeri, A., Giardino, M., Longobardo, A., Magni, G., Palomba, E., McFadden, L. A., Pieters, C. M., Jaumann, R., Schenk, P., Mugnuolo, R., Raymond, C. A., Russell, C. T.,

(2016). Bright carbonate deposits as evidence of aqueous alteration on (1) Ceres, *Nature* 536, 54-57. https://doi.org/10.1038/nature18290

De Sanctis, M.C., Coradini, A., Ammannito, E., Filacchione, G., Capria, M.T., Fonte, S., Magni, G., Barbis, A., Bini, A., Dami, M., Ficai-Veltroni, I., Preti, G., VIR Team, (2011). The VIR spectrometer. *Space Science Reviews* 163, 329-369. https://doi.org/10.1007/978-1-4614-4903-4_13

Duarte, K. D., Schmidt, B. E., Chilton, H. T., Hughson, K. H. G., Sizemore, H., Scully, J. E. C., Nathues, A., Platz, T., Schorghofer, N., Ferrier, K. L., Russell, C. T., Raymond, C. A. (*Submitted to JGR: Planets*) Landslides on Ceres: Diversity and geologic context.

Durham, W. B., Kirby, S. H., and L. A. Stern, (1992). Effects of dispersed particulates on the rheology of water ice at planetary conditions, *J. Geophys. Res.*, 97 (E12), 20883–20897, doi: 10.1029/92JE02326

Durham, W. B., Kirby, S. H. and L. A. Stern, (1997), Creep of water ices at planetary conditions: A compilation, *J. Geophys. Res.*, 102 (E7), 16293–16302, doi:10.1029/97JE00916

Durham, W. B., Kirby, S. H., Stern, L. A., and W. Zhang, (2003), The strength and rheology of methane clathrate hydrate, *J. Geophys. Res*., 108, 2182, doi:10.1029/2002JB001872, B4.

Ermakov, A. I., Kreslavsky, M., Scully, J. E. C., Hughson, K. H. G., Park, R. S., (2019). Surface roughness and gravitational slope distributions of Vesta and Ceres. *Journal of Geophysical Research: Planets* 124, 14– 30. https://doi.org/10.1029/2018JE005813

Ermakov, A. I., Fu, R. R., Castillo-Rogez, J. C., Raymond, C. A., Park, R. S., Preusker, F.,…Zuber, M. T., (2017). Constraints on Ceres' internal structure and evolution from its shape and gravity measured by the Dawn spacecraft. *Journal of Geophysical Research: Planets* 122, 2267–2293. https://doi.org/10.1002/2017JE005302.

Ermakov, A.I., Zuber, M.T., Smith, D.E., Fu, R.R., Raymond, C.A., Park, R.S., Russel, C.T., (2016). *Evaluation of Ceres' compensation state*. Paper presented at Lunar Planet. Sci. XLVII, Abstract 1708.

Evans, S.G., Hunger, O., and E. G. Enegren, (1993). The Avalanche Lake rock avalanche, Mackenzie Mountains, Northwest Territories, Canada: description, dating, and dynamics. Geological Survey of Canada Contribution 45693, 749-768.

Fassett, C. I., and J. W. Head III (2008). The timing of martian valley network activity: Constrains from buffered crater counting. *Icarus* 195, 61-89, doi: 10.1016/j.icarus.2007.12.009

Fleming, R.W., Ellen, S.D., ans M. A. Algus, (1989). Transformation of dilative and contractive landslide debris into debris flows – An example from Marin County, California. *Engineering Geology* 27, 201-223. https://doi.org/10.1016/0013-7952(89)90034-3

Fu, R. R., Ermakov, A. I., Marchi, S., Castillo-Rogez, J. C., Raymond, C. A., Hager, B. H., Zuber, M. T., King, S. D., Bland, M. T., De Sanctis, M. C., Preusker, F., Park, R. S., Russell, C. T., (2017). The interior structure of Ceres as revealed by surface topography. *Icarus* 476, 153-164, https://doi.org/10.1016/j.epsl.2017.07.053

Gault, D. E. and R. Greeley, (1978). Exploratory experiments of impact craters formed in viscous-liquid targets: Analogs for martian rampart craters? *Icarus 34* (3), 486–495. https://doi.org/10.1016/0019-1035(78)90040-4

Giese, B., Wagner, R., Hussmann, H., Neukum, G., Perry, J., Helfenstein, P., Thomas, P. C., (2008). Enceladus: An estimate of heat flux and lithospheric thickness from flexurally supported topography, *Geophys. Res. Lett.* 35, L24204, doi: 10.1029/2008GL036149.

Giese, B., Wagner, R., Neukum, G., Helfenstein, P., Thomas, P. C., (2007). Tethys: Lithospheric thickness and heat flux from flexurally supported topography at Ithaca Chasma, *Geophys. Res. Lett.* 34, L21203, doi:10.1029/2007GL031467.

Goldreich, P. and W. R. Ward, (1973) The formation of planetesimals. The Astrophysical Journal 183, 1051-1062. https://doi.org/10.1086/152291

Goldsby, D. L. and D. L. Kohlstedt (2001). Superplastic deformation of ice: Experimental observations. *J. Geophys. Res.* 106, 11,017–11,030. https://doi.org/10.1029/2000JB900336

Gomes, R., Levison, H.F., Tsiganis, K., Morbidelli A., (2005). Origin of the cataclysmic Late Heavy Bombardment period of the terrestrial planets. *Nature* 435, 466-469.

Gray, J. N. M. T., Shearer, M., Thornton, A. R., (2006). Time-dependant solutions for particle-size segregation in shallow granular avalanches. *Proceed. Royal Society A: Math., Phys., and Eng. Sci.* 462. https://doi.org/10.1098/rspa.2005.1580

Grott, M., Hauber, E., Werner, S. C., Kronberg, P., Neukum, G., (2005). High heat flux on ancient Mars: Evidence from rift flank uplift at Coracis Fossae, *Geophys. Res*. Lett. 32, L21201. doi:10.1029/2005GL023894.

Haeberli, W., Hallet, B., Arenson, L., Elconin, R., Humlum, O., Kääb, A., Kaufmann, V., Ladanyi, B., Matsuoka, N., Springman, S., Mühll, D.V., (2006). Permafrost creep and rock glacier dynamics. *Permafrost and Periglacial Processes* 17, 189-214. https://doi.org/10.1002/ppp.561

Hayne, P. O. and O. Aharonson, (2015). Thermal stability of ice on Ceres with rough topography. *Journal of Geophysical Research: Planets*, 120, 1567–1584. https://doi.org/10.1002/2015JE004887

Head, J.W., Marchant, D.R., Dickson, J.L., Kress, A.M., Baker, D.M., (2010). Northern mid-latitude glaciation in the Late Amazonian period of Mars: Criteria for the recognition of debris-covered glacier and valley glacier landsystem deposits. *Earth and Planetary Science Letters* 194, 306-320. https://doi.org/10.1016/j.epsl.2009.06.041

Heather, D. J. and S. K. Dunkin (2003). Geology and stratigraphy of King crater, lunar farside. *Icarus* 163, 307-329. https://doi.org/10.1016/S0019-1035(02)00063-5

Hiesinger, H., Marchi, S., Scmedemann, N., Schenk, P., Pasckert, J. H., Neesemann, A., O'Brian, D. P., Kneissl. T., Ermakov, A. I., Fu, R. R., Bland, M. T., Nathues, A., Platz, T., Williams, D. A., Jaumann, R., Castillo-Rogez, J. C., Ruesch, O., Schmidt, B., Park, R. S., Pruesker, F., Buczkowski, D. L., Russell, C. T., Raymond, C. A., (2016). Cratering on Ceres Implications for its crust and evolution. *Science* 353, Issue 6303. https://doi.org/10.1126/science.aaf4759

Holsapple, K. A., (1993). The scaling of impact processes in planetary sciences. *Annu. Rev. Earth Planet. Sci.* 21, 333-373. https://doi.org/10.1146/annurev.ea.21.050193.002001

Horner, V. M., and R. Greeley, (1982). Pedestal craters on Ganymede. *Icarus* 51, 549-562. https://doi.org/10.1016/0019-1035(82)90145-2

Howard, K. A., (1972). Ejecta blankets of large craters exemplified by King crater, Apollo 16 Preliminary Science Report, NASA Spec. Publ. SP-315, pp. 29-70-29-77

Hsieh, H. H. and D. Jewitt (2006). A population of comets in the main asteroid belt. *Science* 312, 561-563. DOI: 10.1126/science.1125150

Hughson, K. H. G., Russell, C. T., Williams, D. A., Buczkowski, D. L., Mest, S. C., Pasckert, J. H., Scully, J. E. C., Combe, J. -P., Platz, T., Ruesch, O., Preusker, F., Jaumann, R., Nass, A., Roatsch, T., Nathues, A., Schaefer, M., Schmidt, B. E., Chilton, H. T., Ermakov, A.,

Singh, S., McFadden, L. A., & Raymond, C. A., (2018). The Ac-5 (Fejokoo) quadrangle of Ceres: Geologic map and geomorphological evidence for ground ice mediated surface processes. *Icarus* 316, 63–83. https://doi.org/10.1016/j.icarus.2017.09.035

Hughson, K. H. G., Russell, C. T., Schmidt, B. E., Chilton, H. T., Sizemore, H., Schenk, P. M., Raymond, C. A., (2019a). Fluidized appearing ejecta on Ceres: Implications for the mechanical properties, frictional properties, and composition of its shallow subsurface. *Journal of Geophysical Research:Planets* 124. https://doi.org/10.1029/2018JE005666

Hughson, K. H. G., Russell, C. T., Schmidt, B. E., Travis, B., Preusker, F., Neesemann, A., Sizemore, H. G., Schenk, P. M., Buczkowski, D. L., Castillo-Rogez, J. C., Raymond, C. A., (2019b). Normal faults on Ceres: Insights into the mechanical properties and thermal history of Nar Sulcus. *Geophysical Research Letters* 46, 80-88. https://doi.org/10.1029/2018GL080258

Humlum, O., (2000). The geomorphic significance of rock glaciers: estimates of rock glacier debris volumes and headwall recession rates in West Greenland. *Geomorphology* 35, 41-67. https://doi.org/10.1016/S0169-555X(00)00022-2

Jaumann, R., Clark, R. N., Nimmo, F., Hendrix, A. R., Buratti, B. J., Denk, T., Moore, J. M., Schenk, P. M., Ostro, S. J., Srama, R., (2009). Icy satellites: Geological evolution and surface processes, pp 637-681. In Doughty, M. K., Esposito, L. W., Krimigis, S. M. (eds) *Saturn from Cassini-Huygens*. Dordrecht: Springer. https://doi.org/10.1007/978-1-4020-9217-6_20

Jaumann, R., Stephan, K., Krohn, K., Matz, K.-D., Otto., K., Neumann, W., Kneissl, T., Schmedemann, N., Schroeder, S., Tosi, F., De Sanctis, M.C., Preusker, F., Buczkowski, D.L., Capacioni, F., Carsentry, U., Elgner, S., vod der Gathen, I., Giebner, T., Hiesinger,

H., Hoffmann, M., Kersten, E., Li, J.-Y., McCord, T.B., McFadden, L., Mottola, S., Nathues, A., Neesemann, A., Raymond, C.A., Roatsch, T., Russell, C.T., Schmidt, B., Schulzeck, F., Wagner, R., Williams, D.A., (2016). A*ge-dependent morphological and compositional variations on Ceres*. Paper presented in Lunar Planet. Sci. XLVII, Abstract 1455.

Jaumann, R., Williams, D. A., Buczkowski, D. L., Yingst, R. A., Preusker, F., Hiesinger, H., et al., (2012). Vesta's shape and morphology. *Science* 336, Issue 6082, 687-690. DOI: 10.1126/science.1219122

Jia, J., Liang, Y., Tsuji, T., Murrata, S., Matsuoka, T., (2016). Microscopic origin of strain hardening in methane hydrate. *Scientific Reports* 6, Article number: 23548. doi:10.1038/srep23548

Jones, E., Caprarelli, G., Osinski, G. R., (2016). Insights into complex layered ejecta emplacement and subsurface stratigraphy in Chryse Planitia, Mars, through an analysis of THEMIS brightness temperature data, *J. Geophys. Res. Planets* 121, 986–1015. doi:10.1002/2015JE004879

Komatsu, G., Ori, G. G., Di Lorenzo, S., Rossi, A. P., Neukum, G., (2007). Combinations of processes responsible for martian impact crater ‘‘layered ejecta structures’’ emplacement. *J. Geophys. Res.: Planets* 112 (E6). http://dx.doi.org/10.1029/2006JE002787

Kneissl, T., van Gasselt, S., Neukum, G., (2011). Map-projection-independent crater size-frequency determination in GIS environments - New software tool for ArcGIS. *Planetary and Space Science* 59, 1243-1254. https://doi.org/10.1016/j.pss.2010.03.015

Kneissl, T., Schmedemann, N., Neesemann, A., Raymond, C. A., Russell, C. T., (2014). *Crater counting on small bodies - The influence of topography-related distortions*. Paper presented at Lunar Planet. Sci. XLV, Abstract 2398.

Kneissl, T., Michael, G. G., Platz, T., Walter, S. G. H., (2015). Age determination of linear surface features using the Buffered Crater Counting approach – Case studies of the Sirenum and Fortuna Fossae graben systems on Mars. *Icarus* 250, 384-394. https://doi.org/10.1016/j.icarus.2014.12.008.

Konopliv, A. S., Park, R. S., Vaughan, A. T., Bills, B. G., Asmar, S. W., Ermakov, A. I., Rambaux, N., Raymond, C. A., Castillo-Rogez, J. C., Russell, C. T., Smith, D. E., Zuber, M. T., (2018). The Ceres gravity field, spin pole, rotation period and orbit from the Dawn radiometric tracking and optical data. *Icarus* 299, Pages 411-429, ISSN 0019-1035, https://doi.org/10.1016/j.icarus.2017.08.005.

Konopliv, A.S., Asmar, S.W., Bills, B.G., Mastrodemos, N., Park, R.S., Raymond, C.A., Smith, D.E., Zuber, M.T., (2011). The Dawn gravity investigation at Vesta and Ceres. *Space Science Reviews* 163, 461-486. https://doi.org/10.1007/978-1-4614-4903-4_15

Kraus, R. G., Senft, L. E., and S. T. Stewart, (2011). Impacts onto H2O ice: Scaling laws for melting, vaporization, excavation, and final crater size. *Icarus* 214, 724-738. doi:10.1016/j.icarus.2011.05.016E

Krohn, K., Jaumann, R., Otto, K., Hoogenboom, T., Wagner, R., Buczkowski, D.L., Garry, B., Williams, D.A., Yingst, R.A., Scully, J., De Sanctis, M.C., Kneissl, T., Schmedemann, N., Kersten, E., Stephan, K., Matz, K.-D., Pieters, C.M., Preusker, F., Roatsch, T., Schenk, P., Russell, C.T., Raymond, C.A., (2014). Mass movement on Vesta at steep scarps and crater rims. *Icarus* 244, 120-132. https://doi.org/10.1016/j.icarus.2014.03.013

Kuppers, M., O'Rourke, L., Bockelee-Morvan, D., Zakharov, V., Lee, S., von Allmen, P., Carry, B., Teyssier, D., Martson, A., Muller, T., Crovisier, J., Barucci, M. A., Moreno, R., (2014). Localized sources of water vapour on the dwarf planet (1) Ceres. *Nature* 505, 525-527. https://doi.org/10.1038/nature12918

Kusznir, N. J., G. Marsden, and S. S. Egan, (1991). A flexural-cantilever simple-shear/pure-shear model of continental lithosphere extension: applications to the Jeanne d'Arc Basin, Grand Banks and Viking graben, North Sea. In: Roberts, A.M., Yielding, G., Freeman, B. (Eds.), *The Geometry of Normal Faults*. Geological Society, Special Publication, 56, 41-60. https://doi.org/10.1144/GSL.SP.1991.056.01.04

Lagrange, A.-M., Bonnefoy, M., Chauvin, G., Apai, D., Ehenreich, D., Boccaletti, A., Gratadour, D., Rouan, D., Mouillet, D., Lacour, S., Kasper, M., (2010). A Giant Planet Imaged in the Disk of the Young Star β Pictoris. *Science* 329, 57-59. 10.1126/science.1187187

Lambeck, K., (1983). Structure and evolution of the intracratonic basins of central Australia. *Geophysical Journal of the Royal Astronomical Society* 74, 843-886. doi:10.1111/j.1365-246X.1983.tb01907.

Le Corre, L., Reddy, V., Schmedemann, N., Becker, K. J., O'Brian, D. P., Yamashita, N., Peplowski, P. N., Prettyman, T. H., Li, J.-Y., Cloutis, E. A., Denevi, B. W., Kneissl, T., Palmer, E., GAskell, R. W., Nathues, A., Gaffey, M. J., Mittlefehldt, D. W., Garry, W. B., Sierks, H., Russell, C. T., Raymond, C. A., De Sanctis, M. C., Ammanito, E., (2013). Olivine or impact melt: Nature of the "Orange" material on Vesta from Dawn. *Icarus* 226, 1568-1594. https://doi.org/10.1016/j.icarus.2013.08.013

Legros, F., (2002). The mobility of long run-out landslides. *Eng. Geol.* 63, 301-331. https://doi.org/10.1016/S0013-7952(01)00090-4

Li, J.-Y., Reddy, V., Nathues, A., Le Corre, L., Izawa, M.R.M., Clouts, E.A., Sykes, M.V., Carsentry, U., Castillo-Rogez, J.C., Hoffmann, M., Jaumann, R., Krohn, K., Mottola, S., Prettyman, T.H., Schaefer, M., Schenk, P., Schröder, S.E., , D.A., Smith, D.E., Zuber, M.T., Konopliv, A.S., Park, R.S., Raymond, C.A., Russell, C.T., (2016). Surface albedo and spectral variability of Ceres. Astrophysical Journal Letters 817, L22. http://dx.doi.org/10.3847/2041-8205/817/2/L22

Li, L., Yue, Z., Di, K. and M. Peng, (2015). Observations of Martian layered ejecta craters and constraints on their formation mechanisms. *Meteorit. Planet. Sci.* 50, 508–522. doi:10.1111/maps.12438

Lowry, A. R. and R. B. Smith, (1994). Flexural rigidity of the Basin and Range-Colorado Plateau-Rocky Mountain transition from coherence analysis of gravity and topography, *J. Geophys. Res.*, 99 (B10), 20123–20140. doi: 10.1029/94JB00960

Lucchitta B. K., (1987). Valles Marineris, Mars: Wet debris flows and ground ice. *Icarus* 72, 411–429. https://doi.org/10.1016/0019-1035(87)90183-7

Malin, M. C., (1992). Mass movements on Venus: preliminary results from Magellan cycle 1 observations. *J. Geophys. Res.* 97, 16337-16352. https://doi.org/10.1029/92JE01343

Marchi, S., Bottke, W. F., Cohen, B. A., Wunnemann, K., Kring, D. A., McSween, H. Y., De Sanctis, M. C., O'Brien, D. P., Schenk, P., Raymond, C. A., Russell, C. T., (2013). High-velocity collisions from the lunar cataclysm recorded in asteroidal meteorites. *Nat. Geosci.* 6, 303-307. https://doi.org/10.1038/ngeo1769

Marchi, S., Ermakov, A. I., Raymond, C. A., Fu, R. R., O'Brien, D. P., Bland, M. T., Ammannito, E., De Sanctis, M. C., Bowling, T., Schenk, P., Scully, J. E. C., Buczkowski,

D. L., Williams, D. A., Hiesinger, H., Russell, C. T., (2016). The missing large impact craters on Ceres. *Nature Communications*, article 12257. DOI: 10.1038/ncomms12257

Marchi, S., Massironi, M., Vincent, J. –B., Mobidelli, A., Mottola, S., Marzari, S., Kuppers, M., Besse, S., Thomas, N., Barberi, C., Maletto, G., Sierks, H., (2012). The cratering history of asteroid (21) Lutetia. *Planetary and Space Science* 66, 87-95. https://doi.org/10.1016/j.pss.2011.10.010

Matson D. L., Castillo-Rogez J. C., Schubert G., Sotin C., McKinnon W. B., (2009). The Thermal Evolution and Internal Structure of Saturn's Mid-Sized Icy Satellites. In: Dougherty M.K., Esposito L.W., Krimigis S.M. (eds), *Saturn from Cassini-Huygens*. Springer, Dordrecht.

Matsuoka, N., Ikeda, A., Date, T., (2005). Morphometric analysis of solifluction lobes and rock glaciers in the Swiss Alps. *Permafrost and Periglacial Processes* 16, 99-113. https://doi.org/10.1007/978-1-4020-9217-6_18

McCord, T. B. and J. E. C. Scully, (2015). The composition of Vesta from the Dawn mission. *Icarus* 259, 1-9. https://doi.org/10.1016/j.icarus.2015.03.022

McCord, T. B. and C. Sotin, (2005). Ceres: Evolution and current state. *Journal of Geophysical Research Planets* 110, E05009. https://doi.org/10.1029/2004JE002244

McNutt, M. K., (1984). Lithospheric flexure and thermal anomalies, *J. Geophys. Res.* 89, 11,180–11,194. https://doi.org/10.1029/JB089iB13p11180

McSween, H. Y., Binzel, R. P., De Sanctis, M. C., Ammannito, E. , Prettyman, T. H., Beck, A. W., Reddy, V., Corre, L., Gaffey, M. J., McCord, T. B., Raymond, C. A., Russell, C. T., (2013). Dawn; the Vesta–HED connection; and the geologic context for eucrites,

diogenites, and howardites. *Meteorit. Planet. Sci.* 48: 2090-2104. doi:10.1111/maps.12108

Melosh, H. J., (1979). Acoustic fluidization: A new geologic process?, *J. Geophys. Res.*, 84(B13), 7513–7520. doi:10.1029/JB084iB13p07513

Melosh, H. J., (1989). *Impact Cratering: A Geologic Process*. Oxford University Press: Oxford Monographs on Geology and Geophysics No. 11.

Michael, G. G., and G. Neukum, (2010). Planetary surface dating from crater size – frequency distribution measurements: Partial resurfacing events and statistical age uncertainty. *Earth and Planetary Science Letters* 294, 223-229. https://doi.org/10.1016/j.epsl.2009.12.041

Michael, G. G., Kneissl, T., and A. Neesemann, (2016). Planetary surface dating from crater size-frequency distribution measurements: Poisson timing analysis. *Icarus* Vol. 277, 279-285. doi: 10.1016/j.icarus.2016.05.019

Morbidelli, A., Bottke, W. F., Nesvorny, D., Levison, H. F., (2009). Asteroids were born big. Icarus 204, 558-573. https://doi.org/10.1016/j.icarus.2009.07.011

Mouginis-Mark, P., (1979). Martian fluidized crater morphology: Variations with crater size, latitude, altitude, and target material. *J. Geophys. Res*. 84 (B14), 8011–8022. http://dx.doi.org/10.1029/JB084iB14p08011

Mouginis-Mark, P., (1981). Ejecta emplacement and models of formation of martian fluidized ejecta craters. *Icarus* 45, 60-76. https://doi.org/10.1016/0019-1035(81)90006-3

Mouginis-Mark, P.J., (1987). Water or ice in the martian regolith?: Clues from rampart craters seen at very high resolution. *Icarus* 71 (2), 268–286. http:// dx.doi.org/10.1016/0019-1035(87)90152

Mouginis-Mark, P. J. and S. M. Baloga, (2006). Morphology and geometry of the distal ramparts of martian impact craters. *Meteor. Planet. Sci*. 41 (10), 1469–1482. http://dx.doi.org/10.1111/j.1945-5100.2006.tb00430.x

Nadai, A., (1963). *Theory of Flow and Fracture of Solids, Volume II*. New York: McGraw-Hill.

Nass, A. and The Dawn Mapping Team, (2017). One GID-based data structure for geologic mapping using 15 map sheets – Dawn at Ceres. Paper presented at Lunar Planet. Sci. XLVIII, Abstract 1892.

Nathues, A., Hoffmann, M., Schaefer, M., Le Corre, L., Reddy, V., Platz, T., Cloutis, E. A., Christensen, U., Kneissl, T., Li, J. -Y., Mengel, K., Schmedemann, N., Schaefer, T., Russell, C. T., Applin, D. M., Buczkowski, D. L., Izawa, M. R. M., Keller, H. U., O'Brien, D. P., Pieters, C. M., Raymond, C. A., Ripken, J., Schenk, P. M., Schmidt, B. E., Sierks, H., Sykes, M. V., Thangjam, G. S., Vincent, J. -B., (2015). Sublimation in bright spots on (1) Ceres. *Nature* 528, 237-240. https://doi.org/10.1038/nature15754

Nathues, A., Platz, T., Hoffmann, M., Thangjam, G., Cloutis, E. A., Applin, D. M., Le Corre, L., Reddy, V., Mengel, K., Protopapa, S., Takir, D., Preusker, F., Schmidt, B. E., Russell, C. T., (2017). Oxo crater on (1) Ceres: Geological history and the role of water-ice. *Astronomical Journal* 154, 1538-3881. https://doi.org/10.3847/1538-3881/aa7a04

Neumann, W., Breuer, D., and T. Spohn, (2014). Differentiation of Vesta: Implications for a Shallow Magma Ocean. *EPSL* 395, 267-280. https://doi.org/10.1016/j.epsl.2014.03.033

Nimmo, F., and R. T. Pappalardo, (2004). Furrow flexure and ancient heat flux on Ganymede, *Geophys. Res. Lett*. 31, L19701. doi:10.1029/ 2004GL020763

Nimmo, F., Pappalardo, R. T., and B. Giese, (2002). Effective elastic thickness and heat flux estimates on Ganymede, *Geophys. Res. Lett.* 29(7), 1158. doi:10.1029/2001GL013976

Nimmo, F., and P. Schenk, (2006). Normal faulting on Europa: implications for ice shell properties. *Journal of Structural Geology* 28, 2194-2203. doi:10.1016/j.jsg.2005.08.009

Oberbeck, V. R., (1975). The role of ballistic erosion and sedimentation in lunar stratigraphy. Rev. *Geophys.*, 13(2), 337–362. doi:10.1029/RG013i002p00337

O'Brien, D. P., and M. V. Sykes, (2011). The Origin and Evolution of the Asteroid Belt – Implications for Vesta and Ceres. *Space Science Reviews* 163, 41-61. https://doi.org/10.1007/978-1-4614-4903-4_4

O'Rourke, J. G., and S. E. Smrekar, (2018). Signatures of lithospheric flexure and elevated heat flow in stereo topography at coronae on Venus. *Journal of Geophysical Research: Planets* 123, 369–389. https://doi.org/10.1002/2017JE005358

Osinski, G. R., (2006). Effect of volatiles and target lithology on the generation and emplacement of impact crater fill and ejecta deposits on Mars. *Meteor. Planet. Sci.* 41 (10), 1571–1586. http://dx.doi.org/10.1111/j.1945-5100.2006.tb00436.x

Park, R. S., Konopliv, A. S., Bills., B. G., Rambaux, N., Castillo-Rogez, J. C., Raymond, C. A., Vaughan, A. T., Ermakov, A., Zuber, M. T., Fu, R. R., Toplis, M. J., Russell, C. T., (2016). A partially differentiated interior for (1) Ceres deduced from its gravity field and shape. *Nature* 537, 515-517. https://doi.org/10.1038/nature18955

Osinski, G. R., (2006). Effect of volatiles and target lithology on the generation and emplacement of impact crater fill and ejecta deposits on Mars. *Meteor. Planet. Sci.* 41 (10), 1571–1586. http://dx.doi.org/10.1111/j.1945-5100.2006.tb00436.x

Pasckert, J. H., Hiesinger, H., Ruesch, O., Williams, D. A., Kneissl, T., Mest, S. C., Buczkowski, D. L., Scully, J. E. C., Schmedemann, N., Jaumann, R., Roatsch, T., Preusker, F., Nass, A., Nathues, A., Hoffman, M., Schaefer, M., De Sanctis, M. C., Raymond, C. A., Russell,

C. T., (2018). Geologic mapping of the Ac-2 Coniraya Quadrangle of Ceres from NASA's Dawn Mission: Implications for a heterogeneously composed crust. *Icarus* 316, 28-45. https://doi.org/10.1016/j.icarus.2017.06.015

Pedregosa, F., Varoquaux, G., Gramfort, A., Michel, V., Thirion, B., Grisel, O., Blondel, M., Prettenhofer, P., Weiss, R., Dubourg, V., Vanderplas, J., Passos, A., Cournapeau, D., Brucher, M., Perrot, M., Duchesnay, E., (2011). Scikit-learn: Machine learning in Python. *JMLR* 12, 2825-2830.

Pinte, C., Price, D. J., Menard, F., Duchene, G., Dent, W. R. F., Hill, T., de Gregorio-Monsalvo, I., Hales, A., Mentiplay, D., (2018). Kinematic evidence for an embedded protoplanet in a circumstellar disc. *ApJL* 860, L13; arXiv: 1805.10293. http://dx.doi.org/10.3847/2041-8213/aac6dc

Pitjeva, E., (2003). The dynamic estimation of the mass of the main belt. Highlights in Astronomy, vol. 13, ed. O. Engvold, 772-773.

Platz, T., Nathues, A., Sizemore, H. G., Crown, D. A., Hoffmann, M., Schaefer, M., Schmedemann, N., Kneissl T., Neesemann, A., Mest, S. C., Buczkowski, D. L., Ruesch, O., Hughson, K. H. G., Nass, A., Williams, D. A., Pruesker, F., (2018). Geological mapping of the Ac-10 Rongo Quadrangle of Ceres. *Icarus* 316, 140-153. https://doi.org/10.1016/j.icarus.2017.08.001

Porco, C. C., Baker, E., Barbara, J., Beurle, K., Brahic, A., Burns, J. A., Charnoz, S., Cooper, N., Dawson, D. D., Del Genio, A. D., Denk, T., Dones, L., Dyudina, U., Evans, M. W., Giese, B., Grazier, K., Helfenstein, P., Ingersoll, A. P., Jacobsson, R. A., Johnsom, T. V., McEwen, A., Murray, C. D., Neukum, G., Owen, W. M., Perry, J., Roatsch, T., Spitale, J., Squyres, S., Thomas, P. C., Tiscareno, M., Turtle, E., Vasavada, A. R., Veverka, J.,

Wagner, R., West, R., (2005). Cassini imaging science: Initial results on Phoebe and Iapetus. *Science* 307, 1237-1242. https://doi.org/10.1126/science.1107981

Prettyman, T. H., Feldman, W. C., McSween, H. Y., Dingler, R. D., Enemark, D. C., Patrick, D. E., Storms, S. A., Hendricks, J. S., Morgenthaler, J. P., Pitman, K. M., Reedy, R. C., (2011). Dawn's gamma ray and neutron detector. *Space Science Reviews* 163, 371-459. https://doi.org/10.1007/s11214-011-9862-0

Prettyman, T. H., Yamashita, N., Toplis, M. J., McSween, H. Y., Schorghofer, N., Marchi, S., Feldman, W. C., Castillo-Rogez, J. C., Forni, O., Lawrence, D. J., Ammannito, E., Ehlmann, B. L., Sizemore, H. G., Joy, S. P., Polanskey, C. A., Rayman, M. D., Raymond, C. A., Russell, C. T., (2017). Extensive water ice within Ceres' aqueously altered regolith: Evidence from nuclear spectroscopy. *Science* 355 (6320), 55–59. https://doi.org/10.1126/science.aah6765

Preusker, F., Scholten, F., Matz, K. -D., Elfner, S., Jaumann, R., Roatsch, T. Joy, S. P., Polanskey, C. A., Raymond, C. A., Russell, C. T., (2016). *Dawn at Ceres – Shape model and rotation state*. Paper presented at Lunar Planet. Sci. XLVII, Abstract 1954.

Ramana, Y., V., and B. S. Gogte, (1989). Dependence of coefficient of sliding friction in rocks on lithology and mineral characteristics. *Engineering Geology* 26, 271-279. https://doi.org/10.1016/0013-7952(89)90014-8

Ranalli, G., (1995). *Rheology of the Earth*, 2nd ed., Chapman and Hall, London.

Richardson, J. E., Melosh, H. J., Artemeiva, N. A., Pierazzo, E., (2005). Impact Cratering Theory and Modeling for the Deep Impact Mission: From Mission Planning to Data Analysis. *Space Sci. Rev.* 117:241. https://doi.org/10.1007/s11214-005-3393-5

Rivkin, A. S., Volquardsen, E. L., Clark, B. E., (2006). The surface composition of Ceres: Discovery of carbonates and iron-rich clays. *Icarus* 185, 563-567. https://doi.org/10.1016/j.icarus.2006.08.022

Roatsch, T., Kersten, E., Matz, K. -D., Preusker, F., Scholten, F., Jaumann, R., Raymond, C. A., Russell, C. T., (2016a). Ceres survey atlas derived from Dawn Framing Camera images. *Planetary and Space Science* 121, 115-120. https://doi.org/10.1016/j.pss.2015.12.005

Roatsch, T., Kersten, E., Matz, K. -D., Preusker, F., Scholten, F., Jaumann, R., Raymond, C. A., Russell, C. T., (2016b). High-resolution Ceres high altitude mapping orbit atlas derived from Dawn Framing Camera images. *Planetary and Space Scien*ce 129, 103-107. https://doi.org/10.1016/j.pss.2016.05.011

Roatsch, T., Kersten, E., Matz, K. –D., Preusker, F., Scholten, F., Elgner, S., Schroeder, S. E., Jaumann, R., Raymond, C. A., Russell, C. T., (2016c). DAWN FC2 DERIVED CERES HAMO DTM SPG V1.0, DAWN-A-FC2-5-CERESHAMODTMSPG-V1.0. NASA Planetary Data System. https://pds-smallbodies.astro.umd.edu/data_sb/missions/dawn/index.shtml

Roatsch, T., Kersten, E., Matz, K. –D., Preusker, F., Scholten, F., Elgner, S., Schroeder, S. E., Jaumann, R., Raymond, C. A., Russell, C. T., (2016d). DAWN FC2 DERIVED CERES MOSAICS V1.0, DAWN-A-FC2-5-CERESMOSAIC-V1.0. NASA Planetary Data System. https://pds-smallbodies.astro.umd.edu/data_sb/missions/dawn/index.shtml

Robbins, S. J., Runyon, K., Singer, K. N., Bray, V. J., Beyer, R. A., Schenk, P., McKinnon, W. B., Grundy, W. M., Nimmo, F., Moore, J. M., Spencer, J. R., White, O. L., Binzel, R. P., Buie, M. W., Buratti, B. J., Cheng, A. F., Linscott, I. R., Reitsema, H. J., Reuter, D. C., Showalter, M. R., Len Tyler, G., Young, L. A., Olkin, C. B., Ennico, K. S., Weaver, H.

A., Stern, S. A,. (2018). Investigation of Charon's craters with abrupt terminus ejecta, comparisons with other icy bodies, and formation implications. *Journal of Geophysical Research: Planets* 123, 20–36. https://doi.org/10.1002/2017JE005287

Rosenblatt, M., (1956). Remarks on Some Nonparametric Estimates of a Density Function. *Ann. Math. Statist.* 27, no. 3, 832--837. doi:10.1214/aoms/1177728190

Rubin, A. E., Trigo-Rodriguez, J. M., Huber, H., Wasson, J. T., (2007). Progressive aqueous alteration of CM carbonaceous chondrites. *Geochemica et Cosmochemica Acta* 71, 2361-2382. https://doi.org/10.1016/j.gca.2007.02.008

Ruesch, O., McFadden, L. A., Williams, D. A., Hughson, K. H. G., Pasckert, J. H., Scully, J. E. C., Kneissl, T., Roatsch, T., Platz, T., Preusker, F., Schmedemann, N., Marchi, S., Hiesinger, H., Jaumann, R., Nathues, A., Raymond, C. A., Russell, C. T., (2018). Geology of Ceres' north pole quadrangle with Dawn FC imaging data. *Icarus* 316, 14-27. https://doi.org/10.1016/j.icarus.2017.09.036

Ruesch, O., Platz, T., Schenk, P., McFadden, L. A., Castillo-Rogez, J. C., Byrne, S., Preusker, F., O'Brien, D. P., Schmedemann, N., Williams, D. A., Li, J. -Y., Bland, M. T., Hiesinger, H., Kneissl, T., Neesemann, A., Schaefer, M., Pasckert, J. H., Schmidt, B., Buczkowski, D. L., Sykes, M. V., Nathues, A., Roatsch, T., Haffmann, M., Rayman, C. A., Russell, C. T., (2016). Cryovolcanism on Ceres. *Science* 353, issue 6303. doi: 10.1126/science.aaf4286.

Ruiz, J., (2005). The heat flow of Europa. Icarus, 177, 438 – 446. https://doi.org/10.1016/j.icarus.2005.03.021

Ruiz, J., P. J. McGovern, and R. Tejero, (2006). The early thermal and magnetic state of the cratered highlands of Mars. Earth *Planet. Sci. Lett*. 241, 2 – 10. doi: 10.1016/j.epsl.2005.10.016

Runyon, K. D. and O. S. Barnouin, (2018). Preliminary laboratory investigations of ejecta emplacement dynamics and morphology with planetary applications. *Planetary and Space Science* 160, 39-55. https://doi.org/10.1016/j.pss.2018.03.014

Russell, C.T. and C. A. Raymond, (2011). The Dawn mission to Vesta and Ceres. *Space Sci. Rev.* 163: 3-23. https://doi.org/10.1007/s11214-011-9836-2

Russell, C. T., Raymond, C. A., Ammannito, E., Buczkowski, D. L., De Sanctis, M. C., Hiesinger, H., Jaumann, R., Konopliv, A. S., McSween, H. Y., Nathues, A., Park, R. S., Pieters, C. M., Prettyman, T. H., McCord, T. B., McFadden, L. A., Mottola, S., Zuber, M. T., Joy, S. P., Polanskey, C., Rayman, M. D., Castillo-Rogez, J. C., Chi, P .J., Combe, J. -P., Ermakov, A., Fu, R. R., Hoffmann, M., Jia, Y. D., King, S. D., Lawrence, D .J., Li, J. -Y., Marchi, S., Preusker, F., Roatsch, T., Ruesch, O., Schenk, P., Villarreal, M. N., Yamashita, N., (2016). Dawn arrives at Ceres: Exploration of a small volatile-rich world. *Science* 353, 1008-1010. DOI: 10.1126/science.aaf4219

Savigny, K.W. and N. R. Morgenstern, (1986). In situ creep properties in ice-rich permafrost soil. *Canadian Geotechnical Journal* 23, 504-514. doi/10.1139/t86-080

Schafer, M., Nathues, A., Williams, D. A., Mittlefedhldt, D. W., Le Corre, L., Buczkowski, D. L., Kneissl, T., Thangjam, G. S., Hoffmann, M., Schmedmann, N., Schafer, T., Scully, J. E. C., Li., J. -Y., Reddy, V., Garry, W. B., Krohn, K., Yingst, R. A., Gaskell, R. W., Russell, C. T., (2014). Imprint of the Rheasilvia impact on Vesta – Geologic mapping of

quadrangles Gegania and Lucaria. *Icarus* 244, 60-73. https://doi.org/10.1016/j.icarus.2014.06.026

Schenk, P. M., (1989). Crater formation and modification on the icy satellites of Uranus and Saturn: Depth/diameter and central peak occurrence. *Journal of Geophysical Research* 94, 3813-3832. https://doi.org/10.1029/JB094iB04p03813

Schenk, P., (2010). Atlas of the Galilean satellites: Ganymede. In *Atlas of the Galilean Satellites*. Cambridge, UK: Cambridge University Press.

Schmedemann, N., Kneissl, T., Ivanov, B. A., Michael, G. G., Wagner, R. J., Neukum, G., Ruesch, R., Hiesinger, H., Krohn, K., Roatsch, T., Preusker, F., Sierks, H., Jaumann, R., Reddy, V., Nathues, A., Walter, S. H. G., Neesemann, A., Raymond, C. A., Russell, C. T., (2014). The cratering record, chronology and surface ages of (4) Vesta in comparison to smaller asteroids and the ages of HED meteorites. *Planetary and Space Science* 103, 104-130. http://dx.doi.org/10.1016/j.icarus.2013.05.037

Schmedemann, N., Kneissl, T., Neesemann, A., Stephan, K., Jaumann, R., Krohn, K., Michael, G. G., Matz, K. D., Otto, K. A., Raymond, C. A., Russell, C. T., (2016). Timing of optical maturation of recently exposed material on Ceres. *Geophysical Research Letters* 43, 11987-11993. https://doi.org/10.1002/2016GL071143

Schmidt, B. E., Hughson, K. H. G., Chilton, H. T., Scully, J. E. C., Platz, T., Nathues, A., Sizemore, H., Bland, M. T., Byrne, S., Marchi, S., O'Brian, D. P., Schorghofer, N., Hiesinger, H., Jaumann, R., Pasckert, J. H., Lawrence, J. D., Castillo-Rogez, J. C., Sykes, M. V., Schenk, P .M., De Sanctis, M. C., Mitri, G., Formisano, M., Li, J. -Y., Reddy, V., LeCorre, L., Russell, C. T., Raymond, C. A., (2017). Geomorphological evidence for

ground ice on dwarf planet Ceres. *Nature Geoscience* 10, 338-343. https://doi.org/10.1038/ngeo2936

Schorghofer, N., Mazarico, E., Platz, T., Preusker, F., Schröder, S. E., Raymond, C. A., and Russell, C. T., (2016). The permanently shadowed regions of dwarf planet Ceres. *Geophys. Res. Lett.* 43, 6783–6789. doi:10.1002/2016GL069368

Schröder, S. E., Maue, T., Gutiérrez Marqués, P., Mottola, S., Aye, K. M., Sierks, H., Keller, H. U., Nathues, A., (2013). In-flight calibration of the Dawn framing camera. *Icarus* 226, 1304–1317. https://doi.org/10.1016/j.icarus.2013.07.036

Schröder, S. E., Mottola, S., Matz, K. -D., Roatsch, T., (2014). In-flight calibration of the Dawn framing camera II: Flat fields and stray light correction. *Icarus* 234, 99-108. https://doi.org/10.1016/j.icarus.2014.02.018

Schröder, S., Carsentry, U., Neesemann, A., McFadden, L., Marchi, S., Otto, K., Schenk, P., Jaumann, R., Raymond, C., Russell, C., (2016). Boulders on Ceres. *Geophysical Research Abstracts* 18, EGU2016-12693.

Schulson, E. M., and A. L. Fortt, (2012). Friction of ice on ice. *J. Geophys. Res.* 117, B12204, doi:10.1029/2012JB009219

Schultz, P. H., (1992). Atmospheric effects on ejecta emplacement. *J. Geophys. Res.* 97 (E7), 11623–11662. http://dx.doi.org/10.1029/92JE00613

Schultz, P. H. and D. E. Gault, (1979). Atmospheric effects on martian ejecta emplacement. *J. Geophys. Res. Solid Earth* 84 (B13), 7669–7687. http://dx.doi.org/10.1029/JB084iB13p07669

Scully, J. E. C., Yin, A., Russell, C. T., Buczkowski, D. L., Williams, D. L., Blewett, D. T., Ruesch, O., Hiesinger, H., Le Corre, L., Mercer, C., Yingst, R. A., Garry, W. B.,

Jaumann, R., Roatsch, T., Preusker, F., Gaskell, R. W., Schroder, S. E., Ammannito, E., Pieters, C. M., Raymond, C. A., (2014). Geomorphology and structural geology of Saturnalia Fossae and adjacent structures in the northern hemisphere of Vesta. *Icarus* 244, 23-40. https://doi.org/10.1016/j.icarus.2014.01.013

Scully, J. E. C., Buczkowski, D. L., Neesemann, A., Williams, D. A., Mest, S. C., Raymond, C. A., Hughson, K. H. G., Kneissl, T., Pasckert, J. H., Ruesch, O., Frigeri, A., Nass, A., Marchi, S., Combe, J.-P., Schmedemann, N., Schmidt, B. E., Chilton, H. T., Russell, C. T., Ermakov, A. I., Jaumann, R., Hoffmann, M., Nathues, A., Pieters, C. M., Platz, T., Preusker, F., Roatsch, T., Schaefer, M., (2018). Ceres' Ezinu quadrangle: A heavily cratered region with evidence for localized subsurface water ice and the context for Occator crater. *Icarus* 316, 46-62. https://doi.org/10.1016/j.icarus.2017.10.038

Scully, J. E. C., Russell, C. T., Castillo-Rogez, J. C., Raymond, C. A., Ermakov, A. I., (2019). Introduction to the special issue: The formation and evolution of Ceres' Occator crater. *Icarus* 320, 1-6. https://doi.org/10.1016/j.icarus.2018.02.029

Senft, L. E. and S. T. Stewart, (2008). Impact crater formation in icy layered terrains on Mars. *Met. Planet. Sci.* 43, 1993–2013. doi:10.1111/j.1945-5100.2008.tb00657.x

Senft, L. E. and S. T. Stewart, (2011). Modeling the morphological diversity of impact craters icy satellites. *Icarus* 214, 67-81. https://doi.org/10.1016/j.icarus.2011.04.015

Shoemaker, E. M., (1962). Interpretation of lunar craters. *Physics and astronomy of the Moon*, edited by Kopal, Z. New York: Academic Press. 283-359.

Shreve R. L., (1966). Sherman Landslide, Alaska. *Science* 154, 1639–1643. https://doi.org/10.1126/science.154.3757.1639

Sierks, H., Keller, H. U., Jaumann, R., Michalik, H., Behnke, T., Bubenhagen, F., Büttner, I., Casentry, U., Chritensen, U., Enge, R., Fiethe, B., Gutiérrez Marqués, P., Hartwig, H., Krüger, H., Kühne, W., Maue, T., Mottola, S., Nathues, A., Reiche, K. -U., Richards, M. L., Toatsch, T., Schröder, S. E., Szemerey, I., Tschentscher, M., (2011). The Dawn framing camera. *Space Science Reviews* 163, 263-327. https://doi.org/10.1007/s11214-011-9745-4

Silverman, B. W., (1986). *Density Estimation for Statistics and Data Analysis*. London: Chapman & Hall.

Singer, K. N., McKinnon, W. B., Schenk, P. M. & Moore, J. M., (2012). Massive ice avalanches on Iapetus mobilized by friction reduction during flash heating. *Nat. Geosci.* 5, 574–578. https://doi.org/10.1038/ngeo1526

Singh, S., Combe, J. –P., McFadden, L. A., McCord, T. B., Hughson, K. H. G., Zambon, F., Ciarniello, M., Carrozzo, G. G., Raponi, A., Ammannito, E., De Sanctis, M. C., Frigeri, A., Ruesch, O., Tosi, F., Longobardo, A., Palomba, E., Raymond, C. A., Russell, C. T., (2019). Mineralogy mapping of the Ac-H-5 Fejokoo quadrangle of Ceres. *Icarus* 318, 147-169. https://doi.org/10.1016/j.icarus.2018.08.025

Sizemore, H. G., Platz, T., Schorghofer, N., Prettyman, T. H., De Sanctis, M. C., Crown, D. A., Schmedemann, N., Neesemann, A., Kneissl, T., MArchi, S., Schenk, P. M., Blandm M. T., Schmidt, B. E., Hughson K. H. G., Tosi, F., Zambon, F., Mest, S. C., Yingst, R. A., Williams, D. A., Russell, C. T., Raymond, C. A., (2017). Pitted terrains on (1) Ceres and implications for shallow subsurface volatile distribution. Geophys. *Res. Lett.* 44, 6570–6578. doi:10.1002/2017GL073970

Sizemore, H. G., Schmidt, B. E., Buczkowski, D. L., Sori, M. M., Castillo-Rogez, J. C., Berman, D. C., Ahrens, C., Chilton, H. T., Hughson, K. H. G., Duarte, K., Otto, K. A., Bland, M. T., Neesemann, A., Scully J. E. C., Crown, D. A., Mest, S. C., Williams, D. A., Platz, T., Schenk, P., Landis, M. E., Marchi, S., Schorghofer, N., Quick, L. C., Prettyman, T. H., De Sanctis, M. C., Nass, A., Thangjam, G., Nathues, A., Russell, C. T., Raymond, C. A., (2018). A Global Inventory of Ice-Related Morphological Features on Dwarf Planet Ceres: Implications for the evolution and current state of the cryosphere. *Journal of Geophysical Research: Planets* 123. https://doi.org/10.1029/2018JE005699

Sori, M. M., Byrne, S., Bland, M. T., Bramson, A. M., Ermakov, A. I., Hamilton, C. W., Otto, K. A., Ruesch, O., Russell, C. T., (2017). The vanishing cryovolcanoes of Ceres. Geophys. *Res. Lett.* 44, 1243–1250. doi:10.1002/2016GL072319

Sori, M. M., Byrne, S., Hamilton, C. W., Landis, M. E., (2016). Viscous flow rates of icy topography on the north polar layered deposits of Mars. *Geophys. Res. Lett.* 43, 541–549. doi:10.1002/2015GL067298

Stein, N. T., Ehlmann, B. L., Palomba, E., De Sanctis, M. C., Nathues, A., Hiesinger, H., Ammannito, E., Raymond, C. A., Jaumann, R., Longbardo, A., Russell., C. T., (2017). The formation and evolution of bright spots on Ceres. *Icarus* 320, 188-201. https://doi.org/10.1016/j.icarus.2017.10.014

Stewart, S. T., J. D. O'Keefe, and T. J. Ahrens, (2001). *The relationship between rampart crater morphologies and the amount of subsurface ice*. Paper presented at Lunar Planet. Sci. XXXII. Abstract 2090.

Strom, A.,(2006). Morphology and internal structure of rockslides and rock avalanches: Grounds and constraints for their modelling. Landslides from Massive Rock Slope

Failure, S. G. Evans et al. (eds.). Springer. 305-326. https://doi.org/10.1007/978-1-4020-4037-5_17

Sylvest, M. E., Conway, S. J., Patel, M. R., Dixon, J. C., Barnes, A., (2016). Mass wasting triggered by seasonal CO2 sublimation under Martian atmospheric conditions: Laboratory experiments. *Geophys. Res. Lett.* 43, 12,363– 12,370. doi:10.1002/2016GL071022

Thomass, P. C., Parker, J. M., McFadden, L. A., Russell, C. T., Stern, S. A., Sykes, M. V., Young, E. F., (2005). Differentiation of the asteroid Ceres as revealed by its shape. *Nature* 437, 224-226. https://doi.org/10.1038/nature03938

Travis, B. J., Bland, P. A., Feldman, W. C., Sykes, M. V., (2018). Hydrothermal dynamics in a CM-based model of Ceres. *Meteorit. Planet. Sci.* 53, 2008-2032. doi:10.1111/maps.13138

Wada, K. and O. S. Barnouin-Jha, (2006). The formation of fluidized ejecta on Mars by granular flows. *Meteor. Planet. Sci.* 41 (10), 1551–1569. http://dx.doi.org/10.1111/j.1945-5100.2006.tb00435.x

Walsh, K. J., Morbidelli, A., Raymond, S. N., O'Brian, D. P., Mandall, A. M., (2011). A low mass for Mars from Jupiter's early gas-driven migration. *Nature* 475, 206-209. doi: 10.1038/nature10201

Watkins, J. A., B. L. Ehlmann, and A. Yin, (2015). Long-runout landslides and the long-lasting effects of early water activity on Mars. *Geology* 43, 107-110. doi:10.1130/G36215.1

Weertman, J., (1983). Creep deformation of ice. *Annu. Rev. Earth Planet. Sci.* 11, 215-240. https://doi.org/10.1130/G36215.1

Weiss, D. K., and J. W. Head, (2013). Formation of double-layered ejecta craters on Mars: A glacial substrate model. *Geophys. Res. Lett.* 40 (15), 3819–3824. http://dx.doi.org/10.1002/grl.50778

Weiss, D. K., and J. W. Head, (2014). Ejecta mobility of layered ejecta craters on Mars: Assessing the influence of snow and ice deposits. *Icarus* 233, 131-146. http://dx.doi.org/10.1016/j.icarus.2014.01.038

Weiss, D. K., and J. W. Head, (2018). Testing landslide and atmospheric-effects models for the formation of double-layered ejecta craters on Mars. *Meteorit. Planet. Sci. 53*, 741-777. doi:10.1111/maps.12859

Weissel, J. K., and G. D. Karner, (1989). Flexural uplift of rift flanks due to mechanical unloading of the lithosphere during extension. J. *Geophys. Res*. 94, 13,919 – 13,950. https://doi.org/10.1029/JB094iB10p13919

White, S. E., (1976). Rock glaciers and block fields, review and new data. *Quart. Rev.* 6, 77-97. https://doi.org/10.1016/0033-5894(76)90041-7

Williams, D. A., Buczkowski, D. L., Crown, D, A., Frigeri, A., Hughson, K. H. G., Kneissl, T., Krohn, K., Mest, S. C., Pasckert, J. H., Platz, T., Ruesch, O., Schulzeck, F., Scully, J. E. C., Sizemore, H., Nass, A., Jaumann, R. Raymond, C. A., Russell, C. T., (2018a). Unified Dawn LAMO-based global geologic map of Ceres. Paper presented at Lunar Planet. Sci. XLIX. Abstract 1614.

Williams, D. A., Buczkowski, D. L., Mest, S. C., Scully, J. E. C., Platz, T., Kneissl, T., (2018b). Introduction: The geologic mapping of Ceres. *Icarus* 316, 1-13. https://doi.org/10.1016/j.icarus.2017.05.004

Williams, D. A., Buczkowski, D. L., Mest, S. C., Scully, J. E. C., Krohn, K., Crown, D. A., Nass, A., Jaumann, R., Raymond, C. A., Russell, C. T., (2017). High-resolution geological mapping of dwarf planet Ceres from NASA's Dawn mission. Paper presented at Lunar Planet. Sci. XLVIII. Abstract 1451.

Williams, D. A., R. A. Yingst, and W. B. Garry, (2014). Introduction: The geological mapping of Vesta. *Icarus* 244, 1-12. https://doi.org/10.1016/j.icarus.2014.03.001

Woronow, A., (1981). Preflow stresses in martian rampart ejecta blankets: A means of estimating the water content. *Icarus* 45 (2), 320–330. http://dx.doi.org/10.1016/0019-1035(81)90037-3

Yasui, M., E. M. Schulson, and C. E. Renshaw, (2017). Experimental studies on mechanical properties and ductile-to-brittle transition of ice-silica mixtures: Young's modulus, compressive strength, and fracture toughness. *J. Geophys. Res. Solid Earth* 122, 6014–6030. doi: 10.1002/2017JB014029

Yingst, R.bA., Mest, S. C., Berman, D. C., Garry, W. B., Williams, D. A., Buczkowski, D., Jaumann, R., Pieters, C. M., De Sanctis, M. C., Frigeri, A., Le Corre, L., Preusker, F., Raymond, C. A., Reddy, V., Russell, C. T., Roatsch, T., Schenk, P. M., (2014). Geological mapping of Vesta. *Planetary and Space Science* 103, 2-23. https://doi.org/10.1016/j.pss.2013.12.014

Zolotov, M.Y., (2009). On the composition and differentiation of Ceres. *Icarus* 204, 183-193. https://doi.org/10.1016/j.icarus.2009.06.011